Australian National University

Optoelectronic Devices Based on Two Dimensional Materials

Yi Zhu

August 2020

THIS DISSERTATION IS SUBMITTED FOR THE DEGREE OF DOCTOR OF PHILOSOPHY OF THE AUSTRALIAN NAIONAL UNIVERSITY

Department of Electronic Materials Engineering

Research School of Physics

The Australian National University

Declaration

This dissertation reports the research I conducted during August 2016 to July 2020, at the Research School of Electrical, Energy and Materials Engineering, College of Engineering and Computer Science, and at the Department of Electronic Materials Engineering, Research School of Physics, the Australian National University, Canberra ACT, Australia.

To the best of my knowledge, the materials reported here is originally my own work except where acknowledged and referenced in appropriate manner. It has not been previously published by others or submitted in part or whole to any university for any degree, diploma, or other qualification.

Yi Zhu

August 2020

Acknowledgement

When I was a child, my grandfather always took me to the train station. I was so excited when the train came closer to the platform with clear and loud whistle. This massive iron beast impressed me in my childhood memories. Not only because of the powerful of the train, but also it was the most common way connects the outside world for mountain villagers. Gradually, it became a seed rooted in my heart that I want to work hard and go outside to see our beautiful planet. My childhood was never changed, and it always motivates me to explore the unknown world and encourages me to accomplish every goal along this journey.

As the famous Hellen Keller said, “Alone we can do so little; together we can do so much.” Many people have offered me generous support during my PhD life. Without those help, I would not achieve great success in such a short PhD time. This thesis and my academic success are dedicated to the tremendous contribution from the following individuals. I would like to express my most sincere gratitude to all of them.

First of all, I want to thank all my supervisors, A/Prof. Yuerui (Larry) Lu, Prof. Lan Fu and Prof. Chennupati Jagadish AC. It is my great privilege to join both NEMS in the Research School of Engineering and EME laboratories in the Research School of Physics at the Australian National University as a full time PhD student. Particularly, I would like to express my deepest gratitude towards my supervisor A/Prof. Yuerui (Larry) Lu for recognising and trusting me. He encouraged me to join his group and start my PhD program. In the research, he motivated me to learn active thinking, to do self-learning and to sharpen my problem-solving skills. I have to admit that it was very tough and frustrating at the beginning. However, I realized that I should never give it up. Once I have a little progress, I will become more and more confidence. Eventually, those experiences will become the truly treasures at the end of your PhD period. Therefore, I want to thank him for his unlimited enthusiasm and doing so much to forge my research capabilities. I would also like to thank Prof. Lan Fu for her constant guidance no matter in the research or in the toughest time of my PhD, and I benefitted immensely from her suggestions and wise approach. I would also

like to extend my gratitude to Prof. Chennupati Jagadish AC for his inspiration and enthusiasm for research. His encouragement is a source of energy for the research career.

Second, I would like to thank my lovely colleagues and lab mates Dr. Jiong Yang, Dr. Ankur Sharma, Dr. Shuang Zhang, Dr. Bo Wen, Dr. Jian Zhang, Dr. Linglong Zhang Yilin Tang, Ahmed Khan, Boqing Liu, Xueqian Sun, Bowen Wang, Han Yan and Sharidya Rahman for their constant help and support during my PhD. I really enjoy the time that we worked together to solve all kinds of research problems. It would always be the wonderful moments in my memory. Moreover, I would also like to thank Dr. Fan Wang, Dr. Ziyuan Li, Dr. Tobias Vogl, Dr. Hieu Nguyen, Baolei Liu and Kabilan Sripathy for training me on the optical setups and providing me with the valuable suggestions on designing optical measurements and instruments. In terms of the Australian National Fabrication Facility (ANFF), I would like to acknowledge Dr. Fouad Karouta and Dr. Kaushal Vora for their training and help in the nanofabrication field. Without their help, many of my design would not have been realized from scratch to the real world. I would like to express my appreciations to all my collaborators around the world for their support to my research in the past three years.

For my PhD program, I was fortunate to get the financial support from the Research School of Physics (RSPhys) for HDR Fee Remission Merit Scholarship. I would also like to thank A/Prof Yuerui (Larry) Lu and Prof. Lan Fu for covering my living expenses during my PhD years. I would like to acknowledge Physics HDR Student Admin team for the constant support in terms of PhD daily life. They are the heroes behind the scenes, who made this period of journey safe and enjoyable.

The life in Canberra is peaceful but joyful. I would like to thank my friends Qian Ye, Yuhui Zhang, Punyawat Rojanawisan, Chandan Chakma and Hai Ji. Those people made me feel that we are the family here in Canberra. They always passed me the positive energies whenever I felt terrible. We helped each other in so many small

things such as moving to a new house and fixing our cars. Those long-term friendships will be my precious in my memory all the time. I would like to thank Shengnan Wang. Thank you, Shengnan, for accompany during my PhD life. The existing of you made each of us a better person.

Finally, I would like to thank my parents for their great support both emotionally and financially. Thank you for encouraging me in all my pursuits and always standing by my side whenever I made any decisions to follow my dreams. There is no word for me to express my gratitude to you. This thesis and all of my achievements are dedicated to your strong will and sacrifices to make that internal train in my childhood drive to the distant lands.

Publications

1. **Zhu, Y**.; Yang, J.; Zhang, S.; Mokhtar, S.; Pei, J.; Wang, X.; Lu, Y., Strongly enhanced photoluminescence in nanostructured monolayer MoS_2 by chemical vapor deposition. *Nanotechnology* **2016,** *27* (13), 135706.

2. **Zhu, Y**.; Li, Z.; Zhang, L.; Wang, B.; Luo, Z.; Long, J.; Yang, J.; Fu, L.; Lu, Y., High-efficiency monolayer molybdenum ditelluride light-emitting diode and photodetector. *ACS applied materials & interfaces* **2018,** *10* (50), 43291-43298.

3. Wen, B.*; **Zhu, Y**.*; Yudistira, D.; Boes, A.; Zhang, L.; Yidirim, T.; Liu, B.; Yan, H.; Sun, X.; Zhou, Y., Ferroelectric-driven exciton and trion modulation in monolayer molybdenum and tungsten diselenides. *ACS nano* **2019,** *13* (5), 5335-5343.

4. **Zhu, Y**.*; Wang B.*; Li Z.; Zhang J.; Torres F.; Lipinski W.; Fu L.; Lu Y., High efficiency AC driven WS_2 LED via unsymmetric carrier injection. (Ready for submission)

5. **Zhu, Y**.*; Sun X.*; Fu L.; Lu Y., Highly correlated moiré exciton in freestanding supperlattice. (In preparation)

6. Shu, G.; Yap, L.; **Zhu, Y**.; Zhu B.; Wang, Y.; Ling Y.; Zhao Y.; An T.; Lu Y.; Cheng W., A soft resistive acoustic sensor based on suspended standing nanowire membranes with point crack design. Advanced function materials. (Accept)

7. Sharma, A.; Khan, A.; **Zhu, Y**.; Halbich, R.; Ma, W.; Tang, Y.; Wang, B.; Lu, Y., Quasi-line spectral emissions from highly crystalline one-dimensional organic nanowires. *Nano letters* **2019,** *19* (11), 7877-7886.

8. Yang, I.; Li, Z.; Wong-Leung, J.; **Zhu, Y**.; Li, Z.; Gagrani, N.; Li, L.; Lockrey, M. N.; Nguyen, H.; Lu, Y., Multiwavelength Single Nanowire InGaAs/InP Quantum Well Light-Emitting Diodes. *Nano letters* **2019,** *19* (6), 3821-3829.

9. Zhang, L.; Sharma, A.; **Zhu, Y**.; Zhang, Y.; Wang, B.; Dong, M.; Nguyen, H. T.; Wang, Z.; Wen, B.; Cao, Y., Efficient and Layer-Dependent Exciton Pumping across Atomically Thin Organic–Inorganic Type-I Heterostructures. *Advanced Materials* **2018,** *30* (40), 1803986.

10. Kuriakose, S.; Ahmed, T.; Taylor, P.; **Zhu, Y**.; Spencer, M. J.; Balendhran, S.; Lu, Y.; Bansal, V.; Sriram, S.; Bhaskaran, M., Generating strong room-temperature photoluminescence in black phosphorus using organic molecules. *2D Materials* **2018,** *6* (1), 015009.

11. Xu, R.; Yang, J.; **Zhu, Y**.; Yan, H.; Pei, J.; Myint, Y. W.; Zhang, S.; Lu, Y., Layer-dependent surface potential of phosphorene and anisotropic/layer-dependent charge transfer in phosphorene–gold hybrid systems. *Nanoscale* **2016,** *8* (1), 129-135.

12. Zhang, L.; Yan, H.; Sun, X.; Dong, M.; Yildirim, T.; Wang, B.; Wen, B.; Neupane, G. P.; Sharma, A.; **Zhu, Y**., Modulated interlayer charge transfer dynamics in a monolayer TMD/metal junction. *Nanoscale* **2019,** *11* (2), 418-425.

13. Tedeschi, D.; Blundo, E.; Felici, M.; Pettinari, G.; Liu, B.; Yildrim, T.; Petroni, E.; Zhang, C.; **Zhu, Y**.; Sennato, S.; Yuerui, L.; Polimeni, A., Controlled

Micro/Nanodome Formation in Proton-Irradiated Bulk Transition-Metal Dichalcogenides. *Advanced Materials* **2019,** *31* (44), 1903795.

14. An, Y.; Yang, D.; Ma, G.; **Zhu, Y**.; Wang, S.; Wu, Z.; Liu, J., Role of Co clusters and oxygen vacancies in the magnetic and transport properties of co-doped In_2O_3 films. *The Journal of Physical Chemistry C* **2014,** *118* (19), 10448-10454.

Abstract

Two dimensional (2D) semiconductors have attracted tremendous attention due to their fascinating electrical and optical properties. Transition metal dichalcogenides (TMDs), unlike zero bandgap of graphene, are semiconductors with band gap ranging from 1.57 eV to 2 eV, which are suitable for optoelectronic applications with visible and near-infrared light regime. Because of the reduced physical dimensions, quantum confinement becomes a dominated factor that strongly modulates TMDs properties, and therefore triggers a series of interesting phenomenon that has never been observed in bulk TMDs, including layer dependent indirect to direct band transition, larger exciton binding energy and enhanced light matter interaction. The strong light matter interaction makes TMDs a robust platform to study the physics of quasi-particles such as exciton, trion and even high order exciton particles. In this dissertation we investigate exciton dynamics and especially exciton modulation in single layer TMDs and two type TMDs heterostructures. Then the dissertation will focus on TMDs based optoelectronic device applications.

For two dimensional materials, such as transition metal dichalcogenides (TMDs) and black phosphorus, many novel properties only exist at low dimensional scale. Currently, atomic force microscopy (AFM), the most commonly used method to determine the thickness of two-dimensional (2D) materials, was known to have issues with its low scan speed and inevitable invasion. Fast and non-invasive identification of layer numbers of these 2D materials is important for future materials study. Here, in this dissertation we will first demonstrate that phase-shifting interferometry (PSI) can be used as a rapid and non-invasive method to identify the surface topography of 2D materials. The optical path length (OPL) obtained by PSI shows a good agreement with model calculations and a direct relationship between OPL and the layer number of 2D materials can be established. This technique enables a rapidly study of the surface information of various types 2D materials.

Due to the quantum confinement effect and sizeable semiconductor bandgap, exciton in TMDs becomes a centre topic either for physical research or engineering applications. Many efforts have been made to study the exciton dynamics in TMDs,

but the exciton modulation is still barely been touched. The first part of this dissertation will focus on the ferroelectric driven method to modulate exciton and trion behaviour in monolayer molybdenum and tungsten diselenides. By using a lithium niobate substrate with substrate domain engineering, it can achieve selectively doping of monolayer TMDs upon it. The inverted and pristine domain has been proved to be able to host two different types of ferroelectric doping as a result of the remnant polarization. The photoluminescence spectroscopy is used to spatially probe the exciton and trion dynamics, and it has demonstrated that these ferroelectric domains can significantly enhance or inhibit photoluminescence, leading to strong exciton and trion modulation. This novel modulation method opens a new routine to create optically active heterostructures that can be used for photodetectors and on-chip light sources.

Based on the understanding of the exciton behaviour of TMDs, this dissertation further demonstrates two type of 2D materials optoelectronic device applications. Firstly, the high efficiency monolayer molybdenum ditelluride light emitting diode has been demonstrated. The device is driven by direct current tunnelling effect, and in the meanwhile, the device can be also used as photodetector with low dark current and fast response time. As the counterpart of direct current driven, the alternative current driven monolayer tungsten disulfide light emitting diode has also been successful demonstrated. Due to the emission only happens within the rising and falling edges of AC voltage, the unique pulsed light emission can be achieved in this structure.

In summary, this thesis demonstrates the optical tunability of 2D materials, showing promising properties for optoelectronics applications. Both direct current and alternative current driving 2D materials-based light emitting diode have been demonstrated. The light emitting device design, fabrication and characterization in this work have provided deep insights into the characteristics of the TMDs optoelectronic devices, which may serve as a useful guidance for future development of 2D material-based LED systems. The infrared regime LED based on 2D black

phosphorene and super high efficiency AC driving 2D perovskite LED could be the potential research direction in the future.

Table of Contents

Declaration ..... **i**
Acknowledgement ..... **iii**
Publications ..... **vi**
Abstract ..... **viii**
Table of Contents ..... **xi**
List of Figures ..... **xiv**
List of Abbreviations and Acronyms ..... **xvii**
1. Introduction **1**
1.1. Two Dimensional Materials 2
1.1.1 Transition metal dichalcogenides (TMDs) 2
1.1.2 Exciton in transition metal dichalcogenides 5
1.2. Optoelectronic Devices Based on Two Dimensional Materials 7
1.2.1. Light emitting devices based on 2D materials 8
1.2.1.1. TMD LEDs based on p-n junction 9
1.2.1.2. Vertically stacked TMD LEDs 12
1.2.1.3. Infrared LEDs based on TMDs and phosphorus 15
1.2.1.4. TMD based single photon emitters 18
1.2.1.5. AC driven LEDs based on TMDs 21
1.2.2. TMD Photodetectors 23
1.3. Thesis Outline 25
Reference 28
2. Experimental Techniques **32**
2.1. Chemical Vapor Deposition (CVD) 32
2.2. Microscope 34
2.2.1. Fluorescence Microscope 34
2.2.2. Phase Shift Interferometer 35
2.3. Atomic Force Microscope 36
2.4. Optical Spectroscopy Characterization Techniques 37
2.4.1. Raman Spectroscopy 37
2.4.2. PL Spectroscopy 37
2.4.3. Conditional PL Spectroscopy 38
2.4.4. Anglular Dependent Second Harmonic Generation 41
2.4.5. Electroluminescence Spectroscopy 42
2.5. Device Fabrication 43

2.5.1 Photolithography 43
2.5.2 Electron Beam Evaporator 44
2.6. Home-built Temperature Controller 45
2.7. Home-built Micro Manipulator 45
2.8. Summary 46
Reference 47
3. Identify 2D Materials Thickness by Phase Shift Interferometer 48
3.1. Motivation and Advantages of the PSI 48
3.2. Working Principle of the PSI 49
3.3. Demonstration of the identification thickness of MoS_2 by PSI 51
3.4. Substrate dependent PSI measurement 52
3.5. 2D material dependent PSI measurement 54
3.6. Wavelength dependent PSI measurement 56
3.7. Summary 56
3.8. Experiment 57
Reference 58
Supporting Information for Chapter 3 60
4. Ferroelectric Driven Exciton and Trion Modulation in Monolayer $MoSe_2$ and WSe_2 66
4.1. Introduce of Ferroelectric Lithium Niobate and Hybridization with TMDs ... 67
4.2. Incorporate monolayer TMDs onto domain engineered $LiNbO_3$ substrate 69
4.3. Strong photoluminescence (PL) modulation in monolayer $MoSe_2$ and WSe_2 71
4.4. Laser Excitation Power Dependent PL in Surface Junction Area 74
4.5. Temperature dependent PL modulation in monolayer $MoSe_2$ 76
4.6. Summary 79
4.7. Experimental Section 80
Reference 82
Supporting Information for Chapter 4 85
5. High-Efficiency Monolayer Molybdenum Ditelluride Light Emitting Diode and Photodetector 96
5.1. Motivation 96
5.2. Architecture and Basic Performance of Monolayer $MoTe_2$ LED 98
5.3. High Efficiency Near Infrared Light Emission at 83K 100
5.4. Working principle of the monolayer $MoTe_2$ LED device 104
5.5. Photo-response of monolayer $MoTe_2$ photodetector 107
5.6. Summary 109

5.7. Experimental Section 109
Reference 111
Supporting Information for Chapter 5 113
6. High efficiency monolayer WS_2 AC Driven LED via An Unsymmetrical Pulsed Carrier Injection 126
6.1. Introduction of monolayer TMDs based AC driven LED devices 126
6.2. Symmetrical and unsymmetrical pulsed carrier recombination mechanism 129
6.3. Temperature dependent EL emission length 134
6.4. AC driving frequency induced wavelength tuneable EL emission 138
6.5. Visualization of exciton/trion to defect emission transition and defect levels evolution 141
6.6. Summary 143
6.7. Methods section 144
Reference 146
Supplementary Information for Chapter 6 148
7. Conclusions and Future work 160
7.1. Conclusions 160
7.2. Perspectives for future work 162
7.2.1. Optoelectronic applications based on surface ferroelectric modulation 162
7.2.2. Infrared light emitting devices based on black phosphorene 163
7.2.3. High efficiency AC driven perovskite light emitting diodes and lasers 163
References 165

List of Figures

Figure 1. 1 Typical structures of layered transition metal dichalcogenides 3

Figure 1. 2 The transition metals and chalcogens used, and optical images of the resulting 47 different atomically thin TMCs and heterostructures 4

Figure 1. 3 Quantum confinement and reduced dielectric screening in 2D materials . 6

Figure 1. 4 p-n junction based TMD LEDs 11

Figure 1. 5 LEDs based on TMDs vertical stacking 14

Figure 1. 6 Infrared LEDs based on TMDs and phosphorus 17

Figure 1. 7 Single photon emitter based on TMDs 20

Figure 1. 8 AC driven LEDs based on TMDs 23

Figure 1. 9 Monolayer MoS2 photodetector layout 24

Figure 2. 1 Schematic of the ambient pressure CVD system used in this thesis. 32

Figure 2. 2 Schematic of the modified fluorescence microscope. 34

Figure 2. 3 Comparison between microscope and fluorescent microscope image 35

Figure 2. 4 Schematic plot of the phase shifting interferometry (PSI) system 36

Figure 2. 5 Schematic plot of home-made micro PL system 38

Figure 2. 6 Schematic plot of the optical path in polarization dependent PL measurement 40

Figure 2. 7 Schematic diagram of the TRPL system 41

Figure 2. 8 Schematic plot of the angle dependent SHG setup. 42

Figure 2. 9 Schematic plot of the electroluminescence setup 43

Figure 2. 10 Schematic plot of the photolithography process with positive photoresist 43

Figure 2. 11 The design of photolithography mask 44

Figure 2. 12 The image of the home-built temperature controller. 45

Figure 3. 1 Schematic plot of the phase shifting interferometry (PSI) system 51

Figure 3. 2 Robust identification of mono- and few-layer MoS_2 on SiO_2 by phase shifting interferometry (PSI) 52

Figure 3. 3 Experimental and simulated OPL values of mono- and few-layer of MoS_2 on different substrates (Au, SiO_2/Si and Fused Silica) 54

Figure 3. 4 OPL values of mono- and few-layer of selected TMD materials (Black Phosphorene, h-Boron Nitride and Graphene) 56

Figure 4. 1 Schematic and optical images of monolayer $MoSe_2$ and WSe_2 on PPLN70

Figure 4. 2 Strong photoluminescence (PL) modulation in monolayer $MoSe_2$ and WSe_2 72

Figure 4. 3 RT laser excitation power dependent PL modulation in monolayer WSe_2. 76

Figure 4. 4 Temperature dependent PL modulation in monolayer $MoSe_2$ 77

Figure 5. 1 Architecture of monolayer $MoTe_2$ LED 100

Figure 5. 2 Strong infrared EL emission at 83 K. a, EL spectra from monolayer $MoTe_2$ under different injection current and -20 V back gate voltage 104

Figure 5. 3 Working principle of the monolayer $MoTe_2$ LED device 106

Figure 5. 4 Photo-response of monolayer $MoTe_2$ photodetector 109

Figure 6. 1 Monolayer WS_2 LED devices with large area and ultra-long EL emission length at room temperature and the principle of the unsymmetrical pulsed carrier injection 131

Figure 6. 2 Temperature dependent EL emission length. 137

Figure 6. 3 AC driving frequency induced wavelength tuneable EL emission..... 141

Figure 6. 4 Visualization of exciton/trion to defect emission transition and defect levels evolution 143

List of Abbreviations and Acronyms

PL	photoluminescence
EL	electroluminescence
2D	two-dimensional
TMD	transition metal dichalcogenide
hBN	hexagonal boron nitride
MoS_2	molybdenum disulphide
WS_2	tungsten disulphide
WSe_2	tungsten diselenide
$MoSe_2$	molybdenum diselenide
1L	monolayer
2L	bilayer
3L	trilayer
FET	field effect transistor
DBR	distributed Bragg reflector
SEM	scanning electron microscope

$MoTe_2$	molybdenum ditelluride
PSI	phase shift interferometer
OPL	optical path length
SiO_2	silicon dioxide
AFM	atomic force microscope
TRPL	time resolved PL
TREL	time resolved EL
CVD	chemical vapor deposition
PECVD	plasma enhanced CVD
MOS	metal oxide semiconductor
CCD	charge coupled device
CMOS	complementary MOS
LED	light emitting diode
DC	direct current
AC	alternative current

TCSPC	time correlated single photo counting
SPAD	single photon avalanche diode
SiH_4	silane
N_2O	nitrous oxide
N_2	nitrogen
He	helium
RF	radio frequency
UV	ultra-violet
QW	quantum well
PLE	photoluminescence excitation
FWHM	full width at half maximum
NA	numerical aperature

1. Introduction

In December 1959, a famous lecture called “There's Plenty of Room at the Bottom: An Invitation to Enter a New Field of Physics” was given by physicist Richard P. Feynman at the annual American Physical Society Meeting.[1] During the lecture, physicist Feynman threw up a question of “What would we do with layered structures with just the right layers”. More than half a century later, the 2010 Nobel Prize in Physics has been awarded to Professor Andre Geim and Professor Konstantin Novoselov for their pioneering work on graphene. They firstly demonstrated that it was possible to isolate graphene from bulk graphite and measure its electronic transport properties.[2] They also successfully isolated the monolayers from the bulk layered materials by repeatedly mechanical exfoliation which is known as the Scotch tape method. Eventually, it answered Feynman’s question that by controlling the number of layers in two-dimensional materials, it is possible to engineer their incredible physicochemical properties. Inspired by this ground-breaking work, extensive research has emerged in the field of graphene. Without any exaggeration, the following ten years in layered materials is graphene’s golden ten era with the demonstration of a series of extraordinary properties, such as large intrinsic strength,[3] huge thermal conductivity of ~5000 W/mK at room temperature[4] and gate-tuneable high electric conductivity.[5] Motivated by the success of graphene, Kin Fai Mak, *et al* observed the an indirect to direct bandgap transition behaviour in monolayer molybdenum disulfide (MoS_2) when the material was thinning down to monolayer.[6] This finding opens up a new route for researching of a wide range of layered semiconductors, which was called two-dimensional (2D) semiconductor. Similar to graphene, 2D semiconductors become another important member of 2D materials family. Today, researcher can synthesize a variety of monolayer 2D materials either by bottom-up or top-down approaches, which provided greater opportunities to engineer for real applications. Among various types of applications, their optoelectronic applications have attracted great attention due to the distinct electrical and optical properties of 2D materials. With the right bandgap ranging from ultraviolet to infrared, a series of photodetectors and light emitting devices have been demonstrated covering different spectral regimes. In addition to deposition of a single layer 2D material onto the substrates, researchers can further stack different or same 2D layers on top of each other in desired sequence

and even with designed twist angles, opening up enormous opportunities to achieve artificial structures with novel properties and device performances. Built on the previous research in the field, this dissertation will focus on light matter interaction in 2D materials and their optoelectronic applications including light emitting diodes and photodetectors.

1.1. Two Dimensional Materials

Two-dimensional materials refer to crystalline materials consisting of a single layer of atoms. The size of the material along two dimensions can be very large, but the size of the third dimension is usually less than one nanometer. Therefore, 2D materials have another name of nano sheets or nano flakes. With more research effort being devoted into this field, a great number of 2D materials have been discovered including a library of transition metal dichalcogenides (TMDs),[7] black phosphorene (BP),[8, 9] 2D germanium (Ge),[10, 11] graphene and *etc*. In this dissertation, we present the study of the TMDs with bandgaps within visible and near infrared regions that are of particular importance for optoelectronic applications.

1.1.1 Transition metal dichalcogenides (TMDs)

Unlike zero bandgap graphene, the TMDs are group of materials that have sizeable bandgap. The general formula of the TMDs is MX_2, with M a transition metal atom (M = Mo, W, Ta, *etc*.) and X a chalcogen atom (X = S, Se, or Te.). Depending on the arrangement of transition metal and chalcogen atom, trigonal prismatic (2H) phase, octahedral (tetragonal, T) and their distorted phase (T´) can be formed in TMDs, as presented in figure 1.1.

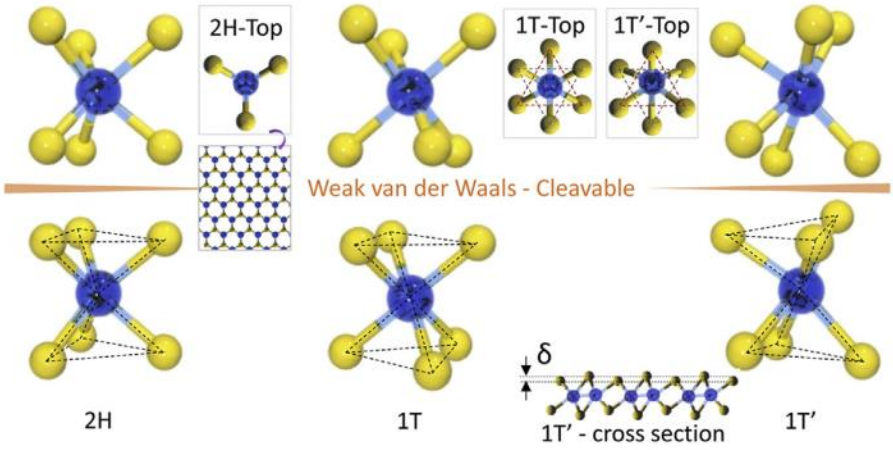

Figure 1. 1 Typical structures of layered transition metal dichalcogenides. Cleavable 2H, 1T and 1T´ structures in layered TMD (adapted with permission from ref [12] Copyright 2016 Wonbong Choi).

One year after the first demonstration of the mechanical cleavage of graphene, Novoselov group applied the mechanical exfoliation method to other layered materials and obtained the monolayers of other 2D materials such as hexagonal boron nitride (hBN), niobium diselenide ($NbSe_2$) and molybdenum disulphide (MoS_2), paving the way for the research of novel 2D TMDs.[13] After that, mechanical exfoliation has been proved to be an effective method to produce 2D monolayers for initially fast property probing. In the meanwhile, many research groups were also motivated to growth 2D TMDs monolayers by CVD method with encouraged by the successful experience with graphene. Yi-Hsien Lee *et al.* first reported synthesis of large area monolayer MoS_2 on SiO_2/Si substrate by CVD.[14] Today, CVD process has become the main synthesis method for 2D thin layers. Although many TMDs are difficult to synthesize due to high melting points of metal and metal oxide precursors. The molten-salt-assisted CVD method has been employed to overcome this issue and therefore, the CVD method can be broadly applied for synthesis of 47 types of TMDs. A library of atomic thin TMDs library has been constructed by Liu's group,[7] as shown in Figure 1.2.

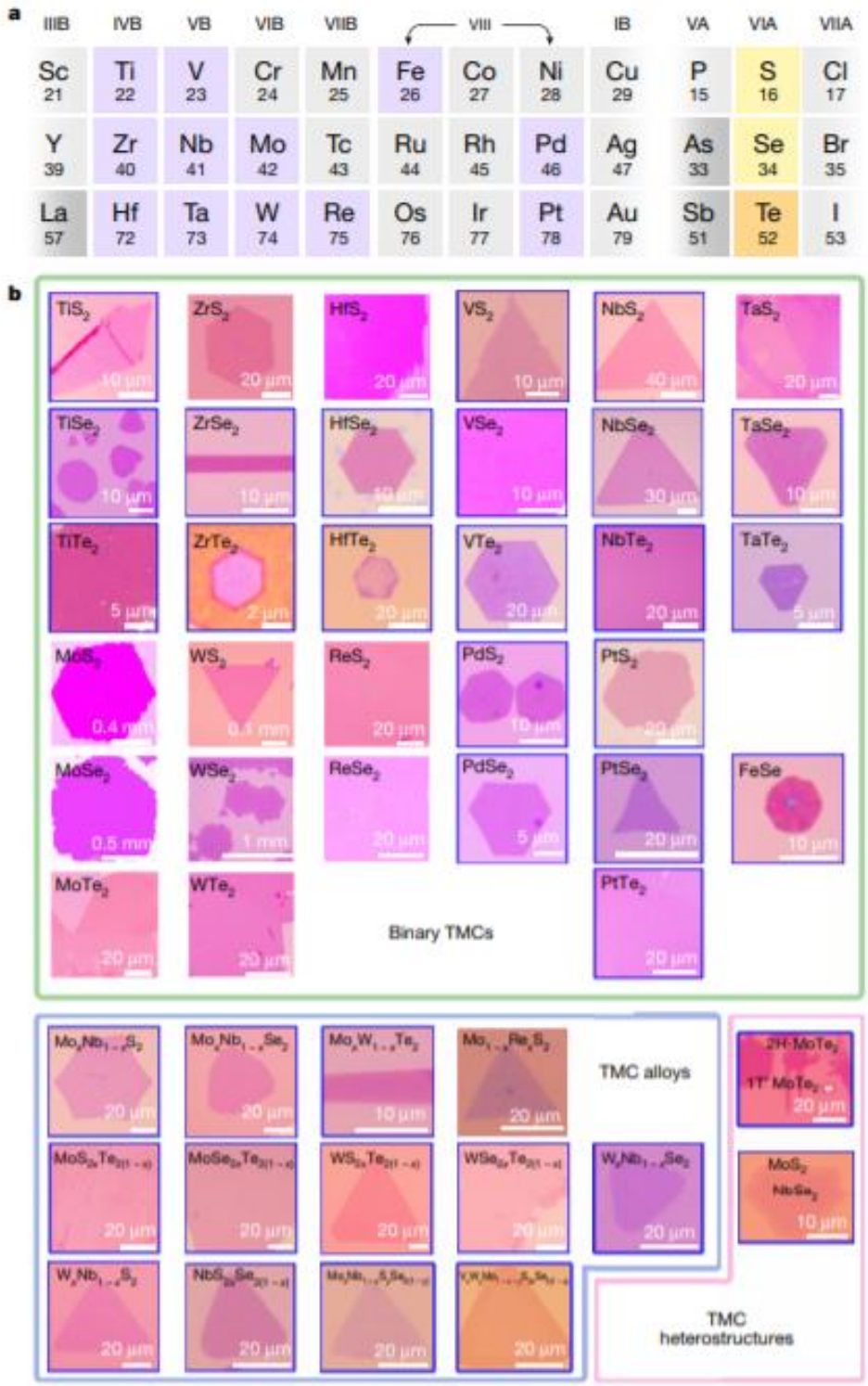

Figure 1. 2 The transition metals and chalcogens used, and optical images of the resulting 47 different atomically thin TMCs and heterostructures. a, Overview of metals (highlighted in purple) and chalcogens (highlighted in yellow and orange) that can form layered sulfides, selenides and tellurides. b, Optical images of 47 TMCs synthesized using our method (adapted with permission from ref [7] Copyright 2018 Springer Nature).

However, some of TMDs such as stannic sulfide (SnS_2) are still hard for CVD synthesis or mechanical exfoliation. A potential method is intercalation assisted exfoliation[15-17] and liquid exfoliation.[18] Plasma thinning process was also proved to be an effective way to produce some of the 2D materials. Jiajie Pei *et al*. firstly reported the producing of the air-stable monolayer black phosphorene by using oxygen plasma etching technique.[19] The layer by layer thinning process can be precisely achieved by fine control of the plasma parameters. The TMDs are characterized to exhibit extraordinary optical and electronic properties, such as strong PL emission and high carrier mobilities. In 2010, Kin Fai Mak, *et al* demonstrated the monolayer molybdenum disulfide (MoS_2) exhibited an indirect to direct bandgap transition when the material was thinning down to monolayer.[6] The strong photoluminescence (PL) emission origin from direct band gap transition was observed subsequently in the same year.[20] Later, a single layer MoS_2 transistor was demonstrated with a mobility of 200 $cm^2V^{-1}s^{-1}$ and on / off ratio of 1×10^8 at room temperature.[21] In monolayer molybdenum diselenide ($MoSe_2$) and tungsten diselenide (WSe_2), strong conduction band spin orbit coupling was observed, giving rise to an effective coupling between spin and valley pseudospin.[22] The strong spin valley coupling leads to interesting phenomenon, including the enhancement of the spin and valley polarization, for valleytronics applications. Owing to their unique properties, the 2D TMDs have been studied widely for electronics and optoelectronics applications.

1.1.2 Exciton in transition metal dichalcogenides

In semiconductors when a valence electron gains sufficient energy, it will move to the conduction band leaving behind a hole in the valence band. This electron becomes conductive electron, which is free to move within the crystal lattice. Meanwhile, this electron and the hole can be attracted to each other by the electrostatic Coulomb force forming a bound state, which is called exciton. The exciton is an electrically neutral quasiparticle that may exist in semiconductor. It has been widely studied as a two particle system in III-V semiconductor system.[23, 24] The exciton binding energy is the minimum energy required to separate electron and hole pairs. For a typical III-V semiconductor such as GaAs, the exciton binding energy is only few meV such that the exciton can only be observed at low

temperature. Compared with III-V semiconductor system, the 2D nature of monolayer TMDs leads to a strong enhancement of Coulomb interaction, as shown in Figure 1.3. The significant consequence of strong Coulomb interaction is the formation of tightly bound excitons.[25]

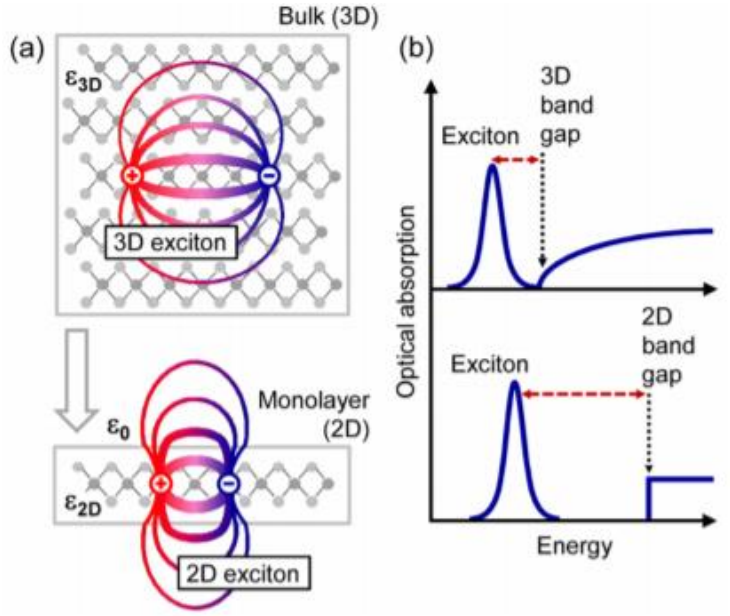

Figure 1. 3 Quantum confinement and reduced dielectric screening in 2D materials. a, Schematic of the confinement of charge carriers and the reduced dielectric screening due to the absence of adjacent layers in 2D materials in comparison to bulk 3D materials. b, Consequent increase of the band gap and exciton binding energy in semiconducting 2D materials (adapted with permission from ref [25] Copyright 2014 American Physical Society)

The exciton binding energy for MoS_2 is predicted to be between 0.5 and 1 eV,[26, 27] and the measured value is 240 meV.[28] The exciton binding energy is measured to be 0.71eV for monolayer WS_2,[29] 0.37 eV for monolayer WSe_2,[30] 0.55 eV for monolayer $MoSe_2$,[31] and 0.58 eV for monolayer $MoTe_2$,[32] which are much larger than those in typical III-V semiconductors with only 3.71 meV for InP and 4.76 meV for GaAs.[33] These large exciton binding energies from 2D materials allow us to observed the exciton dynamic at room temperature. Furthermore, thanks to the strong Coulomb interaction and quantum confinement in TMDs, higher order of exciton quasiparticles can be observed in TMDs system, which provides a distinct platform to study the many-body effect of excitons. In particular, when an exciton bounds with another electron or hole, it becomes a trion. Differed from neutral excitons,

trions are charged quasiparticles. Exciton and trion competition in monolayer TMDs can be tuned by electrostatic gating and chemical doping.[34, 35] If two neutral excitons bound together, this four particles system is biexciton. The binding energy of biexciton is measured to be ~20 meV in monolayer $MoSe_2$ system.[36] Recently, some research groups have even observed charged biexciton, a five particles system, in hBN encapsulated monolayer WSe_2, offering direct route towards deterministic control in many-body quantum phenomena.[37-39] Above introduced exciton species are optically bright that can be directly observed by PL measurements. Moreover, when measuring power dependence of PL with laser excitation, the excitons show linear power law, whereas the biexcitons exhibit superliner power law.[40-42] However, there is another optically dark exciton specie existing in monolayer TMDs, formed due to spin orbit coupling by the conduction band electron and valence band hole with different spin orientations. The dark exciton has been measured to have longer lifetime than the bright exciton,[43] making them promising for long distance exciton transport in 2D materials. The exciton can not only exist in single layer TMDs but also in two-layer TMDs stack, namely the interlayer exciton. In highly coveted heterostructure consisting of two different monolayer TMDs with type II band alignment, electrons and holes are bound together but spatially separated in individual monolayers. Differing from intralayer excitons, the interlayer excitons exhibit long lifetime and electrical dipole, the binding energy of which can be tuned by the vertical electrostatic field along with dipole directions.[44] The long lifetime and large binding energy of interlayer excitons offer a good opportunity to achieve Bose Einstein condensate and exciton-polariton.[45] As described above, 2D TMDs naturally becomes an idea material system to study exciton dynamic and many-body interactions.

1.2. Optoelectronic Devices Based on Two Dimensional Materials

The distinct optical and electronic properties of 2D TMDs have triggered a series of optoelectronic device applications including light emission diodes and photodetectors. Compared with electrical signal, optical signal is much faster and the information that is carried by light can lead to ultra-fast communication speed. However, currently most of the signal processing is based on electronic integrated circuit. Currently, the light transmission and propagating are hosted by the large size

photonic chips, whereas the signal processing is performed in integrated circuits at a nanoscale, which is one of the key challenges in the optical communication systems. This incompatible size issue should be addressed in the next generation optical communication system. One potential solution to this challenge is to use small and chip integrated materials to realized light generation and transmission. The 2D materials are ultra-thin semiconductors in nature, whose optoelectronics properties enable them to be suitable for on-chip light generations and photodetections. In this section, we will introduce several light emitting diodes and photodetectors based on 2D materials.

1.2.1. Light emitting devices based on 2D materials

The bandgap of bulk TMDs is indirect, however, with a single layer it becomes direct,[6] fulfilling the most basic requirement for efficient light emission applications. The variety of TMDs with different bandgaps and work functions, on the one hand, allows for tuneable emissions over a wide range of wavelengths. On the other hand, it provides many opportunities for bandgap engineering of heterostructures.[46] The light emission properties based on TMDs are dominated by exciton species.[47, 48] The exciton in TMDs can be observed at the room temperature owing to the quantum confinement and the strong Coulomb interaction. Excitons can be generated optically or electrically in TMDs forming different exciton species such as exciton, trion, biexciton and localized exciton, etc. Different exciton species can be tuned by chemical doping,[35] electrostatic gating[32, 34] and even excitation power,[49] enabling different approaches to manipulate light emission properties. Light emitting diodes (LEDs) are devices based on electroluminescence in semiconductors. Electroluminescence is a physical phenomenon that converts electrical energy into optical energy, with the devices emit light originated from radiative recombination of electrons and holes under electrical injection. Therefore, LEDs can be direct current (DC) driven and alternative current (AC) driven.[50, 51] In DC driven LEDs, the devices can also be classified into two types, p-n junction based LEDs or vertically chip-based LEDs. For AC driven LEDs, the device structure is similar with a capacitance.[51] In the following, TMDs based LEDs with different structures and designs will be introduced.

1.2.1.1. TMD LEDs based on p-n junction

The p-n junction is a key building block in optoelectronic applications including photodetectors and LEDs. Owing to the ultra-thin nature of TMDs, TMDs materials are sensitive to the surrounding environment, allowing the possibility of electrostatic gating control of monolayer TMDs doping. Formation of a p-n junction by applying two split gates beneath the monolayer TMDs is a common technique. This concept has been employed to fabricate monolayer WSe_2 LED devices (Figure 1.4 a and b), demonstrating total photon emission rate of ~ 16 million per second at the largest applied current of 35 nA, which corresponds to one photon per 10^4 injected electron-hole pairs.[52] Although the total estimated quantum efficiency is only 0.01%, the emission wavelength can be tuned between regimes of impurity-bound, charged and neutral excitons, as shown in Figure 1.4 c. This splitting gate concept becomes popular for TMDs based LEDs. The electrical control enables a single device to have multiple functionalities. For example, ambipolar monolayer WSe_2 devices with splitting local gates have achieved both PN and NP configurations with diode ideality factors of n = 1.9 and a rectification factor of 10^5. The estimated electroluminescence quantum efficiency reached to ~1%.[53] To achieve light emitting in monolayer TMDs, the ambipolar field-effect transistor (FET) is another structure to form p-n junction within 2D materials.[54] By applying gate voltage, the TMDs can be effectively doped to neutral. Therefore, the TMDs based FET devices are able to operate in the ambipolar injection regime with electrons and holes injected simultaneously at the two opposite contacts of the devices in which light emission from the FET channel can be observed. This light emitting transistor based on monolayer WSe_2 devices have been achieved as shown in Figure 1.4 d,[55] emitting circularly polarized electroluminescence from p-i-n junctions electrostatically formed in transistor channels (Figure 1.4 e). This unique phenomenon can be explained qualitatively by the electron-hole overlap controlled by the in-plane electric field. The external quantum efficiency ranges from 0.002% to 0.06% depending on samples (Figure 1.4 f). However, light emission from this lateral p-n junction devices is limited by the narrow one-dimensional junction interface, which results in low efficiency of LEDs. Therefore, stacking TMDs to form p-n junction are more favourable because the optical active area has increased from a 1D line to a 2D overlapping area. MoS_2 and WSe_2 vertical p-n junction LEDs are presented in Figure 1.4 g, where the p-n junction area is covered over the entire

MoS_2/WSe_2 overlapping area.[56] The electroluminescence from this device shows prominent band edge excitonic emission and strikingly enhanced hot-electron luminescence (Figure 1.4 h). However, the EL emission is localized at the overlapping area in close proximity to the electrodes instead of the entire overlapping area as shown in Figure 1.4 i. This phenomenon can be explained by the current injection in such p-n junction, which is limited by lateral contacts and lateral carrier transport owing to the depletion of the ultrathin TMDs. To realise a large and uniform area LEDs using this vertical p-n junction structure, it is imperative to achieve vertical current injection. Graphene as a uniform conductor can be employed into designing vertical p-n junction TMD LEDs. However, directly fabricating vertical contact on both top and bottom TMDs could lead to significant current leakage through ultrathin 2D materials. By using a quantum well structure, inserting a thin dielectric material between graphene and TMDs will dramatically minimized the current leakage and hence increase LEDs efficiency. This structure is usually used in vertical stacking geometry and will be discussed in detail in the following sections.

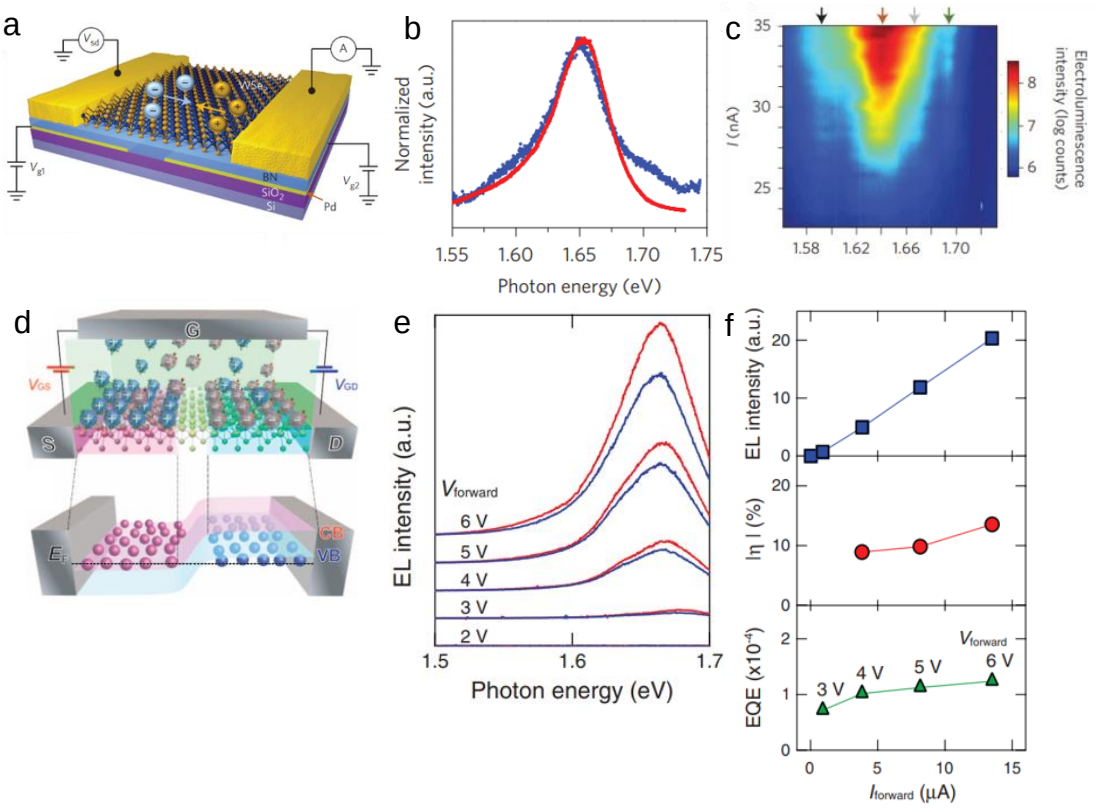

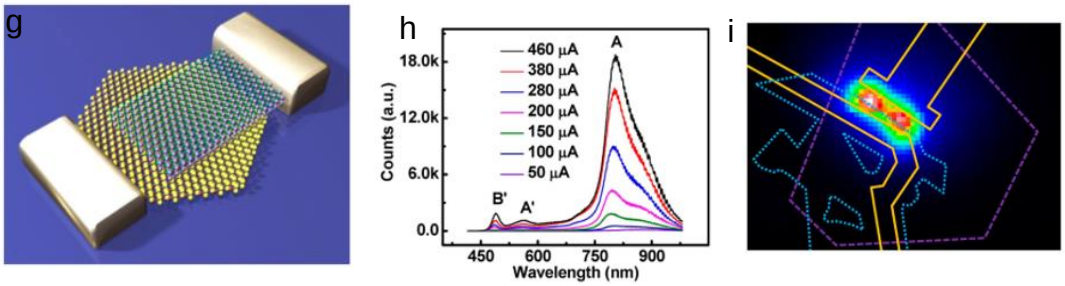

Figure 1. 4 p-n junction based TMD LEDs. a, Schematic plot of multiple monolayer WSe_2 p–n junction devices with palladium backgates (Vg_1 and Vg_2) and source (S) and drain (D) contacts. The source–drain voltage (Vsd) is applied to one contact and the current (A) is read out of the other. During electroluminescence in the WSe_2, electrons (blue) and holes (yellow) move towards each other (arrows) and recombine. The backgates are separated from the WSe_2 by hexagonal BN. The device sits on a layer of silicon dioxide on a silicon substrate. b, Electroluminescence spectrum (blue) generated by a current of 5 nA closely resembles the photoluminescence spectrum (red), at 300 K. c, Electroluminescence intensity plot as a function of bias current and photon energy. From left to right, the arrows indicate the impurity-bound exciton (XI), the charged excitons (X- then X+) and the neutral exciton (X0). d, The upper panel is device structure of TMD EDLT under ambipolar charge accumulation. The bottom panel shows schematic band structure of EDLT induced p-i-n junction under equilibrium. e, Voltage dependence of EL spectra of the device. f, Upper: Current dependence of total EL intensity extracted from e. Middle: Current dependence of EL polarization extracted from e. Bottom: Current dependence of external quantum efficiency extracted from e. g, Schematic illustration of the WSe_2/MoS_2 vertical heterojunction p−n diode. h, The EL spectra of a ML-WSe_2/MoS_2 heterojunction at different injection current. i, The false colour EL image of the heterojunction device under an injection current of 100 μA. The purple dashed line outlines the ML-WSe_2, the blue dotted line outlines the MoS_2 and the golden solid line outlines the gold electrodes. (a -c adapted with permission from ref [52] Copyright 2014 Springer Nature, d-f adapted with permission from ref [55] Copyright 2014 American Association for the Advancement of Science, and g-i adapted with permission from ref [56] Copyright 2014 Journal of the American Chemical Society)

1.2.1.2. Vertically stacked TMD LEDs

High efficiency and large area light emission of LEDs is desirable for many applications. Considering the drawbacks of p-n junction structures, people come up with a new design, namely vertically chip-based LEDs by stacking 2D materials layer by layer. In such a geometry, it usually consists of graphene, hexagonal boron nitride (hBN), and TMDs. For single optical active devices, two graphene layers, which acted as the transparent uniform electrode contacts, are separated by an hBN/MoS_2/hBN sandwich quantum well, as shown in Figure 1.5 a. The crucial part in this structure is the hBN. The few layer hBN serves as a tunnel barrier, which significantly reduces the leakage current when the device is operating with a current flowing from top to bottom layers. Especially, the thickness of the hBN flake plays an important role in the LEDs operation. When the thickness of the h-BN flake is more than one atomic layer, the lifetime of the carriers could be sufficiently prolonged for the formation of excitons, which subsequently recombine to give efficient light emission (Figure 1.5 b). However, with the increase of the thickness of the hBN, the current tunnelling through the hBN will dramatically decrease,[57, 58] resulting in very weak LEDs emissions (Figure 1.5 c). The well-designed single hBN/MoS_2/hBN QW LEDs device exhibits ~1% quantum efficiency.[59] This efficiency can be further pushed to 8.4% by stacking four QWs due to increased radiatively recombination.[59] This vertical stacking structure remarkably increased the light emitting quantum efficiency many orders of magnitude larger than the LEDs with p-n junction geometry. In addition, the emission spectrum can be fine-tuned by combining different 2D semiconductors. The quantum efficiency of combinational device reaches ~5% that is nearly comparable to those of current organic LEDs and state-of-the-art quantum dot LEDs. Based on those pioneering work, many following up work have been focussing on further optimisation of the quantum efficiency by substrate modulation and integration with photonic crystal cavity. Room temperature high efficiency WSe_2 vertical stacking LEDs have been reported with refractive distributed Bragg refractor (DBR) substrates, as shown in Figure 1.5 d and e. The function of DBR is to reduce the emission light scattering into SiO_2/Si substrates and enhance the light collection. Based on such DBRs, up to 30% of the emitted light can be collected, as opposed to just 2% from the Si/SiO_2 substrate. The EQE of WSe_2 devices increases with temperature increasing (Figure 1.5 f) due to the increased bright exciton population by the thermal activation, with

room temperature EQE reaching 5%,[50] which is ~250 times more than the previous best performance of MoS_2 quantum wells in ambient conditions.[59] In Figure 1.5 g and h, the WSe_2 vertical stacking LEDs with integrated photonic crystal cavity has been reported. The EL emission efficiency has been enhanced more than 4 times compared with LEDs on bare SiO_2/Si substrate.[60] Such an enhancement was attributed to the strong coupling between the photonic crystal mode and exciton EL in WSe_2, leading to an increased emission rate. Moreover, the emission at the cavity resonance is single mode and highly linear polarized (84%) alone the cavity mode, as shown in Figure 1.5 i. The photonic crystal cavity has realized the electrically pumped single mode light source, which is an essential step toward on-chip optical information technologies clearly indicating the important advantage of the vertical stacking LED structure. However, one challenge for this structure, as mentioned earlier, is the proper selection and preparation of the thickness of hBN. The traditional method of mechanical exfoliation for preparing hBN turns out to be difficult in term of observing the few layer hBN flakes under microscope. Similar optical refractive index between hBN and SiO_2 makes hBN with less than five-layer nearly invisible. Many methods have been proposed to solve this problem, such as using thinner SiO_2 (~80 nm) and using 470 nm or 590 nm light source to increasing contrast.[61] Despite the complicate fabrication process of vertical stacking LEDs, it is still a giant leap for high efficiency TMDs based LEDs. With the rapid progress in technology of chemical vapor deposition growth of wafer scale TMDs will allow scaling up of production of such fancy LEDs devices.

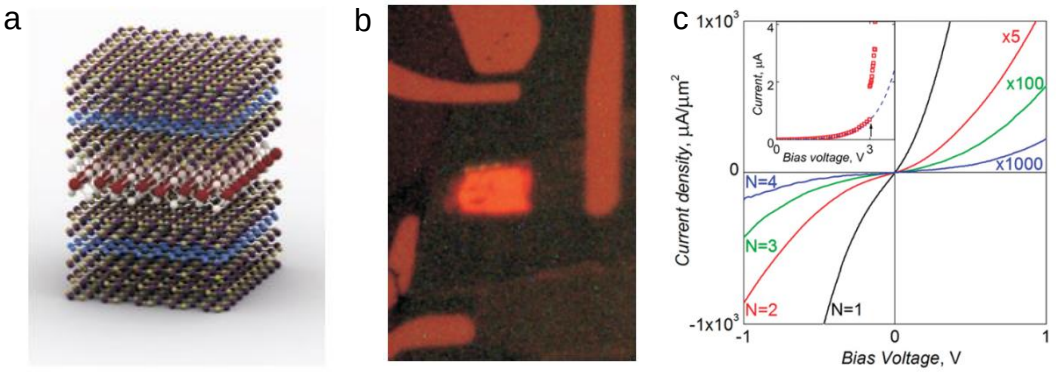

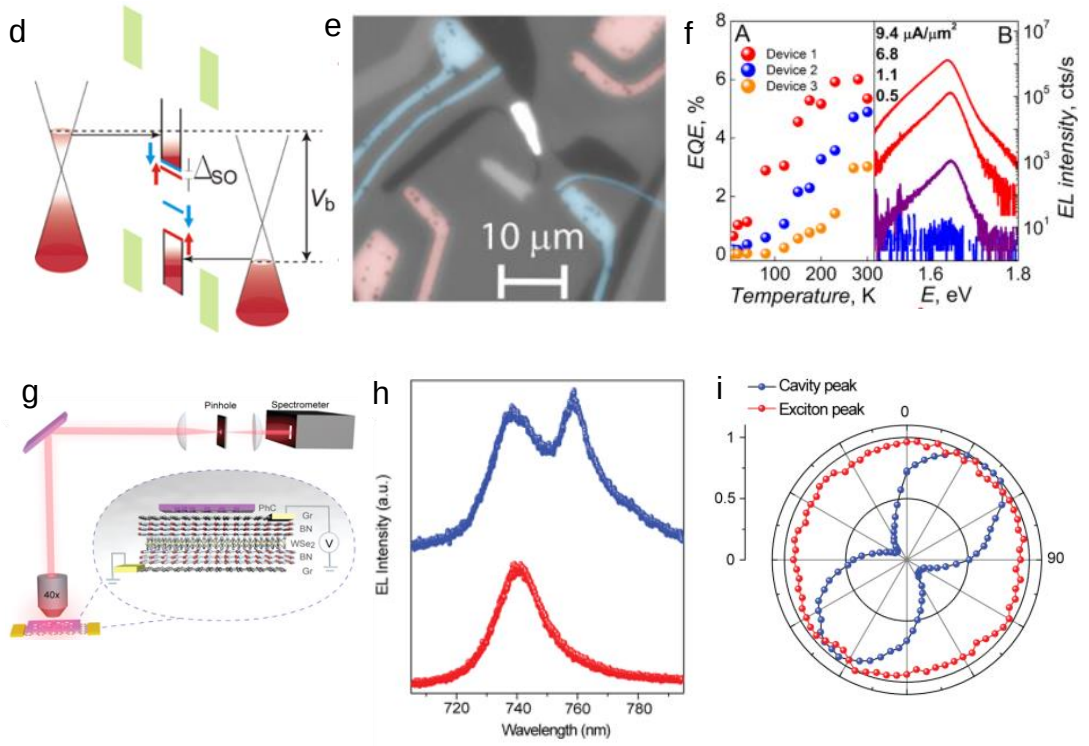

Figure 1. 5 LEDs based on TMDs vertical stacking. a, Schematic of the SQW heterostructure hBN/Gr_B/2hBN/WS_2/2hBN/Gr_T/hBN. b, Optical image of EL from the same device. Vb=2.5V, T=300 K. 2hBN and 3hBN stand for bi- and trilayer hBN, respectively. c, Characteristic I−V curves for graphite/BN/graphite devices with different thicknesses of BN insulating layer: black curve, monolayer of BN; red, bilayer; green, triple layer; and blue, quadruple layer. Note the different scale for the four curves. Current was normalized by the realistic area of the tunnelling barrier, which ranged 2−10 μm^2 depending on the particular device. The inset shows a typical I−V curve where a breakdown in the BN is observed at +3 V, the thickness of the flake is 4 layers of BN (1.3 nm). The dotted line indicates the continuation of the exponential dependence. d, Band alignment at high bias of a WSe_2 LEQW. e, Magnification (50×) monochrome image of a WSe_2 LEQW device with an applied bias of V_b = 2 V and current of 2 μA taken in ambient conditions with weak backlight illumination (Central white area corresponds to strong electroluminescence). Red false colour, Au contacts to bottom graphene, blue false colour, Au contacts to top graphene. f, Left panel: temperature dependence of the quantum efficiency for three typical WSe_2 LED devices measured at bias voltages and injection currents of 2.8 V and j = 0.15 $\mu A/\mu m^2$ (Device 1), 2.8 V and j = 0.5 $\mu A/\mu m^2$ (Device 2), and 2.3 V and j = 8.8 $\mu A/\mu m^2$ (Device 3). Right panel: Individual electroluminescence spectra plotted for four different injection current

densities for Device 3. g, Schematic of the EL measurement set-up and device architecture. h, EL measured from (blue dots) and away (red dots) from the cavity area with V_b = 2 V. i, Normalized cavity-enhanced peak intensity (blue dots) and exciton peak intensity (red dots) as a function of polarization detection angle. (a-b adapted with permission from ref [59] Copyright 2015 Springer Nature, c adapted with permission from ref [57] Copyright 2012 American Chemical Society, d-f adapted with permission from ref [50] Copyright 2015 American Chemical Society, and g-i adapted with permission from ref [60] Copyright 2017 American Chemical Society).

1.2.1.3. Infrared LEDs based on TMDs and phosphorus

Infrared light spectral range is the vital part of wavelength band for optical communication and thermal imaging. It has been immensely used for civilian and military applications. Light sources and photodetectors within this bandwidth present on-going challenge.[62, 63] Traditional approaches for infrared light sources and lasers are based on III-V semiconductors and they are off-chip or wafer-bonded. Alternatively, the on-chip light source shows advantages for integrating into electronic or photonic circuits. The emerging 2D TMDs offer a new path way for optical interconnection components that can be integrated with industry silicon-based devices.[64-66] Monolayer $MoTe_2$, a special member in 2D TMDs, has an electrical bandgap of ~1.72 eV,[32, 67] with an exciton emission peak from monolayer $MoTe_2$ located at ~1.1 eV, which makes it a promising candidate for near infrared optoelectronic applications. Graphene/hBN/$MoTe_2$ vertical stacking LEDs is presented in Figure 1.6 a, where the device structure has been simplified from double tunnel barriers to a single tunnel barrier.[68] The $MoTe_2$ LED shows a very high quantum efficiency of 9.5% at 83K, as shown in Figure 1.6 b and c. Such high quantum efficiency arises from two aspects: 1) the delicate device structure, ultra-clean interface of devices, dry membrane transfer and photolithography-free electrodes pattern technique; 2) low substrate absorption at the emission wavelength of $MoTe_2$. It further confirms that the surface and substrate engineering is crucial for those atomic thin TMDs especially for device applications. In Figure 1.6 d, the bilayer $MoTe_2$ based lateral p-n junctions with an electrostatic splitting gate configuration is presented. Moreover, the device was integrated with a silicon

photonic crystal waveguide to demonstrate the potential for on-chip integration of light source and photodetector.[69] The strong EL emission intensity has been observed within p-n junction area where recombination happens. The EL emission wavelength is located at 1090 nm at 6 K and 1175 nm at room temperature respectively, as shown in Figure 1.6 e. The Figure 1.6 f shows the EL intensity overlaps with a false-color optical image of the structure at room temperature. The estimated waveguide coupling efficiency is 5%. This work demonstrates the possibility of integration of light emitting diodes and photodetectors with silicon photonic crystal waveguide, which enables point-to-point optical links and shows the potential of TMDs based near infrared light emitting system. Apart from $MoTe_2$, black phosphorus (BP) has emerged as another powerful 2D material with the bandgap ranging from ~0.3 eV to ~1.8 eV.[8, 9, 19, 70-72] The tuneable bandgap with different thicknesses covers the visible to mid-infrared spectral range, bridging the gap between graphene and TMDs. However, the stability issue greatly limits its optoelectronic application. Although the BP has been intensively studied since 2014, its device applications are mainly focused on photodetection properties. The BP based LEDs have been barely reported, due to the difficulties in device fabrications. To the best of our acknowledge, so far there is only one report on BP based LEDs, as presented in Figure 1.6 g.[73] The device consists of a 70 nm p-type BP layer on a 10 nm n-type MoS_2 layer to form a vertical p-n junction. The EL emission is at mid-infrared range of 3.68 μm (Figure 1.6 h), which agrees well with the reported PL measurements on thick BP flakes.[74] The emission pattern is polarized with a polarization ratio of ~3 for the AC to ZZ orientation intensity as shown in Figure 1.6 i. The reported external quantum efficiency is about 0.03%, which is common for the p-n junction-based LEDs. Regardless of the stability issue with BP, this 2D material shows very promising potential for applications in the infrared spectral range. For example, the five layers of BP gives optical emission at 1550 nm, which is located in optical communication bandwidth. The BP transistors show ambipolar field-effect with high hole mobility (in the order of 10 cm^2/Vs to 1000 cm^2/Vs) and current switching ratio of 100 to 10000.[75-79] With the further technology development in BP stabilization and large area material growth, continuing effort should be made to fabricate BP based high efficiency and fast speed optoelectronic devices.

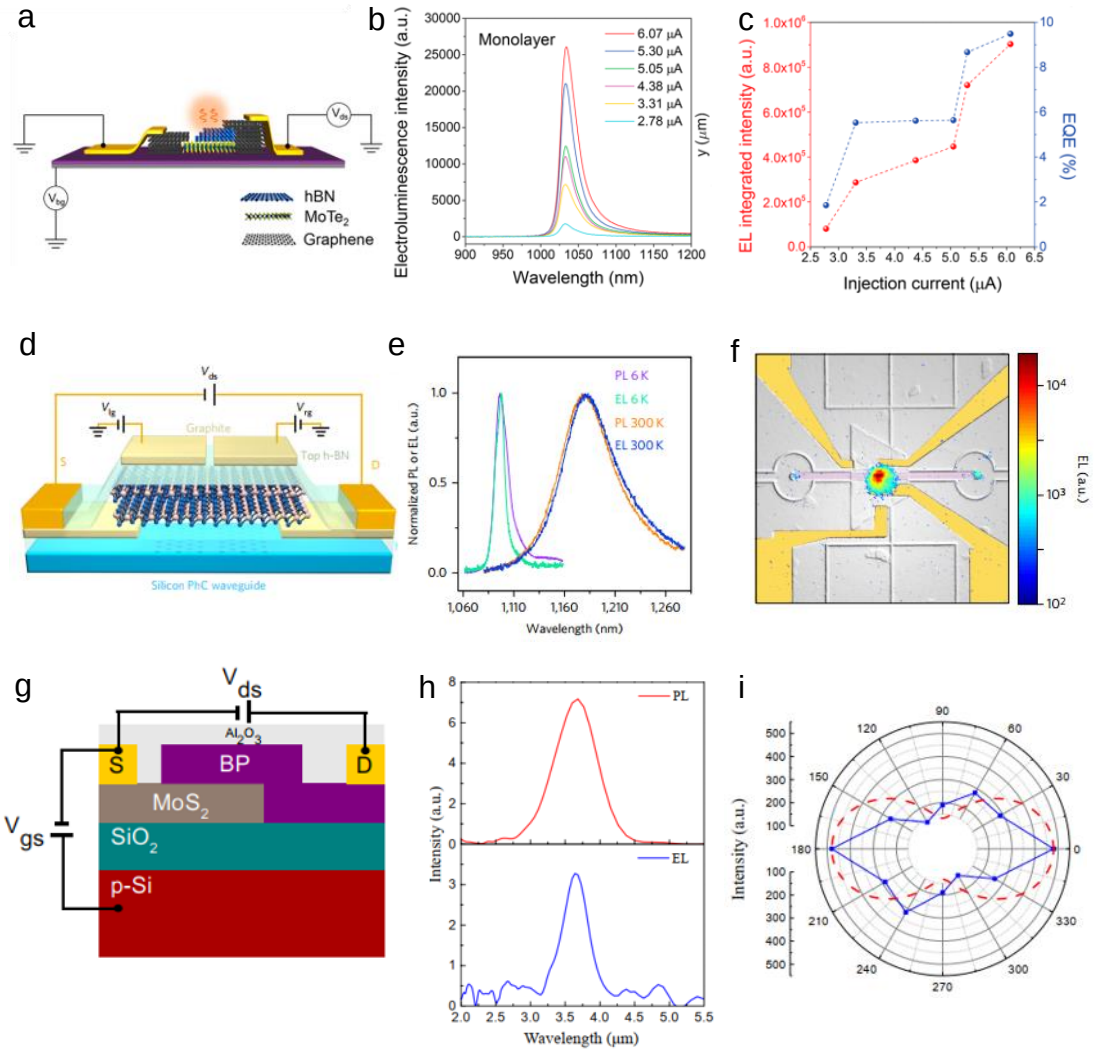

Figure 1. 6 Infrared LEDs based on TMDs and phosphorus. a, Schematic of the monolayer $MoTe_2$ LED and electrical connections for EL measurements. b, EL spectra from monolayer $MoTe_2$ under different injection current and -20 V back gate voltage. c, EL intensity (left) and EQE (right) of monolayer $MoTe_2$ as a function of the injection current. d, Cross-sectional schematic of the encapsulated bilayer $MoTe_2$ p–n junction on top of a silicon PhC waveguide. The carrier concentration in $MoTe_2$ is controlled by the split graphite gates, with the separation of the two gates of 400 nm. The dielectric layer is hBN on top of the $MoTe_2$, and the thickness of hBN is 8 nm. The source (S) and drain (D) electrodes are thin graphite flakes connected to Cr/Au leads. e, Spectrally resolved PL of the bilayer $MoTe_2$ flake and EL of the $MoTe_2$ p–n junction at room temperature and at 6 K respectively. The gate voltages of the p–n junction were set with opposite polarity $V_{lg} = -8$ V and $V_{rg} = 8$ V at a bias of $V_{ds} = 2$ V. f, EL emission image at room temperature overlaid on top of a false-colour optical image of the device. Two extra emission spots from the grating

couplers demonstrate coupling of the light source and silicon waveguide. g, Schematic illustration the cross-sectional view of the BP/MoS_2 heterojunction device. h, Photoluminescence (red) and electroluminescence (blue) of the BP/MoS_2 diode. i, Polarization resolved measurements of the EL intensity. (a-c, adapted with permission from ref [68] Copyright 2018 American Chemical Society, d-f, adapted with permission from ref [69] Copyright 2017 Springer Nature, and g-i, adapted with permission from ref [73]).

1.2.1.4. TMD based single photon emitters

Integrating high quality and high efficiency single photon sources into optoelectronic circuit is a key challenge to develop scalable quantum communication technologies.[80] Single photon emitters have been observed optically in monolayer WSe_2 due to the crystal structure imperfections that act as efficient carrier trapping center.[81] As the counterpart of optical pump, the electrical pumped single photon emissions are particularly suitable for developing quantum light generating devices. Inspired by the successful technique that used in TMDs based vertical stacking LEDs, WSe_2 and WS_2 atomically thin quantum LEDs have been reported.[82] The quantum LEDs employed a graphene/hBN/TMD structure by changing the Femi level in graphene to realize carrier injections as shown in Figure 1.7 a and b. When the device is on operation, the uniform light emitting is generated from entire WSe_2 area. However, there is a hot spot observed in both monolayer and bilayer WSe_2 samples (Figure 1.7 d). Spectrum studies show that the emission behaviors are different from free exciton recombination. In Figure 1.7 c, the remarkably sharp peaks located at near infrared regime with linewidths ranging between 0.8 and 3 nm, suggesting that they belong to quantum emitters. To confirm they are single photon source, the intensity correlation function, $g^{(2)}(\tau)$, of EL emission from WSe_2 based quantum LEDs has been plotted as shown in Figure 1.7 e. The value of the normalized $g^{(2)}(0)$, drops to 0.29 ± 0.08, well below the threshold value of 0.5, expected for a single-photon source.[83] Similarly, in WS_2 based quantum LEDs, quantum emitter was also observed with $g^{(2)}(0)$, drops to 0.31 ± 0.05, indicating that WS_2 supports stable QLED operation, generating single photons in the visible spectral range (Figure 1.7 f and g). It is noteworthy that single photon emission also can be achieved in WSe_2 LEDs with lateral p-i-n structures, as presented in Figure 1.7 h.[84] The devices show

three single defects within narrow p-i-n junction area (Figure 1.7 i). Those defect emissions have a doublet with the characteristic exchange splitting and linearly polarized selection rules, which are consistent with previously reported properties of single photon emitters by optical measurements. Compared with the traditional solid-state single photon emitters, which are typically embedded in bulk materials, 2D materials are more suitable for on-chip integration with electronic circuits. However, the low yield of single photon emitter in 2D materials remains to be a challenge. How to create single photon emitters by controlled introduction of defects in TMDs is the next steppingstone in developing TMD based single photon emitters.

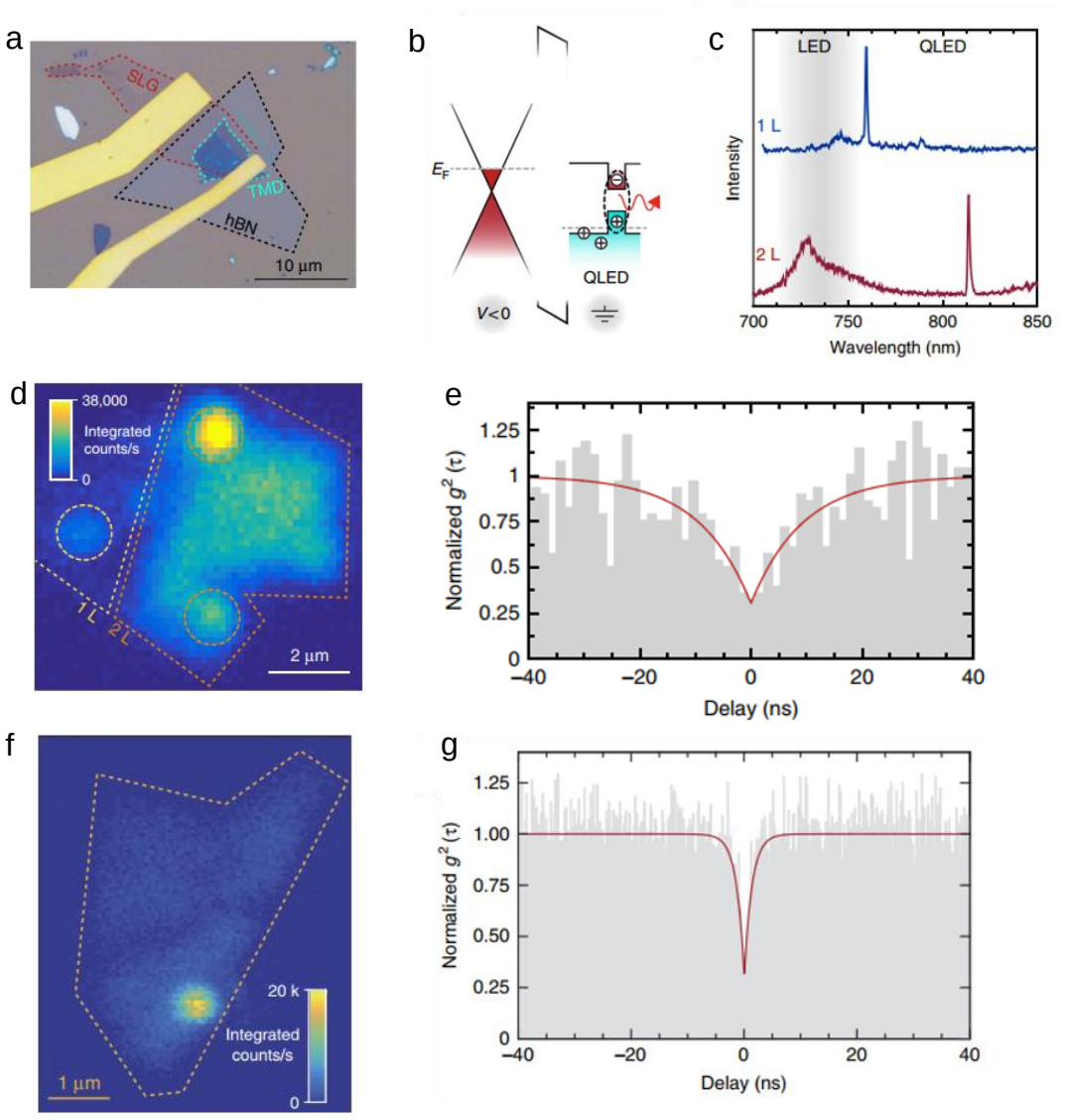

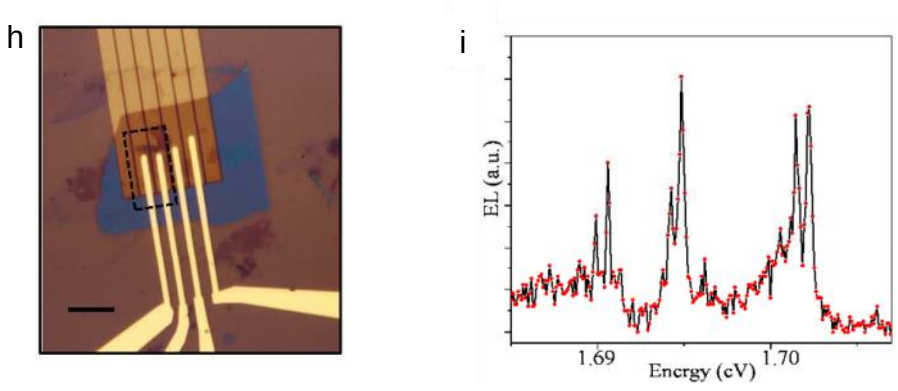

Figure 1. 7 Single photon emitter based on TMDs. a, Optical microscope image of a typical device used in the experiments. The dotted lines highlight the footprint of the single layer graphenen (SLG), hBN and the TMD layers individually. The Cr/Au electrodes contact the SLG and TMD layers to provide an electrical bias. b, Heterostructure band diagram. Illustration shows the case for a finite negative bias applied to the SLG. c, Typical EL emission spectra for quantum dots in the monolayer (top) and bilayer (bottom) WSe_2. The shaded area highlights the spectral window for LED emission due to bulk WSe_2 excitons, whereas QLED operation produces spectra at longer wavelengths. d, A raster-scan map of integrated EL intensity from monolayer and bilayer WSe_2 areas of the QLED for an injection current of 3 mA (12.4 V). The dotted circles highlight the submicron localized emission in this device. e, Intensity-correlation function, $g^{(2)}(\tau)$, for the same emitter displaying the anti-bunched nature of the EL signal, $g^{(2)}(0) = 0.29 \pm 0.08$, and a rise-time of 9.4 ± 2.8 ns. f, A raster-scan map of integrated EL intensity from the monolayer WS_2 area of the device at 0.570 mA (1.97 V), where the highly localized QLED emission dominates over the unbound WS_2 exciton emission. g, Intensity-correlation function, $g^{(2)}(\tau)$, for the same quantum dot displaying the anti-bunched nature of the EL signal, $g^{(2)}(0) = 0.31 \pm 0.05$, and a rise-time of 1.4 ± 0.15 ns. h, Optical image of a lateral LED device. Scale bar, 15 μm. i, EL spectrum for a lateral LED device showing emission from three single defects. (a-g adapted with permission from ref [82] Copyright 2016 Springer Nature and h-i adapted with permission from ref [84] Copyright 2016 American Chemical Society).

1.2.1.5. AC driven LEDs based on TMDs

In above described LEDs structures, the electrical driven methods are all under direct current injection. It usually requires complicated structure and two electrode contacts. One challenge for them is that the Ohmic contacts in LEDs devices are essential to minimize resistive losses and achieve high injection levels.[85] Narrow p-n junctions and complicated structures limit the applications for large area LEDs, for example the millimetre or even centimetre scale LEDs. Due to above limitations, research focus has been shifted from direct current injection to alternative current injection to seek breakthrough for large area scale emissions. The AC driven LEDs consist of a monolayer TMD sitting on a heavily doped Si substrate with a 50 nm thick SiO_2 and a single gold contact (Figure 1.8 a). The LEDs have been demonstrated for all four types of TMDs including WS_2, WSe_2, MoS_2, and $MoSe_2$, as presented in Figure 1.8 b.[51] Time resolved EL measurements indicate the device only operates at the voltage transition with a transient EL signal, as presented in Figure 1.8 c and d. With high frequency band bending of TMDs, electrons and holes are injected into the monolayer TMDs in separate cycles. The new injected carriers recombine with exit carriers that have opposite sign then a bright light emission has been generated. Although the EL external quantum efficiency for WSe_2 LEDs, at current stage, is only 0.01%, the beauty of this AC driven LEDs is that the device does not require complex p-n junctions or heterostructures to achieve light emission, which provides the opportunity to scale up the devices to larger sizes. Based on this structure, centimetre scale monolayer AC driven LEDs have been be achieved.[86] In Figure 1.8 e to g, the WS_2 based centimetre-scale (≈ 0.5 cm^2) visible (640 nm) display has been demonstrated. In addition, the AC driven LEDs have been proved to be a promising platform to observe the electrically driven high order correlated exciton states (Figure 1.8 h).[87] By tailoring the AC pulse parameters, it is possible to create either an electron- or a hole rich environment in the 2D semiconductor, consequently favouring the enhanced or diminished EL from the different exciton species (Figure 1.8 i and j). Compared with DC driven LEDs, AC driven LEDs show the advantages on device simplicity and driving flexibility (frequency and amplitude). Unlike the DC driven LEDs, where electrons and holes are simultaneously injected into the materials, the carriers injected in the AC driven LEDs is either electrons or holes, which provides more opportunity and freedom in studying carrier dynamics in such structures. However, improving the EL efficiency of AC driven LEDs is highly

desirable. Optimising the system capacitance, engineering the radiative lifetime and biexciton recombination rate may be promising approach for further improve the performance of TMD based AC driven LEDs.

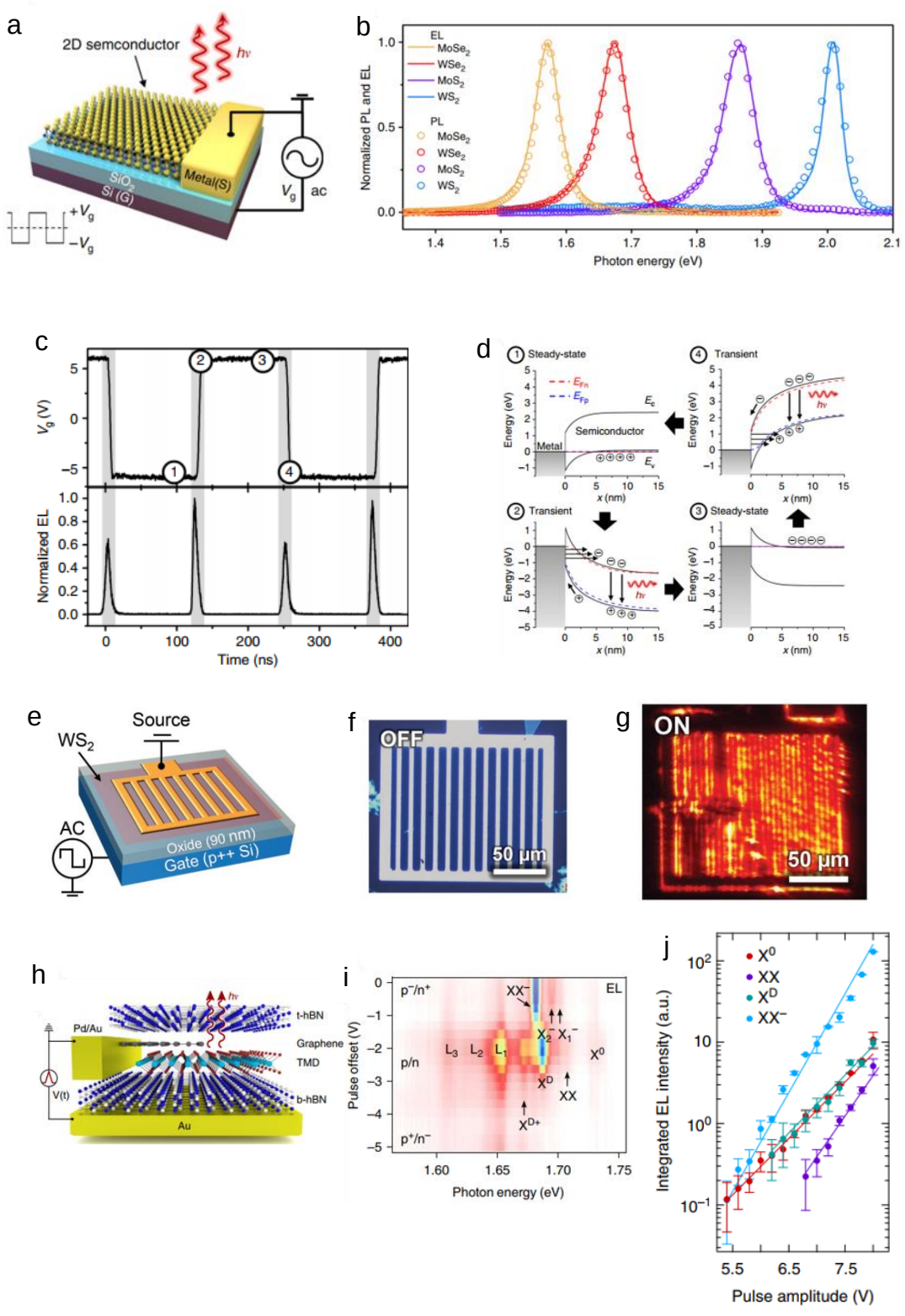

Figure 1. 8 AC driven LEDs based on TMDs. a, Schematic of the t-EL device. An AC voltage is applied between the gate and source electrodes and emission occurs near the source contact edge. b, EL and PL spectra measured for MoSe2, WSe2, MoS2, and WS2 monolayer devices. c, Time-resolved electroluminescence and the corresponding Vg, showing that EL occurs at the Vg transients (time points 2 and 4). d, Band diagrams at different times during the operation cycle, corresponding to c. EFn and EFp indicate the quasi-Fermi levels for electrons and holes, respectively. e, Schematic of the t-EL device. f, Optical microscope image of the fabricated t-EL device. g, EL image of the device, showing emission is concentrated near the metal contacts. h, Schematic drawing of the sample. The monolayer TMD and graphene are sandwiched between two multilayer hBN flakes. i, Emission spectra and tunability at T = 5 K. Pulsed EL from WSe_2. j, Semi-logarithmic plot of the integrated EL intensity as a function of the pulse amplitude. The circles represent the experimental data for WSe2, while the lines depict the fit to an exponential function. (a-d adapted with permission from ref [51] Copyright 2018 Springer Nature, e-g adapted with permission from ref [86] Copyright 2019 WILEY-VCH Verlag GmbH & Co. KGaA, Weinheim, and h-j adapted with permission from ref [87] Copyright 2019 Springer Nature).

1.2.2. TMD Photodetectors

Photodetectors are the optoelectronic devices that convert optical signals to electrical signals, which have been widely used in communication, imaging and sensing systems.[88, 89] There are different types of photodetectors with different device structural design and operate under different modes.[90] In particular for 2D material based photodetectors, photovoltaic and photogating effects[91] have been commonly employed to achieve high speed and high responsive photodetection. In photovoltaic mechanism, the photogenerated electron and hole pairs are separated under the built-in electric field at the PN junction area, leading to a photocurrent. Due to the built-in electric field, the generated electron and hole pairs can be quickly swept to the separate direction. Therefore, photodetectors based on photovoltaic effect are capable of ultrafast photodetection.[92] For photogating effect, it is a special branch of photoconductor, considered as the method to modulate the conductance of channel by photo-induce trap,[93, 94] which is usually observed in photodetectors based on low

dimensional materials. The active material absorbs photons and produces electron-hole pairs, one type carriers will be captured to form a localized field. The photo-induced localized field prolong the lifetime of photogenerated carrier, results in a high gain.[91] Therefore, the photodetectors with photogating effect exhibit high gain which is more suitable for sensitive photodetection. The 2D TMDs are well known for their high light absorption features with bandgap energy located in visible and near infrared regime.[95] With improved mobility of monolayer MoS_2 and contact quality, high performance monolayer MoS_2 photodetector was firstly demonstrated with a maximum photoresponsivity of ~880 AW^{-1} at the wavelength of 561 nm,[96] as shown in Figure 1.9.

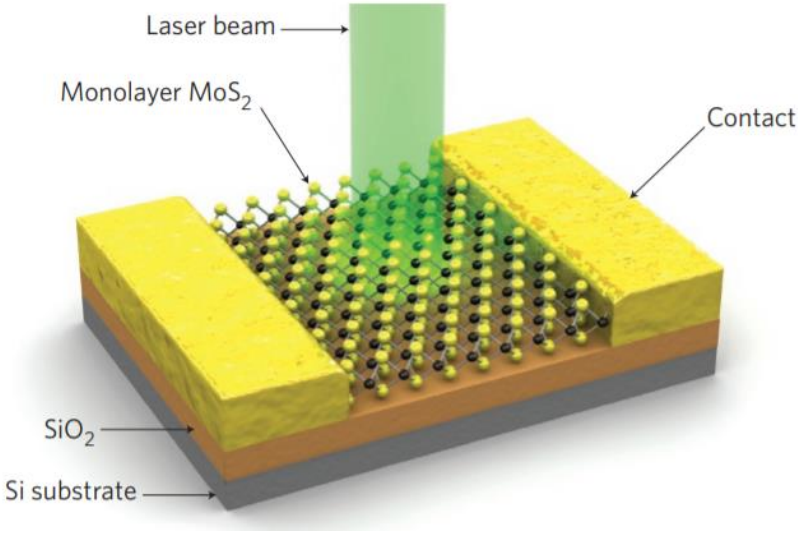

Figure 1. 9 Monolayer MoS_2 photodetector layout (adapted with permission from ref [102] Copyright 2013 Springer Nature).

Due to the intrinsic defect states in monolayer TMDs, their carrier mobility is limited. The photo generated carriers which are far away from electrode contact (beyond the carrier diffusion length) are hardly collected by electrodes. Wenjin Zhang *et al*. have demonstrated a photodetector based on graphene and MoS_2 heterostructure with photoconductive gain larger than 10^8 and a responsivity higher than 10^7 AW^{-1}.[97] The photo generated electron-hole pairs in monolayer MoS_2 layers, and then electrons can transfer to graphene due to the built-in electric field, while the holes were trapped in MoS_2 layer. The high electron mobility in graphene and the long

charge-trapping lifetime of the holes leading to multiple recirculation of electrons in graphene, result in a very high photo gain.

1.3. Thesis Outline

This dissertation will firstly discuss the basic characterization methods for 2D materials *via* phase shift interferometer. Then the exciton behaviour in monolayer TMDs is modulated by a novel ferroelectric modulation method and studied by Raman and PL spectroscopy. After building the understanding of the optical properties of 2D TMDs, the dissertation will be focused on optoelectronic device applications based on different types of 2D TMD materials.

In Chapter 1, we will introduce the history of 2D materials and how it emerges as a hot topic in materials research field. The physical properties of 2D material and its optoelectronic applications are discussed.

Chapter 2 will introduce all the related experimental techniques and setups used in this dissertation.

In Chapter 3, a fast and non-invasive method to identify the layer numbers of 2D materials will be presented. The Phase shift interferometry (PSI) will be employed to scan the surface topography of 2D materials. According to different phase shift originated from materials refractive index, the thickness and the layer number of 2D materials can be determined. The phase shift interferometer model will be built in MATLAB. Then the monolayer MoS_2 will be used as an example. The optical path length (OPL) of monolayer MoS_2 on SiO_2/Si substrate will be measured. The OPL obtained by PSI shows a good agreement with simulated value by MATLAB. The direct relationship of OPL value and layer numbers can be demonstrated. After that, the OPL value of the same material on different substrate and different materials on the same substrate will be measured. By comparing those real time data with the simulated OPL value, the full picture of the relationship between OPL value and the thickness of material can be determined.

In Chapter 4, the ferroelectric driven exciton and trion modulation mechanism in monolayer $MoSe_2$ and WSe_2 has been investigated. The domain engineered lithium niobate substrates have been used to support monolayer $MoSe_2$ and WSe_2. A micro-PL/Raman system is used to obtain spatially resolved images of the differently doped transition metal dichalcogenides (TMDs). The domain inverted lithium niobate causes changes in the TMDs due to electrostatic doping as a result of the remnant polarization from the substrate. Moreover, the differently doped TMDs (n-type $MoSe_2$ and p-type WSe_2) exhibit opposite PL modulation. Distinct oppositely charged domains were obtained with a 9-fold PL enhancement for the same single $MoSe_2$ sheet when adhered to the positive (P+) and negative (P-) domains. This sharp PL modulation on the ferroelectric domain is due to the different carrier doping levels in the material conduction band as the PL intensity is sensitive to the empty density of state in the conduction band. Moreover, excitons dissociate rapidly at the interface between the P+ and P- domains due to the built-in electric field. We are able to adjust the charge on the P+ and P- domains via the pyroelectric effect and observe rapid PL quenching over a narrow temperature range illustrating the observed PL modulation is electronic in nature.

With the understanding of optical behaviour in monolayer TMDs, Chapter 5 aims to demonstrate optoelectronic device applications based on monolayer TMDs materials. In this chapter, the near infrared monolayer $MoTe_2$ light emitting diode (LED) has been demonstrated on SiO_2 on Si substrate because of low light absorption from at its emission wavelength. By taking advantage of the quantum tunnelling effect, the device has achieved a very high external quantum efficiency (EQE) of 9.5% at 83 K, which is the highest EQE obtained from LED devices fabricated from monolayer TMDs so far. When the device is operated as a photodetector, the $MoTe_2$ device exhibits a strong photoresponsivity at resonant wavelength 1145 nm. The low dark current of ~5pA and fast response time 5.06 ms are achieved due to the hBN tunnelling layer to prevent current leakage under dark condition.

In chapter 6, we continue to investigate the light emitting applications of monolayer TMDs based on different device configurations. An AC driven LED with large area electroluminescence emission will be presented. An unsymmetrical pulsed carrier recombination mechanism has been revealed, which is induced by the initial doping in the light emitting material. Normally the initial doping in TMDs significantly weakens the PL emission, however, it helps increase the EL intensity and emission area in AC LED. Time resolved electroluminescence and temperature dependent time resolved electroluminescence measurements confirmed that the unsymmetrical pulsed carrier recombination is caused by initial doping of TMDs. Based on doped sample, the wavelength tunable EL emission at low temperature is observed, due to the exciton, trion and the defect emissions. The quantum efficiency of defect EL emission is 39.7 times larger than free exciton and trion EL emission.

Finally, Chapter 7 presents the conclusion of this dissertation and future perspectives of the research in this field.

References

1. R. P. Feynman, There's plenty of room at the bottom. *California Institute of Technology, Engineering and Science magazine*, (1960).
2. K. S. Novoselov *et al.*, Electric field effect in atomically thin carbon films. *science* **306**, 666-669 (2004).
3. C. Lee, X. Wei, J. W. Kysar, J. Hone, Measurement of the elastic properties and intrinsic strength of monolayer graphene. *science* **321**, 385-388 (2008).
4. A. A. Balandin *et al.*, Superior thermal conductivity of single-layer graphene. *Nano letters* **8**, 902-907 (2008).
5. K. S. Novoselov *et al.*, Two-dimensional gas of massless Dirac fermions in graphene. *nature* **438**, 197-200 (2005).
6. K. F. Mak, C. Lee, J. Hone, J. Shan, T. F. Heinz, Atomically thin MoS 2: a new direct-gap semiconductor. *Physical review letters* **105**, 136805 (2010).
7. J. Zhou *et al.*, A library of atomically thin metal chalcogenides. *Nature* **556**, 355-359 (2018).
8. S. Zhang *et al.*, Extraordinary photoluminescence and strong temperature/angle-dependent Raman responses in few-layer phosphorene. *ACS nano* **8**, 9590-9596 (2014).
9. J. Yang *et al.*, Optical tuning of exciton and trion emissions in monolayer phosphorene. *Light: Science & Applications* **4**, e312-e312 (2015).
10. C.-C. Liu, W. Feng, Y. Yao, Quantum spin Hall effect in silicene and two-dimensional germanium. *Physical review letters* **107**, 076802 (2011).
11. M. Dávila, L. Xian, S. Cahangirov, A. Rubio, G. Le Lay, Germanene: a novel two-dimensional germanium allotrope akin to graphene and silicene. *New Journal of Physics* **16**, 095002 (2014).
12. W. Choi *et al.*, Recent development of two-dimensional transition metal dichalcogenides and their applications. *Materials Today* **20**, 116-130 (2017).
13. K. S. Novoselov *et al.*, Two-dimensional atomic crystals. *Proceedings of the National Academy of Sciences* **102**, 10451-10453 (2005).
14. Y. H. Lee *et al.*, Synthesis of large-area MoS2 atomic layers with chemical vapor deposition. *Advanced materials* **24**, 2320-2325 (2012).
15. H. Ramakrishna Matte *et al.*, MoS2 and WS2 analogues of graphene. *Angewandte Chemie International Edition* **49**, 4059-4062 (2010).
16. Z. Zeng *et al.*, Single-Layer Semiconducting Nanosheets: High-yield preparation and device fabrication. *Angewandte Chemie International Edition* **50**, 11093-11097 (2011).
17. G. Eda *et al.*, Photoluminescence from chemically exfoliated MoS2. *Nano letters* **11**, 5111-5116 (2011).
18. K. G. Zhou, N. N. Mao, H. X. Wang, Y. Peng, H. L. Zhang, A mixed-solvent strategy for efficient exfoliation of inorganic graphene analogues. *Angewandte Chemie International Edition* **50**, 10839-10842 (2011).
19. J. Pei *et al.*, Producing air-stable monolayers of phosphorene and their defect engineering. *Nature communications* **7**, 10450 (2016).
20. A. Splendiani *et al.*, Emerging photoluminescence in monolayer MoS2. *Nano letters* **10**, 1271-1275 (2010).
21. B. Radisavljevic, A. Radenovic, J. Brivio, V. Giacometti, A. Kis, Single-layer MoS 2 transistors. *Nature nanotechnology* **6**, 147 (2011).
22. D. Xiao, G.-B. Liu, W. Feng, X. Xu, W. Yao, Coupled spin and valley physics in monolayers of MoS 2 and other group-VI dichalcogenides. *Physical review letters* **108**, 196802 (2012).
23. R. Miller, D. Kleinman, W. Tsang, A. Gossard, Observation of the excited level of excitons in GaAs quantum wells. *Physical Review B* **24**, 1134 (1981).
24. R. Miller, D. Kleinman, Excitons in GaAs quantum wells. *Journal of Luminescence* **30**, 520-540 (1985).

25. A. Chernikov *et al.*, Exciton binding energy and nonhydrogenic Rydberg series in monolayer WS 2. *Physical review letters* **113**, 076802 (2014).
26. T. Cheiwchanchamnangij, W. R. Lambrecht, Quasiparticle band structure calculation of monolayer, bilayer, and bulk MoS 2. *Physical Review B* **85**, 205302 (2012).
27. A. Ramasubramaniam, Large excitonic effects in monolayers of molybdenum and tungsten dichalcogenides. *Physical Review B* **86**, 115409 (2012).
28. S. Park *et al.*, Direct determination of monolayer MoS2 and WSe2 exciton binding energies on insulating and metallic substrates. *2D Materials* **5**, 025003 (2018).
29. B. Zhu, X. Chen, X. Cui, Exciton binding energy of monolayer WS 2. *Scientific reports* **5**, 9218 (2015).
30. K. He *et al.*, Tightly bound excitons in monolayer WSe 2. *Physical review letters* **113**, 026803 (2014).
31. M. M. Ugeda *et al.*, Giant bandgap renormalization and excitonic effects in a monolayer transition metal dichalcogenide semiconductor. *Nature materials* **13**, 1091-1095 (2014).
32. J. Yang *et al.*, Robust excitons and trions in monolayer MoTe2. *ACS nano* **9**, 6603-6609 (2015).
33. J. Kübler, The exciton binding energy of III–V semiconductor compounds. *physica status solidi (b)* **35**, 189-195 (1969).
34. J. S. Ross *et al.*, Electrical control of neutral and charged excitons in a monolayer semiconductor. *Nature communications* **4**, 1-6 (2013).
35. S. Mouri, Y. Miyauchi, K. Matsuda, Tunable photoluminescence of monolayer MoS2 via chemical doping. *Nano letters* **13**, 5944-5948 (2013).
36. K. Hao *et al.*, Neutral and charged inter-valley biexcitons in monolayer MoSe 2. *Nature communications* **8**, 1-7 (2017).
37. M. Barbone *et al.*, Charge-tuneable biexciton complexes in monolayer WSe 2. *Nature communications* **9**, 1-6 (2018).
38. Z. Ye *et al.*, Efficient generation of neutral and charged biexcitons in encapsulated WSe 2 monolayers. *Nature communications* **9**, 1-6 (2018).
39. Z. Li *et al.*, Revealing the biexciton and trion-exciton complexes in BN encapsulated WSe 2. *Nature communications* **9**, 1-7 (2018).
40. Y. You *et al.*, Observation of biexcitons in monolayer WSe 2. *Nature Physics* **11**, 477-481 (2015).
41. J. Pei *et al.*, Excited state biexcitons in atomically thin MoSe2. *ACS nano* **11**, 7468-7475 (2017).
42. G. Plechinger *et al.*, Identification of excitons, trions and biexcitons in single‐layer WS2. *physica status solidi (RRL)–Rapid Research Letters* **9**, 457-461 (2015).
43. C. Jiang *et al.*, Microsecond dark-exciton valley polarization memory in two-dimensional heterostructures. *Nature communications* **9**, 1-8 (2018).
44. P. Rivera *et al.*, Observation of long-lived interlayer excitons in monolayer MoSe 2–WSe 2 heterostructures. *Nature communications* **6**, 1-6 (2015).
45. T. Low *et al.*, Polaritons in layered two-dimensional materials. *Nature materials* **16**, 182-194 (2017).
46. J. Kang, S. Tongay, J. Zhou, J. Li, J. Wu, Band offsets and heterostructures of two-dimensional semiconductors. *Applied Physics Letters* **102**, 012111 (2013).
47. G. Moody, J. Schaibley, X. Xu, Exciton dynamics in monolayer transition metal dichalcogenides. *JOSA B* **33**, C39-C49 (2016).
48. T. Jakubczyk *et al.*, Radiatively limited dephasing and exciton dynamics in MoSe2 monolayers revealed with four-wave mixing microscopy. *Nano letters* **16**, 5333-5339 (2016).
49. M. Amani *et al.*, Near-unity photoluminescence quantum yield in MoS2. *Science* **350**, 1065-1068 (2015).

50. F. Withers *et al.*, WSe2 light-emitting tunneling transistors with enhanced brightness at room temperature. *Nano letters* **15**, 8223-8228 (2015).
51. D.-H. Lien *et al.*, Large-area and bright pulsed electroluminescence in monolayer semiconductors. *Nature communications* **9**, 1-7 (2018).
52. J. S. Ross *et al.*, Electrically tunable excitonic light-emitting diodes based on monolayer WSe 2 p–n junctions. *Nature nanotechnology* **9**, 268 (2014).
53. B. W. Baugher, H. O. Churchill, Y. Yang, P. Jarillo-Herrero, Optoelectronic devices based on electrically tunable p–n diodes in a monolayer dichalcogenide. *Nature nanotechnology* **9**, 262-267 (2014).
54. S. Jo, N. Ubrig, H. Berger, A. B. Kuzmenko, A. F. Morpurgo, Mono-and bilayer WS2 light-emitting transistors. *Nano letters* **14**, 2019-2025 (2014).
55. Y. Zhang, T. Oka, R. Suzuki, J. Ye, Y. Iwasa, Electrically switchable chiral light-emitting transistor. *Science* **344**, 725-728 (2014).
56. R. Cheng *et al.*, Electroluminescence and photocurrent generation from atomically sharp WSe2/MoS2 heterojunction p–n diodes. *Nano letters* **14**, 5590-5597 (2014).
57. L. Britnell *et al.*, Electron tunneling through ultrathin boron nitride crystalline barriers. *Nano letters* **12**, 1707-1710 (2012).
58. G.-H. Lee *et al.*, Electron tunneling through atomically flat and ultrathin hexagonal boron nitride. *Applied physics letters* **99**, 243114 (2011).
59. F. Withers *et al.*, Light-emitting diodes by band-structure engineering in van der Waals heterostructures. *Nature materials* **14**, 301-306 (2015).
60. C.-H. Liu *et al.*, Nanocavity integrated van der Waals heterostructure light-emitting tunneling diode. *Nano letters* **17**, 200-205 (2017).
61. R. V. Gorbachev *et al.*, Hunting for monolayer boron nitride: optical and Raman signatures. *Small* **7**, 465-468 (2011).
62. F. Pyatkov *et al.*, Cavity-enhanced light emission from electrically driven carbon nanotubes. *Nature Photonics* **10**, 420 (2016).
63. M. D. Birowosuto *et al.*, Movable high-Q nanoresonators realized by semiconductor nanowires on a Si photonic crystal platform. *Nature materials* **13**, 279-285 (2014).
64. K. Kang *et al.*, High-mobility three-atom-thick semiconducting films with wafer-scale homogeneity. *Nature* **520**, 656-660 (2015).
65. H. Wang *et al.*, Integrated circuits based on bilayer MoS2 transistors. *Nano letters* **12**, 4674-4680 (2012).
66. B. Radisavljevic, M. B. Whitwick, A. Kis, Integrated circuits and logic operations based on single-layer MoS2. *ACS nano* **5**, 9934-9938 (2011).
67. C. Ruppert, O. B. Aslan, T. F. Heinz, Optical properties and band gap of single-and few-layer MoTe2 crystals. *Nano letters* **14**, 6231-6236 (2014).
68. Y. Zhu *et al.*, High-efficiency monolayer molybdenum ditelluride light-emitting diode and photodetector. *ACS applied materials & interfaces* **10**, 43291-43298 (2018).
69. Y.-Q. Bie *et al.*, A MoTe 2-based light-emitting diode and photodetector for silicon photonic integrated circuits. *Nature nanotechnology* **12**, 1124 (2017).
70. J. Lu *et al.*, Light–matter interactions in phosphorene. *Accounts of chemical research* **49**, 1806-1815 (2016).
71. R. Xu *et al.*, Extraordinarily bound quasi-one-dimensional trions in two-dimensional phosphorene atomic semiconductors. *ACS nano* **10**, 2046-2053 (2016).
72. R. Xu *et al.*, Exciton brightening in monolayer phosphorene via dimensionality modification. *Advanced Materials* **28**, 3493-3498 (2016).
73. J. Wang *et al.*, Mid-infrared polarized emission from black phosphorus light-emitting diodes. *arXiv preprint arXiv:1911.09184*, (2019).
74. C. Chen *et al.*, Bright Mid-Infrared Photoluminescence from Thin-Film Black Phosphorus. *Nano letters* **19**, 1488-1493 (2019).

75.L. Li *et al.*, Black phosphorus field-effect transistors. *Nature nanotechnology* **9**, 372 (2014).
76.S. P. Koenig, R. A. Doganov, H. Schmidt, A. Castro Neto, B. Özyilmaz, Electric field effect in ultrathin black phosphorus. *Applied Physics Letters* **104**, 103106 (2014).
77.H. Liu *et al.*, Phosphorene: an unexplored 2D semiconductor with a high hole mobility. *ACS nano* **8**, 4033-4041 (2014).
78.M. Buscema *et al.*, Fast and broadband photoresponse of few-layer black phosphorus field-effect transistors. *Nano letters* **14**, 3347-3352 (2014).
79.F. Xia, H. Wang, Y. Jia, Rediscovering black phosphorus as an anisotropic layered material for optoelectronics and electronics. *Nature communications* **5**, 1-6 (2014).
80.A. Politi, J. C. Matthews, J. L. O'brien, Shor's quantum factoring algorithm on a photonic chip. *Science* **325**, 1221-1221 (2009).
81.M. Koperski *et al.*, Single photon emitters in exfoliated WSe 2 structures. *Nature nanotechnology* **10**, 503 (2015).
82.C. Palacios-Berraquero *et al.*, Atomically thin quantum light-emitting diodes. *Nat Commun* **7**, 12978 (2016).
83.Z. Yuan *et al.*, Electrically driven single-photon source. *science* **295**, 102-105 (2002).
84.G. Clark *et al.*, Single defect light-emitting diode in a van der Waals heterostructure. *Nano letters* **16**, 3944-3948 (2016).
85.S. Nakamura, M. Senoh, T. Mukai, High-power InGaN/GaN double-heterostructure violet light emitting diodes. *Applied Physics Letters* **62**, 2390-2392 (1993).
86.J. Cho *et al.*, Centimeter-Scale and Visible Wavelength Monolayer Light-Emitting Devices. *Advanced Functional Materials* **30**, 1907941 (2020).
87.M. Paur *et al.*, Electroluminescence from multi-particle exciton complexes in transition metal dichalcogenide semiconductors. *Nature communications* **10**, 1-7 (2019).
88.C. Chen, K. Choi, W. Chang, D. Tsui, Two-color corrugated quantum-well infrared photodetector for remote temperature sensing. *Applied physics letters* **72**, 7-9 (1998).
89.T. Mueller, F. Xia, P. Avouris, Graphene photodetectors for high-speed optical communications. *Nature photonics* **4**, 297 (2010).
90.S. M. Sze, K. K. Ng, *Physics of semiconductor devices*. (John wiley & sons, 2006).
91.J. Wang, J. Han, X. Chen, X. Wang, Design strategies for two-dimensional material photodetectors to enhance device performance. *InfoMat* **1**, 33-53 (2019).
92.K.-J. Tielrooij *et al.*, Generation of photovoltage in graphene on a femtosecond timescale through efficient carrier heating. *Nature nanotechnology* **10**, 437 (2015).
93.C. M. Drain, B. Christensen, D. Mauzerall, Photogating of ionic currents across a lipid bilayer. *Proceedings of the National Academy of Sciences* **86**, 6959-6962 (1989).
94.J. Hou, S. Fonash, Quantum efficiencies greater than unity: A computer study of a photogating effect in amorphous silicon p-i-n devices. *Applied physics letters* **61**, 186-188 (1992).
95.Q. H. Wang, K. Kalantar-Zadeh, A. Kis, J. N. Coleman, M. S. Strano, Electronics and optoelectronics of two-dimensional transition metal dichalcogenides. *Nature nanotechnology* **7**, 699 (2012).
96.O. Lopez-Sanchez, D. Lembke, M. Kayci, A. Radenovic, A. Kis, Ultrasensitive photodetectors based on monolayer MoS 2. *Nature nanotechnology* **8**, 497-501 (2013).
97.W. Zhang *et al.*, Ultrahigh-gain photodetectors based on atomically thin graphene-MoS 2 heterostructures. *Scientific reports* **4**, 3826 (2014).

2. Experimental Techniques

This chapter will describe in details all experimental techniques that have been used in this dissertation. It will also introduce many home-built setups that assists sample preparations and characterizations.

2.1. Chemical Vapor Deposition (CVD)

Chemical vapour deposition (CVD) is a coating process that uses thermally induced chemical reactions at the surface of a heated substrate, with reagents supplied in gaseous form. CVD is a high efficiency method that can be commercialized once robust recipe has been established. With decades' of development, the CVD has been developed into different types, including plasma enhanced CVD (PECVD), low pressure CVD (LPCVD), metalorganic CVD (MOCVD), and ambient pressure CVD. In this section, we will mainly introduce the ambient pressure CVD and PECVD, which have been used in this thesis. The ambient pressure CVD system consists of two main parts. One is the centre tube furnace, which provides a designed temperature zone and also a designed inert gas atmosphere to protect samples. Another part is gas mass controller. This controller can precisely adjust carry gas flow rate that is transported into the tube.

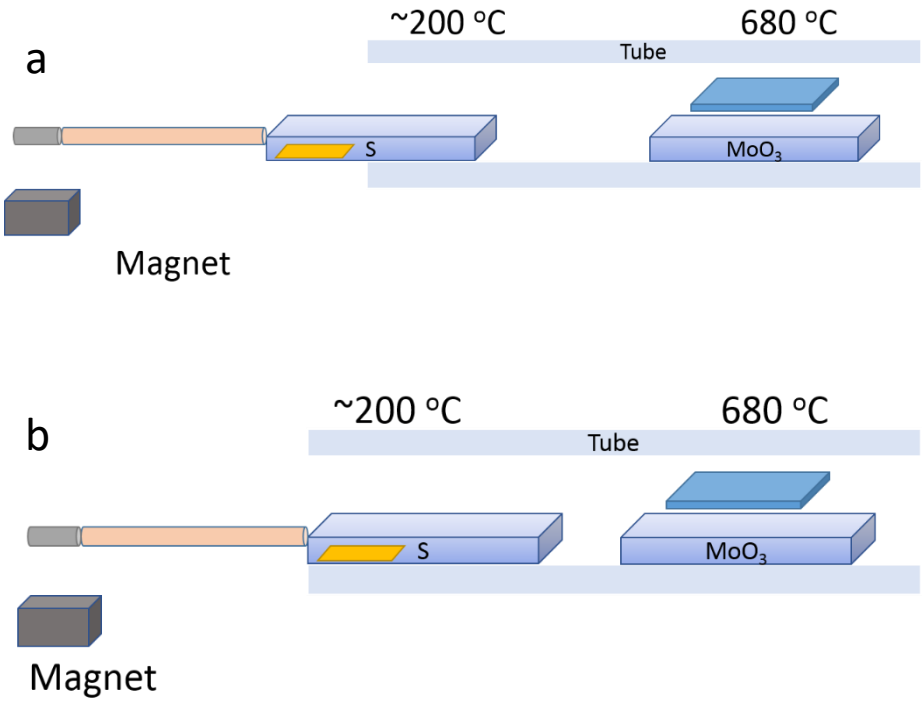

Figure 2. 1 Schematic of the ambient pressure CVD system used in this thesis.

Using growth of monolayer MoS_2 as an example. The target substrate is placed face down to MoO_3 on the quartz boat at downstream. The furnace heats up two precursors which are S and MoO_3 powders. Then the two types of powders located in different location due to different evaporating temperature were evaporated into gas phase. The carry gas Ar is used to take sulphur vapor to MoO_3 area and react with the MoO_3 vapor. During the sulphurising process, the MoO_3 becomes MoOx due to the loss of oxygen and then deposited onto substrate. With the sulphur continuously being pumped in, all the oxygen in MoOx are replaced by sulphur, forming MoS_2. After the reaction, the monolayer and bulk MoS_2 can be deposited onto the target substrate.

The plasma enhanced CVD is used to prepare SiO_2/Si substrate with desired SiO_2 thickness for increasing the optical contrast of few layer hBN. The PECVD used here is a Plasmalab 100 Dual Frequency Model. In the PECVD system, two power generators (13.56 MHz and 50 kHz - 450kHz) are connected through a matching network to the top electrode of the reactor; the bottom electrode is grounded and also serves as a sample holder. There reacting gases, including silane (SiH_4), nitrous oxide (N_2O) and nitrogen (N_2), are used in the PECVD system. They are precisely sent into the reactor through the high accurate mass controllers. The plasma is ignited and maintained by the radio frequency (RF) electronic oscillations between the two electrodes. Firstly, the mixed reacting gases are converted into plasma, following the chemical reaction, which can be expressed as:

$$SiH_4 + 4N_2O \rightarrow SiO_2 + N_2 + H_2O$$

The reaction gas flow rates are 9, 710 and 200 sccm for SiH_4, N_2O and N_2, respectively. The plasma RF power is 20 W and the reaction temperature is 100 ^{0}C. The reaction time is 105 s. The chamber pressure is maintained at 650 mTorr. Under those conditions, a thickness of silicon oxide layer is ~80 nm is obtained and found to be the best for hBN contrast.[1]

2.2. Microscope

2.2.1. Fluorescence Microscope

Mechanical exfoliation is a common method to quickly prepare 2D materials. The exfoliated 2D flake is firstly loaded onto a gel film (purchased from Gel Pak). Then the flake will be checked under microscope to identify the thickness and layer number by optical contrast. However, the optical contrast of monolayer TMDs is typically small. Locating monolayer TMDs becomes a difficult and time-consuming task. Here, we modified the standard optical microscope to convert it to a fluorescence microscope for identifying monolayer samples.

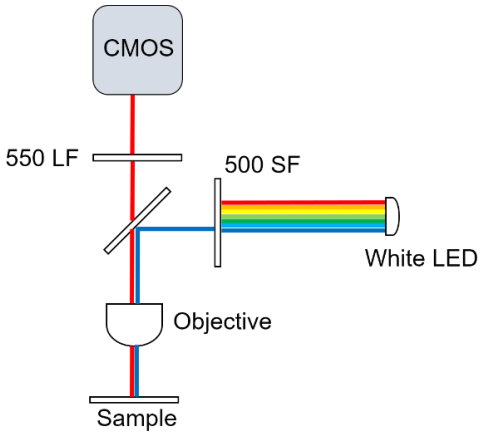

Figure 2. 2 Schematic of the modified fluorescence microscope.

Thanks to the fact that the band gaps of monolayer TMDs are located in visible spectrum regime, hence the monolayer TMDs emit photon when they are excited by higher energy light. In this case, the microscope uses white LED as illumination source. The white LED usually consists of blue, green and red LEDs. A 500 short pass filter will be used to select only blue light component and then use it to excited TMDs samples. The 550 long pass filter is used to block excitation light. The emit photon from TMDs will be detected via a CMOS camera. For instance, the monolayer WS_2 will emit red light, however, the bilayer or even more layer WS_2 flakes emissions are too weak to be detected by CMOS. Figure 2.3 present the images of a monolayer WS_2 under normal microscope and fluorescent microscope.

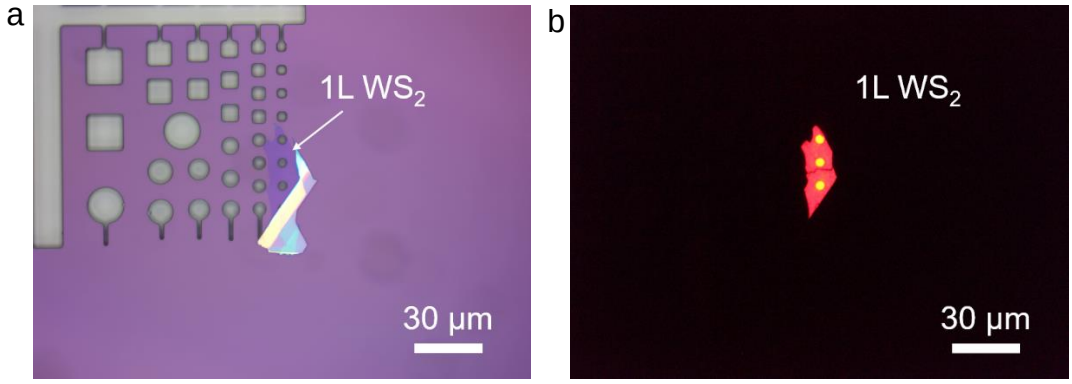

Figure 2. 3 Comparison between microscope and fluorescent microscope image. a, 1L freestanding WS_2 microscope image. b, 1L freestanding WS_2 fluorescent microscope image.

The strong light emission gives a clear signature of the monolayer WS_2. The freestanding area further enhances the signal strength. However, the relatively weak LED light used as light source in this modification limits the ability of exciting samples with weak fluorescence emissions. For example, monolayer MoS_2 can not be identified by this fluorescence microscope because of its weak emission light. In order to extend the microscope working range, a laser source should be employed to replace the LED light source. The scanning mirror is also needed to fast scan the field of view. However, since these two items are typically expensive, they are not normally used for an economic home-made fluorescence microscope system.

2.2.2. Phase Shift Interferometer

Phase shift interferometer (PSI) is an optical system used to measure the optical path length (OPL) of the light incident into a material and then reflected out. This OPL value is typically decided by the optical refractive index of the materials and the thickness of the material. Through PSI, a series of images are acquired with each image having a well-controlled phase shift introduced by the Mirau interferometer objective lens. By comparing the OPL of 2D materials on substrate and the OPL of the pure substrate, one can extract the OPL difference that only originates from the target 2D materials. Figure 2.4 shows schematic of the PSI optical path.

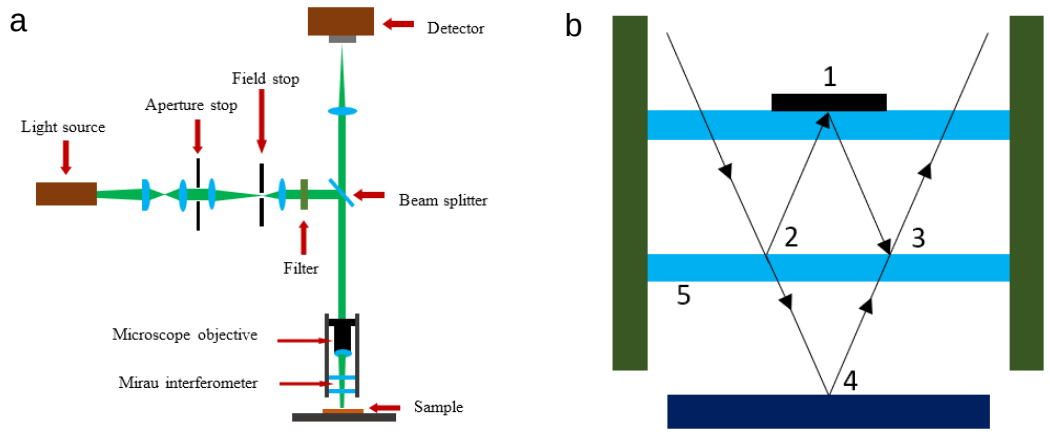

Figure 2. 4 Schematic plot of the phase shifting interferometry (PSI) system. a, Schematic plot of the PSI system. b, Zoomed view of the Mirau interferometer (Adapter with permission from ref [2]).

The Vecco NT9100 PSI system is used in this dissertation with a green LED light source at 535 nm and a 10 nm bandpass filter. More details about how to employ PSI into 2D material layer number characterizations will be demonstrated comprehensively in Chapter 3.

2.3. Atomic Force Microscope

Atomic Force Microscope (AFM) is a technique for high resolution scanning probe microscopy.[3] The information is gathered by sensing atomic force between the material surface and a mechanical probe. Typically, AFM operates under tapping mode or contact mode during the measurement. When the AFM takes images, it measures the force on a sharp tip created by the proximity to the sample surface, and this force is kept small and at a constant level with a feedback mechanism.[3] The tip is fastened to a cantilever spring that has a lower spring constant than the effective spring between two atoms and it will follow the sample contour when moving along the sample.[4] With sufficient sensitivity in the spring deflection sensor, the tip can reveal surface profiles with atomic resolution.[4] In this dissertation, a Bruker MultiMode Ⅷ AFM in ScanAsyst mode is used to measure the thickness of monolayer and few layer 2D materials. The cantilever used is NT-MDT CSG30 with

force constant of 0.6 Nm^{-1} so that the cantilever is soft and flexible. Therefore, it will not damage the sample surface during the image scanning.

2.4. Optical Spectroscopy Characterization Techniques

In this section we will introduce some basic optical spectroscopy methods that commonly used for 2D materials characterisation.

2.4.1. Raman Spectroscopy

Raman spectroscopy comprises the family of spectral measurements made on molecular media based on inelastic scattering of monochromatic radiation. During this process energy is exchanged between the photon and the molecule such that the scattered photon is of higher or lower energy than the incident photon. The difference in energy is made up by a change in the rotational and vibrational energy of the molecule and gives information on its energy levels.[5] Therefore, Raman spectroscopy can be used to determine different 2D materials. The Raman spectroscopy used in this dissertation is the Horiba LabRAM system, which is equipped with a confocal microscope, a charge-coupled device (CCD) Si detector, and a 532 nm diode-pumped solid-state (DPSS) laser as the excitation source. The micro Raman system has installed two grating one is 150 gr/mm, and another is 1200 gr/mm. For Raman measurement, the 1200 gr/mm grating will be used.

2.4.2. PL Spectroscopy

Photoluminescence spectroscopy is a contactless, versatile, non-destructive, powerful optical method of probing the electronic structure of materials. Light is directed onto a sample, where it is absorbed and imparts excess energy into the material in a process called photo excitation. One way this excess energy can be dissipated by the sample is through the emission of light, or luminescence. In the case of photo excitation, this luminescence is called photoluminescence. Thus, photoluminescence is the spontaneous emission of light from a material under optical excitation. This light can be collected and analysed spectrally, spatially, and also temporally. The intensity and spectral content of this photoluminescence is a direct measure of

various important material properties. Two PL Spectroscopy systems have been used in this dissertation. First one is commercial Horiba LabRAM system equipped with a charge-coupled device (CCD) Si detector and a liquid N_2 cooling InGaAs detector. The 532 nm diode-pumped solid-state (DPSS) laser and a SuperK EXTREME supercontinuum laser are used as the excitation source. The second one is a home-made micro PL system equipped with a Kymera 328i spectrograph and an ANDOR iDus 416 charge-coupled device. The solid-state Gem 532 laser from Laser Quantum and the NPI 1064 nm picosecond pulsed laser are used as the excitation laser source. The full picture of system schematic is shown in Figure 2.5.

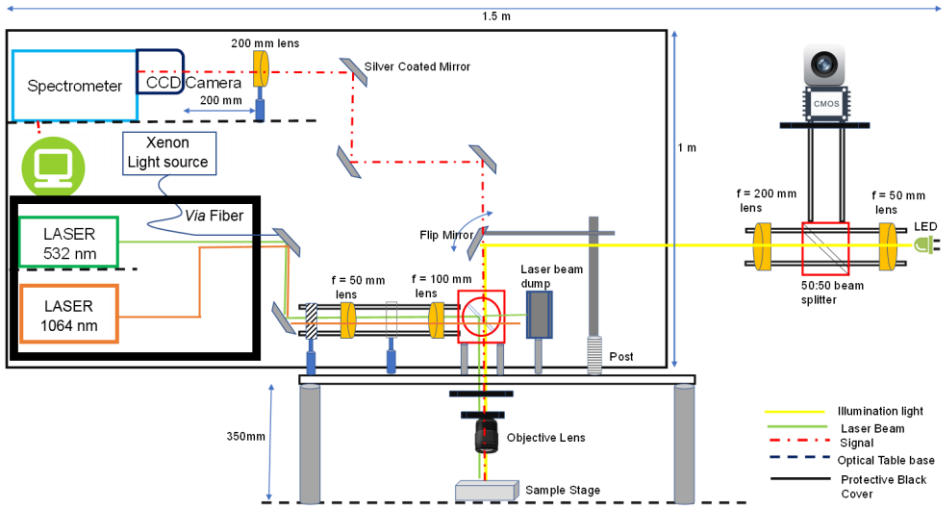

Figure 2. 5 Schematic plot of home-made micro PL system.

The home-made system is designed for PL measurement and Second Harmonic Generation (SHG) measurement.

2.4.3. Conditional PL Spectroscopy

In this section, we will introduce different PL spectroscopy including temperature dependent PL, electrostatic gate dependent PL, and polarization resolved PL, time resolved PL. The PL spectrums under different temperature could provide rich information on carrier transport and some localized states in semiconductor materials. The gate dependent PL and polarization resolved PL techniques are widely used to investigate the exciton optical behaviours and polarized emission light from exciton recombination in 2D materials. Time resolved PL can be used to get information of

the carrier dynamics in time regime. The carrier lifetime can be extracted by this type of measurement. Combined those conditional PL spectrums, the full physical picture of electronic and optical properties of studied 2D materials can be obtained.

2.4.3.1. Temperature Dependent PL Spectroscopy

Temperature dependent PL measurement can be further performed by placing samples in two type of low temperature cryostats. For temperature to ~80 K, the liquid N_2 is used and couple with a Linkam THMS 600 cryostat. For temperature cooling down to ~4K, the Janis ST-500 liquid Helium cryostat is used to load samples. The liquid N_2 is circulating with the Linkam TP94 liquid nitrogen controller, while the liquid Helium is pumping into ST-500 cryostat and then recycled *via* helium pipes that connected into the He recycle centre in the school building. The Linkam THMS 600 cryostat can directly fit into the PL system. However, the ST-500 cryostat can only be fitted into TRPL system, which will be introduced in later section. Moreover, ST-500 cryostat will need pump to vacuum before cooling down the temperature.

2.4.3.2. Electrostatic Gate Dependent PL Spectroscopy

The low temperature gate dependent PL measurement is performed with either Linkam THMS 600 or ST-500 cryostat. The Linkam THMS 600 is equipped with 4 probes, and the electrical signal can be directly applied onto the substrate with probe contact. The ST-500 is equipped with an additional electrical feedthrough. The sample is required to be wire bonded or soldered to the electrical feedthroughs. The gate voltage is applied with Keithley 4200-SCS Parameter Analyzer. The triaxial cables are used to make electrical connection in order to reduce the signal noise.

2.4.3.3. Polarization Resolved PL Spectroscopy

For the polarization resolved PL measurement, it can be performed as excitation polarization dependent or emission polarization dependent. As shown in Figure 2.6, the 532 nm solid state laser source is linear polarized. One half-wave plate will be inserted into excitation beam path.

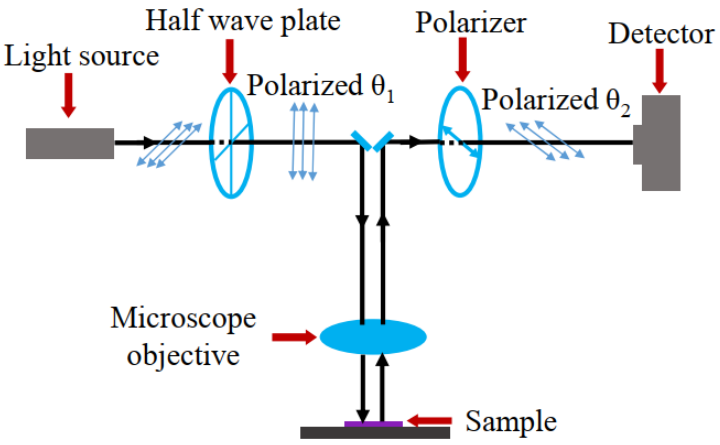

Figure 2. 6 Schematic plot of the optical path in polarization dependent PL measurement (Adapted with permission from ref [6] Copyright 2016 American Chemical Society).

By rotating the half-wave plate, the polarization angle of the excitation laser beam can be rotated. Every one degree of half wave plate change will result in two-degree change of excitation polarization angle. If the emission signals from the sample is polarized light, then they can be distinguished by the polarizer that has been inserted into the emission beam path. The polarizer only allows light pass though when the light polarization aligns with polarizer itself. By rotating 360 degrees of polarizer, one can obtain the polarization information from emission signals.

2.4.3.4. Time-resolved PL/EL Spectroscopy

Differed from steady state PL spectroscopy, time-resolved PL (TRPL) spectroscopy is a transient PL measurement. It can give the ultrafast optical decay information, which can be used as study of photon dynamic. By statistically analysing the time difference between the laser pulse and the photon recorded time by the avalanche photodetector, the carrier lifetime of TMDs can be extracted. The carrier lifetime in TMDs provides the information of the average time that carriers can stay in excited states after the electron-hole generation and before the recombination. The equation for it can be written as:

$$\frac{1}{\tau_{measure}} = \frac{1}{\tau_{nr}} + \frac{1}{\tau_r}$$

where τ_{nr} is the non-radiative recombination lifetime and τ_r is the radiative recombination lifetime. $\tau_{measure}$ can be obtained by fitting the TRPL decay curve.[7] Figure 2.7 shows the schematic diagram of the TRPL system used in this work.

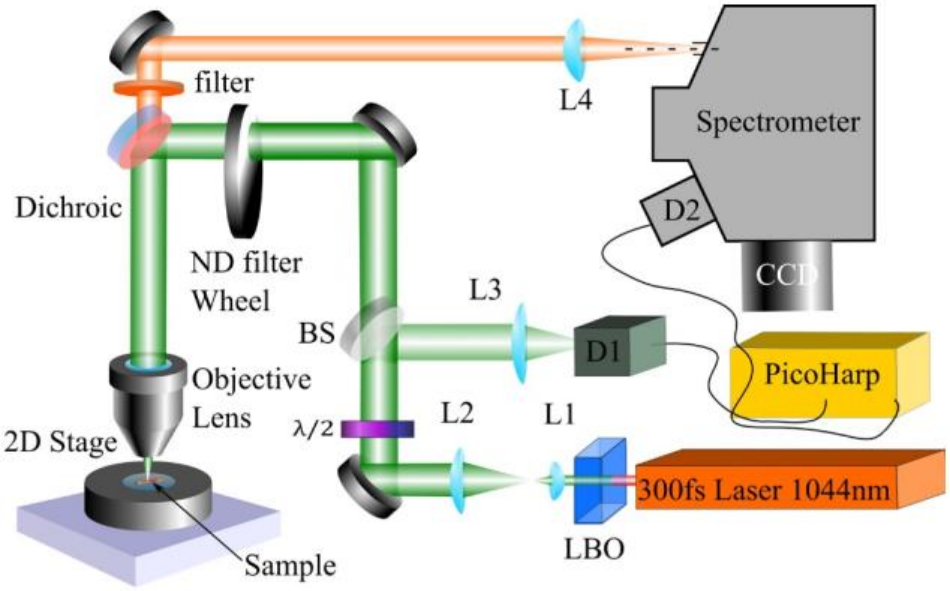

Figure 2. 7 Schematic diagram of the TRPL system ((Adapter with permission from ref [7] Copyright 2015 American Chemical Society).

In the system, a 300 fs pulsed laser has been used, for a time resolution up to 50 ps. The pulsed laser wavelength is frequency doubled to 522 nm with 20.8 MHz repetition rate. A time-correlated single photon counting TCSPC system is used as time tagger. PL signal is collected by a grating spectrometer, by either recording the PL spectrum through a Si CCD (Princeton Instruments, PIXIS) or detecting the PL intensity decay by a Si single photon avalanche diode (SPAD) and the TCSPC (PicoHarp 300) system. A neutral density filter wheel is used to control the laser excitation power.

2.4.4. Anglular Dependent Second Harmonic Generation

Second harmonic generation (SHG) is a nonlinear optical process. When two photons with same frequency interact with a nonlinear crystal, then two photons combine and emit a new photon with twice photon energy than initial photon. The 2D TMDs with odd layer numbers have been demonstrated to have the nonlinear property. The SHG signal can be detected in monolayer, triple layer, five-layer, and

etc 2D TMDs. Interestingly, the SHG signal intensity is very sensitive to the TMDs crystal orientation. Therefore, the angular dependent SHG measurement are commonly used in determining the 2D TMDs orientation. The NPI 1064 nm picosecond pulsed laser has been used in SHG measurement. The total angle dependent SHG setup is shown in Figure 2.8.

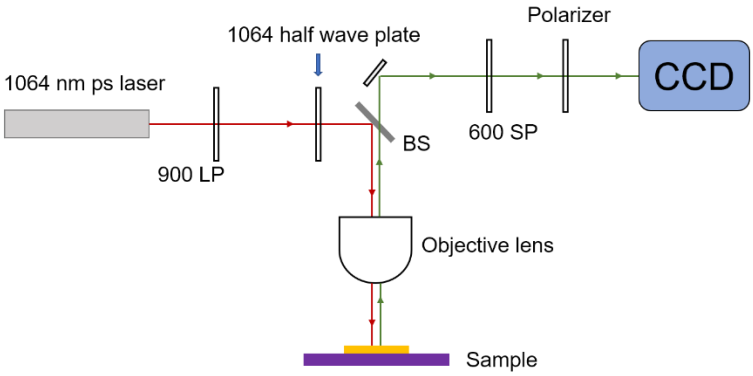

Figure 2. 8 Schematic plot of the angle dependent SHG setup.

The 900 nm long pass filter is used to block light residual that generated from laser head and only let 1064 nm near infrared laser pass through. In order to measure the angle dependent SHG signal, the half-wave plate in excitation side and polarizer in emission side are required to rotate simultaneously with exactly the same degrees. The 600 nm short pass filter used in emission side ensures the signal cleanness to increase the signal to noise ratio.

2.4.5. Electroluminescence Spectroscopy

The electroluminescence (EL) measurement is a key experiment for LED characterization. The optical signal is collected by the commercial Horiba LabRAM system equipped with a charge-coupled device (CCD) Si detector, a liquid N_2 cooling InGaAs detector, and a Kymera 328i spectrograph with an ANDOR iDus 416 charge-coupled device. Different from PL measurement, the excitation laser source has been replaced by electrical components. For DC driven LED device, the Keithley 4200-SCS Parameter Analyzer is used as a voltage and current source to drive the device. For AC driven LED device, the function generator and a signal amplifier has been used in the measurement. The schematic of the whole

measurement setup is shown in Figure 2.9. The Linkam THMS 600 cryostat is used as sample stage.

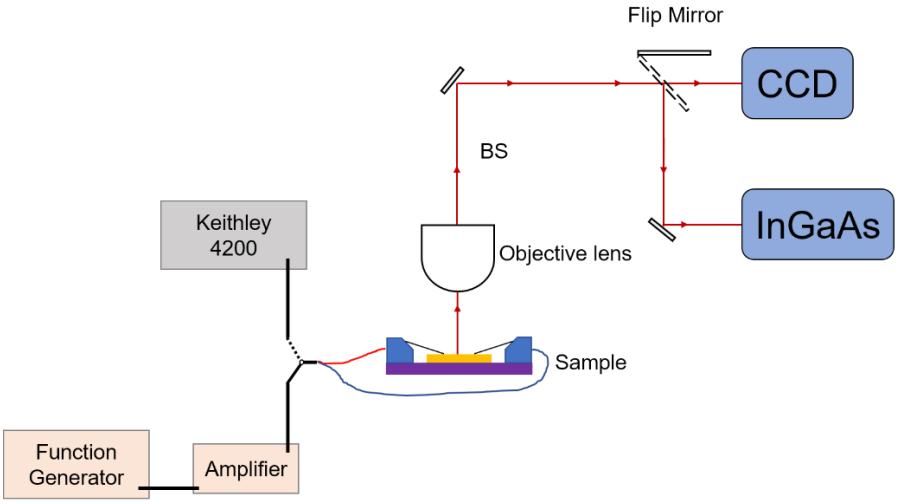

Figure 2. 9 Schematic plot of the electroluminescence setup.

2.5. Device Fabrication

2.5.1 Photolithography

Photolithography is a commonly used technique to define specific patterns in semiconductor research and industry.[8] In this work, photolithography has been used to pattern micro-size electrodes on top of SiO_2/Si substrates. It consists of several steps, including substrate cleaning, photoresist spin-coating, mask alignment, ultra-violet (UV) light exposure and development. Figure 2.10 shows the schematic plot of the photolithography process.

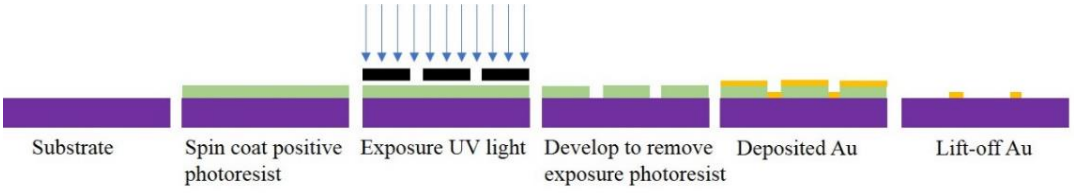

Figure 2. 10 Schematic plot of the photolithography process with positive photoresist.

During the process, the SiO_2/Si substrate (265 nm thermal oxide on n_+-Si) is firstly cleaned with acetone and isopropanol and baked on a hotplate for 2 min at 100 °C. For photoresist spin-coating process, LOR 3A lift-off photoresist and AZ MIR 701 positive photoresist are spin-coated subsequently. LOR 3A is spin coated onto the

clean substrate at 500 rpm for 5 s and 4000 rpm for 45 s, followed by prebake of 2 min at 180 °C with a UniTemp GmbH HPP-155-L hotplate. Then the AZ MIR 701 positive photoresist is spin-coated at 500 rpm for 5 s and 6000 rpm for 1 min, followed by prebake of 2 min at 85 °C with the same hotplate. The photolithography mask is designed with Raith 150 e-beam lithography software, as shown in Figure 2.11.

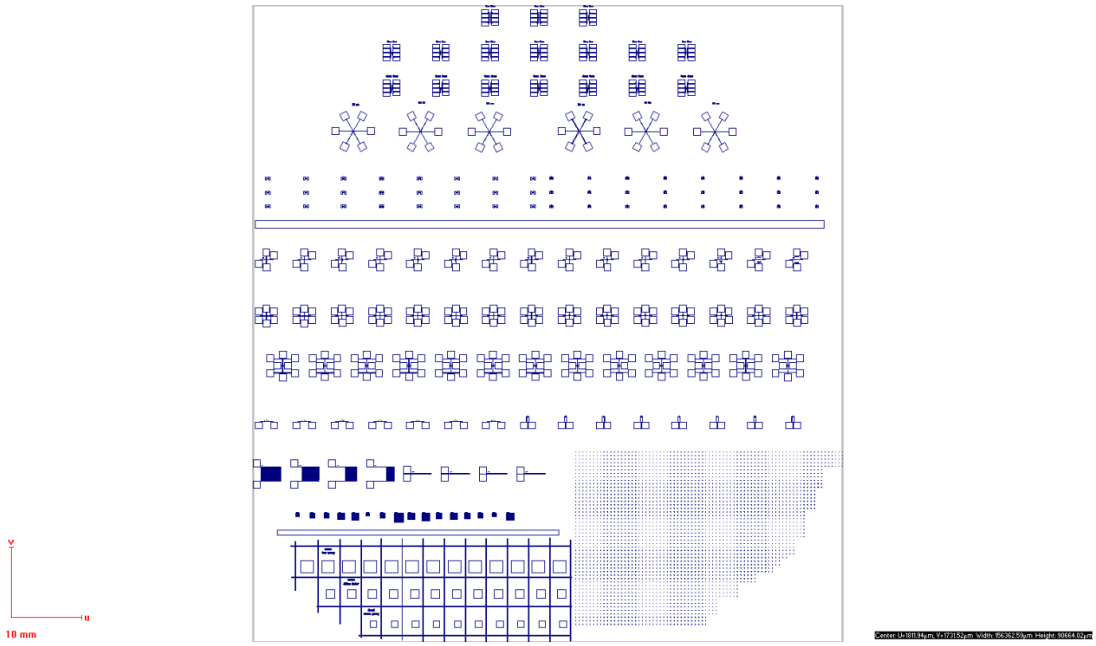

Figure 2. 11 The design of photolithography mask.

After spin coating with designed photoresist, photolithography mask is aligned with the substrate using a Karl Suss MA6/BA6 mask aligner and the gap between mask and substrate is 20 μm. The substrate coated with LOR 3A and AZ MIR 701 is exposed for 35 s in soft contact mode with UV light in the wavelength range of 280-350 nm. In the last step, the exposed substrate is developed in AZ 726 MIF developer for 45-60 s, depending on the development results. After development, the wafer is checked with an optical microscope for the outcome of the photolithography process.

2.5.2 Electron Beam Evaporator

With designed patterned obtained by the photolithography, SiO_2/Si substrates with photoresist patterns are loaded into a Temescal BJD-2000 electron beam thermal evaporator to deposit 5 nm of Ti and 100 nm of Au thin film for electrical contact

fabrication. Electron beam evaporation is a high vacuum deposition technique where electron beam is used to heat the target metal to above its melting point, resulting in its evaporation and deposition as thin film onto the substrates. In our experiment, the deposition rate for Ti and Au thin film is 0.5 Å/s and 2 Å/s, respectively. The deposition happens at room temperature, and the filament current is 30 A and the emission current is 338 mA.

2.6. Home-built Temperature Controller

The mechanical exfoliated monolayer is firstly loaded onto gel films, then the monolayer is dry transferred to target SiO_2Si substrate. However, the difficulty is increasing as stacking multiple monolayer or few layer TMDs together. To overcome this issue, increasing the substrate temperature will increase the adhesion force between TMDs and SiO_2/Si substrate. The small heat plate is required to fit into transfer platform. Therefore, the home-made temperature controller with a Peltier plate is used due to the small size of the plate. The temperature controller is made from the Arduino UNO, and the PID close loop control algorithm is achieved by using a thermocouple. Figure 2.12 shows the real design of the temperature controller. The temperature control range is ranging from -2 ^{0}C to 150 ^{0}C.

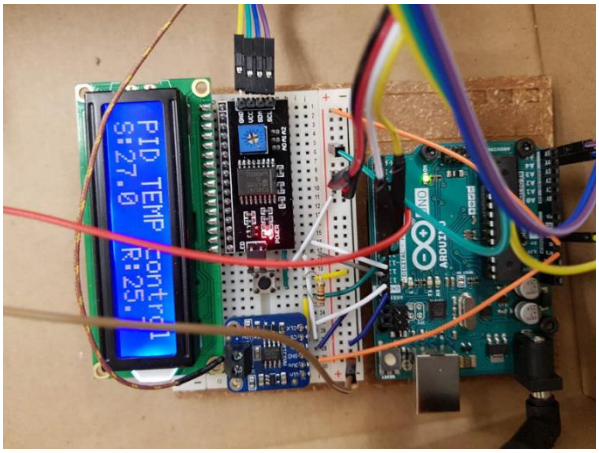

Figure 2. 12 The image of the home-built temperature controller.

2.7. Home-built Micro Manipulator

The electrode transfer method is used in some fast electrode contact task.[8] The pre-patterned Au electrode bars are cut by the micro manipulator. The cut Au bars are

peeled off and then dropped onto designed TMDs device as electrodes. The micro manipulator consists of a three-axis translation stage and a tungsten probe holder. The diameter of the tungsten probe tip is only 1 μm.

2.8. Summary

In this chapter, all the experimental techniques that have been used in this thesis have been briefly introduced, with a typical research flow starting firstly from CVD growth or mechanical exfoliation of 2D material samples. Then AFM and PSI techniques have been used to determine the thickness and layer number of prepared 2D materials. Raman and PL spectroscopy are intensively used to probe the optical properties of the 2D samples. Temperature dependent and gate dependent PL spectroscopy will help to understand the underlying exciton behaviours and the physical picture of the exciton and many body dynamics. Time-resolved PL measurement is carried out to extract the carrier lifetime of 2D materials. Then micro fabrication methods such as photolithography and electron beam evaporation are used to fabricate 2D materials-based devices including field effect transistors, photodetectors and LEDs. The electrical properties of the devices are characterized by Keithley 4200 Semiconductor Parameter Analyzer. Finally, the optoelectronic properties are characterized by electroluminescence spectroscopy and time resolved EL measurements.

References

1. R. V. Gorbachev *et al.*, Hunting for monolayer boron nitride: optical and Raman signatures. *Small* **7**, 465-468 (2011).
2. J. Yang, Inelastic and Elastic Light-Matter Interactions in Two-Dimensional Semiconductors. (2017).
3. G. Binnig, C. F. Quate, C. Gerber, Atomic force microscope. *Physical review letters* **56**, 930 (1986).
4. D. Rugar, P. Hansma, Atomic force microscopy. *Physics today* **43**, 23-30 (1990).
5. J. J. Laserna, An introduction to Raman spectroscopy: introduction and basic principles. *Raman/Infrared Spectroscopy*, (2014).
6. R. Xu *et al.*, Extraordinarily bound quasi-one-dimensional trions in two-dimensional phosphorene atomic semiconductors. *ACS nano* **10**, 2046-2053 (2016).
7. F. Wang *et al.*, Spatially resolved doping concentration and nonradiative lifetime profiles in single Si-doped InP nanowires using photoluminescence mapping. *Nano letters* **15**, 3017-3023 (2015).
8. J. W. Lathrop, The Diamond Ordnance Fuze Laboratory's Photolithographic Approach to Microcircuits. *IEEE Annals of the History of Computing* **35**, 48-55 (2011).
9. Y. Zhang *et al.*, Probing carrier transport and structure-property relationship of highly ordered organic semiconductors at the two-dimensional limit. *Physical review letters* **116**, 016602 (2016).

3. Identify 2D Materials Thickness by Phase Shift Interferometer

Two dimensional materials, such as transition metal dichalcogenides (TMDs) and black phosphorus, exhibit novel electrical and optical properties compared with their bulk forms and thus have great potential for future electronic and optoelectronic applications. Currently, atomic force microscopy (AFM), the most common method used to determine the thickness of two-dimensional (2D) materials, has some limitations due to its low scan speed and inevitable invasion. Fast and non-invasive identification of layer numbers of these 2D materials is worthy to develop for 2D materials field. In this chapter, we will introduce the phase-shifting interferometry (PSI), which has been demonstrated as a rapid and non-invasive method to identify the surface topography of 2D materials. It provides much convenience for future 2D material studies.

3.1. Motivation and Advantages of the PSI

Driven by vast achievements in recent studies of graphene,[1-6] other 2D materials, like MoS_2, WS_2 and phosphorene have attracted further attention due to their extraordinary electrical and optical properties.[7-15] Interestingly, many of the novel properties are highly related to the material thickness. The band gap nature of many 2D materials presents strongly layer dependence, for example, the band structure of TMD materials, such as MoS_2 and WSe_2,[16, 17] will change from indirect to direct as the material thinned from bulk to monolayer. In nonlinear optics, 2D layered materials like WS_2 and 2H-stacked MoS_2 have been reported as potential semiconducting materials for future nonlinear optoelectronic devices due to their strong second harmonic generation (SHG).[18-20] However, the strong SHG can only be observed in these 2D materials with odd layer number because of the broken inversion symmetry.[21] Hence, how to determine the layer number of 2D materials becomes critical for fundamental research of 2D materials. Currently, atomic force microscope (AFM), transmission electron microscope (TEM), and even scanning tunnelling microscope (STM) are used to obtain materials' surface information. All these characterization methods need complicated loading process or very long sample preparation time. However, some materials such as phosphorene[14] and

perovskite[22] decompose rapidly in ambient atmosphere, greatly limiting the measurement accuracy of above methods. Here, we demonstrate that the method of phase-shifting interferometry (PSI) to directly detect surface topography of target 2D materials. Compared with aforementioned characterization methods, PSI has many advantages, including fast response, easy sample loading, and one-step, non-invasive measurement, etc. In this work, we demonstrate the feasibility and capability of PSI method by comparing OPL values with AFM measured results for different cases. With deep analysis of light interference physics in PSI, we successfully built a simulation model and show that our statistical experimental data agree well with the simulation results. This optical interferometry method provides a new approach for future 2D material surface topography characterization.

3.2. Working Principle of the PSI

Interference is a phenomenon already been used in film thickness study since it was first reported. Famous experiments like Newton's ring and air wedge interference are all early stage work and have been employed in some equipment such as Air-wedge shearing interferometer, Newton interferometry, Fresnel interferometry, etc.[24, 25] Here we report a phase-shifting interferometry (PSI) system to investigate the surface topography of thin-layer 2D materials. Basically, the PSI system analyses the digitized interference data obtained from a well-controlled phase shift introduced by the Mirau interferometer and then provides OPL responses after complicated mathematical calculation.[26, 27] The PSI system (Vecco NT9100) used in our experiments operates with a green LED light source centred near 535 nm with a 10 nm band-pass filter.[28] Figure 3.1 a shows the schematic of our PSI system. The whole system consists of light source, detector, Mirau interferometer and other optical components. The illumination from the light source passes a series of lens to the beam splitter and is split into two parts. One beam goes to the detector directly as the reference light. Another beam of light passes through microscope objective and Mirau interferometer and finally reach the target sample. After interacting with sample material, the reflection light carrying phase information goes back to detector. During this process, the sample stage is fixed. To complete data collection, a well-controlled phase shift needs to be introduced to the system. The Mirau interferometer plays a significant role in that and its schematic is shown in Figure 3.1 b. Mirau

interferometer can be integrated in a microscope objective. At the semi-transparent mirror, the source light is split into a reference beam and a sampling beam, indicated as line 2-1-3 and line 2-4-3, respectively. These two beams recombine to form a reference image. By changing the distance between microscope objective and sample, interference images can be acquired at a sequence of phase differences of 0, λ/4, λ/2, 3λ/4. These phase differences are what we want to introduce, and the specific mathematical explanations are shown in supporting information. By understanding PSI system setting, we can generate common equations of optical thickness and optical path difference.

$$h(x,y) = \frac{\lambda\phi(x,y)}{4\pi}$$

$$OPD(x,y) = 2h(x,y) = \frac{\lambda\phi(x,y)}{2\pi}$$

where $\phi(x,y)$ is the measured phase shifts, λ is the wavelength of light source. Here, we want to use this method to obtain topography information of 2D TMD materials. We use optical path length (OPL) to correlate with surface thickness.

$$OPL_{TMD} = -(OPD_{TMD} - OPD_{substrate}) = -\frac{\lambda}{2\pi}(\phi_{TMD} - \phi_{substrate})$$

λ is the wavelength of light source, ϕ_{TMD} and $\phi_{substrate}$ are the measured phase shifts of related light from the TMD material flake and the substrate, respectively. The mathematical derivation is discussed in detail in supporting information. Figure 3.1 c shows the schematic plot of light interacts with our sample. Three important parameters, including substrates, refractive index of materials and the wavelength of light source will influence our measured optical path length (discuss later).

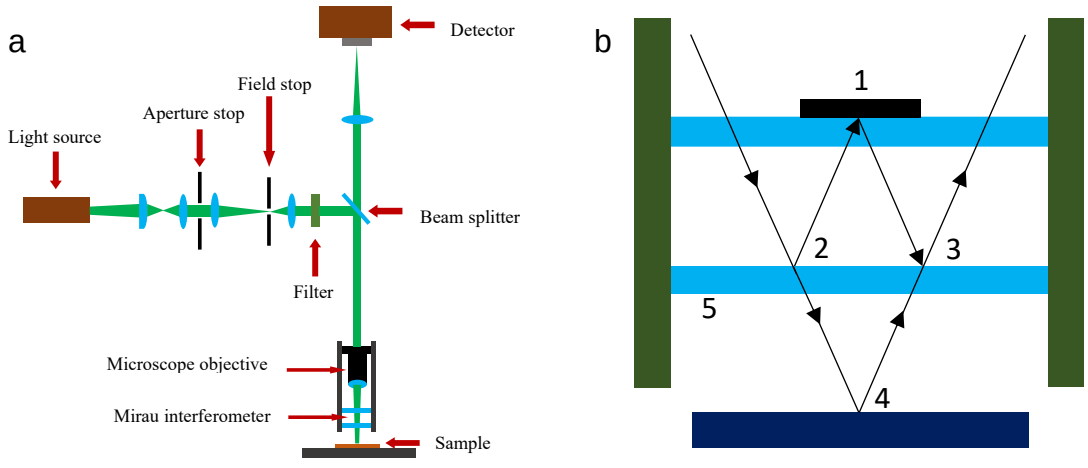

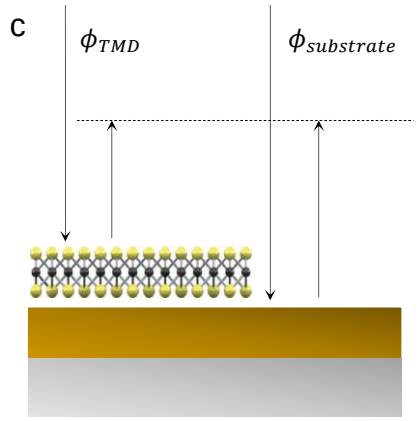

Figure 3. 1 Schematic plot of the phase shifting interferometry (PSI) system. a, Schematic plot of the PSI system. b, Zoomed view of the Mirau interferometer. 1. Reference mirror; 2. First reflection of the reference beam; 3. Third reflection of the reference beam; 4. Reflection of the test/objective beam; 5. Semi-transparent mirror. 2-1-3 represents the reference beam and 2-4-3 represents the test/objective beam. **c,** Schematic plot indicating the PSI measured phase shifts of the reflected light from the TMD material flake (ϕ_{TMD}) and the substrate($\phi_{substrate}$). (Adapter with permission from ref [23]).

3.3. Demonstration of the identification thickness of MoS_2 by PSI

After further understanding of the PSI principle, we immediately realized that it can be a good method to identify the layer number of 2D material, especially for very-few-layer vulnerable samples. To testify its feasibility, thin-layer MoS_2 samples were mechanically exfoliated onto a SiO_2/Si substrate (275 nm thermal oxide). The sample was first characterized by an optical microscope. Different colours from different sample areas in the optical microscope image indicate different layer numbers (Figure 3.2 a). Afterwards, the same sample was measured by PSI (Figure 3.2 b and c), two huge step changes (38 nm and 86 nm) were observed, showing a direct relationship between the OPL and the layer number, marked as 1L MoS_2 and 2L MoS_2, respectively. Subsequent to PSI measurements, the layer thickness was also confirmed by AFM scanning (Figure 3.2 d). Step differences of 0.7 nm and 0.74 nm were identified to be corresponding to mono- and bi-layer MoS_2. The AFM scanning further demonstrates the robust identification of the layer number by PSI. Besides, the real thickness ~0.7 nm of the MoS_2 flake is amplified by more than 50 times in the optical interferometry, which indicates that optical interferometry highly

enhances the resolution of layer identification. The OPL measurement in our experiment is compatible with previous results.[29]

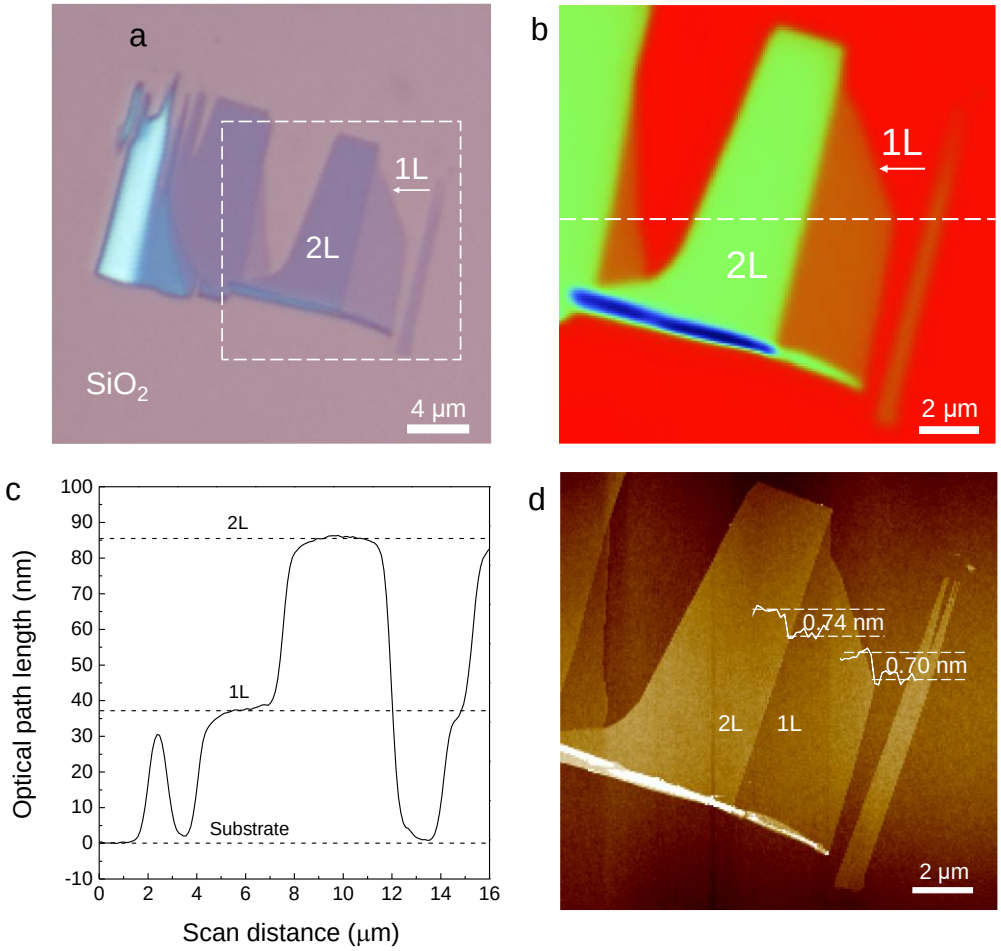

Figure 3. 2 Robust identification of mono- and few-layer MoS_2 on SiO_2 by phase shifting interferometry (PSI). a, Optical microscope image of a monolayer and a bilayer MoS_2 (labeled as "1L" and "2L"). b, PSI image of the same MoS_2 as dash box indicated in (a). c, PSI measured optical path length (OPL) values along the dash line indicated in (b). d, AFM image of 1L to 2L MoS_2 indicated in the dash line boxes in (a).

3.4. Substrate dependent PSI measurement

As we mentioned above, three parameters including substrates, refractive indices of materials and the wavelength of light source, will influence the OPL measurements. The impact of substrates on OPL measurements will be firstly discussed. Here, the OPL values of the same TMD materials (MoS_2 randomly chosen) on different substrates were investigated. We characterized multiple MoS_2 mono- and few-layer

samples on gold, SiO_2/Si (275 nm thermal oxide SiO_2), and fused silica to obtain statistical OPL values of MoS_2 on different substrates (Figure 3.3). The measured OPL values agree very well with our theoretical simulations and show a perfect linear relationship with layer number. Interestingly, OPL values can be either positive or negative with different substrates (Figure 3.3 a, c and e). From the equation we generated, the OPL is proportion to phase shift between light coming out from TMD materials and the substrate, which is $\phi_{substrate} - \phi_{TMD}$. For fused silica substrate, phase shift of TMD materials comparing to the substrate is negative, while the phase shift is positive for TMD materials on gold or SiO_2/Si substrate. Meanwhile, SiO_2/Si substrate offers a better condition for generating a giant OPL of thin-layer MoS_2, which are about an order of magnitude larger than those from gold and fused silica substrates.

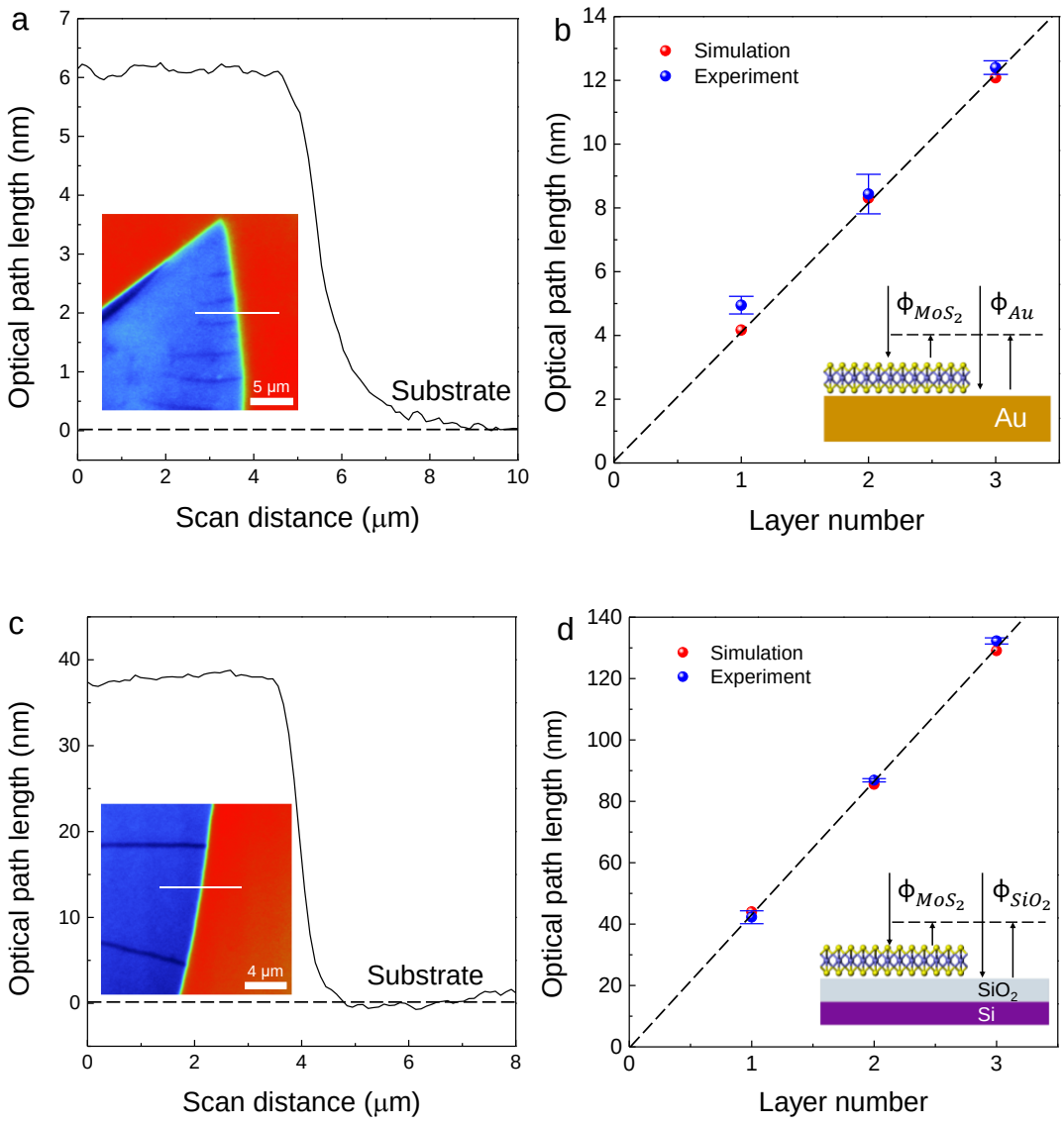

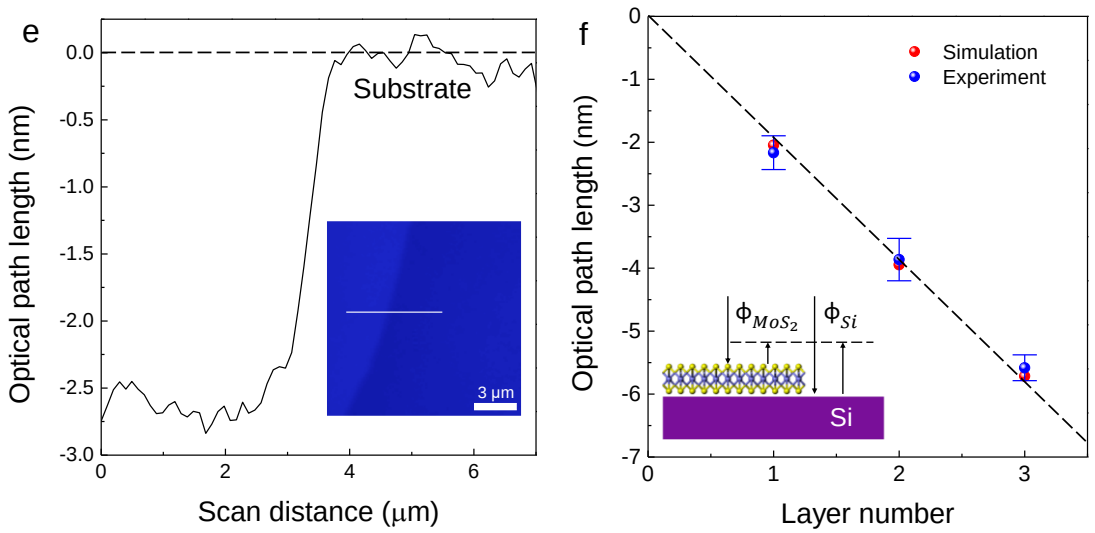

Figure 3. 3 Experimental and simulated OPL values of mono- and few-layer of MoS_2 on different substrates (Au, SiO_2/Si and Fused Silica). a, PSI measured optical path length (OPL) profile of MoS_2 on gold substrate. Inset picture is PSI image of target area and solid line is our OPL scan section. b, statistical OPL values of MoS_2 on gold substrate from 1L to 3L with simulation values. c, PSI measured OPL curve of MoS_2 on SiO_2 substrate alone with solid line indicated in inset PSI image. d, statistical OPL values of MoS_2 on SiO_2 substrate from 1L to 3L with simulation values. e, PSI measured OPL curve of MoS_2 on Fused Silica substrate alone with solid line indicated in inset PSI image. f, statistical OPL values of MoS_2 on Fused Silica substrate from 1L to 3L with simulation values. For each layer number on these three different substrates, at least five samples were characterized to get the statistical values, with error bar shown.

3.5. 2D material dependent PSI measurement

After investigating the effect of different substrates to OPL, here we pick up different 2D materials to test robustness of the PSI system. Firstly, theoretical simulations were carried out to determine the OPL values on SiO_2/Si substrates for different 2D materials with constant thickness 0.67 nm, shown as the solid line in Figure 3.4 a. Obviously, the OPL values increase rapidly with the increase of material refractive index. The OPL values for specific 2D materials, including 0.67 nm SiO_2, 1L (0.42 nm) boron nitride, 1L (0.34 nm) graphene, 1L (0.65 nm) phosphorene, 0.67 nm Si and 1L (0.67 nm) MoS_2 are also presented in Figure 3.4 a marked as solid spheres

with different colours. The solid spheres corresponding to materials with thickness of 0.67 nm sit on the solid line, which confirms the adequacy of our simulation model. The statistical average OPL values with standard error and theoretically calculated OPL values for monolayer (1L) to trilayer (3L) phosphorene, hexagonal boron nitride (hBN) and graphene are presented in Figure 3.4 b, c and d, which is consistent with previous reports.[14, 28, 30, 31] The OPL values collected with our PSI system of 1L to 3L phosphorene are 21.99 ± 3.57 nm, 43.77 ± 3.26 nm and 61.45 ± 3.36 nm; the OPL values for 1L to 3L for hBN are 1.83 ± 0.29 nm, 4.45 ±0.21 nm and 6.09 ± 0.08 nm; and the OPL values for 1L to 3L graphene are 3.86 ± 0.62 nm, 6.06 ± 1.04 nm and 9.86 ± 0.80 nm. All the measured and calculated OPL values for these semiconductors show a good linear relationship with layer number and consist well with each other.

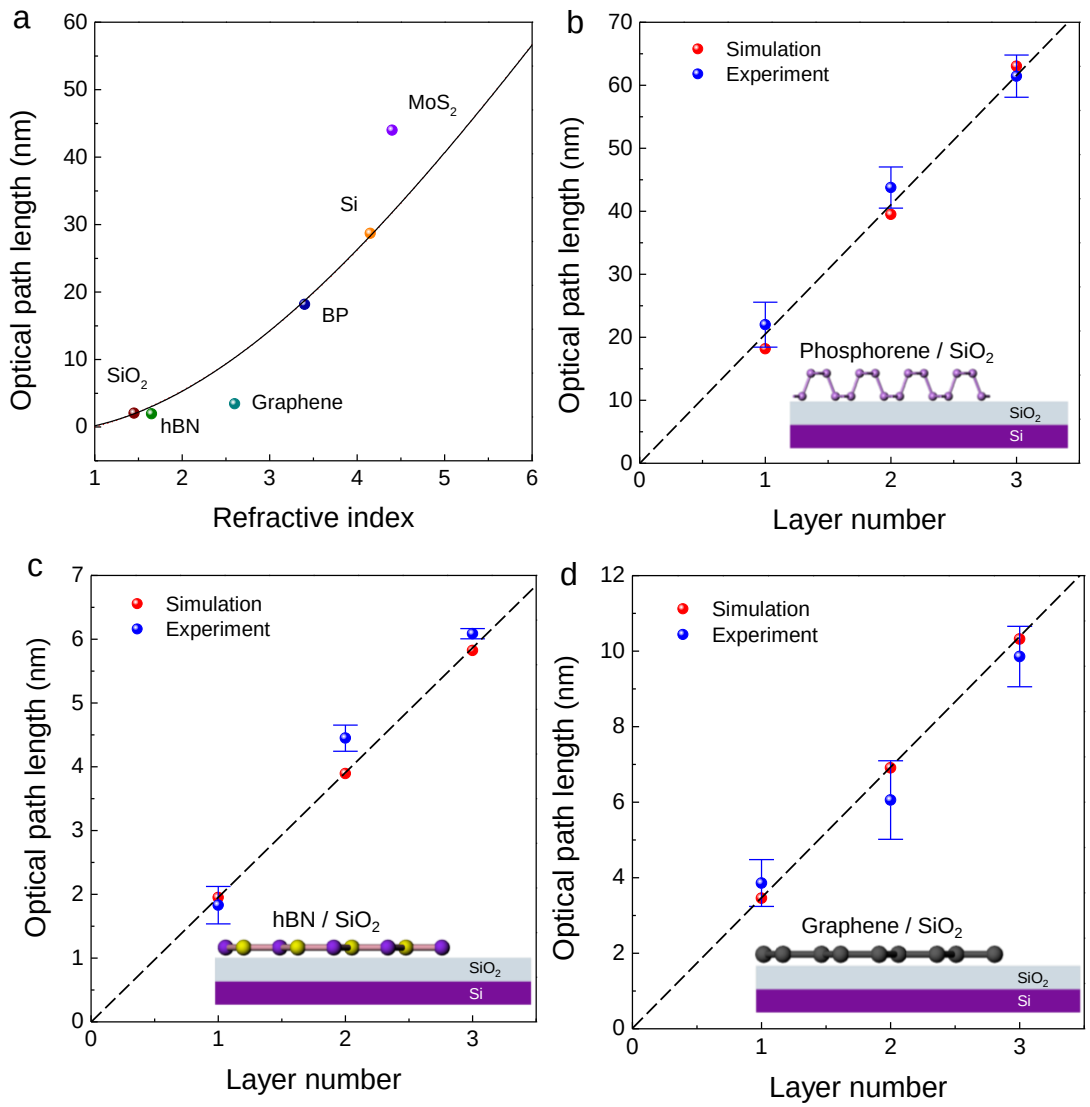

Figure 3. 4 OPL values of mono- and few-layer of selected TMD materials (Black Phosphorene, h-Boron Nitride and Graphene). The calculated OPL values of 0.67 nm SiO_2, 1L (0.42 nm) h-boron nitride, 1L (0.34 nm) graphene, 1L (0.65 nm) phosphorene, 0.67 nm Si and 1L (0.67 nm) MoS_2 are represented by markers. Solid black line is our OPL simulation results as a function of refractive index. b, statistical OPL values of phosphorene samples from 1L to 3L compared with numerical simulation OPL values. c, statistical OPL values of h-boron nitride samples from 1L to 3L compared with numerical simulation OPL values. d, statistical OPL values of graphene samples from 1L to 3L compared with numerical simulation OPL values. For each layer number of these three semiconductors, at least five samples were characterized to get the statistical data, with error bar shown.

3.6. Wavelength dependent PSI measurement

For the PSI measurements, a non-focused and low-density 535 nm green light generated from a light-emitting diode is the only light source in our PSI system, and thus the impact of the wavelength of light source to OPL values cannot be demonstrated in the experiments. Unlike other methods such as confocal Raman system, this non-focused light source is a non-invasive source and causes almost no damage to our samples, making it especially favourable for vulnerable materials such as phosphorene.

3.7. Summary

In summary, we have demonstrated a rapid, non-invasive, highly accurate and easy-to-operate approach to identify the surface topography of different 2D materials on different substrates by using phase-shifting interferometry. We showed the robustness of PSI for identifying the layer number of 2D materials by comparing with AFM results. Meanwhile, PSI also presents extremely high resolution in determining the layer number because of the giant OPL. Furthermore, the impact of substrates, refractive indices of different materials and the wavelength of light source on OPL values are discussed to better understand the principle of phase-shifting interferometry. Our measured OPL values of different materials on different substrates show a linear relationship with layer numbers and consist very well with

calculations, demonstrating that PSI can be used as a fast and non-invasive method to characterize the layer number of 2D materials.

3.8. Experiment

Sample preparation. All samples were transferred onto substrates by mechanically exfoliated from their bulk material using GEL film. For rapid degradation material, black phosphorus, the sample was rapidly measured after it first be prepared to keep measurement accurate.

Sample Characterization. PSI measurement was carried out with a Vecco NT9100 phase-shifting interferometry. AFM measurement was carried out in ambient atmosphere at room temperature by a Bruker Multi-Mode III atomic force microscopy.

References

1. A. K. Geim, K. S. Novoselov, The rise of graphene. *Nature materials* **6**, 183-191 (2007).
2. H. Goncalves *et al.*, Enhancement of graphene visibility on transparent substrates by refractive index optimization. *Opt Express* **21**, 12934-12941 (2013).
3. E. J. Santos, E. Kaxiras, Electric-field dependence of the effective dielectric constant in graphene. *Nano Lett* **13**, 898-902 (2013).
4. T. T. Tang *et al.*, A tunable phonon-exciton Fano system in bilayer graphene. *Nat Nanotechnol* **5**, 32-36 (2010).
5. J. Xia, F. Chen, J. Li, N. Tao, Measurement of the quantum capacitance of graphene. *Nat Nanotechnol* **4**, 505-509 (2009).
6. K. S. Novoselov *et al.*, A roadmap for graphene. *Nature* **490**, 192-200 (2012).
7. M. Buscema *et al.*, Fast and broadband photoresponse of few-layer black phosphorus field-effect transistors. *Nano Lett* **14**, 3347-3352 (2014).
8. L. Li *et al.*, Black phosphorus field-effect transistors. *Nat Nanotechnol* **9**, 372-377 (2014).
9. K. F. Mak *et al.*, Tightly bound trions in monolayer MoS2. *Nat Mater* **12**, 207-211 (2013).
10. D. Mao *et al.*, WS2 mode-locked ultrafast fiber laser. *Sci Rep* **5**, 7965 (2015).
11. B. Radisavljevic, A. Radenovic, J. Brivio, V. Giacometti, A. Kis, Single-layer MoS2 transistors. *Nat Nanotechnol* **6**, 147-150 (2011).
12. J. S. Ross *et al.*, Electrical control of neutral and charged excitons in a monolayer semiconductor. *Nat Commun* **4**, 1474 (2013).
13. F. Withers *et al.*, Light-emitting diodes by band-structure engineering in van der Waals heterostructures. *Nat Mater* **14**, 301-306 (2015).
14. J. Yang *et al.*, Optical tuning of exciton and trion emissions in monolayer phosphorene. *Light: Science & Applications* **4**, e312 (2015).
15. S. Zhang *et al.*, Extraordinary photoluminescence and strong temperature/angle-dependent Raman responses in few-layer phosphorene. *ACS nano* **8**, 9590-9596 (2014).
16. A. Splendiani *et al.*, Emerging photoluminescence in monolayer MoS2. *Nano Lett* **10**, 1271-1275 (2010).
17. W. Zhao *et al.*, Evolution of electronic structure in atomically thin sheets of WS2 and WSe2. *ACS nano* **7**, 791-797 (2013).
18. C. Janisch *et al.*, Extraordinary Second Harmonic Generation in tungsten disulfide monolayers. *Sci Rep* **4**, 5530 (2014).
19. Y. Li *et al.*, Probing symmetry properties of few-layer MoS2 and h-BN by optical second-harmonic generation. *Nano Lett* **13**, 3329-3333 (2013).
20. K. L. Seyler *et al.*, Electrical control of second-harmonic generation in a WSe 2 monolayer transistor. *Nature nanotechnology* **10**, 407-411 (2015).
21. L. Mennel, M. Paur, T. Mueller, Second harmonic generation in strained transition metal dichalcogenide monolayers: MoS2, MoSe2, WS2, and WSe2. *APL Photonics* **4**, 034404 (2019).
22. J. Yang, B. D. Siempelkamp, D. Liu, T. L. Kelly, Investigation of CH3NH3PbI3 Degradation Rates and Mechanisms in Controlled Humidity Environments Using in Situ Techniques. *ACS nano* **9**, 1955-1963 (2015).
23. J. Yang, Inelastic and Elastic Light-Matter Interactions in Two-Dimensional Semiconductors. (2017).
24. S. A. Pikuz *et al.*, A simple air wedge shearing interferometer for studying exploding wires. *Review of Scientific Instruments* **72**, 1098 (2001).
25. S.-W. Kim, G.-H. Kim, Thickness-profile measurement of transparent thin-film layers by white-light scanning interferometry. *Applied Optics* **38**, 5968-5973 (1999).
26. R. Leach, *Optical measurement of surface topography*. (Springer, 2011).
27. M. Vaupel, A. Dutschke, U. Wurstbauer, F. Hitzel, A. Pasupathy, Topography, complex refractive index, and conductivity of graphene layers measured by correlation of optical

interference contrast, atomic force, and back scattered electron microscopy. *Journal of Applied Physics* **114**, 183107 (2013).
28. D. K. Venkatachalam, P. Parkinson, S. Ruffell, R. G. Elliman, Rapid, substrate-independent thickness determination of large area graphene layers. *Applied Physics Letters* **99**, 234106 (2011).
29. J. Yang *et al.*, Atomically Thin Optical Lenses and Gratings. *arXiv preprint arXiv:1411.6200*, (2014).
30. R. Xu *et al.*, Layer-dependent surface potential of phosphorene and anisotropic/layer-dependent charge transfer in phosphorene–gold hybrid systems. *Nanoscale* **8**, 129-135 (2016).
31. S. Zhang *et al.*, Extraordinarily bound quasi-one-dimensional trions in two-dimensional phosphorene atomic semiconductors. *arXiv preprint arXiv:1411.6124*, (2014).

Appendix:

Supporting Information for Chapter 3

1. Phase-shifting interferometry (PSI) working principle

PSI is used to investigate surface topography based on analyzing the digitalized interference data obtained during a well-controlled phase shift introduced by the Mirau interferometer.[1] PSI is capable of measuring the optical path length within an error of $\lambda/1000$, where λ is the wavelength of light. The PSI system (Vecco NT9080) used in our experiments operates with a green LED source centered near 532 nm by a 10 nm band-pass filter.[2]

The working principle of our PSI system is as follows.[3] For simplicity, wave front phase will be used for analysis. The expressions for the reference and test wavefronts in the phase shift interferometer are:

$$w_r(x,y) = a_r(x,y)e^{i\phi_r(x,y)} \tag{S1}$$

$$w_t(x,y,t) = a_t(x,y)e^{i[\phi_t(x,y)+\delta(t)]} \tag{S2}$$

where $a_r(x,y)$ and $a_t(x,y)$ are the wavefront amplitudes, $\phi_r(x,y)$ and $\phi_t(x,y)$ are the corresponding wavefront phases, and $\delta(t)$ is a time-dependent phase shift introduced by the Mirau interferometer. $\delta(t)$ is the relative phase shift between the reference beam and the test beam.

The interference pattern of these two beams is:

$$w_i(x,y,t) = a_r(x,y)e^{i\phi_r(x,y)} + a_t(x,y)e^{i[\phi_t(x,y)+\delta(t)]} \tag{S3}$$

The interference intensity pattern detected by the detector is:

$$\boldsymbol{I}_i(x,y,t) = w_i^*(x,y,t) * w_i(x,y,t) = \boldsymbol{I}'(x,y) + \boldsymbol{I}''(x,y)\cos[\phi(x,y) + \delta(t)] \tag{S4}$$

where $\boldsymbol{I'}(x,y) = a_r^2(x,y) + a_t^2(x,y)$ is the averaged intensity, $\boldsymbol{I''}(x,y) = 2a_r(x,y) * a_t(x,y)$ is known as intensity modulation and $\phi(x,y)$ is the wavefront phase shift $\phi_r(x,y) - \phi_t(x,y)$.

From the above equation, a sinusoidally varying intensity of the interferogram at a given measurement point as a function of $\delta(t)$ is shown below:

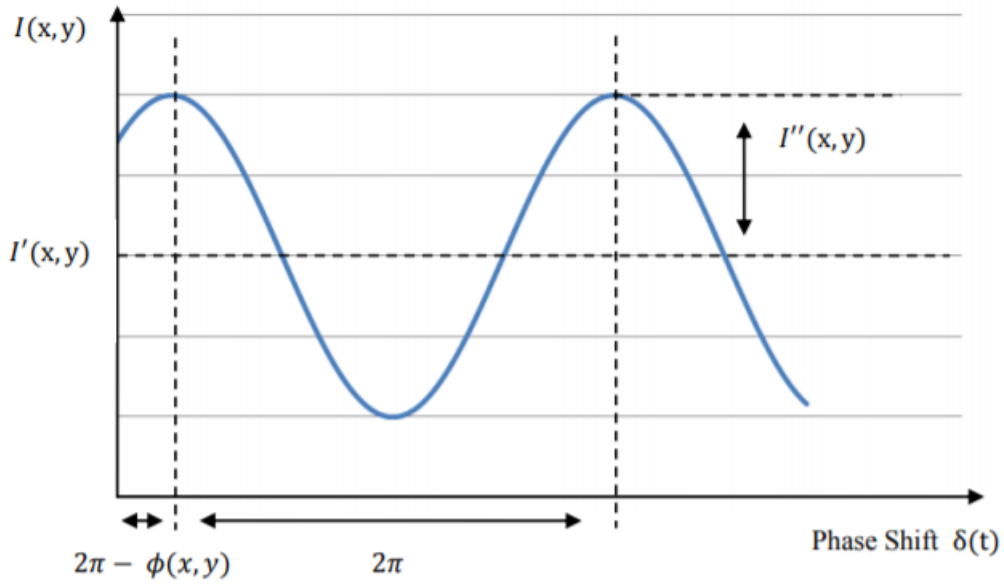

Figure S1 | Variation of intensity with the reference phase at a point in an interferogram. $\boldsymbol{I'}(x,y)$ is the averaged intensity, $\boldsymbol{I''}(x,y)$ is the half of the peak-to-valley intensity modulation and $\phi(x,y)$is the temporal phase shift of this sinusoidal variation.

$\delta(t)$ is introduced by the Mirau interferometer. When the Mirau interferometer gradually moves toward the sample platform, the optical path length (OPL) of the test beam decreases while the OPL of the reference beam keeps invariant.

The computational method of PSI is the four-step algorithm, which needs to acquire four separate recorded and digitalized interferograms of the measurement region. For each separate and sequential recorded interferograms, the spacing phase shift is:

$$\delta(t_i) = 0, \frac{\pi}{2}, \pi, \frac{3\pi}{2};\ \ i = 1,2,3,4 \tag{S5}$$

Substitute these four values into the equation S4, the following four equations describing the four measured intensity patterns of the interferogram are given:

$$\boldsymbol{I}_1(x,y) = \boldsymbol{I}'(x,y) + \boldsymbol{I}''(x,y)\cos[\phi(x,y)] \tag{S6}$$

$$\boldsymbol{I}_2(x,y) = \boldsymbol{I}'(x,y) + \boldsymbol{I}''(x,y)\cos[\phi(x,y) + \frac{\pi}{2}] \tag{S7}$$

$$\boldsymbol{I}_3(x,y) = \boldsymbol{I}'(x,y) + \boldsymbol{I}''(x,y)\cos[\phi(x,y) + \pi] \tag{S8}$$

$$\boldsymbol{I}_4(x,y) = \boldsymbol{I}'(x,y) + \boldsymbol{I}''(x,y)\cos[\phi(x,y) + \frac{3\pi}{2}] \tag{S9}$$

After the trigonometric identity, it yields:

$$\boldsymbol{I}_1(x,y) = \boldsymbol{I}'(x,y) + \boldsymbol{I}''(x,y)\cos[\phi(x,y)] \tag{S10}$$

$$\boldsymbol{I}_2(x,y) = \boldsymbol{I}'(x,y) - \boldsymbol{I}''(x,y)\sin[\phi(x,y)] \tag{S11}$$

$$\boldsymbol{I}_3(x,y) = \boldsymbol{I}'(x,y) - \boldsymbol{I}''(x,y)\cos[\phi(x,y)] \tag{S12}$$

$$\boldsymbol{I}_4(x,y) = \boldsymbol{I}'(x,y) + \boldsymbol{I}''(x,y)\sin[\phi(x,y)] \tag{S13}$$

The unknown variables $\boldsymbol{I}'(x,y)$, $\boldsymbol{I}''(x,y)$ and $\phi(x,y)$ can be solved by only using three of the four equations; but for computational convenience, four equations are used here. Subtracting equation S11 from equation S13, we have:

$$\boldsymbol{I}_4(x,y) - \boldsymbol{I}_2(x,y) = 2\boldsymbol{I}''(x,y)\sin[\phi(x,y)] \tag{S14}$$

And subtract equation S12 from equation S10, we get:

$$\boldsymbol{I}_1(x,y) - \boldsymbol{I}_3(x,y) = 2\boldsymbol{I}''(x,y)\cos[\phi(x,y)] \tag{S15}$$

Taking the ratio of equation S14 and equation S15, the intensity modulation $\boldsymbol{I}''(x,y)$ will be eliminated as following:

$$\frac{\boldsymbol{I}_4(x,y) - \boldsymbol{I}_2(x,y)}{\boldsymbol{I}_1(x,y) - \boldsymbol{I}_3(x,y)} = \tan[\phi(x,y)] \tag{S16}$$

Rearrange equation S16 to get the wavefront phase shift term $\phi(x,y)$:

$$\phi(x,y) = \tan^{-1}\frac{\boldsymbol{I}_4(x,y) - \boldsymbol{I}_2(x,y)}{\boldsymbol{I}_1(x,y) - \boldsymbol{I}_3(x,y)} \tag{S17}$$

This equation is performed at each measurement point to acquire a map of the measured wavefront. Also, in PSI, the phase shift is transferred to the surface height or the optical path difference (OPD):

$$h(x,y) = \frac{\lambda\phi(x,y)}{4\pi} \tag{S18}$$

$$OPD(x,y) = \frac{\lambda\phi(x,y)}{2\pi} \tag{S19}$$

Here, the OPL of the MoS_2 flake is calculated as:

$$OPL_{MoS_2} = -(OPD_{MoS_2} - OPD_{SiO_2}) = -\frac{\lambda}{2\pi}(\phi_{MoS_2} - \phi_{SiO_2}) \tag{S20}$$

where λ is the wavelength of the light source, ϕ_{MoS_2} and ϕ_{SiO_2} are the measured phase shifts of the reflected light from the MoS_2 flake and the SiO_2 substrate, respectively. In our experiments, ϕ_{SiO_2} was typically set to be zero.

2. Positive and negative phase shift for TMD on different substrates

The positive and negative OPL values have both been observed in Figure 3.3. When MoS_2 layer sits on top of the SiO_2, it yields the positive OPL value. However, the negative OPL value has been achieved when MoS_2 is on top of Si. From equation of S20, we have:

$$OPL_{MoS_2} = -(OPD_{MoS_2} - OPD_{SiO_2}) = -\frac{\lambda}{2\pi}(\phi_{MoS_2} - \phi_{SiO_2}) \tag{S20}$$

$$OPL_{MoS_2} = -(OPD_{MoS_2} - OPD_{Si}) = -\frac{\lambda}{2\pi}(\phi_{MoS_2} - \phi_{Si}) \tag{S21}$$

The phase shift difference between MoS_2 and SiO_2 is negative, while the phase shift difference between MoS_2 and Si is positive. Hence, it causes positive and negative OPL values. The only difference between SiO_2 and Si substrate is their refractive index. Hence, we have simulated the OPL as a function of substrate refractive index, as shown in Figure S2.

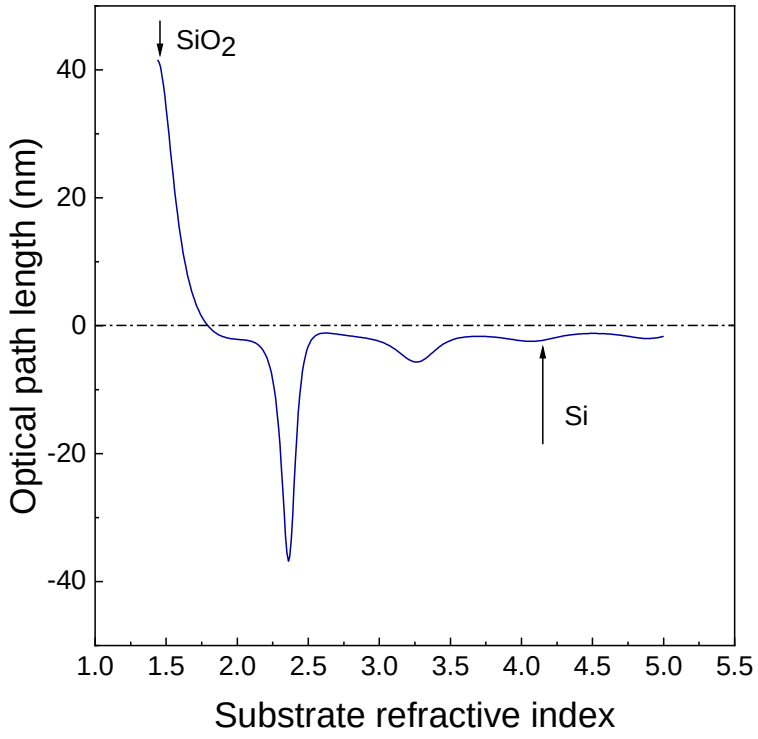

Figure S2 | Substrate refractive index dependent optical path length. SiO_2 substrate can generate the positive OPL, while Si substrate gives the negative OPL values.

With small refractive index, the positive OPL can be generated, while the larger refractive index gives the negative OPL values. The light wavefront phases from SiO_2 and from Si have different phase shift comparing with wavefront phases from TMD, leading the different sign of OPL value.

References

1. R. Leach, *Optical measurement of surface topography*. (Springer, 2011), vol. 14.
2. D. K. Venkatachalam, P. Parkinson, S. Ruffell, R. G. Elliman, Rapid, substrate-independent thickness determination of large area graphene layers. *Applied Physics Letters* **99**, 234106 (2011).
3. H. Schreiber, J. H. Bruning, Optical shop testing. *Phase Shifting Interferometry*, (2007).

4. Ferroelectric Driven Exciton and Trion Modulation in Monolayer $MoSe_2$ and WSe_2

In past few years, it has been shown that monolayer TMDs present a great platform for studying exciton dynamics due to its large binding energy. Much effort has been made to observe exciton and high order exciton many body effects in 2D materials. With the improved understanding of exciton behaviours in TMDs, the next stage would be exploring the manipulation and modulation of the exciton species, for the TMD based optoelectronic applications. In this chapter, we show how domain engineered lithium niobate can be used to selectively dope monolayer molybdenum selenide ($MoSe_2$) and tungsten selenide (WSe_2) and demonstrate that these ferroelectric domains can significantly enhance or inhibit photoluminescence (PL) with the most dramatic modulation occurring at the heterojunction interface between two domains. A micro-PL and Raman system is used to obtain spatially resolved images of the differently doped transition metal dichalcogenides (TMDs). The domain inverted lithium niobate causes changes in the TMDs due to electrostatic doping as a result of the remnant polarization from the substrate. Moreover, the differently doped TMDs (n-type $MoSe_2$ and p-type WSe_2) exhibit opposite PL modulation. Distinct oppositely charged domains were obtained with a 9-fold PL enhancement for the same single $MoSe_2$ sheet when adhered to the positive (P^+) and negative (P^-) domains. This sharp PL modulation on the ferroelectric domain results from different free electron or hole concentrations in the materials conduction band or valence band. Moreover, excitons dissociate rapidly at the interface between the P^+ and P^- domains due to the built-in electric field. We are able to adjust the charge on the P^+ and P^- domains using temperature *via* the pyroelectric effect and observe rapid PL quenching over a narrow temperature range illustrating the observed PL modulation is electronic in nature. This observation creates an opportunity to harness the direct bandgap TMD 2D materials as an active optical component for the lithium niobate platform using domain engineering of the lithium niobate substrate to create optically active heterostructures that could be used for photodetectors or even electrically driven optical sources on-chip.

The content of this chapter has been published in ACS Nano 2019, 13, 5, 5335-5343. https://doi.org/10.1021/acsnano.8b09800.

4.1. Introduce of Ferroelectric Lithium Niobate and Hybridization with TMDs

Direct bandgap monolayer transition metal dichalcogenides (TMDs) have attracted tremendous interest due to their optically controlled valley polarization and coherence, giant spin-valley coupling and tightly bound excitonic states.[1-10] Owing to their atomically thin structure, monolayer TMDs act as semiconductors which can undergo a complete transition from indirect to a direct bandgap, with energy gaps located at the Brillouin zone producing a strong exciton pumping efficiency.[2] In particular, monolayer TMDs provide a platform for investigating the dynamics of excitons in reduced dimensions at room temperature and fundamental many-body interactions.[11-17] The ability to access exciton behaviors at room temperature with this platform creates opportunities for high quality optical detection and ultimately optical sources.[18] So far, many investigations for TMD p-n diodes (positive-negative) consist of one monolayer TMD material and two splitting gate metals.[19-21] This method sets a gate voltage through the metallic contacts to dope the TMDs achieving strong charge-density tuning and therefore creates a lateral p-n junction. However, the metal gates can result in an inhomogeneous charge distribution and unavoidable quenching of light emission at the TMD surface.

Owing to ultra-thin nature of TMDs TMD materials are sensitive to the surrounding ionic environment, which opens the possibility of ferroelectric gating control of monolayer TMDs due to quantum confinement, high carrier mobility and a tunable bandgap. Ferroelectric (FE) materials possess a spontaneous electrical polarization resulting in a strong built in electric field along polar axis and very strong surface charges with positive charges on one surface and negative charges on the other. The spontaneous electrical polarization can be inverted through application of a strong electric field and this can be done locally to create a spatial domain pattern of positive or negative polar surfaces. This domain pattern can offer a strategy for lateral modulation in TMDs to create electro-statically driven p-n homojunction, which offers an alternative to complex split-gate electrodes.[22] Importantly, if the ferroelectric substrate is optically transparent, then the quenching of light emission often encountered with split-gate electrodes can be overcome.

Lithium niobate ($LiNbO_3$, LN) is a widely known ferroelectric material for optical waveguides, optical modulators, piezoelectric sensors and is an industry standard platform for wavelength conversion, high speed communications, microwave photonics and emerging platform for quantum optics.[23-27] Its utility in photonics is based on its excellent optical transparency from visible to mid infrared wavelengths and its strong ferroelectric nature leads to relatively efficient and ultra-high speed electro-optic and nonlinear optic properties. Due to the ability to integrate so many functionalities LN has recently been proposed as a next generation optical integration platform.[26] However, since LN is not a semiconductor, it cannot inherently provide high speed photodetectors or laser sources. This has led to many researchers exploring hybrid integration to obtain these functionalities.[25]

Hybridization of TMDs with $LiNbO_3$ thus presents a tantalizing opportunity to introduce electronically driven active optical functionality to the LN platform – essentially completing the toolbox of functional components that can be integrated on a single chip. By domain engineering patterns into a LN substrate it could be possible to modulate the carrier density in a monolayer TMD and create optically active p-n junctions – with geometry defined by the substrate poling pattern - independent of the alignment of the TMD film.[28-30] To pursue this vision, there is still a great deal of fundamental research to be done. The atomistic details and environment (temperature, pressure *etc*.) governing the interaction and the resulting charge density changes inside TMDs still remains elusive. In addition, poly-domain ferroelectrics and their interactions with TMDs have received limited theoretical and experimental attention.

Herein, we explore the interaction of domain engineered LN with monolayer $MoSe_2$ and WSe_2 and observe dramatic modulation of the PL intensity and spectra. The LN substrates are domain engineered with an arbitrarily chosen periodic hexagonal patterns to illustrate the ability to engineer domains in arbitrary 2D configurations.[30] Using a confocal micro-PL system, TMDs (n-type $MoSe_2$ and p-type WSe_2) with different initial doping show opposite PL modulation mappings on LN substrates, demonstrating distinct behaviors on the two domain orientations. Moreover, an

intriguing p-n homojunction platform in both monolayer $MoSe_2$ and WSe_2 integrated on the LN substrate was observed with distinct PL behavior observed at the interface between two domains. The LN substrate provides a non-volatile control of TMD doping and produces a p-n homojunction band structure. LN is pyroelectric with the surface charge being strongly temperature dependent. We show that small changes in temperature can result in dramatic changes in PL emission, illustrating the electronic nature of the PL phenomenon and suggesting that similar modulation could be achieved electronically. Experimental observations of the PL intensity modulation in TMD/LN match the intuitive predictions of compensation for ferroelectric polarization. This technology is also suitable for other types of 2D materials.[31-37] These results will be used for LN optoelectronic components and in particular may enable electrically driven optical sources to be integrated on the LN photonic chips.

4.2. Incorporate monolayer TMDs onto domain engineered $LiNbO_3$ substrate

A schematic plot of a TMD/LN homojunction is shown in Figure 4.1 a and the fabrication process is summarized in the Methods section. The optical microscope images of the $MoSe_2$ and WSe_2 on domain engineered LN are shown in the Supporting Information Figures S1b and c, respectively. As indicated in the scheme plot of Figure 4.1 b, the LN substrate domains can be used to monitor the doping level and density in a TMD. On the up-domain state (P^+), the substrate is rich in negative interface charges and likely to enhance the intrinsic n-type character of $MoSe_2$. On the down-domain state (P^-) of the $LiNbO_3$, the interaction between the $MoSe_2$ and the substrate has the opposite effect.

The domain engineered LN substrate has different polarization states on the surface however, the optical properties are not modified making it difficult to locate the hexagonal structures from microscope directly. To overcome this challenge, a phase-shifting interferometer (Vecco NT9100) has been used to characterize the number of layers of the TMD samples and for the location of the hexagonal domains in the LN. The different surface charges on the two LN domains modify the index of the TMD films differently making it possible to observe the locations of the domains as small

changes in phase shift through the TMD films. The spatial distribution of the hexagonal structures was precisely identified by phase-shifting interferometry (PSI) (Figures 4.1 c and d). On the basis of the intuitive picture of the up and down polarized domains, we expect that these poly-domain states could create periodic spatial carrier charge modulation across the interface of the TMD/LN. The PSI was also used to identify the number of layers of the TMDs.[38] Owing to the multiple interfacial light reflections, the optical path length (OPL) of the light reflected from the TMDs determines the layer number precisely. As shown from the green box in Figure 4.1 c, the uniform OPL yield indicates a good quality of TMD sample after it had been transferred to the substrate.

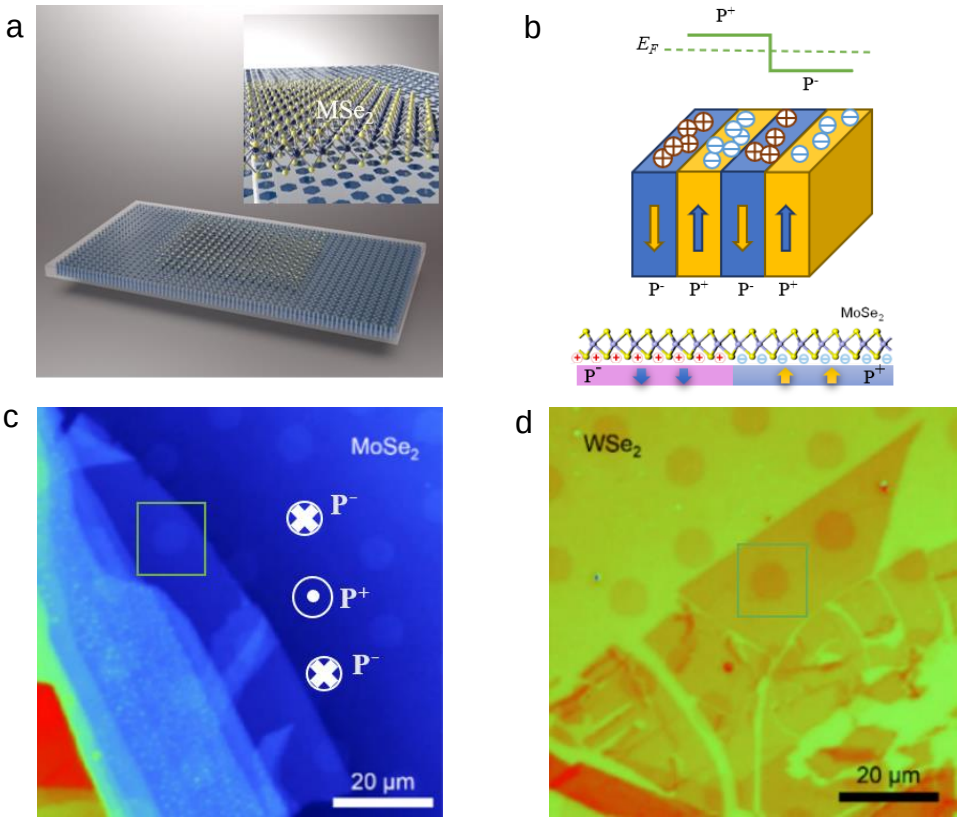

Figure 4. 1 Schematic and optical images of monolayer $MoSe_2$ and WSe_2 on PPLN. a) Schematic of MSe_2 (M: Mo or W) on 2D domain patterned LN for spatial carrier density modulation. Both polarization states (down state P^- and up state P^+) on a ferroelectric LN can directly affect the carrier density of the monolayer TMDs. b) Schematic diagram of the surface doping on domain patterned LN surface which can reconstruct the band of the TMD samples. For the monolayer $MoSe_2$ on 2D domain patterned LN, the P^- surface is rich of positive interface charges, which increases the

electron transfer out of the $MoSe_2$ sample and decreases the intrinsic n-doped character of the $MoSe_2$. c, d) Phase-shifting interferometry (PSI) image of the exfoliated monolayer $MoSe_2$ and WSe_2 on 2D domain patterned LN. Domain direction was marked in the PSI image (c) as cross (⊗) to down domain (P^-) and dot (⊙) to up domain (P^+). PSI images show exfoliated monolayer $MoSe_2$ with optical thickness 4 nm and 3.7 nm. The box indicated by the green line in (c) indicates the further PL mapping area.

4.3. Strong photoluminescence (PL) modulation in monolayer $MoSe_2$ and WSe_2

After the PSI measurement, LN chips were placed into a microscope-compatible chamber (Linkam THMS 600) for photoluminescence (PL) measurements to spatially probe the carrier density in the TMDs by optical method (Figure 4.2). The spectroscopy measurements were taken using a confocal microscopic setup with an excitation laser wavelength of 532 nm. Typical emission spectra and PL mapping of the monolayer TMD samples were recorded under an optical pump power at about 18 μW and the results are presented in Figure 4.2. For comparison, the results of the PL mapping from two different TMD samples are presented in Figures 4.2 a and c, respectively. Normally, monolayer TMDs have large PL emission performance due to large quantum yield of radiative exciton recombination. The large binding energy of these photo-excited electrons and holes can form excitons and/or trions at room temperature. A trion is a charged exciton composed of two electrons and one hole or opposite composition, analogous to H^- (or H^{2+}).

Inside the P^- domain area, the PL emission of the monolayer $MoSe_2$ was enhanced 9 times compared to the P^+ domain as shown in the spatial modulation image in Figure 4.2 a and confirmed by the PL spectra as shown in Figure 4.2 b. The PL of the monolayer WSe_2 shows the opposite PL emission performance for both polarized domains compared to the $MoSe_2$ (Figure 4.2 c). The PL modulation of the TMDs from the P^- to P^+ domain shows a sharp transition at the ferroelectric domain boundary. On the basis of the PL mapping, the polarization orientation of the 2D domain patterns create regions of different charge carrier density in the TMD samples; the spatially modulated PL mappings revealed increased and decreased

electron concentrations in the TMD samples. Due to the different doping types of the semiconductors, monolayer WSe_2 and $MoSe_2$ samples presented opposite PL intensity modulation after their integration with domain engineered LN. As schematically shown in Figure 4.2 e, the doping level is changed to the opposite direction on different polarized domains. The enhanced PL emission of $MoSe_2$ in the P^- area indicates the low doping level of $MoSe_2$, which is attributed to decreased n-type carrier concentrations in the $MoSe_2$.[39-41] Photoluminescence mapping revealed that periodic regimes of quenched/enhanced intensity are directly correlated with inverted ferroelectric polarization. This domain engineered ferroelectric substrate can provide simple emission modulation in TMD materials without the need for complex electrodes or multiple layers of semiconducting material.

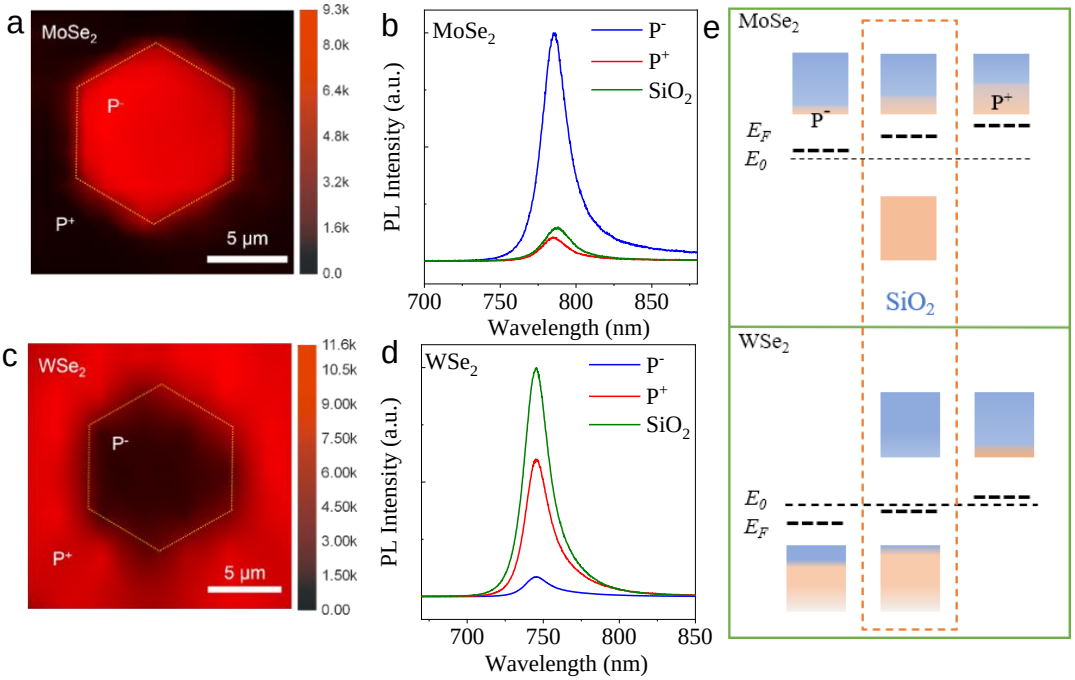

Figure 4. 2 Strong photoluminescence (PL) modulation in monolayer $MoSe_2$ and WSe_2. a) PL mapping of exfoliated monolayer $MoSe_2$ on a single polarized domain. The gold dash line indicates one single dipole. b) PL spectrums come from monolayer $MoSe_2$ on different polarized areas and SiO_2/Si substrate as control. c) PL mapping of exfoliated monolayer WSe_2 on a single polarized domain. d) PL mapping of exfoliated monolayer WSe_2 on a single polarized domain. e) Schematic plot of ferroelectricity-induced doping level modulation in TMD materials.

In order to investigate surface doping that originates from the ferroelectric polarization effects due to monolayer PL emission, monolayer $MoSe_2$ and WSe_2 metallic oxide semiconductor field effect transistor (MOS) devices were fabricated to obtain the electrically gated PL spectrum (Supporting Information Figure S2 and S3). Monolayer $MoSe_2$ and WSe_2 were exfoliated onto SiO_2/Si substrates from the same matrix crystal to keep the initial doping level the same. The initial doping level, surface doping level and photo doping level in monolayer TMDs were extracted by comparing PL spectra from the mapping data with the gate-dependent PL spectra from the MOS devices. Here, a monolayer WSe_2 was used to quantitively study charge transfer mechanisms. The gate dependent PL spectrum of monolayer WSe_2 is shown in Figure S2. By fitting all of the PL spectra under different gate voltages, the exciton and trion peak energies can be extracted. Then the Fermi level can be calculated by

$$E_A - E_T = E_F + E_{binding} \qquad (1)$$

where E_A is the exciton peak energy, E_T is the trion peak energy, E_F is the Fermi energy level and $E_{binding}$ is the binding energy of trion.

Fermi level of monolayer WSe_2 was extracted through Equation (1). By plotting energy difference between the exciton and trion peak as a function of gate voltage linear trend between energy difference and Fermi level can be observed. For monolayer TMDs, the density of state in the conduction band and valence band is linearly distributed along the energy level.[42] The extracted binding energy of the monolayer WSe_2 was 34 meV, consistent with previously reported results.[34, 43] To extract the doping level of the monolayer TMDs from the experimentally obtained Fermi level, the following two equations were used

$$E_F = \frac{\hbar\pi n}{2m_h e^2} \qquad (2)$$

$$ne = CV_g \qquad (3)$$

where h is Planck's constant, π is the pi constant, n is the electron density, e is the fundamental unit of charge, m_h is the effective mass of a hole, C is the back-gate capacitance and V_g is the gate voltage.

Equation (2) and (3) were used to extract the doping level *n* of the monolayer TMDs from the Fermi level and to convert the gate voltage into the induced hole doping level, respectively, where *C* is the back-gate capacitance $C = 1.2 \times 10^{-8}\ Fcm^{-2}$. As shown in Figure S2b and S2d, monolayer WSe_2 will approach a zero Fermi level when a -20V gate voltage is applied and this means monolayer WSe_2 is slightly p-type doped with an initial doping level of $1.5 \times 10^{12}\ cm^{-2}$ (when no gate voltage is applied). In Figure S4a and S4b, the value of $E_A - E_T$ for PL enhancement and quenching have been extracted as 31.47 meV and 41.41 meV, respectively (Supporting Information Figure S4). According to the linear relationship between Fermi level and $E_A - E_T$, the Fermi level and hole doping level for the P^+ domain are 0.92 meV and $2.54 \times 10^{11}\ cm^{-2}$, respectively, while for the P^- domain they are 15.39 meV and $4.24 \times 10^{12}\ cm^{-2}$, respectively. Considering initial doping of monolayer WSe_2, the P^+ domain has induced $1.25 \times 10^{12}\ cm^{-2}$ electrons and the P^- domain has induced $2.74 \times 10^{12}\ cm^{-2}$ holes. Overall, the P^- domain has a lower hole doping level than the P^+ domain meaning the P^- domain will have a higher density of vacant state in the valence band for PL emission (Figure 4.2 e). The more neutral the monolayer TMD, the stronger PL emission.[40, 44]

4.4. Laser Excitation Power Dependent PL in Surface Junction Area

The surface doping can effectively modify the doping level of two-dimensional materials.[28] Although, the optical behavior within the P^- and P^+ domains have been subject to detailed investigations in the above discussion; the adjacent vicinity at the contact of the P^- and P^+ domains (of the domain engineered LN and TMD), however, still has not been fully explored yet. In Figure 4.3, power dependent PL measurements were employed to unveil the behavior of the surface junction area. Figure 4.3 a and b present confocal PL mapping under 1.8 and 178 μW, respectively. The PL intensity evolution increased with the laser power excitation as expected. As the excitation power increased, the PL intensity of junction area P2 dramatically increased compared with the P^- domain (P1) and P^+ domain (P3), which the line curve is also presented in Figure 4.3 d. In the P2 domain, the surface doping level is near zero because negative and positive charges are neutralized forming a depletion region and an internal built-in electrical field exists in this domain (Figure 4.3 c). When the laser excitation power is very small, only a small number of photons can

be injected into the material. Assuming a quantum efficiency of 1, only a small number of excitons are generated in this domain. They are quickly dissociated because of the internal built-in electric field.[45] Therefore, the P2 domain has lower PL emission compared with the P^- and P^+ domains when the excitation power is 1.8 μW. However, when a larger excitation power is used, more excitons are formed and also dissociated. Electrons and holes accumulate at the edge of this depletion region. These accumulated charges create an electron/hole concentration gradient toward the depletion region, which is opposite to the built-in electrical field. These concentration gradients stop the dissociation process of excitons within the P2 area and eventually they reach a dynamic balance. When the laser power was increased to 178 μW, more excitons are generated in all P1, P2 and P3 areas. However, the material doping level for P2 is much smaller than P1 and P3 due to the depletion region. As shown in the scheme plot of Supporting Information Figure S5, due to the lower interface charge density of P2, the exciton in this junction area would increase more than other domains with increasing laser power (Supporting Information Figure S6a). This lower doping level and more unoccupied electron density in the conduction band can contribute to more PL emissions excited by larger laser power. Due to the lower doping level, PL performance in P2 area shows higher exciton emission efficiency, as shown in Figure S6b. With abundant electrons on the surface of P3 state, the p-type WSe_2 shows lower trion emission with increasing laser power as shown in in Figure S6b. With the balance of the built-in electric field, the intensity ratio between exciton and trion shows continuous reduction with increasing laser power, as shown in Figure S6c. Hence, as shown in Figure 4.3 d, the PL emission in P2 is much stronger than P1 and P3.

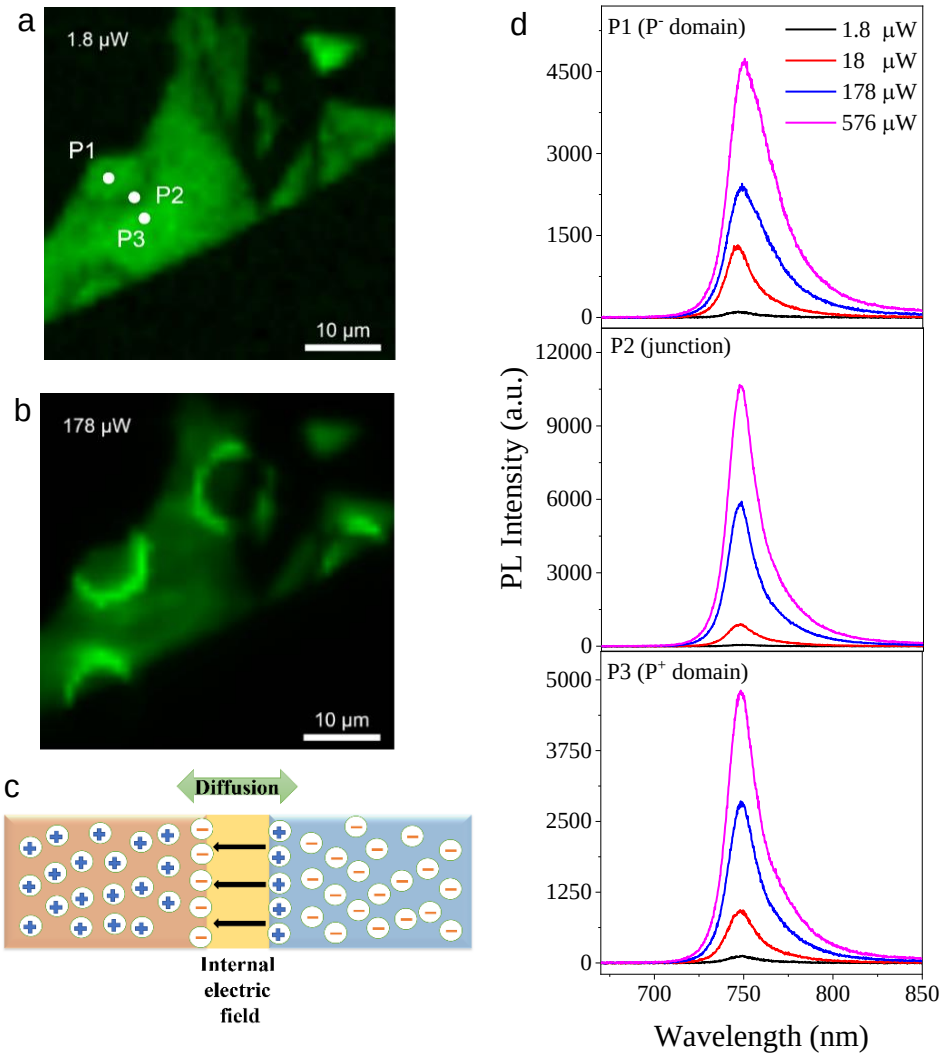

Figure 4. 3 RT laser excitation power dependent PL modulation in monolayer WSe_2. a, b) measured spatial PL mapping with various excitation power of 1.8 μW (b). c) scheme plot of exciton diffusion on junction area by internal electric field. d) extracted PL spectra from PL mapping with various spatial position as P^- (P1), junction area (P2) and P^+ (P3) at different excitation laser power.

4.5. Temperature dependent PL modulation in monolayer $MoSe_2$

Monolayer TMD samples on LN shows sizable interaction across the interface which affects the doping level and carrier density due to the remnant surface polarization of the FE substrate. Furthermore, due to the asymmetric polarization structure, the LN has an inimitable pyroelectric effect with changing temperature.[46] The surface interaction of ferroelectric LN and monolayer TMD materials at low temperature is largely unexplored. To study the thermal stability and spatial charge modulation

properties of the TMD/LN, temperature dependent PL measurements with an excitation laser power of 18 μW have been conducted. The surface charge density may reduce due to absorption or reconstruction within the TMD/LN system with decreasing temperature.

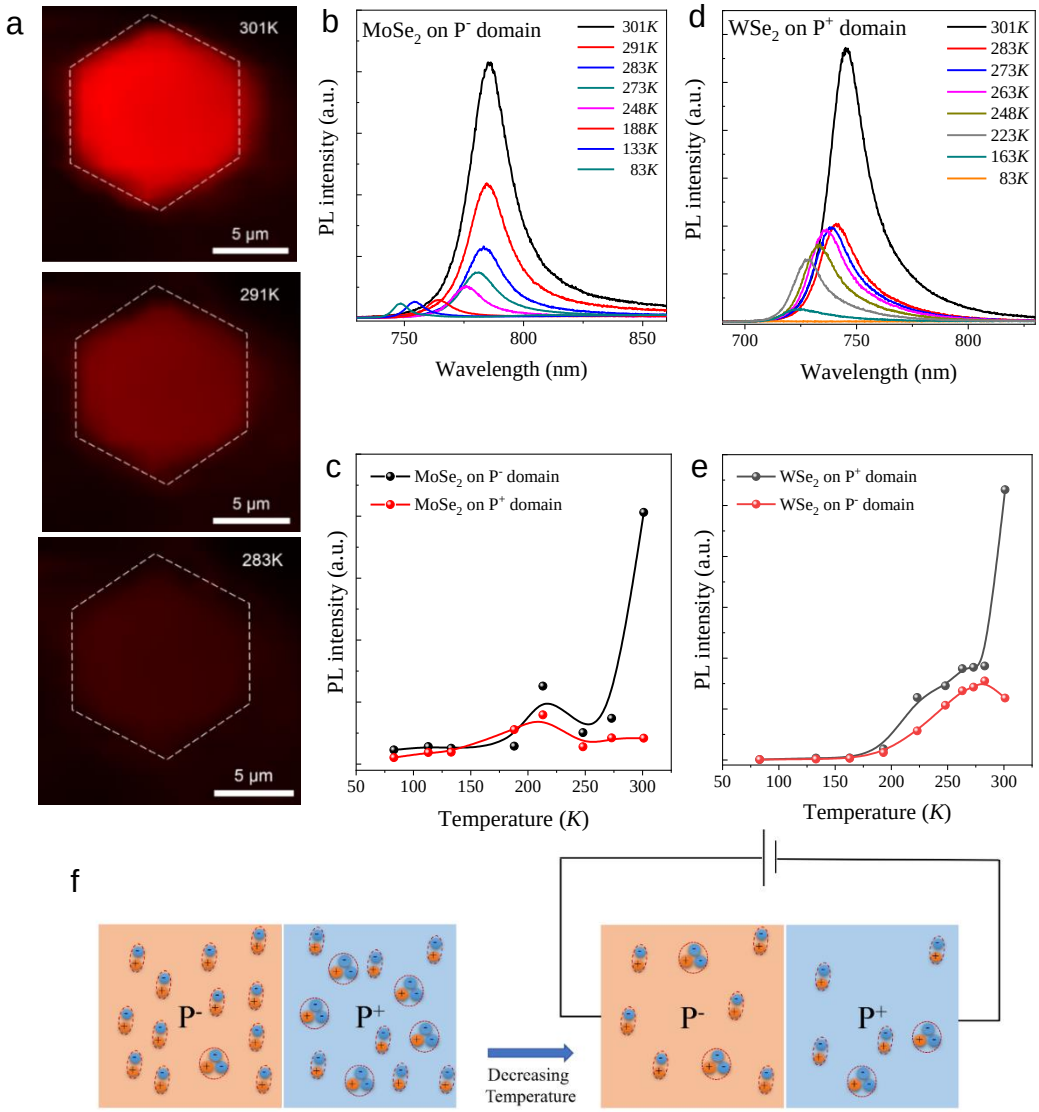

Figure 4. 4 Temperature dependent PL modulation in monolayer $MoSe_2$. a) PL mapping of exfoliated monolayer $MoSe_2$ on a single polarized domain under 301 *K*, 291 *K* and 283 *K*. The white dash lines in (a) indicate the single hexagonal dipole in the domain engineered LN substrate. b) PL spectrums of monolayer $MoSe_2$ on the P^- domain from 301 *K* to 83 *K*. c) Integrated PL intensity of the $MoSe_2$ on P^- and P^+ domains with decreasing temperature. d) PL spectrums of monolayer WSe_2 on the P^+ domain from 301 *K* to 83 *K*. c) Integrated PL intensity of the WSe_2 on P^- and P^+

domains with decreasing temperature. f) Schematic plot of the TMD samples on the domain engineered LN when decreasing the temperature.

As shown in Figure 4.4 a, PL mapping demonstrates the emission characteristics at near room temperature. By reducing the temperature only slightly from 301 *K* to 283 *K*, the PL intensity within the P^- domain is rapidly quenched by nearly 75% (Supporting Information Figure S7). The PL intensity continues decreasing with decreased temperature down to 273 *K* (Figure 4.4 b), then the PL intensity keeps almost stable until liquid nitrogen temperature (83 *K*) (Figure 4.4 b). The temperature dependent PL of $MoSe_2$ on $LiNbO_3$ are quite different from the PL performances of monolayer $MoSe_2$ on SiO_2, which increases with decreasing temperature (Supporting Information Figure S8a). Temperature changes can significantly affect the spatial carrier concentration of the TMD samples through the impact of the pyroelectric effect on spontaneously polarized surface charges.

The remnant polarization of the $LiNbO_3$ increases quickly with decreasing temperature from room temperature (RT) to 247*K*.[47] As illustrated in Figure S10, the interface charges would also increase quickly. The electron density in the $MoSe_2$ in the P^- domain rapidly reduces and transfers to the substrate around RT to 247*K*. The doping level of $MoSe_2$ on different domains would form a device similar to a p-n junction. With decreasing temperature, interface charges in the P^- and P^+ domains (hole and electron) would both increase, which is likely to apply a voltage to the overlayer $MoSe_2$ (Figure 4.4 f). Combined with the $MoSe_2$ in the P^+ domain, the majority carriers (as holes in $MoSe_2$ on P^- domain) would transfer to the nearby domains, which balances the charge density of different domains and the PL would also be balanced between different domains. As shown in Figure 4c, the PL intensity on the P^- domain is quickly reduced and becomes similar to the PL intensity on the P^+ domain. The PL intensity of WSe_2 on the P^+ domain also decreased with decreasing temperature down to 83 *K* and equals the PL emission on the P^- domain (Figure 4.4 d and e). When the temperature decreased from 247 *K* to 83 *K*, the polarization of the substrate also decreased (Supporting Information Figure S9). With continuous cooling, the distance between the overlayer $MoSe_2$ and the substrate is

decreasing, which enhanced the interaction between TMD samples and the FE substrate.[48] Therefore, the overlayer transport properties between different domains are enhanced and quenched the PL emission on the P^- domain. The recovery (the hump around 220 *K*) attributed to the coupling effect of enhanced interface charge transfer and decreased polarization of the LN substrate, which delayed the inflection point from 247 *K* to 220 *K*. So, the PL emission is slightly recovered and shown a hump around 220 *K* as shown in Figure 4c and e. The PL emission intensity is rapidly quenched in the P^- region due to the pyroelectric effect of LN (Figure 4.4 f). The decreasing speed was indicated by the quench factor as shown in the Supporting Information Figure S10. This observation clearly illustrates the electronic nature of the observed PL behavior. Due to the electrostatic doping as a result of the remnant polarization from the substrate, the band structure of monolayer $MoSe_2$ has no or little change. Therefore, the peak energy is almost the same on P^- and P^+ domain (Supporting Information Figure S11b). Due to the electrostatic doping nature across the interface, little difference of peak energy and full width at half maxima (FWHM) of monolayer $MoSe_2$ on LN and SiO_2 is indicated, as shown in the Supporting Information Figure S11d and S11e. The temperature dependent PL could be harnessed directly as a highly sensitive temperature sensor, however we believe that the insight into the optoelectronic behavior of the TMD material on the domain engineered LN presents a far more significant opportunity for electronically powered and controlled optical sources on the LN integrated photonic platform.

4.6. Summary

In summary, we have shown that monolayer transition metal dichalcogenides (TMD) $MoSe_2$ and WSe_2 can be interfaced onto the surface of ferroelectric lithium niobate (LN) and that the domain orientation of the LN has a strong effect of the TMD optoelectronic properties. Domain engineering of the LN substrate results in an in-plane heterostructure within the TMD which has been demonstrated by our measured spatial PL mapping. Due to the underlying domain engineered ferroelectric, PL emissions are modulated approximately 9 times by different surface doping between the P^- and P^+ domains. Monolayer WSe_2 on LN also shows enhanced PL emission at the junction between domains with increasing laser power, this is due to overcoming the micro internal electric field between the P^- and P^+ domains, which stops dissociation of excitons. With decreasing temperature, the PL emission of monolayer

$MoSe_2$ was quickly quenched in the P^- domain in stark contrast to behavior observed on non-ferroelectric substrates. This performance shows the fast increase of positive charge in the P^- domain due to the pyroelectric effect and the restructure of the surface doping between $MoSe_2$ and the LN substrate. Overall, our research shows that monolayer TMD sheets can be engineered to create a p-n homojunction by engineering the underlying ferroelectric domains with sensitive response to laser power and ambient temperature. This approach could lay the foundations for creating active electrically driven and controlled optoelectronic components on LN integrated photonic platforms with the ultimate goal of electrically driven optical sources within LN photonic chips.

4.7. Experimental Section

Device fabrication and characterization. Monolayer TMD samples were produced by mechanical exfoliation from bulk crystal. Then, monolayer TMD samples were dry transferred onto a 500-µm-thick Z-cut LN substrate with periodical honeycomb lattice and hexagonal shape of the domain-inverted inclusions. Hexagonal inclusions are fabricated in trigonal (3m) LN crystal by electric field poling. The inclusion boundaries are along the symmetry planes in the *Z*-cut. The side length of the hexagon is about 6.16 µm. The PPLN substrate was cleaned with O_2 plasma as pretreatment, using a plasma cleaner. For the MOS structure, we also used mechanical exfoliation to dry transfer the TMD flake onto a SiO_2/Si substrate (275nm thermal oxide on n^+-doped silicon), with half on a pre-patterned gold electrode and half on the substrate. The gold electrodes were patterned by conventional photolithography, metal deposition and lift-off processes.

Optical characterization. All the OPL characterizations were obtained using a phase-shifting interferometer (Vecco NT9100). PL measurements were conducted using a Horiba LabRAM system equipped with a confocal microscope, a charge-coupled device (CCD) Si detector, and a 532 nm diode-pumped solid-state (DPSS) laser as the excitation source. The electrical bias was applied using a Keithley 4200 semiconductor analyzer. The laser light was focused on the sample surface *via* a 50x objective lens. The spectral response of the entire system was determined with a calibrated halogen-tungsten light source. The PL signal was collected by a grating

spectrometer, thereby recording the PL spectrum through the CCD (Princeton Instruments, PIXIS). All the PL spectra were corrected for the instrument response. For temperature-dependent measurements, TMD/LN chips were put into a Linkam THMS 600 chamber and the temperature was set to a constant (range from 301K to 83K) during the PL measurements using a low-temperature controller with liquid nitrogen coolant.

References

1. Y. Zhang *et al.*, Direct Observation of the Transition from Indirect to Direct Bandgap in Atomically Thin Epitaxial $MoSe_2$. *NATURE NANOTECHNOLOGY* **9**, 111-115 (2014).
2. A. Splendiani *et al.*, Emerging Photoluminescence in Monolayer MoS_2. *nano letters* **10**, 1271-1275 (2010).
3. F. Xia, H. Wang, D. Xiao, M. Dubey, A. Ramasubramaniam, Two-Dimensional Material Nanophotonics. *nature photonics* **8**, 899–907 (2014).
4. Q. Zhang *et al.*, Strain Relaxation of Monolayer WS_2 on Plastic Substrate. *ADVANCED FUNCTIONAL MATERIALS* **26**, 8707-8714 (2016).
5. Z. Ye, D. Sun, T. F. Heinz, Optical Manipulation of Valley Pseudospin. *NATURE PHYSICS* **13**, 26-29 (2017).
6. B. Zhu, H. Zeng, J. Dai, Z. Gong, X. Cui, Anomalously Robust Valley Polarization and Valley Coherence in Bilayer WS_2. *Proceedings of the National Academy of Sciences* **111**, 11606–11611 (2014).
7. K. He *et al.*, Tightly Bound Excitons in Monolayer WSe_2. *physical review letters* **113**, 026803 (2014).
8. A. Chernikov *et al.*, Exciton Binding Energy and Nonhydrogenic Rydberg Series in Monolayer WS_2. *physical review letters* **113**, 076802 (2014).
9. Y. You *et al.*, Observation of Biexcitons in Monolayer WSe_2. *NATURE PHYSICS* **11**, 477-481 (2015).
10. A. F. Morpurgo, Gate Control of Spin-Valley Coupling. *NATURE PHYSICS* **9**, 532-533 (2013).
11. D. Y. Qiu, F. H. d. Jornada, S. G. Louie, Optical Spectrum of MoS_2: Many-Body Effects and Diversity of Exciton States. *physical review letters* **111**, 216805 (2013).
12. A. Molina-S´anchez, D. Sangalli, K. Hummer, A. Marini, L. Wirtz, Effect of Spin-Orbit Interaction on the Optical Spectra of Single-Layer, Double-Layer, and Bulk MoS_2. *PHYSICAL REVIEW B* **88**, 045412 (2013).
13. F. Huser, T. Olsen, K. S. Thygesen, How Dielectric Screening in Two-Dimensional Crystals Affects the Convergence of Excited-State Calculations: Monolayer MoS_2. *PHYSICAL REVIEW B* **88**, 245309 (2013).
14. G. Berghäuser, E. Malic, Analytical Approach to Excitonic Properties of MoS_2. *PHYSICAL REVIEW B* **89**, 125309 (2014).
15. A. Ramasubramaniam, Large Excitonic Effects in Monolayers of Molybdenum and Tungsten dichalcogenides. *PHYSICAL REVIEW B* **86**, 115409 (2012).
16. H.-P. Komsa, A. V. Krasheninnikov, Effects of Confinement and Environment on the Electronic Structure and Exciton Binding Energy of MoS_2 from First Principles. *PHYSICAL REVIEW B* **86**, 241201 (2012).
17. T. C. Berkelbach, M. S. Hybertsen, D. R. Reichman, Theory of Neutral and Charged Excitons in Monolayer Transition Metal Dichalcogenides. *PHYSICAL REVIEW B* **88**, 045318 (2013).
18. W. Yu *et al.*, Near-Infrared Photodetectors Based on $MoTe_2$/Graphene Heterostructure with High Responsivity and Flexibility. *Small* **13**, 1700268 (2017).
19. D. Jariwala *et al.*, Gate-Tunable Carbon Nanotube–MoS_2 Heterojunction p-n Diode. *Proceedings of the National Academy of Sciences* **110**, 18076–18080 (2013).
20. B. W. H. Baugher, H. O. H. Churchill, Y. Yang, P. Jarillo-Herrero, Optoelectronic Devices Based on Electrically Tunable p–n Diodes in A Monolayer Dichalcogenide. *NATURE NANOTECHNOLOGY* **9**, 262-267 (2014).
21. J. S. Ross *et al.*, Electrically Tunable Excitonic Light-Emitting Diodes Based on Monolayer WSe_2 p–n Junctions. *NATURE NANOTECHNOLOGY* **9**, 268-272 (2014).
22. J.-W. Chen *et al.*, A Gate-Free Monolayer WSe_2 pn Diode. *Nature Communications* **9**, 3143 (2018).

23. C. Campbell, *Surface Acoustic Wave Devices and their Signal Processing Applications*. (Academic Press, 1989), pp. 484.
24. L. Arizmendi, Photonic Applications of Lithium Niobate Crystals. *Physica Status Solidi (a)* **201**, 253-283 (2004).
25. A. Boes, B. Corcoran, L. Chang, J. Bowers, A. Mitchell, Status and Potential of Lithium Niobate on Insulator (LNOI) for Photonic Integrated Circuits. *Laser and Photonics Reviews* **12**, 1700256 (2018).
26. H. Emami, N. Sarkhosh, L. Bui, A. Mitchell, Amplitude Independent RF Instantaneous Frequency Measurement System Using Photonic Hilbert Transform. *Optics Express* **16**, 13707-13710 (2008).
27. S. Kasture *et al.*, Frequency Conversion Between UV and Telecom Wavelengths in A Lithium Niobate Waveguide for Quantum Communication with Yb^+ Trapped Ions. *Journal of optics* **18**, 1-5 (2016).
28. C. Baeumer *et al.*, Ferroelectrically Driven Spatial Carrier Density Modulation in Graphene. *NATURE COMMUNICATIONS* **6**, 6136 (2015).
29. Y. Zheng *et al.*, Gate-Controlled Nonvolatile Graphene-Ferroelectric Memory. *APPLIED PHYSICS LETTERS* **94**, 163505 (2009).
30. M. Lu, L. Feng, Y. Chen, Phononic Crystals and Acoustic Metamaterials. *Materials Today* **12**, 34-42 (2009).
31. L. Zhang *et al.*, Efficient and Layer-Dependent Exciton Pumping across Atomically Thin Organic-Inorganic Type-I Heterostructures. *Advanced materials* **30**, e1803986 (2018).
32. J. Pei *et al.*, Excited State Biexcitons in Atomically Thin $MoSe_2$. *ACS Nano* **11**, 7468-7475 (2017).
33. J. Lu *et al.*, Light-Matter Interactions in Phosphorene. *Accounts of Chemical Research* **49**, 1806-1815 (2016).
34. R. Xu *et al.*, Extraordinarily Bound Quasi-One-Dimensional Trions in Two-Dimensional Phosphorene Atomic Semiconductors. *ACS nano* **10**, 2046-2053 (2016).
35. J. Pei *et al.*, Producing Air-Stable Monolayers of Phosphorene and Their Defect Engineering. *Nature Communications* **7**, 10450 (2016).
36. J. Yang *et al.*, Robust Excitons and Trions in Monolayer $MoTe_2$. *ACS nano* **9**, 6603-6609 (2015).
37. S. Zhang *et al.*, Extraordinary Photoluminescence and Strong Temperature/Angle-Dependent Raman Responses in Few-Layer Phosphorene. *ACS nano* **8**, 9590-9596 (2014).
38. J. Yang *et al.*, Atomically Thin Optical Lenses and Gratings. *Light: Science & Applications* **5**, e16046 (2016).
39. J. S. Ross *et al.*, Electrical Control of Neutral and Charged Excitons in A Monolayer Semiconductor. *Nature Communications* **4**, 14741-14746 (2013).
40. J. Kang, W. Liu, D. Sarkar, D. Jena, K. Banerjee, Computational Study of Metal Contacts to Monolayer Transition-Metal Dichalcogenide Semiconductors. *Physical Review X* **4**, 031005 (2014).
41. G. Giovannetti *et al.*, Doping Graphene with Metal Contacts. *Physical Review Letters* **101**, 026803 (2008).
42. K. F. Mak *et al.*, Tightly Bound Trions in Monolayer MoS_2. *Nature Materials* **12**, 207-211 (2013).
43. J. Yang *et al.*, Optical Tuning of Exciton and Trion Emissions in Monolayer Phosphorene. *Light: Science & Applications* **4**, 1-7 (2015).
44. Y. Wang *et al.*, Does p-Type Ohmic Contact Exist in WSe_2–Metal Interfaces? *Nanoscale* **8**, 1179-1191 (2016).
45. Q. Ou *et al.*, Strong Depletion in Hybrid Perovskite p–n Junctions Induced by Local Electronic Doping. *Advanced Materials* **30**, 1705792 (2018).
46. A. M. Glass, M. E. Lines, Low-Temperature Behavior of Spontaneous Polarization in $LiNbO_3$ and $LiTaO_3$. *PHYSICAL REVIEW B* **13**, 180-191 (1976).

47.H. Bo *et al.*, Temperature-Dependent Ferroelectric Properties of Near Stoichiometric Lithium Niobate Single Crystal. *Applied Physics A* **124**, 691 (2018).
48.F. Wang *et al.*, Tuning Coupling Behavior of Stacked Heterostructures Based on MoS_2, WS_2, and WSe_2. *Scientific Report* **7**, 44712 (2017).
49.Connie H. Li, Kathleen M. McCreary, B. T. Jonker, Spatial Control of Photoluminescence at Room Temperature by Ferroelectric Domains in Monolayer WS_2/PZT Hybrid Structures. *ACS Omega* **1**, 1075–1080 (2016).

Appendix:

Supporting Information for Chapter 4

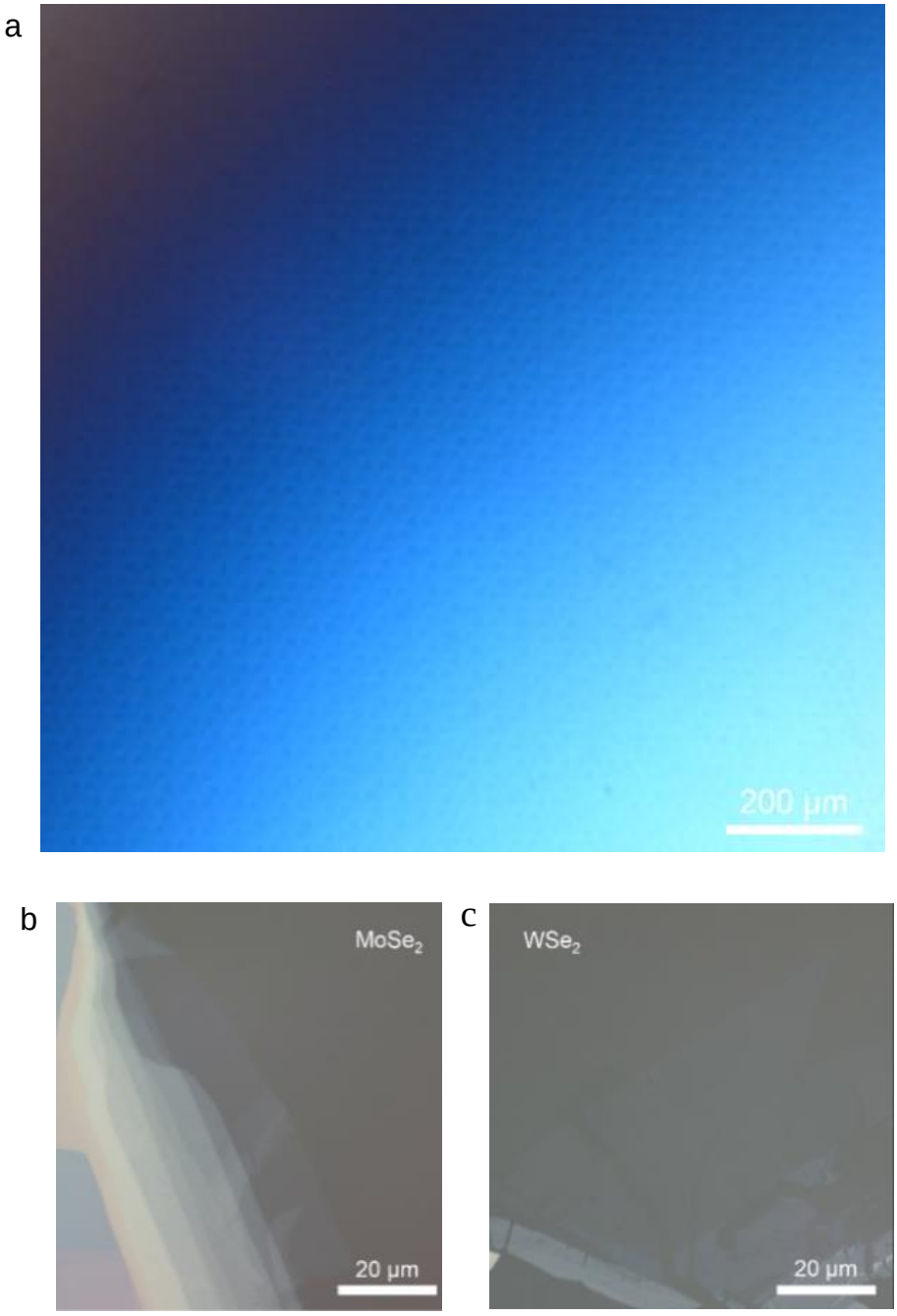

Figure S1 | Microscope images of TMD samples on LN. a) 20x polarizing microscope image of PPLN surface with hexagonal reversed ferroelectric phase structure. b, c) Optical microscope images of mechanically exfoliated monolayer $MoSe_2$ flakes (b) and WSe_2 flakes (c) on PPLN substrate.

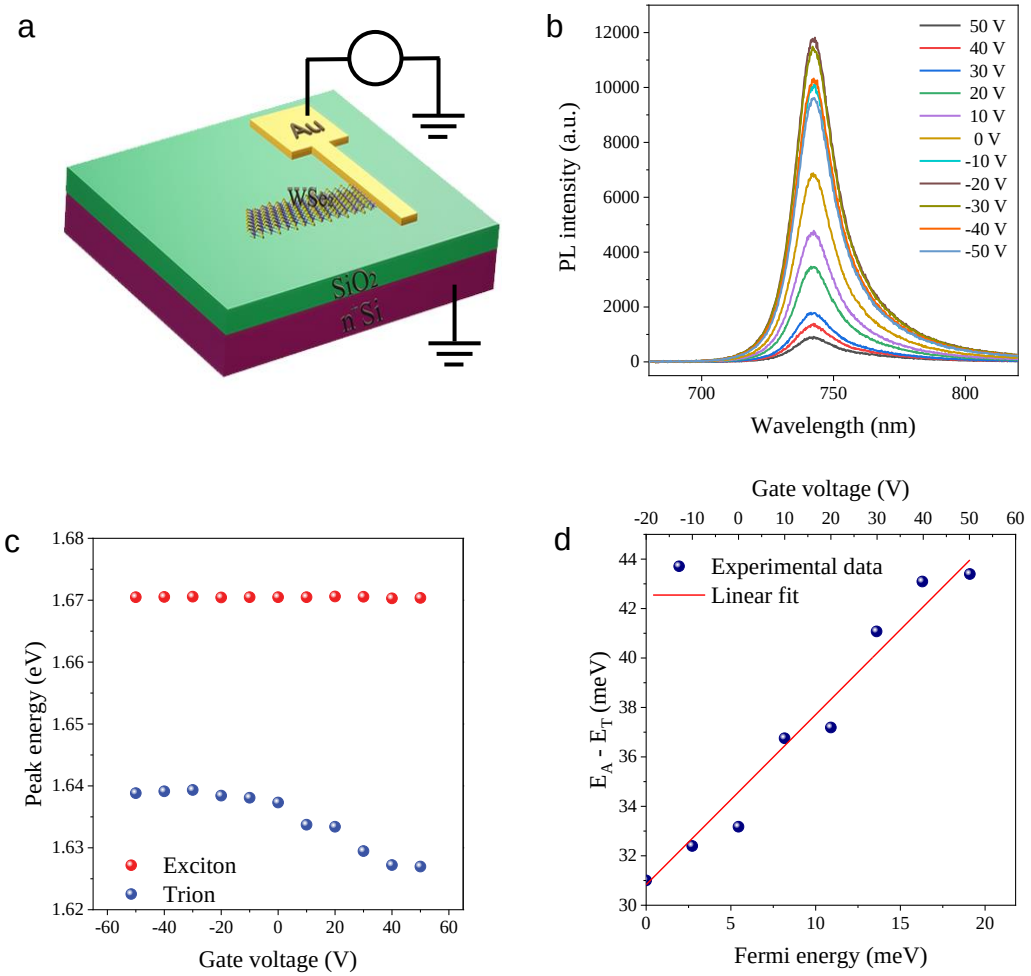

Figure S2 | Gate-dependent PL modulation towards monolayer WSe_2. a) Schematic image of 1L WSe_2 MOS device structure. b) Measured PL spectra under various gate voltages. c) Peak energy of exciton (E_A) and trion (E_T) as a function of gate voltage. d) A linear fit to the EF-dependence from the difference in the exciton and trion energies, (E_A - E_T), has an intercept of 31.4 meV, which determines the trion binding energy.

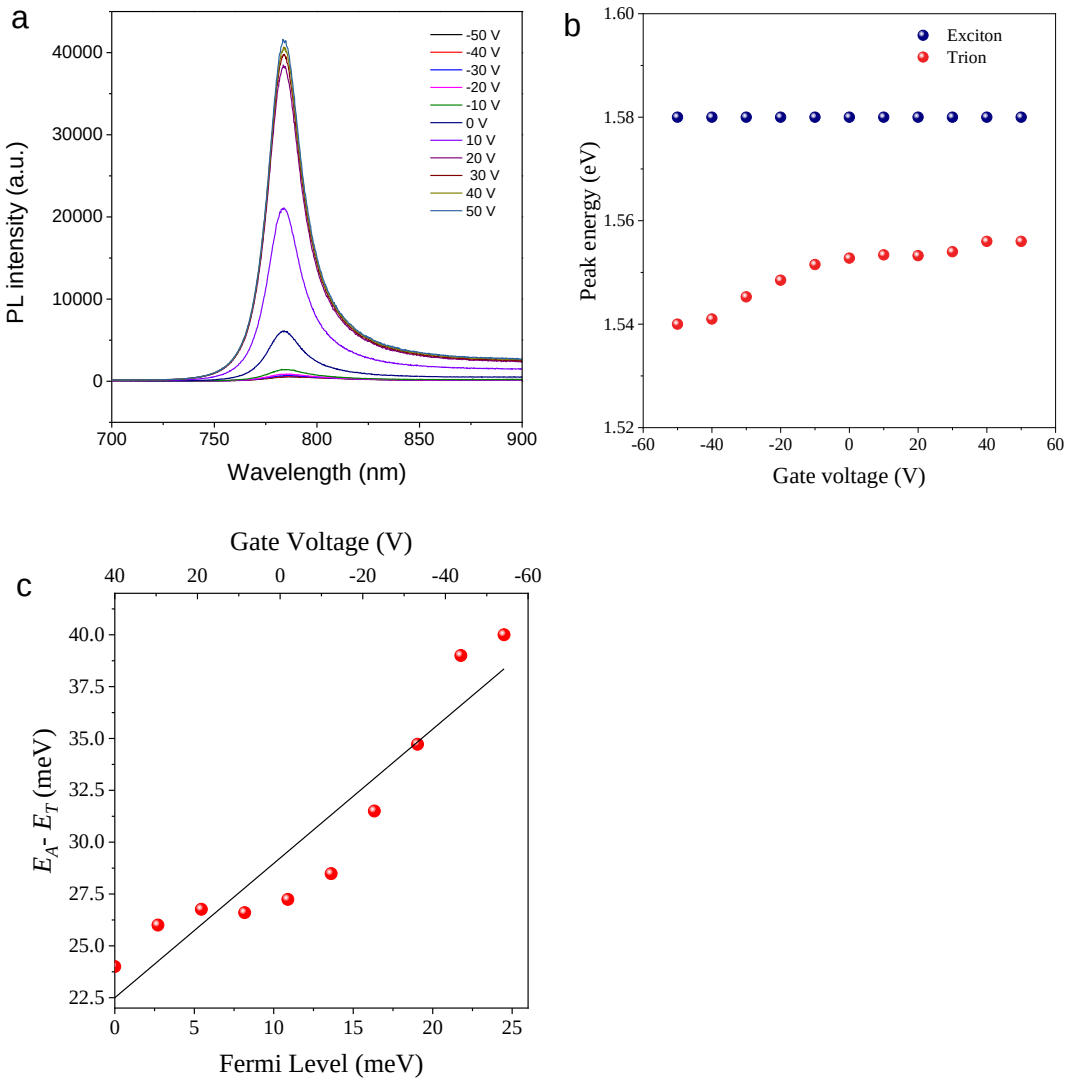

Figure S3 | Gate-dependent PL modulation towards monolayer $MoSe_2$. a) Measured PL spectra under various gate voltages. b) Peak energy of exciton (E_A) and trion (E_T) as a function of gate voltage. c) The difference in the exciton and trion energies, (E_A - E_T), as a function of Fermi energy E_F. The intercept as the trion binding energy of $MoSe_2$ is ~22.49 meV.

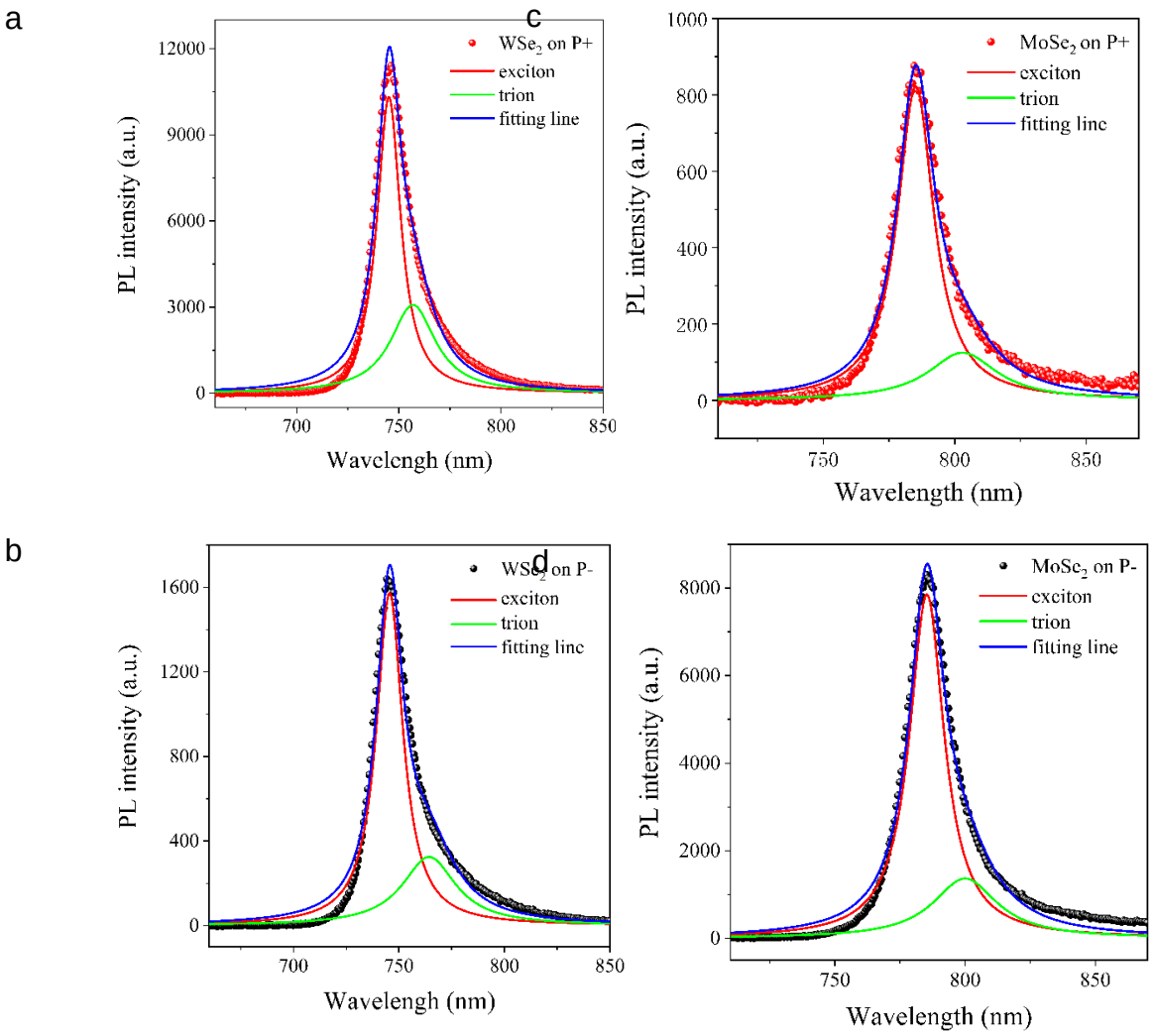

Figure S4 | PL spectra fitted Lorentzian functions towards different domain states. a, b) Measured PL spectra (dot lines) of WSe_2 on P^+ state (a) and P^- state (b). PL spectra are fit to Lorentzian functions (red lines are labeled as exciton peak, green lines are labeled as trion peak, and blue lines are the cumulative fitting results). c, d) Measured PL spectra (dot lines) of $MoSe_2$ on P^+ state (c) and P^- state (d).

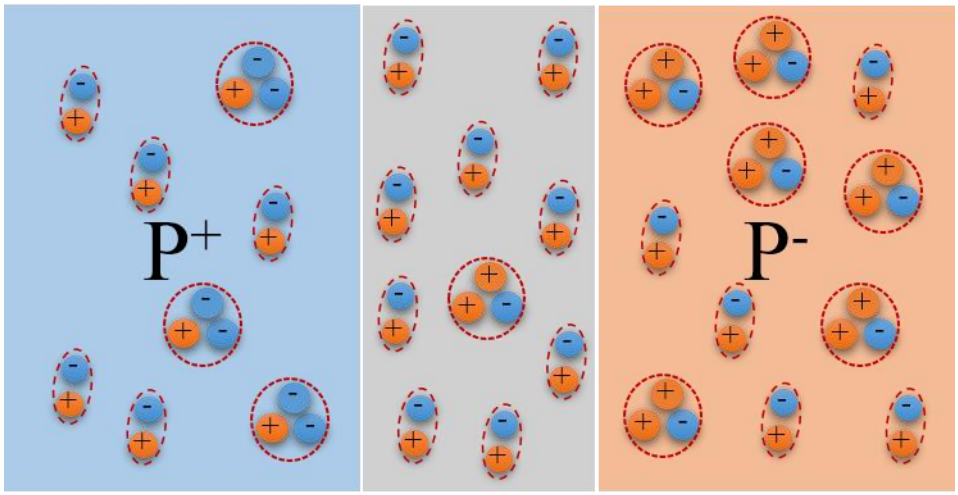

Figure S5 | Scheme of exciton and trion distribution of WSe_2 on PPLN substrate. Due to the low surface doping level, the exciton in junction area would increase more than other domains with increasing laser power.

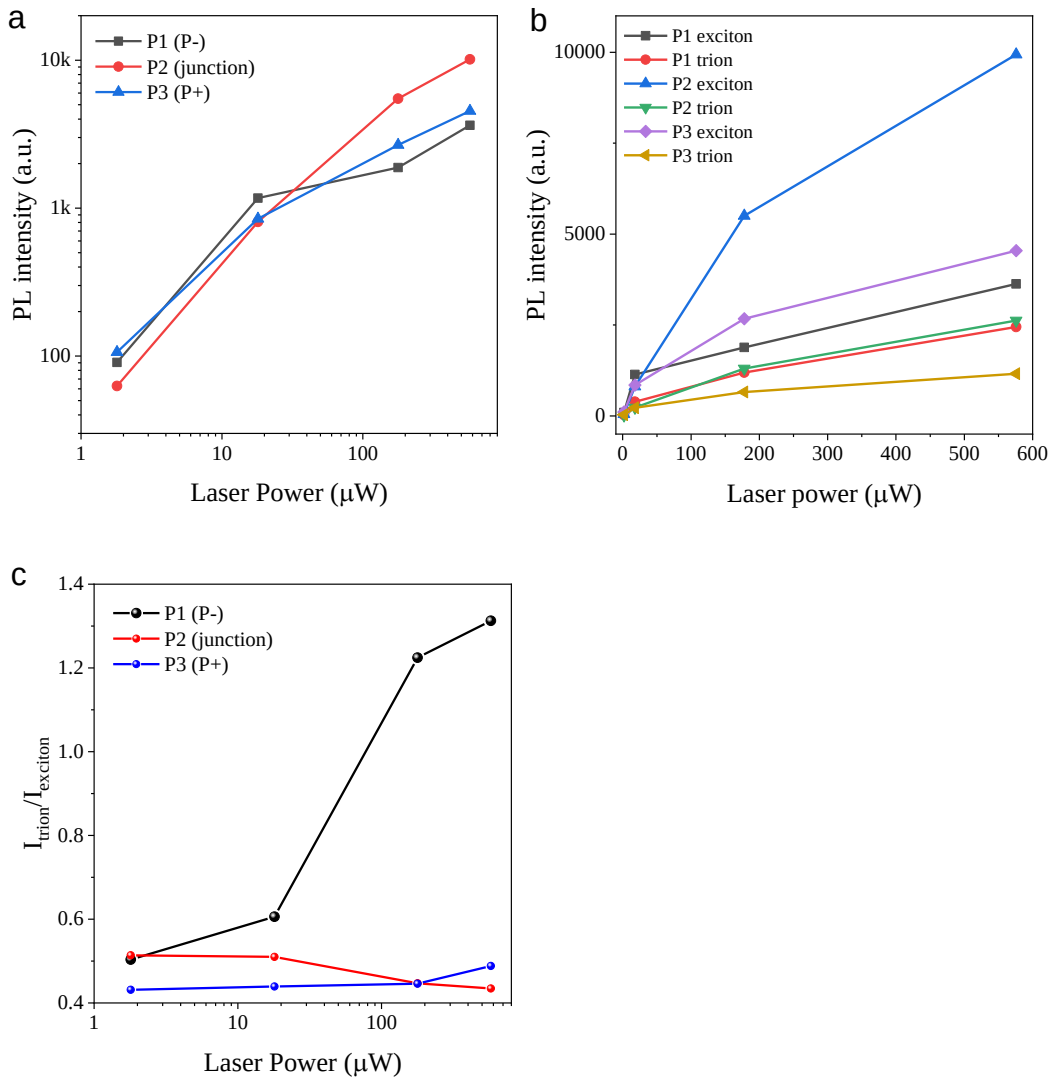

Figure S6 | PPLN substrate induced PL modification of monolayer WSe_2 with increasing excited laser power. a) Measured power dependent PL intensity of monolayer WSe_2 sample on a PPLN substrate. b) PL intensity of exciton and trion on different domain states. c) The PL intensity ratio of trion to exciton.

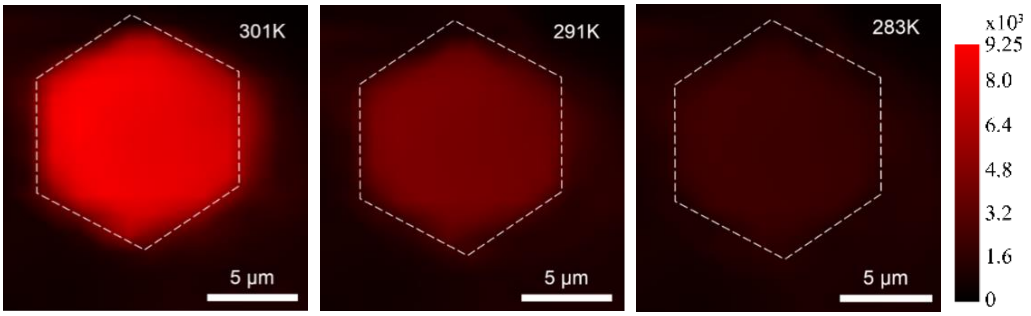

Figure S7 | PL mapping of exfoliated monolayer $MoSe_2$ on a single polarized domain under 301 *K*, 291 *K* and 283 *K*.

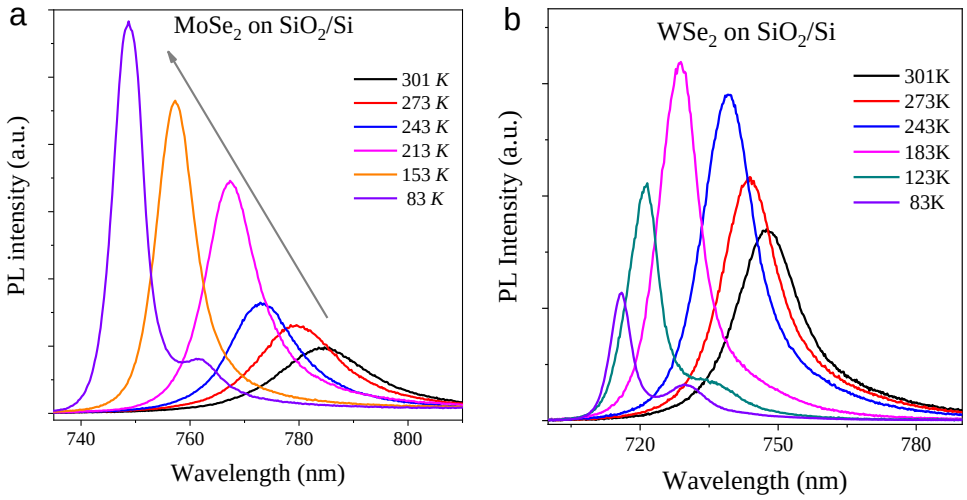

Figure S8 | Measured PL spectra of the 1L TMD samples on SiO_2/Si substrate under various temperatures. a) $MoSe_2$ temperature dependent PL on SiO_2. b) WSe_2 temperature dependent PL on SiO_2.

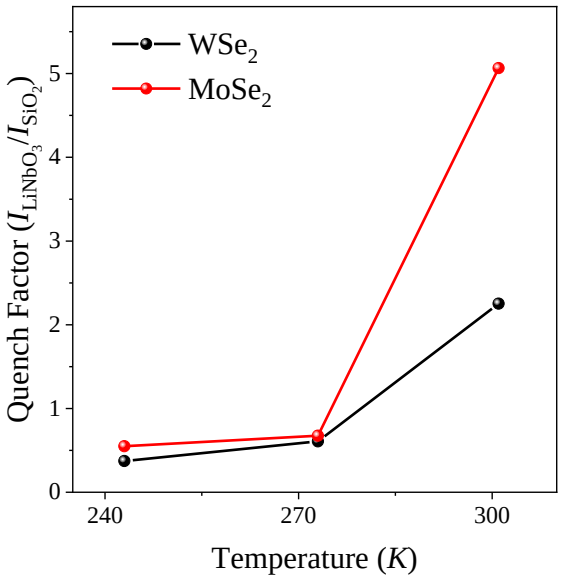

Figure S9 | Quench factor obtained as the ratio between the PL intensity of 1L TMD on $LiNbO_3$ and SiO_2/Si.

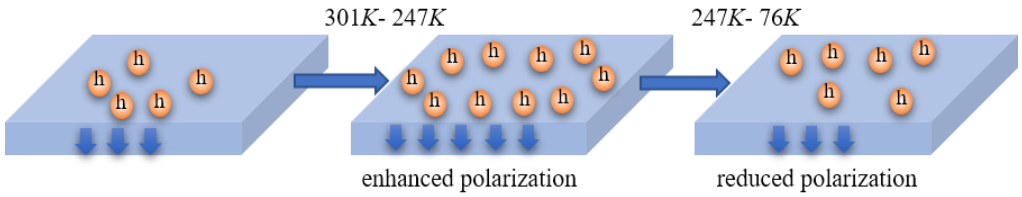

Figure S10 | Scheme of pyroelectric performance of LN under decreasing temperature, which caused by changing polarization.

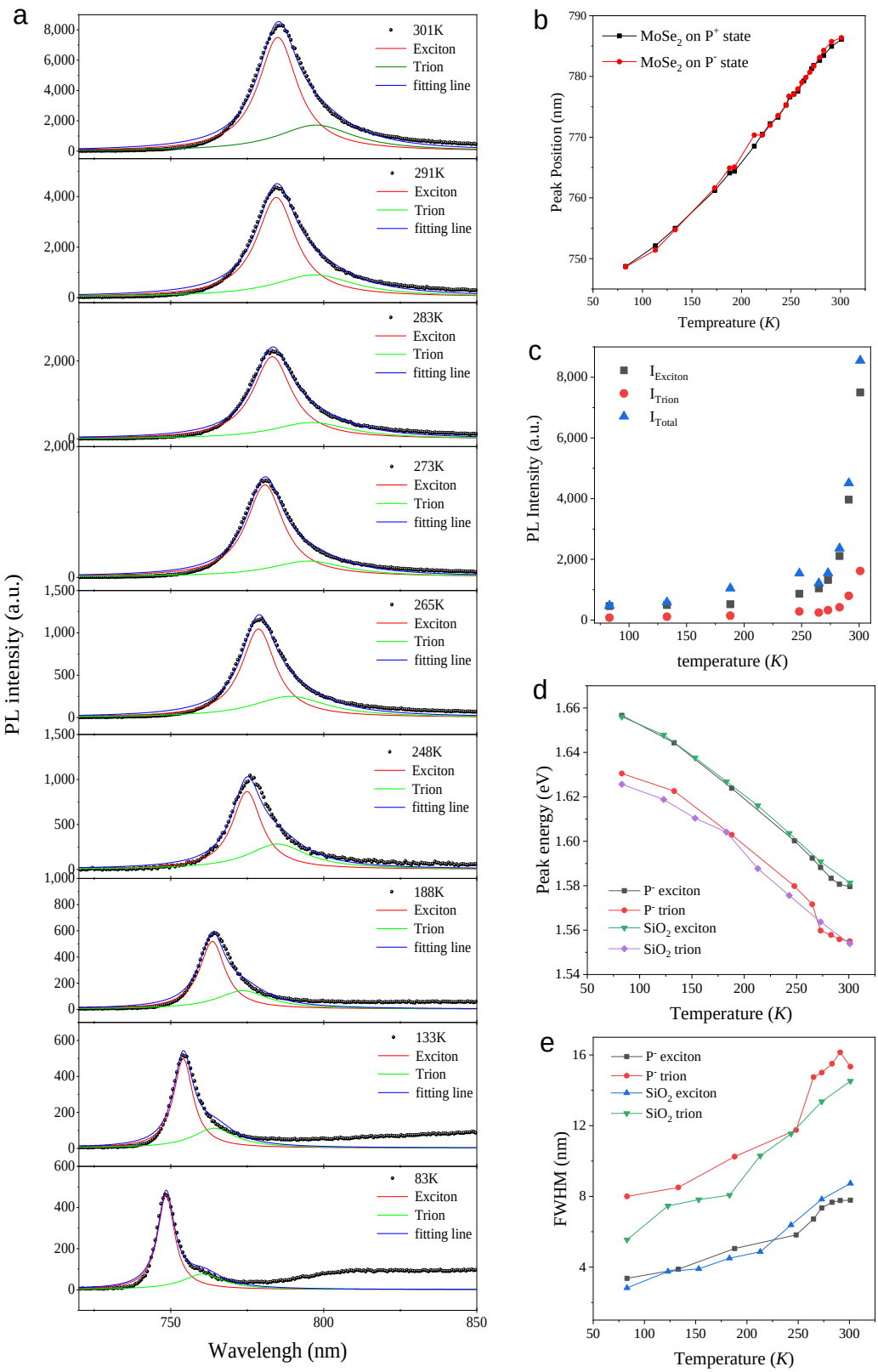
a
301K
Exciton
Trion
fitting line
291K
283K
273K
265K
248K
188K
133K
83K
PL intensity (a.u.)
Wavelengh (nm)
b
MoSe2 on P+ state
MoSe2 on P- state
Peak Position (nm)
Tempreature (K)
c
IExciton
ITrion
ITotal
PL Intensity (a.u.)
temperature (K)
d
P- exciton
P- trion
SiO2 exciton
SiO2 trion
Peak energy (eV)
Temperature (K)
e
FWHM (nm)
Temperature (K)

Figure S11 | PL spectra fitted Lorentzian functions with decreasing temperature. a) Temperature-dependent PL spectra (black dot line) of monolayer $MoSe_2$ sample at temperature ranging from 83 to 301 K. Each PL spectrum is fit to two Lorenz peaks which attributed to exciton and trion. b) Peak position of monolayer $MoSe_2$ on P^- and P^+ domain. c) Exciton and trion intensity of monolayer $MoSe_2$ at elevated temperature. d) Peak energy of exciton and trion of $MoSe_2$ on $LiNbO_3$ and SiO_2 substrate. e) Peak energy of exciton and trion of $MoSe_2$ on $LiNbO_3$ and SiO_2 substrate.

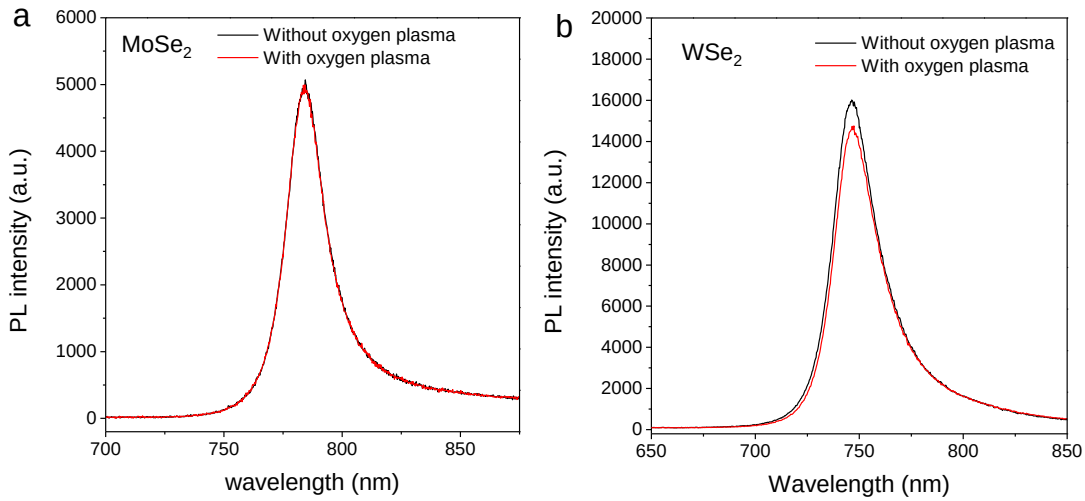

Figure S12 | PL spectra of $MoSe_2$ and WSe_2 with and without oxygen plasma treated substrate. a) PL spectra from $MoSe_2$ with and without substrate treated by oxygen plasma. b) PL spectra from WSe_2 with and without substrate treated by oxygen plasma.

Effect of residual oxygen on PL spectra

During the sample preparation, the oxygen plasma has been used to clean the substrate before transferring samples. To eliminate the effect of residual oxygen molecules on PL results, we perform the control experiments. Both monolayer $MoSe_2$ and WSe_2 samples have been transferred into two type of SiO_2/Si substrates. One has been treated by oxygen plasma and another one has not. The PL spectra show no difference between samples with and without oxygen plasma treated, as

shown in Figure S12. The results confirm that the residual oxygen molecules will not affect the emission behavior of the monolayer TMD.

Gate-dependent PL

Based on previous report, the charge neutrality of WSe_2 was achieved at a gate bias of ~-20 V, corresponding to E_F = 0.[1] We then converted the gate voltage to the induced hole doping density using equation:

$$ne = CV_g,$$

where the back-gate capacitance C = 1.2x10^{-8} F·cm^{-2}. Next, we further converted the hole doping density to the Fermi energy through relation:

$$E_F = \frac{\hbar\pi n}{2m_h e^2} \quad ,$$

using the hole effective mass $m_h = \sqrt{m_x^* m_y^*}$ = 0.41m_0, where m_0 is the mass of free electron.

We use the same way to estimate the charge doping level of $MoSe_2$ as above. The charge neutrality of $MoSe_2$ was achieved at a gate bias of ~40 V, corresponding to E_F = 0.[2]

LN polarization

Due to pinned domain, the remnant polarization of LN increases abruptly with decreasing temperature from RT to 247K. With further decreasing from 247K to 76K, the remnant polarization of LN would decrease smoothly.[3]

Temperature-dep PL of $MoSe_2$ and WSe_2 on SiO_2/Si

As shown in Figure S8, the PL intensity of $MoSe_2$ on SiO_2/Si substrate increases with decreasing temperature, whereas the PL intensity of WSe_2 increases then decreases with decreasing temperature, which is consistent with previous reports.[4-8]

References

1. K. L. Seyler *et al.*, Electrical Control of Second-Harmonic Generation in A WSe_2 Monolayer Transistor. *Nature Nanotechnology* **10**, 407–411 (2015).
2. J. S. Ross *et al.*, Electrical Control of Neutral and Charged Excitons in A Monolayer Semiconductor. *Nature Communications* **4**, 14741-14746 (2013).
3. H. Bo *et al.*, Temperature-Dependent Ferroelectric Properties of Near Stoichiometric Lithium Niobate Single Crystal. *Applied Physics A* **124**, 691 (2018).
4. J. Pei *et al.*, Excited State Biexcitons in Atomically Thin $MoSe_2$. *ACS Nano* **11**, 7468-7475 (2017).
5. J. Pei *et al.*, Exciton and Trion Dynamics in Bilayer MoS_2. *Small* **11**, 6384-6390 (2015).
6. X. Zhang, Y. You, S. Yang, F. Zhao, T. F. Heinz, Experimental Evidence for Dark Excitons in Monolayer WSe_2. *PHYSICAL REVIEW LETTERS* **115**, 257403 (2015).
7. F. Wang *et al.*, Tuning Coupling Behavior of Stacked Heterostructures Based on MoS_2, WS_2, and WSe_2. *Scientific Report* **7**, 44712 (2017).
8. A. Splendiani *et al.*, Emerging Photoluminescence in Monolayer MoS_2. *nano letters* **10**, 1271-1275 (2010).

5. High-Efficiency Monolayer Molybdenum Ditelluride Light Emitting Diode and Photodetector

Developing a high efficiency and low-cost light source with emission wavelength transparent to silicon is an essential step toward silicon based nanophotonic devices and micro/nano industry platforms. In this chapter, a near infrared monolayer $MoTe_2$ light emitting diode (LED) has been demonstrated and its emission wavelength is transparent to silicon. By taking advantage of the quantum tunneling effect, the device has achieved a very high external quantum efficiency (EQE) of 9.5% at 83 K, which is the highest EQE obtained from LED devices fabricated from monolayer TMDs so far. When the device is operated as a photodetector, the $MoTe_2$ device exhibits a strong photoresponsivity at resonant wavelength 1145 nm. The low dark current of ~5pA and fast response time 5.06 ms are achieved due to suppression of hBN tunneling layer. Our results open a new route for the investigation of novel near-infrared silicon integrated optoelectronic devices.

The content of this chapter has been published in ACS Appl. Mater. Interfaces 2018, 10, 50, 43291-43298. https://doi.org/10.1021/acsami.8b14076.

5.1. Motivation

Recently, monolayer TMDs have attracted tremendous attention due to their unique properties, including the indirect-to-direct bandgap transition[1, 2], the large exciton and trion binding energy[3, 4] and tunable band alignment[5] in atomically thin layers. Those distinct properties make them promising active materials for next-generation optoelectronic applications, including excitonic lasers,[6] photodetectors,[7] and LEDs.[8] Currently, much effort has been put to investigate TMD-based LEDs in the visible range. Research progress in the near infrared to infrared range has been barely reported. However, the infrared light source is usually a key component of on-chip silicon-based optical interconnects and high-speed communication systems. Thus, to explore and fabricate high-efficiency advanced infrared LED light sources becomes a crucial task. Typically, there are two popular architectures for fabricating TMD-based LED devices. One is lateral monolayer devices[9, 10] by using electrostatic doping to form an adjacent p-n junction within the material. The other one is vertical tunneling devices[11-13] that artificially introduce quantum wells (QWs) to engineer

the recombination of electrons and holes. EQE is considered to be a critical parameter in LED devices. By using splitting gates, Ross et al. have reported a lateral p-n junction monolayer WSe_2 LED with ~1% efficiency.[10] They also demonstrated that emissions of LED can be tuned between excitons and trions via modulating the injection bias. Compared to the lateral structure, a vertical structure allows higher injection current efficiency via larger contact area, more emission area, and thus higher efficiency. Although a high EQE (~8.4% at 6 K) has been achieved by using multiple QWs,[14] the quantum efficiency for most single QW TMD-based LED is still quite low. Withers et al. have demonstrated a vertical tunneling $MoSe_2$ LED and a tunneling WSe_2 LED by using boron nitride as tunnel barriers and graphene as contact electrodes.[13] They reported that the monolayer WSe_2 tunneling LED achieved 5% efficiency at room temperature. Besides, Carmen el at also successfully demonstrated the vertical tunneling WSe_2 and WS_2 quantum LED devices by taking advantage of boron nitride as tunnel layer.[12] They proposed that those LED devices have single photon behavior. In addition, the emission wavelength of lateral or vertical structure LED devices have been limited within CCD detection range so far and silicon (Si) or silicon dioxide (SiO_2) is used as host substrates. However, silicon substrate itself has a very strong absorption in CCD detection range. F. Withers et al.[13] reported that, in a monolayer tungsten diselenide (WSe_2) LED with highly reflective distributed Bragg reflector (DBR) substrates, the EQE reached 5% at room temperature. Up to 30% of the emitted light could be collected by the detector for LEDs based on such DBR substrate compared to only 2% from those with Si/SiO_2 substrates. In order to achieve a high-efficiency infrared light source, a high-quality optical gain material is necessary. Monolayer $MoTe_2$, a special family member of two-dimensional (2D) TMDs, has an electrical bandgap of ~1.72 eV.[4, 15] The exciton emission peak from monolayer $MoTe_2$ is located at ~1.1 eV[15] and is very close to the silicon bandgap, making it nearly transparent for silicon, which is essential for on-chip integrated high-efficiency silicon photonics and optoelectronics. Bilayer $MoTe_2$ has been successfully demonstrated to fabricate infrared LEDs and photodetectors by applying electrostatic doping to form a lateral adjacent p-n junction[16]. However, this electrostatic doping method is more difficult to achieve in monolayer $MoTe_2$ because of the complicated fabrication process and low electrical excitation tolerance. In this work, we demonstrate the vertical structure monolayer $MoTe_2$ LED via a solution- and lithography-free transfer process. The total emission

area reaches 80 μm^2. Importantly, we show that our $MoTe_2$ LED device has an extremely high EQE of around 9.5% at 83K, which is the highest EQE that has been achieved in monolayer TMD LEDs. Moreover, this vertical structure can also be extended to be a photodetector. The response time of our $MoTe_2$ photodetector has been measured to be ~5.06 ms with an extremely low dark current of ~5 pA, which is comparable to other $MoTe_2$-based photodetectors.[17] Our results pave the way for the investigation of the next-generation silicon-integrated on-chip infrared optoelectronic devices.

5.2. Architecture and Basic Performance of Monolayer $MoTe_2$ LED

Figure 5.1 a & b show the schematic and optical microscope image of the monolayer $MoTe_2$ LED. The single tunneling junction is made of stacked graphite, hexagonal boron nitride (hBN) and monolayer $MoTe_2$ from top to bottom. A monolayer $MoTe_2$ sample identified by a phase shift interferometer (PSI) was firstly mechanically exfoliated onto a SiO_2/Si (275 nm thermal oxide on n^+ -doped silicon) substrate and then the sample was stored in vacuum to avoid any oxidation or contamination (Supporting Figure S1). A 6 to 8 layers hBN identified by PSI was also exfoliated onto the SiO_2/Si substrate for subsequent processes (Supporting Figure S2). We used a dry-peel-and-lift van der Waals technique to assemble our devices,[18] and the whole transfer process was solution-free (Supporting Note 1). From bottom to top, $MoTe_2$ monolayer and thin-layer sample with irregular shape (white dashed line in Figure 5.1 b) was mostly covered by a large piece of thin-layer hBN (blue dashed line in Figure 5.1 b), with graphite (black dashed line in Figure 5.1 b) located on top of monolayer-$MoTe_2$/hBN heterostructure serving as one electrode. The top thin layer hBN serves not only as a tunneling layer to realize device function but also as a capping layer to protect the active $MoTe_2$ layer from contamination to enhance device performance and stability. Figure 5.1 c illustrates the measured Raman spectrum from the monolayer $MoTe_2$/hBN/graphite overlapping area excited with a 532 nm laser. The characteristic phonon response of the A_{1g} at 172.1 cm^{-1} and E_{2g} at 235.9 cm^{-1} is consist with previously report in monolayer $MoTe_2$.[15] The small peak B located at 183 cm^{-1} may be the second order Raman modes of monolayer $MoTe_2$, as observed in other TMDs.[19-21] The Raman peak of hBN was observed at around 1366 cm^{-1}, corresponding to the characteristic peak of E_{2g} phonon mode. This

extremely low peak intensity indicates that our hBN flake is very thin, which is consistent with the previous report that the peak intensity becomes progressively weaker as hBN layer number decreases.[22] The characteristic peaks of graphite were also observed in the high frequency region at 1581 cm^{-1} (G band) and 2718 cm^{-1} (2D band).[23] Figure 5.1 d shows typical electroluminescence (EL) and photoluminescence (PL) spectra of our monolayer $MoTe_2$ LED. By applying a negative bias onto top graphite electrode and grounding monolayer $MoTe_2$, electrons and holes would tunnel through the hBN layers into the active $MoTe_2$ monolayer, leading to the I-V curve shown in Supporting Figure S5. Strong EL from monolayer $MoTe_2$ can be obtained at an even higher temperature (83 K) compared to previous reports,[12, 13] as illustrated (red) in Figure 5.1 d. In order to understand the nature of the EL, the PL spectrum (blue) at 83 K from the same location is also presented. The measured PL spectrum exhibits two clear peaks with central wavelengths at ~1036 nm (1.197 eV) and ~1051 nm (1.179 eV) and they are noted as exciton and trion emission from monolayer $MoTe_2$, which matches well with the previous observation.[4] In the PL spectrum, one broad peak located at 1121.6 nm (1.1 eV) can also be observed and is assigned to be the PL emission from n^+-doped silicon (Supporting Figure S4). The center peak of the EL spectrum is located at 1034.6 nm (1.198 eV) with 29 meV full-width-at-half-maximum (FWHM). The similar peak positions between the EL and PL spectra and the extremely small FWHM for the EL peak indicate that the EL emission is exciton dominant. Less trion contributions in EL spectrum compared with PL spectrum reflects that the initial doping of our monolayer MoTe2 is slightly n-type after LED device fabrication (Supporting Note 5). The injected electrons and holes would form excitons before the radiative recombination, reflecting the large exciton binding energy at high temperature due to the strong Coulomb interaction in monolayer $MoTe_2$.

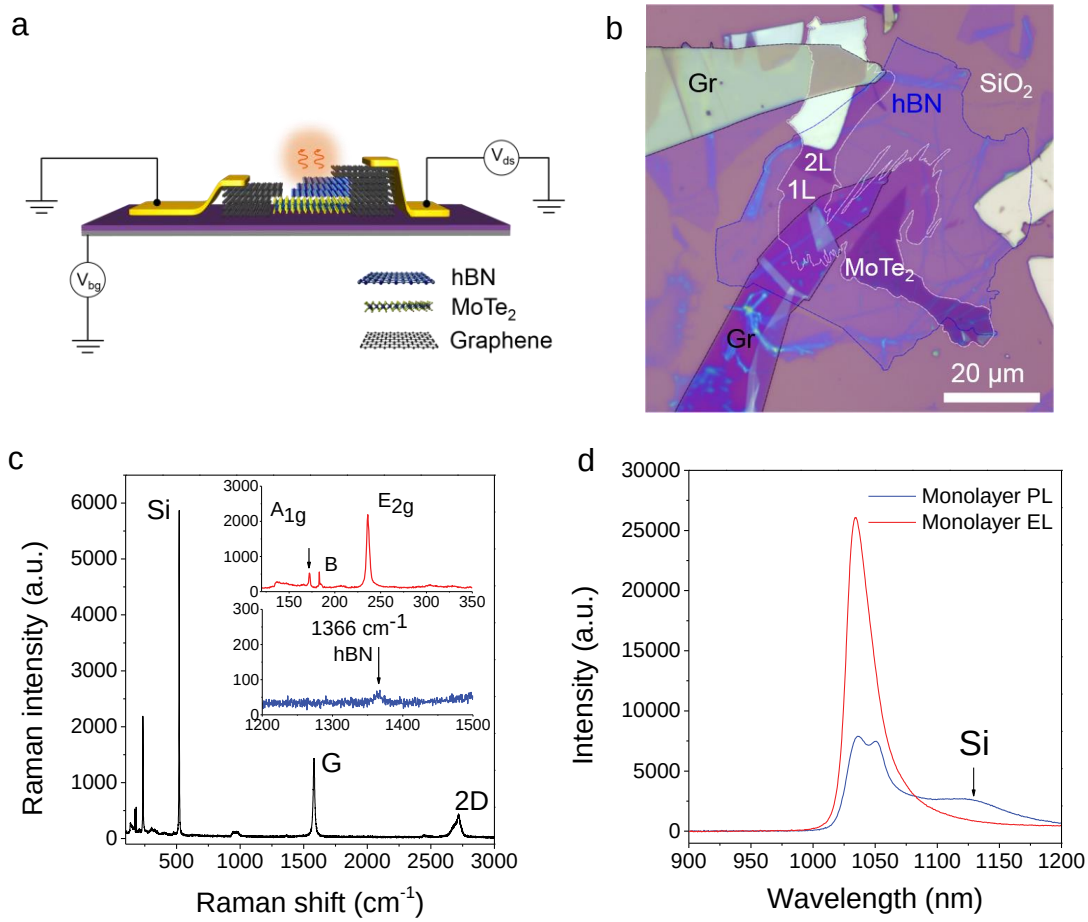

Figure 5. 1 Architecture of monolayer $MoTe_2$ LED. a, Schematic of our monolayer $MoTe_2$ LED and electrical connections for EL measurements. b, Optical microscope image of the monolayer $MoTe_2$ LED. The white, blue and black dashed line outline the footprint of $MoTe_2$, hBN, and graphite, respectively. Monolayer and bilayer $MoTe_2$ area are marked as 1L and 2L. c, Raman spectrum of the $MoTe_2$/hBN/graphite overlapping area. Inset: Zoom-in raman peak of the $MoTe_2$ (red curve) and the hBN (blue curve). d, Measured PL and EL spectrum from the same location of the monolayer $MoTe_2$ LED device at 83 K. The injection current for EL emission is 6.07 μA under back gate voltage at -20 V.

5.3. High Efficiency Near Infrared Light Emission at 83K

Figure 5.2 a shows EL spectra of monolayer $MoTe_2$ LED with increasing injection current. A single EL peak located at 1034.6 nm can be observed from all spectra under different injection currents, indicating that our monolayer $MoTe_2$ remained in high quality after complicated device fabrication process. Figure 5.2 b is a spatial

mapping of the EL peak intensity from the $MoTe_2$ LED device at 83 K. Monolayer $MoTe_2$, few-layer hBN, and graphite region is outlined by white, blue, and black dashed line, respectively. The EL mapping shows uniform and strong emission from the entire monolayer $MoTe_2$ region, suggesting that the injected current evenly flows through the monolayer region. The total illuminating area reached around 80 μm^2, which is 10 to 20 times larger than that in typical lateral structure LEDs.[10] With an illuminating area of 80 μm^2, the current density of measured highest EL spectra in Figure 5.2 a is only 75.9 nA/μm^2. The plot of the integrated EL intensity as a function of injection current shows two different slopes with an apparent threshold at 5.05 μA (Figure 5.2 c red curve). The integrated EL intensity increases slowly below the threshold, and it increases dramatically above the threshold. This current threshold may result from the direct tunneling (DT) and Fowler-Nordheim tunneling (FNT) transition (discussed later).[24] Furthermore, the strong EL emission under the small drive current suggests that our device has a very high EQE. Here the EQE is defined as $EQE = eN_{ph}/\eta I$, where e is the electron charge, N_{ph} is the number of photons detected by the detector, η is the system collection efficiency (Supporting Figure S3), and I is the current passing through the device active area. Figure 5.2 c shows the EQE as the function of the injection current (blue curve). Similar to the trend of integrated EL intensity, the EQE curve also exhibits the doubled-slope feature with the transition at 5.05 μA. We believe that the double sloped EQE and integrated EL intensity are related to the transition of DT and FNT effect. Apart from the definition of EQE above, the EQE can also be expressed as follows: $EQE = \eta_{Radiative} \cdot \eta_{Injection} \cdot \eta_{Extraction}$. Here, $\eta_{Radiative}$ is the radiative recombination efficiency, $\eta_{Injection}$ is the current injection efficiency and is defined as the fraction of current injected into the QW that recombines radiatively and non-radiatively with respect to the injected and escaped current, and $\eta_{Extraction}$ is the extraction efficiency and is defined as the ratio of the generated photon that can be extracted from a device to total photons from a QW.[25] In our experiment, all EL spectra were collected with the same system, and thus $\eta_{Extraction}$ was the same for all spectra. The EQE in this case is determined by $\eta_{Radiative}$ and $\eta_{Injection}$. The radiative recombination efficiency is typically a constant, and this value is mostly determined by material itself. Therefore, the overall EQE is related to current injection efficiency which can be expressed as:

$$\eta_{Injection} = \frac{I_{Qw\_total}}{I_{QW\_total} + + I_{Barrier\_total}}$$

where I_{Qw_total} is total recombination current in the $MoTe_2$ layer and $I_{Barrier\_total}$ is total recombination current in the hBN barrier area. The total injection current (I_{total}) is the sum of both I_{Qw_total} and $I_{Barrier\_total}$.

Before further discussion, it is necessary to note that our EL measurement was conducted in the small current regime, which is far away from the quantum efficiency saturation or EQE suppression (efficiency droop) regime. Therefore, the escaping current from the QW can be considered to be a small constant. The device operated when electrons were injected into the $MoTe_2$ layer after tunneling through the few layer hBN barrier. The DT process typically happens at low voltage region, while the FNT process dominating at high voltage region (Supporting Figure S6). Under small voltage (DT process), electrons in graphite need to tunnel a trapezoidal hBN barrier into the QW (Supporting Figure S6a). No matter how high the graphite Femi level rises, the barrier thickness will never change and the current loss in the barrier area ($I_{Barrier\_total}$) is proportional to I_{total}, which results in a low and uniform current injection efficiency. However, the hBN barrier shape changes from trapezoid to triangle when the tunneling process becomes FNT (Supporting Figure S6b) at higher biases. In triangular barrier scenario, the barrier thickness becomes narrower as the graphite Femi level rises, which causes easier tunneling of electrons into the QW and significantly decreased current loss in the barrier area ($I_{Barrier\_total}$), leading to higher and increasing current injection efficiency, as shown in Figure 5.2 c.

To further demonstrate the high EQE of our device, we have compared the EQE of our monolayer $MoTe_2$ LED with previously reported monolayer TMD-based LEDs, as presented in Figure 5.2 d.[8, 10, 13, 14] For vertical structure LED devices (ref 13 and 14), they were both measured in the small injection current regime where the EQE monotonically increases with the injection current and the EQE was recorded at their highest injection current. In our measurement, the highest injection current was much smaller than those in reported devices. The EQE of our device at highest injection

current (75.9 nA/μm^2) was measured to be 9.5%, which is nearly twice of what was measured in a monolayer WSe_2 LED with an injection current of 9.4 μA/μm^2.[13] Taking into account the 124 times smaller injection current, the total EQE enhancement reaches a maximum of ~236 times. Such high quantum efficiency in our device arises from two aspects: 1) the delicate device structure, ultra clean interface of devices, dry membrane transfer and photolithography-free electrodes pattern technique; 2) low substrate absorption at the emission wavelength of $MoTe_2$. Considering the vulnerability of the active monolayer $MoTe_2$, our device structure was designed to be an inversion of the common vertical structure.[12] Our PL studies showed that bottom-placed $MoTe_2$ layer successfully avoided surface contamination and sample degradation (Supporting Figure S7). Besides, a dry and lithography-free method was used to transfer membranes and to pattern electrodes (Supporting Note 1).[26, 27] Therefore, our device was assembled under a totally dry environment and no molecules were introduced from any organic solution, which can be seen in our clear PL spectra without any defect related peaks. Compared to other visible TMD-based LEDs, our monolayer $MoTe_2$ LED has an emission wavelength at ~1035 nm that is very close to the Si bandgap. Silicon has a weak absorption coefficient at 1.1 eV of ~ 1.5 cm^{-1},[28, 29] therefore the emitted light from $MoTe_2$ monolayer is nearly transparent to silicon. By introducing a back-reflecting mirror or other light trapping structure on the back of the substrate, the device EQE can be further improved.

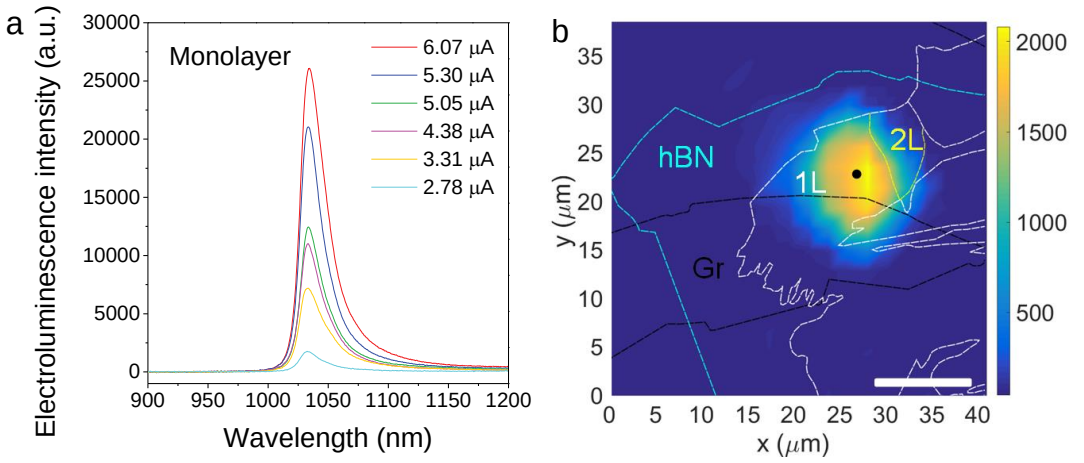

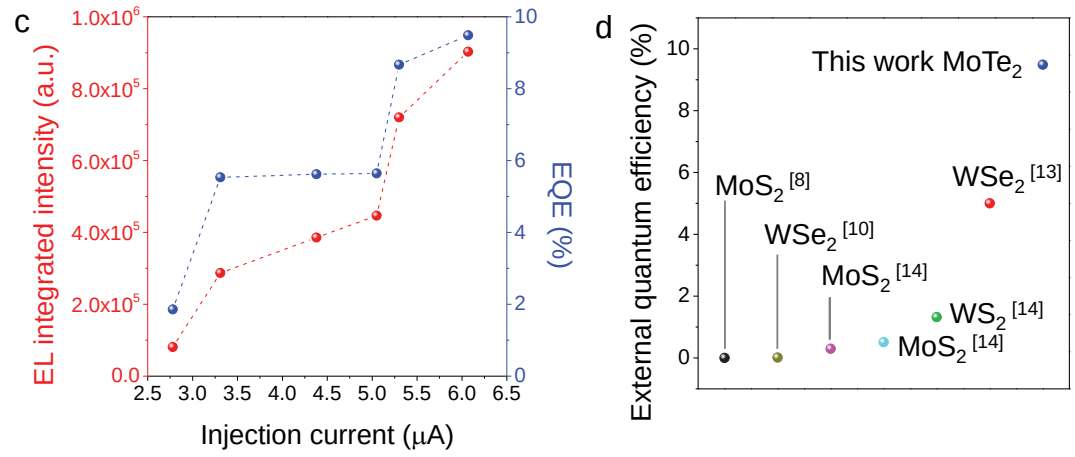

Figure 5. 2 Strong infrared EL emission at 83 K. a, EL spectra from monolayer $MoTe_2$ under different injection current and -20 V back gate voltage. The spectra are collected from black dot in b. b, EL mapping image of the $MoTe_2$ LED device under an injection current of 9.7 μA and -20 V back gate. The blue, white and black dashed line outlines hBN, $MoTe_2$, and graphite. Scale bar, 20 μm. c, EL intensity (left) and EQE (right) of monolayer $MoTe_2$ as a function of the injection current. d, Quantum efficiency for different monolayer TMD devices.

5.4. Working principle of the monolayer $MoTe_2$ LED device

To further understand the tunneling effect of our LED device, we measured its electrical properties. The I_{ds}–V_{ds} curve of the device under different back-gate voltages and corresponding analysed band diagrams are illustrated in Figure 5.3. Here we discuss 6 different states labeled in Figure 5.3 a & b. The corresponding band diagrams are presented in Figure 5.3 c-f. The whole device consists of three parts in the band diagram, including Schottky barrier (SB), $MoTe_2$ active layer, and hBN barrier. Firstly, the device is under 20 V back-gate voltage (V_{bg} = 20 V), leading to a relatively large SB between graphite and $MoTe_2$ (State 1 and 2). A positive bias (V_{ds} = 40 V) applied to another graphite electrode lowers the graphite Femi level (E_F) below the valence band (E_V) of gated $MoTe_2$, which induces holes to tunnel through the hBN barrier into $MoTe_2$ layer (State 1, as illustrated in Figure 5.3 c). On the contrary, a negative bias (V_{ds} = -40 V) applied to graphite electrode will raise its E_F above the conduction band (E_C) of gated $MoTe_2$, resulting in electrons tunneling into $MoTe_2$ layer (State 2, as illustrated in Figure 5.3 d). Meanwhile, holes in the other

side graphite cannot be injected into $MoTe_2$ monolayer because of the large energy barrier for hole. In the above two scenarios, there is no radiative recombination due to lack of electrons or holes in monolayer $MoTe_2$. Subsequently, state 3 and 4 show that when the device is under -20 V back-gate voltage (V_{bg} = -20 V), the conduction and valence band of $MoTe_2$ bend upwards, which narrows the SB width. If the E_F of graphite closed to hBN side is lowered below E_V of the gated $MoTe_2$, holes can also tunnel into $MoTe_2$, similar to the situation in Figure 5.3 c, but with a larger current because of the smaller SB (State 3, as illustrated in Figure 5.3 e). In state 4 (Figure 5.3 f), when our device is under -20 V back-gate voltage (V_{bg} = -20 V) and graphite closed to hBN side is under a large negative bias (V_{ds} = -40 V), electrons in this graphite can tunnel into the $MoTe_2$ monolayer after raising the E_F. In the meantime, holes are also able to tunnel through the SB into $MoTe_2$ monolayer. And then electrons and holes recombine radiatively leading to a great of photon emissions. The state 5 and state 6 illustrate the scenario before our device emitting light, which has been explained in supporting note 3. By modulating the Femi level of the graphite, we can manipulate the injection of electrons and holes in this type of vertical structure device and thereby realize device control.

As the initial doping of the monolayer $MoTe_2$ is quite small,[4] the doping level of $MoTe_2$ could significantly change when it is under different gates.[30] Therefore, it is worth discussing the gate effect on behaviours of the device. Firstly, the source and drain current in Figure 5.3 a and b is compared at a given V_{ds} equals to 40 V. The source and drain current for V_{bg} at -20 V is larger than the V_{bg} at 20 V. When V_{bg} is set at 20 V, the channel type in $MoTe_2$ is n-type and electrons are the majority of charge carriers. In this case, holes injected from tunneling through hBN could not generate large current. However, the channel type in $MoTe_2$ switches to p-type when V_{bg} is set to -20 V. The holes become majority carriers leading to larger current. Conversely, the current for V_{bg} at -20 V is smaller than the V_{bg} at 20 V when the given V_{ds} is at -40 V. In this scenario, electrons are injected through hBN. The channel type changes from p-type to n-type when V_{bg} increasing from -20 V to 20 V. Our results are consistent with previous report.[30]

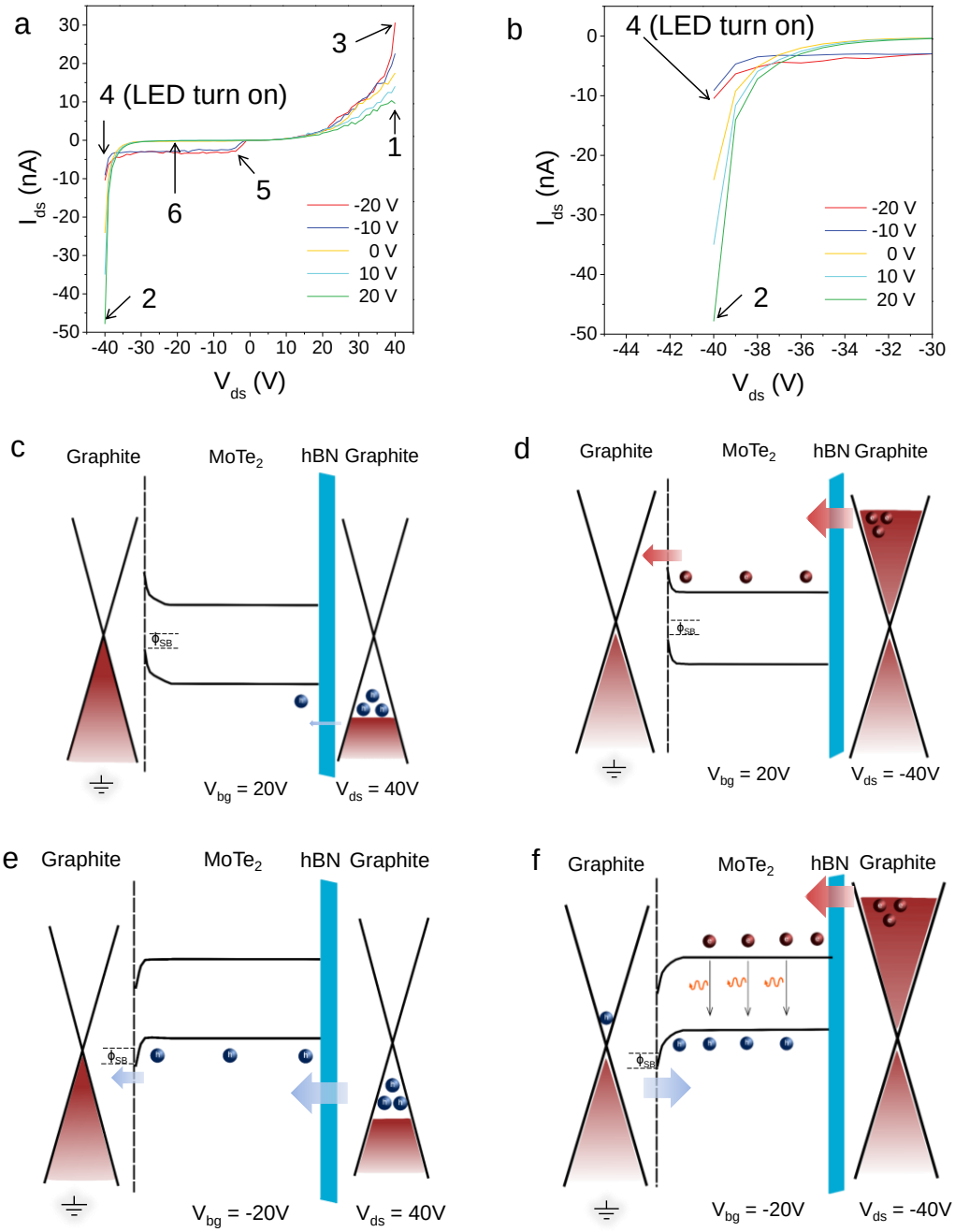

Figure 5. 3 Working principle of the monolayer $MoTe_2$ LED device. a, I_{ds} – V_{ds} curve for the device under various back-gate voltages at room temperature. State 1 to 6 are marked in different locations. b, Zoom-in image of the left part of I_{ds} – V_{ds} curve in a. c, Band diagram of the device operating at state 1 (V_{bg} = 20V, V_{ds} = 40V) in a. d, Band diagram of the device operating in state 2 (V_{bg} = 20V, V_{ds} = -40V) in a. e, Band diagram of the device operating in state 3 (V_{bg} = -20V, V_{ds} = 40V) in a. f, Band diagram of the device operating in state 4 (V_{bg} = -20V, V_{ds} = -40V) in a.

5.5. Photo-response of monolayer $MoTe_2$ photodetector

The above electrical and light emitting studies demonstrate excellent optoelectronic performance in our vertical tunneling structure. However, the photodetection property based on $MoTe_2$ material and such tunneling structure are barely reported. Here we have further extended our device into photodetector and conducted some initial characterizations of photo response properties. Figure 5.4 a up-panel shows the optical microscope image of our monolayer $MoTe_2$ photodetector that has the same configuration as our LED device. The monolayer $MoTe_2$ is fully covered by a few-layer hBN flake. The corresponding photocurrent mapping at 5 V bias (V_{ds} = 5 V) with a 532-nm laser excitation (9 nW) is presented in Figure 5.4 a bottom panel, with the graphite and $MoTe_2$ region outlined by black and white dashed line, respectively. The photocurrent mapping clearly indicates that photo-response comes from the monolayer $MoTe_2$ close to the edge of the graphite. Under 5 V bias, the E_F of graphite is lowered and thus only some of holes can tunnel into the $MoTe_2$ monolayer. This small amount of tunneling holes contributes dark current in this case, as shown in Figure 5.4 b, left panel. By inserting the hBN tunneling layer, the dark current can be highly suppressed. With light illumination, the minority electron population in the conduction band of $MoTe_2$ is significantly enhanced and can tunnel into graphite to generate light current (Figure 5.4 b, right panel). However, photoexcited electrons beyond the carrier diffusion length will recombine radiatively or non-radiatively before arriving the graphite electrode, which causes the photo-response only showing near the edge of the graphite.

The spectral photoresponsivity of our device is measured and illustrated in Figure 5.4 c. This wavelength-dependent photoresponsivity is largely attributed to light absorption by $MoTe_2$ monolayer. The photoresponsivity is negligible for photons with wavelength longer than 1180 nm (energy smaller than 1.05 eV), corresponding to the exciton bandgap of monolayer $MoTe_2$. Apart from $MoTe_2$ exciton photoresponsivity peak, we also observed that the photoresponsivity reached its maximum increase rate at 690 nm, indicating the monolayer $MoTe_2$ band edge, which is consistent with previous report[4]. Remarkably, another strong resonate peak located at 450 nm can also be observed in the spectrum. We attribute this peak to C peak originated from the regions of parallel bands near the Γ point, which rises

from the band nesting effect (Supporting Note 2).[4] We also measured the response time of our device, as displayed in Figure 5.4 d. The rise and fall time in our device are 5.34 and 5.06 ms, respectively. Such short response time is attributed to the flat hBN surface above the $MoTe_2$, which minimizes charge transfer at the hBN/$MoTe_2$ interface and again, reflects our ultra-clean device fabrication process. Finally, the photo-detectivity, one of the most important parameters in photodetector, indicates the capability of a device to detect weak signal and it can be calculated by using following formula:[17]

$$D = \frac{EQE(qA)^{1/2}}{h\upsilon(2I_{dark})^{1/2}}$$

Where external quantum efficiency $EQE = R(h\upsilon/e)$, q is the elementary charge, h is Planck constant, $\upsilon = c/\lambda$, c is the speed of light in vacuum, λ is 1145 nm and I_{dark} is 5 $\times 10^{-12}$ A. The detectivity is calculated to be 2.6 $\times 10^{9}$ cm $Hz^{1/2}W^{-1}$.

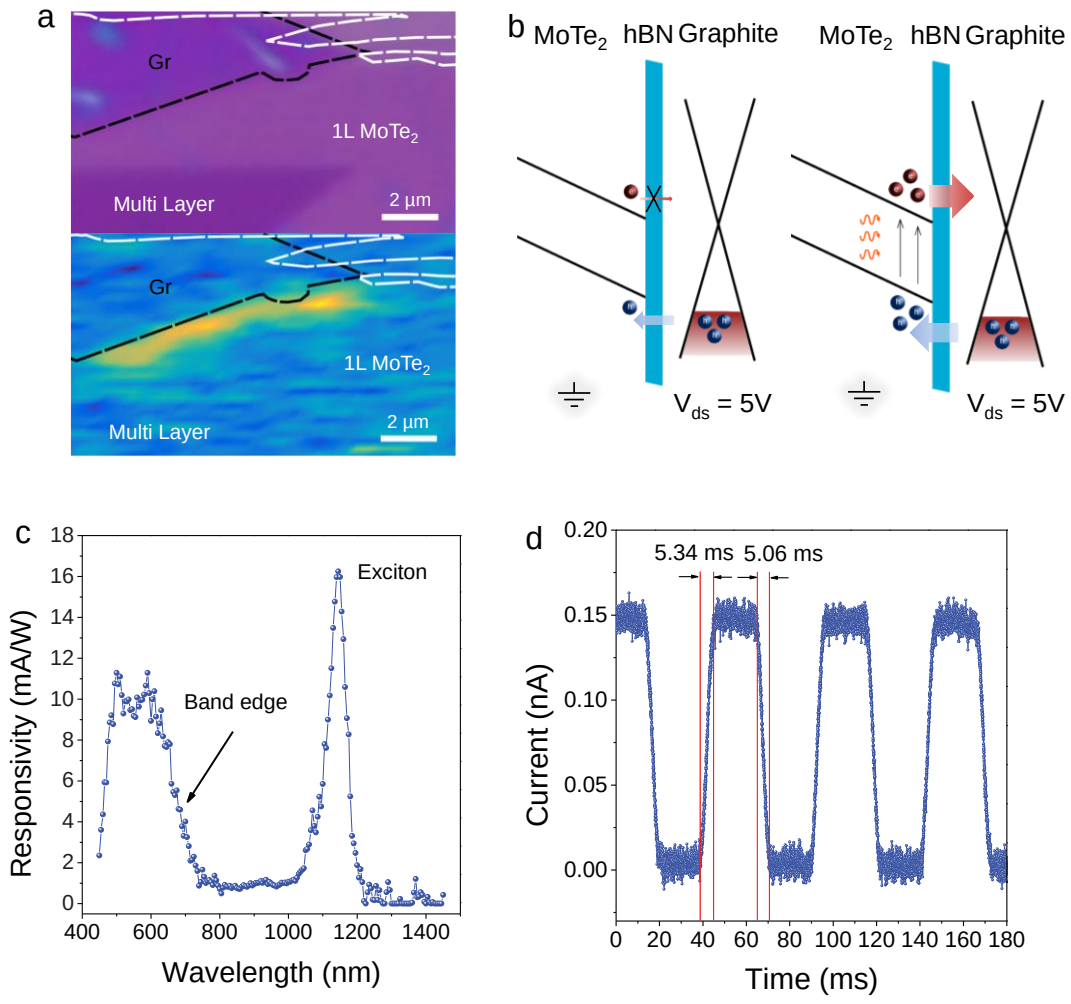

Figure 5. 4 Photo-response of monolayer $MoTe_2$ photodetector. a, up panel: Optical microscope image of the monolayer $MoTe_2$ photodetector. White and black dashed line outlines $MoTe_2$ and graphite. Few-layer hBN is located between graphite and $MoTe_2$. Bottom panel: Photocurrent mapping image of the same area. The image was acquired at V_{ds} = 5 V and V_{bg} =0 V under 532-nm excitation laser (9 nW). b, Band diagram of the monolayer $MoTe_2$ photodetector. Left and right side shows the device working without and with light illumination, respectively. c, Photo-responsivity as function of wavelength under 10 nW white light, with V_{ds} = 5 V and V_{bg} = 0 V. d, Temporal photocurrent of the monolayer $MoTe_2$ photodetector. Incident light: 10 nW white light, V_{ds} = 5 V, V_{bg} = 0 V. The rise time (5.34 ms) is defined as the time of the photocurrent increases to 90% of the ON-state current. The fall time (5.06 ms) is defined as the time for the photocurrent decreases to 10% of the ON-state current.

5.6. Summary

In summary, we have demonstrated vertical structured high-efficiency monolayer $MoTe_2$ LED for the first time, and it shows extremely high performance with an EQE of ~9.5% at 83 K. The working principle of this vertical tunneling device has been identified by band diagram study under different situations. Such kind of LED presents a huge potential to be future near-infrared on-chip light sources. And their efficiencies can be further improved by creating multiple QWs[13] and delicate tuning of the hBN barrier thickness. Furthermore, this hBN encapsulated structure can also be extended to photodetection with strong photoresponsivity and fast response time. Our results open a new route for the investigation of novel infrared optoelectronic devices.

5.7. Experimental Section

5.7.1. Device fabrication and characterization. The Monolayer $MoTe_2$ and the few layers hBN were mechanically exfoliated onto the SiO_2/Si substrate. Transfer stacking process was done with a homemade transfer platform (Supporting Note 1). The 100nm thickness gold electrodes were directly patterned in a plain SiO_2/Si substrate by conventional photolithography, metal deposition and lift-off process.

The homemade micromanipulator was used to peel off Au electrodes and then transfer them to LED devices.

5.7.2. Optical characterization. PL, Raman and EL measurements were conducted using a Horiba LabRAM system equipped with a confocal microscope, a charge-coupled device (CCD) Si detector, and a 532 nm diode-pumped solid-state (DPSS) laser as the excitation source. For temperature-dependent (above 83 K) measurements, the sample was placed into a microscope-compatible chamber with a low-temperature controller (using liquid nitrogen as the coolant). The electrical bias for LED was applied using a Keithley 4200 semiconductor analyzer. The spectral response of the photodetector devices was measured using the conventional amplitude modulation technique with a tungsten-halogen lamp as a white illumination source, a mechanical chopper, an Acton SpectraPro 2300i monochromator, a Stanford SR570 low noise current pre-amplifier and a Stanford SR830 DSP lock-in amplifier. The two-dimensional photocurrent mapping was performed with a WITec alpha300S scanning microscopy system.

Reference

1. K. F. Mak, C. Lee, J. Hone, J. Shan, T. F. Heinz, Atomically thin MoS(2): a new direct-gap semiconductor. *Phys Rev Lett* **105**, 136805 (2010).
2. W. Zhao *et al.*, Origin of indirect optical transitions in few-layer MoS2, WS2, and WSe2. *Nano Lett* **13**, 5627-5634 (2013).
3. K. F. Mak *et al.*, Tightly bound trions in monolayer MoS2. *Nat Mater* **12**, 207-211 (2013).
4. J. Yang *et al.*, Robust excitons and trions in monolayer MoTe2. *ACS nano* **9**, 6603-6609 (2015).
5. B. Zheng *et al.*, Band alignment engineering in two-dimensional lateral heterostructures. *Journal of the American Chemical Society*, (2018).
6. Y. Ye *et al.*, Monolayer excitonic laser. *Nature Photonics* **9**, 733-737 (2015).
7. F. H. Koppens *et al.*, Photodetectors based on graphene, other two-dimensional materials and hybrid systems. *Nat Nanotechnol* **9**, 780-793 (2014).
8. R. Sundaram *et al.*, Electroluminescence in single layer MoS2. *Nano letters* **13**, 1416-1421 (2013).
9. C. H. Lee *et al.*, Atomically thin p-n junctions with van der Waals heterointerfaces. *Nat Nanotechnol* **9**, 676-681 (2014).
10. J. S. Ross *et al.*, Electrically tunable excitonic light-emitting diodes based on monolayer WSe2 p-n junctions. *Nat Nanotechnol* **9**, 268-272 (2014).
11. C. H. Liu *et al.*, Nanocavity Integrated van der Waals Heterostructure Light-Emitting Tunneling Diode. *Nano Lett* **17**, 200-205 (2017).
12. C. Palacios-Berraquero *et al.*, Atomically thin quantum light-emitting diodes. *Nat Commun* **7**, 12978 (2016).
13. F. Withers *et al.*, WSe(2) Light-Emitting Tunneling Transistors with Enhanced Brightness at Room Temperature. *Nano Lett* **15**, 8223-8228 (2015).
14. F. Withers *et al.*, Light-emitting diodes by band-structure engineering in van der Waals heterostructures. *Nat Mater* **14**, 301-306 (2015).
15. C. Ruppert, O. B. Aslan, T. F. Heinz, Optical properties and band gap of single- and few-layer MoTe2 crystals. *Nano Lett* **14**, 6231-6236 (2014).
16. Y. Q. Bie *et al.*, A MoTe2-based light-emitting diode and photodetector for silicon photonic integrated circuits. *Nat Nanotechnol* **12**, 1124-1129 (2017).
17. W. Yu *et al.*, Near-Infrared Photodetectors Based on MoTe2 /Graphene Heterostructure with High Responsivity and Flexibility. *Small*, (2017).
18. F. Pizzocchero *et al.*, The hot pick-up technique for batch assembly of van der Waals heterostructures. *Nat Commun* **7**, 11894 (2016).
19. H. Li *et al.*, From Bulk to Monolayer MoS2: Evolution of Raman Scattering. *Advanced Functional Materials* **22**, 1385-1390 (2012).
20. W. Zhao *et al.*, Lattice dynamics in mono-and few-layer sheets of WS 2 and WSe 2. *Nanoscale* **5**, 9677-9683 (2013).
21. A. Berkdemir *et al.*, Identification of individual and few layers of WS2 using Raman Spectroscopy. *Scientific reports* **3**, (2013).
22. R. V. Gorbachev *et al.*, Hunting for monolayer boron nitride: optical and Raman signatures. *Small* **7**, 465-468 (2011).
23. A. C. Ferrari, Raman spectroscopy of graphene and graphite: disorder, electron–phonon coupling, doping and nonadiabatic effects. *Solid state communications* **143**, 47-57 (2007).
24. Q. A. Vu *et al.*, Tuning Carrier Tunneling in van der Waals Heterostructures for Ultrahigh Detectivity. *Nano Lett* **17**, 453-459 (2017).
25. H. Zhao, G. Liu, J. Zhang, R. A. Arif, N. Tansu, Analysis of Internal Quantum Efficiency and Current Injection Efficiency in III-Nitride Light-Emitting Diodes. *Journal of Display Technology* **9**, 212-225 (2013).

26. F. Pizzocchero *et al.*, The hot pick-up technique for batch assembly of van der Waals heterostructures. *Nature communications* **7**, (2016).
27. P. Zomer, M. Guimarães, J. Brant, N. Tombros, B. Van Wees, Fast pick up technique for high quality heterostructures of bilayer graphene and hexagonal boron nitride. *Applied Physics Letters* **105**, 013101 (2014).
28. M. A. Green, M. J. Keevers, Optical properties of intrinsic silicon at 300 K. *Progress in Photovoltaics: Research and Applications* **3**, 189-192 (1995).
29. R. Hull, *Properties of crystalline silicon*. (IET, 1999).
30. Y. F. Lin *et al.*, Ambipolar MoTe2 transistors and their applications in logic circuits. *Advanced Materials* **26**, 3263-3269 (2014).

Appendix for:

Supporting Information for Chapter 5

1. PSI characterization of monolayer $MoTe_2$ sample.

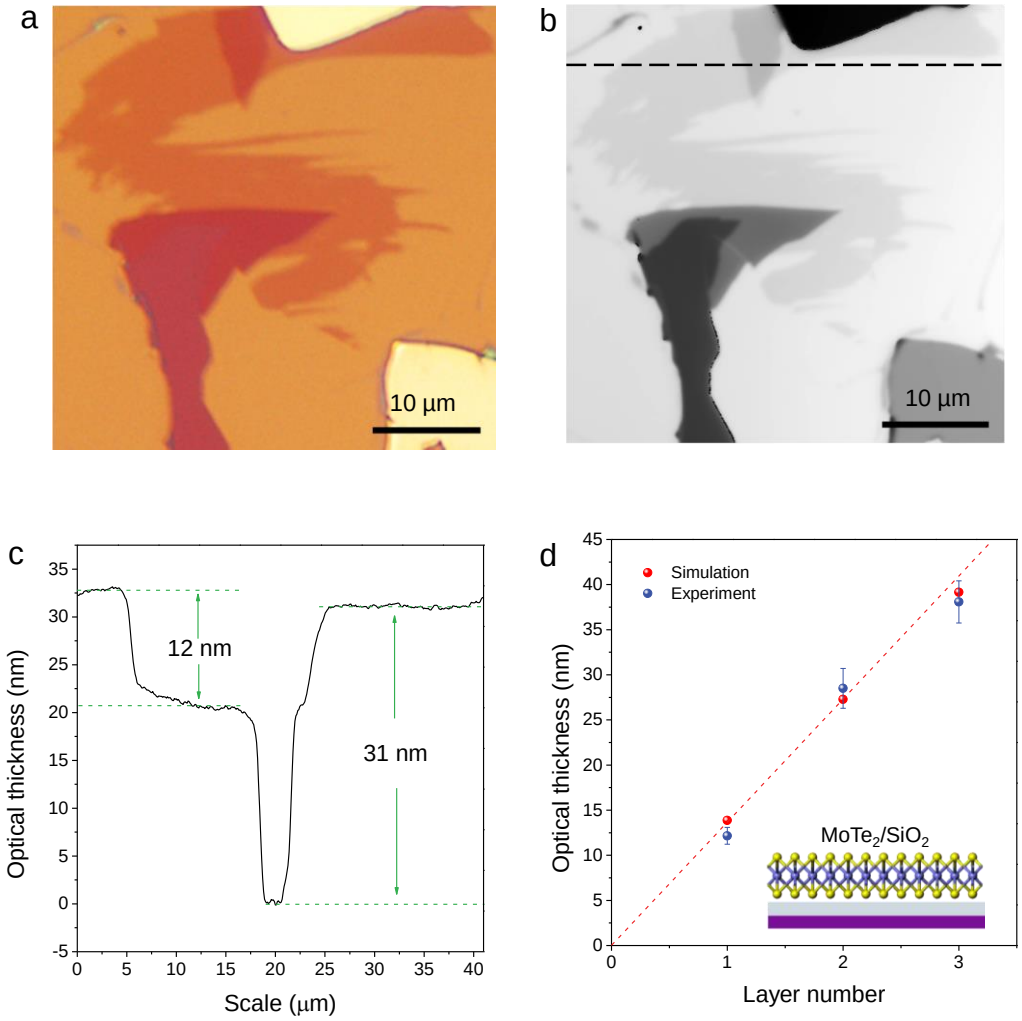

Figure S1 PSI characterization of monolayer $MoTe_2$ sample. a, Optical microscope image of monolayer $MoTe_2$ sample prepared by mechanical exfoliation. b, PSI image of the same monolayer $MoTe_2$ sample in a. c, PSI measured optical thicknesses along the dashed line in b. d, Optical thicknesses for 1L to 3L $MoTe_2$ samples from both simulation (red sphere) and experimental measurements (blue sphere with error bar). The red dashed line is the linear fit for statistical data measured with the PSI system.

2. PSI characterization of few-layer hBN sample.

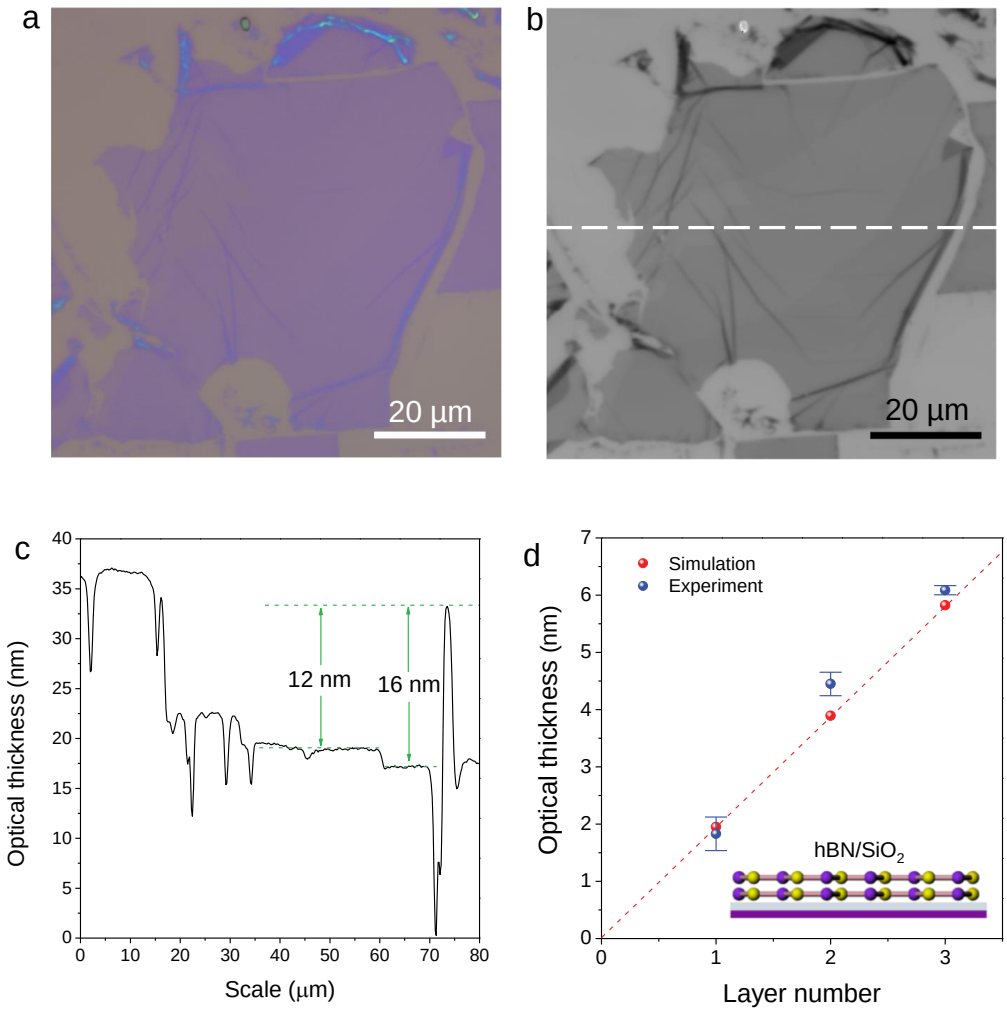

Figure S2 PSI characterization of few-layers hBN sample. a, Optical microscope image of few-layer hBN sample prepared by mechanical exfoliation. b, PSI image of the same hBN sample in a. c, PSI measured optical thicknesses along the dashed line in b. The layer number of the hBN is estimated as 6 to 8 layers. d, Optical thicknesses for 1L to 3L hBN samples from both simulation (red sphere) and experimental PSI measurements (blue sphere with error bar). The red dash line is the linear fit for statistical data measured with the PSI system.

3. InGaAs detector efficiency calibration and collection efficiency estimation.

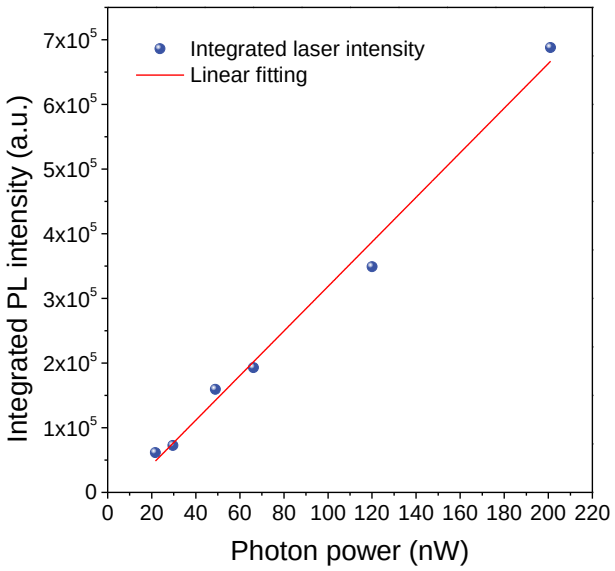

Figure S3 InGaAs detector efficiency calibration by using a 1.17 eV laser diode. Dark blue spheres represent integrated counts collected by detector under different photon power emitted by the laser diode. The red solid line is a linear fit.

Quantum efficiency is defined as the number of photons emitted with respect to the number of injected electron-hole pairs, *Ne*/*I*, where *N* is the number of emitted photons per second, *e* electron charge, *I* is the current passing through collection area.[1, 2] In order to estimate the number of emitted photons we need to estimate collection efficiency. The total loss is defined as:

$$\eta = \eta_{lens} \cdot \eta_{optic} \cdot \eta_{system}$$

η_{optic} is the loss when emitted light passes through all components in the optical circuit. We use a 1060 nm laser diode and a power meter to measure the total loss in the optical circuit. The η_{optic} in our system is estimated to be 0.194.

η_{system} is the loss of photons which pass through slit and grating into the InGaAs detector. By recording spectrum of the 1060-nm laser diode at different power, we

can get detector counts as a function of the laser power (Figure S3). For our detector, we have 3447 integrated counts/sec/nW. Considering increasing 1 nW for the 1060-nm laser corresponds to 5.33×10^9 photons and ND3 filter is used to reduce laser power, the actual injected photons are 5.33×10^6. Therefore, our system efficiency will be $\eta_{system} = 3447/5.33 \times 10^6$, which is 6.46×10^{-4}.

η_{lens} is the lens collection efficiency.[3] Our objective lens is 50x with a numerical aperture (NA) of 0.55. The monolayer $MoTe_2$ is fully encapsulated under few layers hBN with refractive index n = 2.2.[4]

$$\eta_{lens} = \frac{1}{4\pi}\int_0^{2\pi} d\varphi \int_0^{\arcsin(\frac{NA}{n})} d\theta \, sin\theta = \frac{1}{2}\left[1 - \sqrt{1 - (\frac{NA}{n})^2}\right] = 0.016$$

Our total efficiency $\eta = \eta_{lens} \cdot \eta_{optic} \cdot \eta_{system} = 2 \times 10^{-6}$.

4. PL spectra of monolayer $MoTe_2$ sample and pure SiO_2/Si substrate.

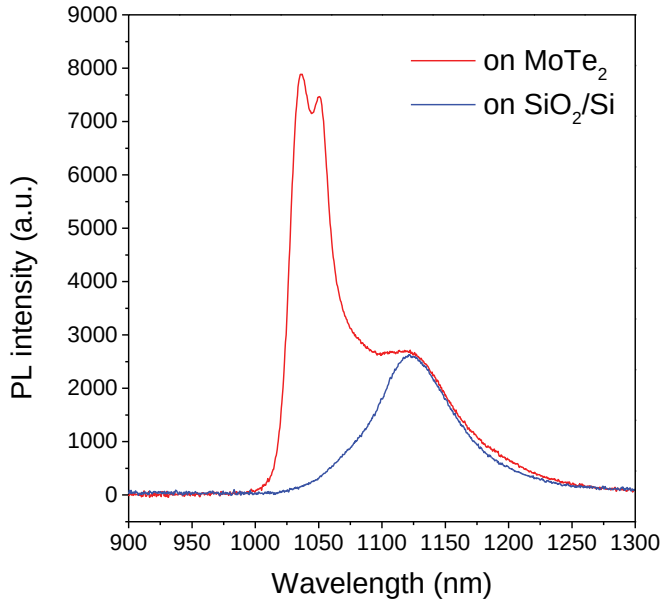

Figure S4 PL spectra on monolayer $MoTe_2$ sample and SiO_2/Si substrate, indicating that the broad peak is from Si.

5. Monolayer $MoTe_2$ LED operation I-V curve at 83 K.

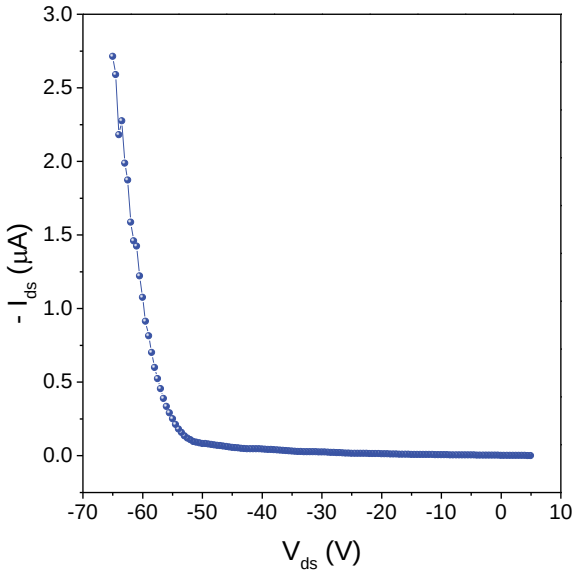

Figure S5 Monolayer $MoTe_2$ LED device working I-V curve at 83 K.

6. Direct tunneling and Fowler-Nordheim tunnelling.

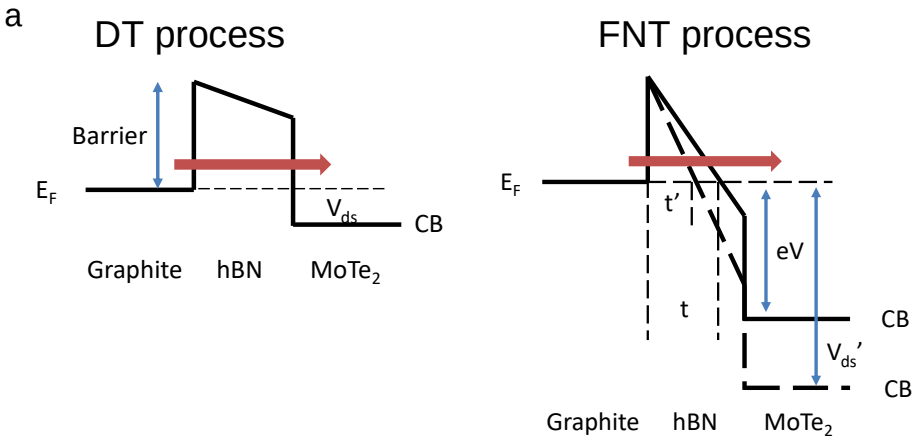

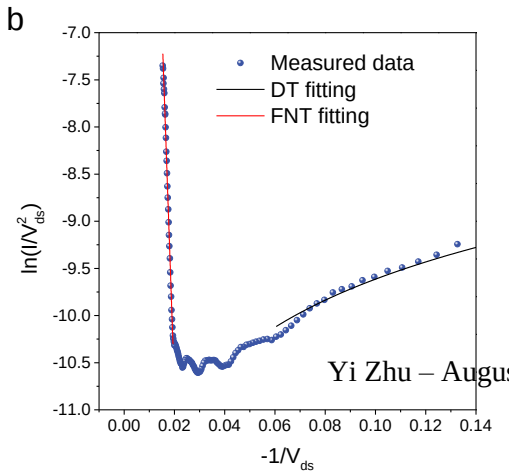

Figure S6 a, Schematic band diagram of the direct tunneling (DT) and Fowler-Nordheim tunneling (FNT). b, DT and FNT fitting of the measured I-V curve in Figure S5.

Figure S6a presents the band diagrams of graphite/hBN/$MoTe_2$ heterojunction under low and high voltage bias. The direct tunneling process occurs at low voltage regime, while Fowler-Nordheim tunneling process dominates at high voltage regime. When the applied voltage is smaller than the barrier height, electrons from graphite tunnel into $MoTe_2$ layer via a trapezoidal barrier (Figure S6 left). The barrier thickness keeps constant all the time, leading to constant current injection efficiency. This process corresponds to the direct tunneling (DT) with an equation:

$$I_{DT}(V) = \frac{A_{eff}\sqrt{m\varphi_B}q^2V_{ds}}{h^2d}exp\left[\frac{-4\pi\sqrt{m^*\varphi_B d}}{h}\right]$$

A_{eff}, φ_B, q, m, m^*, d and h are effective contact area, barrier height, electron charge, free electron mass, effective electron mass, barrier width, and Plank's constant, respective.

When the applied voltage is larger than the barrier height, the trapezoidal barrier changes into the triangular barrier. The barrier thickness will become narrower as applied voltage increases. As a consequence of that, the injection current exponentially increases (Figure S6 right). This process is Fowler-Nordheim tunneling (FNT) and can be expressed by the equation:

$$I_{FNT}(V) = \frac{A_{eff}q^3m{V_{ds}}^2}{8\pi h\varphi_B d^2m^*}exp\left[\frac{-8\pi\sqrt{2m^*}\varphi_B^{\frac{3}{2}}d}{3hqV_{ds}}\right]$$

In our device, the I-V curve shows in Figure S5 can be simulated by above models.[5, 6] To better fit FNT model, we change FNT equation to:

$$\ln\left(\frac{I_{FNT}(V)}{{V_{ds}}^2}\right) = \ln\left(\frac{A_{eff}q^3m}{8\pi h\varphi_B d^2 m^*}\right) - \frac{8\pi\sqrt{2m^*}\varphi_B^{\frac{3}{2}}d}{3hqV_{ds}}$$

The experimental data match well with the fitting curves of the DT and FNT models. In the FNT regime, the $\ln\left(\frac{I_{FNT}(V)}{{V_{ds}}^2}\right)$ will decrease linearly with $\frac{1}{V_{ds}}$, while logarithmic behaviour in the DT regime.

7. Sample degradation as fabrication process and time evolution.

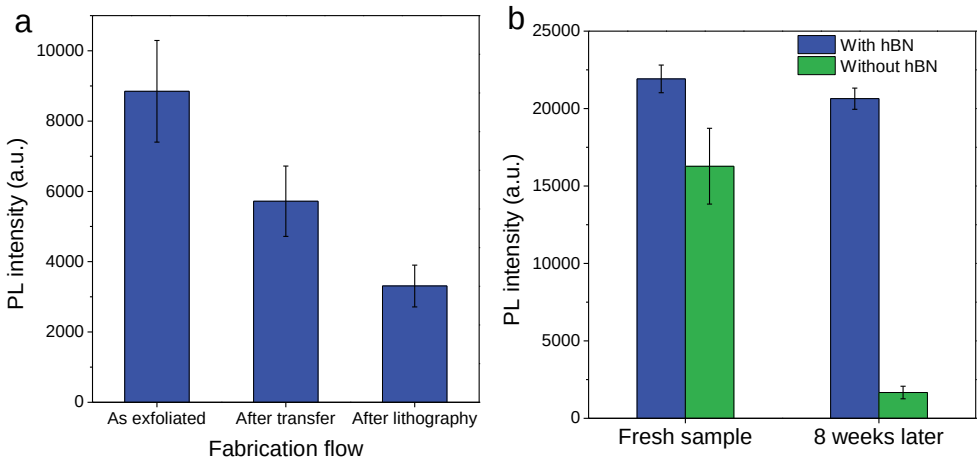

Figure S7 PL degradation as fabrication process and time evolution. a, PL intensity of the monolayer $MoTe_2$ sample after a series of the fabrication process. b, Stability comparison of the monolayer $MoTe_2$ samples with and without hBN capping layer.

In addition to the monolayer $MoTe_2$ devices presented in the main text, here we show some other monolayer $MoTe_2$ samples and their PL behaviour under different fabrication and environmental conditions. Figure S7 left panel shows the PL intensity evolution during the different fabrication process. As we can see, the freshly exfoliated monolayer samples achieve high PL intensity indicating the high sample quality and surface cleanness. Here we use wet chemical transfer method to peel off samples and relocated on another SiO_2/Si substrate. The PL intensity decreased 30%, suggesting that samples have been contaminated by organic solution used for removing polymer residuals. Following transfer, samples were prepared for the lithography process. After lithography, the PL intensity further decreased to around

30% of that of freshly exfoliated samples. PL behaviour clearly reflects that samples quality will be seriously affected by external contamination and thus influence their optical properties. Figure S7 right panel presents the time evolution of the PL intensity from monolayer $MoTe_2$ samples protected and unprotected by hBN capping layers. In this PL tracking experiment, samples covered by hBN show nearly the same PL intensity as fresh samples even after 8 weeks exposed to air at room temperature. For those samples without hBN encapsulation, PL intensity significantly dropped to only few hundred counts. Here, we also notice that monolayer $MoTe_2$ samples with hBN capping layers show higher intensity than those without hBN layers, indicating that hBN layers effectively change the $MoTe_2$ doping level and reduce non-radiative decay channels due to their defects.[7-9]

8. Relaxation pathway for photo-excited carriers.

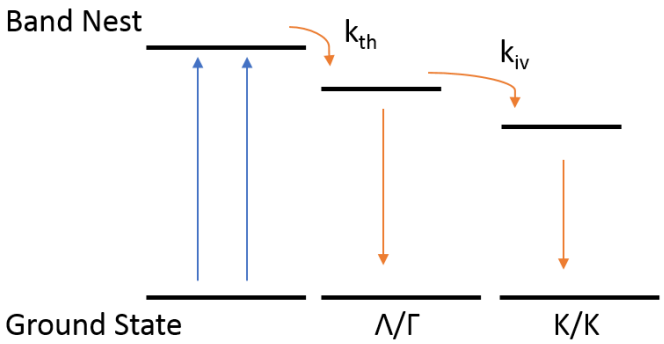

Figure S8 Relaxation pathways for photo-excited carriers. K_{th} indicates intravalley thermalization process. K_{iv} indicates intervalley scattering process.

9. Band diagram of state 5 and 6 in main text figure 3a.

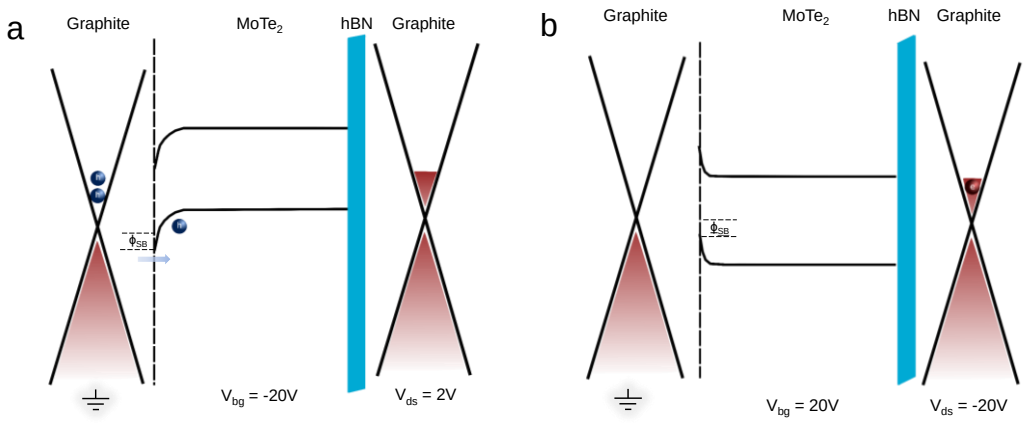

Figure S9 Band diagram of state 5 and state 6. a, Band diagram of the device operating in state 5 (V_{bg} = -20V, V_{ds} = -2V) in figure 3a. b, Band diagram of the device operating in state 6 (V_{bg} = 20V, V_{ds} = -20V) in figure 3a.

9. Device stability and statistics.

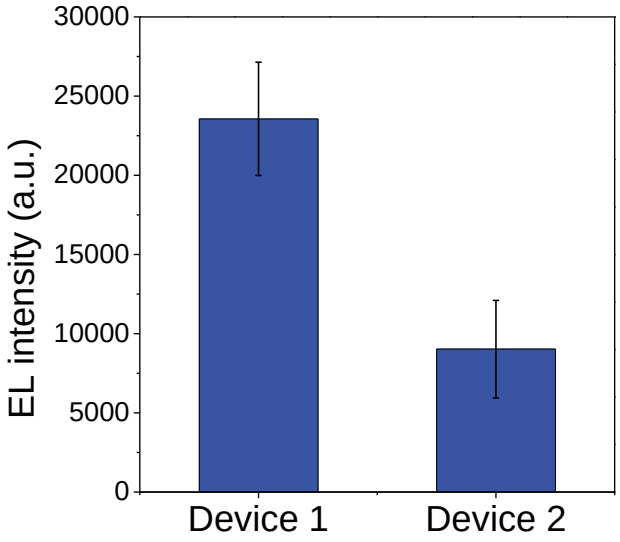

Figure S10 Device stability and statistics. EL measurement of two different devices. All EL was measured at 83 K with same injection current. The error bars represent the measurement variation from different date within 2 months after fabricated.

Supporting Note 1. Device fabrication

To prepare the vertical LED structure, the hBN and $MoTe_2$ flakes were mechanically exfoliated onto the SiO_2/Si substrate pre-treated by oxygen plasma.[10] For device application, we selected 8 to 10 layers hBN flakes with a large area and flat surface. One yellow light source (~590 nm) has been used to replace the white light source of the microscope to achieve maximum optical contrast in identifying thin-layer hBN flakes.[4] Later, the monolayer $MoTe_2$ and thin-layer hBN flakes were confirmed by PSI.[11] After collecting suitable materials, we used the modified drily transfer method to vertically stack these thin flakes.[12, 13] Here, polydimethylsiloxane (PDMS) mixed solution (1:10 mix ratio) was directly dropped onto a microscope glass slide. And then, a polypropylene carbonate (PPC) film was transferred to the PDMS glass

slide. It is essential to use oxygen-plasma treated PDMS glass slides before transferring the PPC layer, which will significantly increase the adhesion between the PPC and PDMS. The hBN and graphite transfer process were carried out by a homemade transfer platform with a Peltier plate to control the temperature. In our device, the monolayer $MoTe_2$ is bottom placed, and thus we only need transfer few-layer hBN and graphite flakes. When the PPC film fully touched hBN layers, a high temperature of 120 ˚C is applied to increase adhesion between PPC and hBN layers. Once the temperature drops to 40 ˚C, the PDMS glass slide was lifted as fast as possible. The faster the detaching, the easier hBN layers can be peeled off. For drop-down process, PDMS glass slide should rise as slow as possible to ensure that hBN layers stayed with the monolayer $MoTe_2$. The same process was used to transfer graphite. The contact electrodes were prepared by using Au transfer method.[14] Photolithography, metal deposition (100nm, Au), and lift-off processes were used to prepare gold bars on another SiO_2/Si substrate. We used micromanipulator with a probe tip to cut gold bars into our designed length. The cut gold bars were then peeled off and transferred onto our device by a needle with 1 micro diameter tungsten tip. This Au transfer method gives an ultra-clean interface between material and metal, which could enhance device performance. Particularly, the method is perfect for organic materials that react with photoresists and organic solvents. However, the complicated steps and operation of micro-manipulator increase the difficulty of fabrication flow. Moreover, the relatively larger size sample is required for alignment of Au electrodes owing to the uncertainty of operating micro-manipulator. Therefore, employment of this method has been further limited.

Supporting Note 2. Band nesting

The photocarrier relaxation pathway is illustrated in Figure S8. When the excitation wavelength is in resonance with the band nesting energy, the system will be initially excited from the ground state to the band nesting excited state. Later, a large fraction of these excited carriers will thermally relax to Λ/Γ state, many of which will also scatter intervalley to the lowest excited state (K/K) and then radiatively recombine, leading to the resonate peak at 1.05 eV. The radiative and non-radiative decay channel exists either at Λ/Γ state or K/K state. To obtain high photoresponsivity, it is necessary to achieve high radiative recombination rate and to suppress the non-

radiative process, which is normally a fast process. Hence, it is crucial to extend the lifetime of photoexcited carriers before they are collected by electrodes. The monolayer $MoTe_2$ sample in our photodetector is fully encapsulated by a few-layer hBN flake, which could effectively passivate the MoTe2 surface and reduce non-radiative decay channels (Figure S7).[15-17] Therefore, our photodetector shows two strong resonate peaks at 450 nm and 1145 nm.

Supporting Note 3. Band diagram of state 5 and state 6 in main text figure 3a

In state 5, the device is under a -20 V back-gate voltage (V_{bg} = -20 V), and a small SB forms between the graphite and $MoTe_2$ (Figure S9a). Such small SB directly causes a small current flow through the device when a small bias is applied in another graphite electrode. By further increasing V_{ds}, more holes will be injected into the $MoTe_2$ monolayer. However, available hole density states in the counterpart graphite electrode decreases as the E_F of graphite raises. The above two behaviors will eventually reach an equilibrium, resulting in the small constant current across a large negative voltage range in main text Figure 3a. In state 6, as illustrated in Figure S9b, there is no current in the device when E_F of the graphite is located between E_C and E_V of the monolayer $MoTe_2$.

Supporting Note 4. Thermal effect on photodetector measurement

Seebeck effect has been widely found in traditional semiconductors, which might affect optoelectronic devices. Concerning this effect on our photodetector measurements, some threshold calculations have been done to exclude it. The temperature change of our photodetector device after each measurement would not go beyond 100 degrees Celsius. Considering worst scenario, we assume temperature change on our device has reached 100 degrees Celsius. Based on published results, the 2H-$MoTe_2$ has been found a Seebeck coefficient of -385 μV/K at room temperature.[18] Therefore, the maximum voltage change is only 0.0385 V, which is a very small value compared to our testing voltage.

Supporting Note 5. Less trion contribution in EL spectrum compared with PL spectrum

In main text figure 1d, less trion contribution is observed in EL spectrum compared with Pl spectrum. Typically, the monolayer $MoTe_2$ sample is intrinsic neutral and doping level is very low compared with other 2D material, such as monolayer MoS_2. Therefore, electrically injection electrons or holes could lead to a significantly transition between exciton and trion. However, the initial doping level could be slightly changed in our monolayer $MoTe_2$ after LED fabrication flow. In our measurement, the PL spectrum was measured without applying any gate bias, while EL spectrum was collected under back gate at negative 20 V. This gate voltage could neutralize initial doping of $MoTe_2$ to decrease the trion contribution in EL spectrum.

Reference

1. F. Withers *et al.*, Light-emitting diodes by band-structure engineering in van der Waals heterostructures. *Nat Mater* **14**, 301-306 (2015).
2. F. Withers *et al.*, WSe(2) Light-Emitting Tunneling Transistors with Enhanced Brightness at Room Temperature. *Nano Lett* **15**, 8223-8228 (2015).
3. T. Mueller *et al.*, Efficient narrow-band light emission from a single carbon nanotube p-n diode. *Nat Nanotechnol* **5**, 27-31 (2010).
4. R. V. Gorbachev *et al.*, Hunting for monolayer boron nitride: optical and Raman signatures. *Small* **7**, 465-468 (2011).
5. J. G. Simmons, Generalized Formula for the Electric Tunnel Effect between Similar Electrodes Separated by a Thin Insulating Film. *Journal of Applied Physics* **34**, 1793-1803 (1963).
6. Q. A. Vu *et al.*, Tuning Carrier Tunneling in van der Waals Heterostructures for Ultrahigh Detectivity. *Nano Lett* **17**, 453-459 (2017).
7. M. Buscema, G. A. Steele, H. S. J. van der Zant, A. Castellanos-Gomez, The effect of the substrate on the Raman and photoluminescence emission of single-layer MoS2. *Nano Research* **7**, 561-571 (2015).
8. D. Kozawa *et al.*, Photocarrier relaxation pathway in two-dimensional semiconducting transition metal dichalcogenides. *Nat Commun* **5**, 4543 (2014).
9. K. F. Mak, K. He, J. Shan, T. F. Heinz, Control of valley polarization in monolayer MoS2 by optical helicity. *Nat Nanotechnol* **7**, 494-498 (2012).
10. Y. Huang *et al.*, Reliable exfoliation of large-area high-quality flakes of graphene and other two-dimensional materials. *ACS nano* **9**, 10612-10620 (2015).
11. J. Yang *et al.*, Optical tuning of exciton and trion emissions in monolayer phosphorene. *Light: Science & Applications* **4**, e312 (2015).
12. F. Pizzocchero *et al.*, The hot pick-up technique for batch assembly of van der Waals heterostructures. *Nature communications* **7**, (2016).
13. P. Zomer, M. Guimarães, J. Brant, N. Tombros, B. Van Wees, Fast pick up technique for high quality heterostructures of bilayer graphene and hexagonal boron nitride. *Applied Physics Letters* **105**, 013101 (2014).
14. Y. Zhang *et al.*, Probing carrier transport and structure-property relationship of highly ordered organic semiconductors at the two-dimensional limit. *Physical review letters* **116**, 016602 (2016).
15. D. Kozawa *et al.*, Photocarrier relaxation pathway in two-dimensional semiconducting transition metal dichalcogenides. *Nature communications* **5**, 4543 (2014).
16. K. F. Mak, K. He, J. Shan, T. F. Heinz, Control of valley polarization in monolayer MoS 2 by optical helicity. *Nat. Nanotechnol.* **7**, 494 (2012).
17. M. Buscema, G. A. Steele, H. S. van der Zant, A. Castellanos-Gomez, The effect of the substrate on the Raman and photoluminescence emission of single-layer MoS 2. *Nano research* **7**, 561-571 (2014).
18. K. Ikeura, H. Sakai, M. S. Bahramy, S. Ishiwata, Rich structural phase diagram and thermoelectric properties of layered tellurides Mo1− x Nb x Te2. *APL materials* **3**, 041514 (2015).

6. High efficiency monolayer WS_2 AC Driven LED via An Unsymmetrical Pulsed Carrier Injection

In the previous chapter, we have introduced a monolayer $MoTe_2$ LED device, which is driven by direct current (DC). In this chapter, we will extend our discussion to the alternative current (AC) driven LED device based on monolayer WS_2. To date, the understanding of the working principle of AC LED devices is still not fully explored. The potential ability of this AC injection method is still undeveloped. Here, we further discuss the AC driving ability and demonstrate an ultra-long electroluminescence emission length AC LED by an unsymmetrical pulsed carrier recombination mechanism, which is induced by the initial doping in the emitting material. This mechanism helps to increase the EL intensity and emission area for the AC LED. Time resolved electroluminescence and temperature dependent time resolved electroluminescence measurements confirmed that the unsymmetrical pulsed carrier recombination is caused by initial doping of TMDs. Based on the doped sample, we observed the wavelength tunable EL emission under low temperature, which can be tuned between the exciton, trion emission, and the defect emission. The quantum efficiency of defect EL emission is 24.5 times larger than free exciton and trion EL emission. By taking advantage of the sperate carrier injection in the AC driving LED, we have successfully distinguished the different defect emissions and their evolution in real space. Those defects are assigned to be negatively charged sulfur vacancies. The results in this chapter provide crucial insights into optimizing the performance of AC driving LED devices for future practical applications and open a new route to study the defect states and defect engineering for the tunable LED device.

6.1. Introduction of monolayer TMDs based AC driven LED devices

Recently, layered transition metal dichalcogenides (TMDs), especially in their monolayer status, have attracted considerable interest for their unique electronic and optical properties.[1-3] The monolayer WS_2 and WSe_2 exhibit a direct bandgap with strong photoluminescence and are of particular interest for novel optoelectronic devices such as a light emitting diode (LED).[4, 5] In previous work, the direct current (DC) injection LED was obtained in TMDs by forming a p-n junction *via*

electrostatic doping.[5] Alternatively, the complex vertically stacked heterostructures using hexagonal boron nitride tunnel barriers have also been demonstrated. [4, 6] However, the complicated device structures and long fabrication process further limit the application of this DC driving LED. As the counterpart of the DC driving LED, the alternating current (AC) driving LED has attracted more attention recently.[7] Compared to DC structured LED, the AC LED only uses a two-terminal capacitor structure *via* a single metal semiconductor contact, which has intensively reduced fabrication difficulty. More importantly, unlike the working principle of DC LED which electrons and holes are injected into the system at the same time, the EL emission from AC LED is achieved by injecting electrons or holes separately under different AC voltage polarities. Then those new injected carriers radiatively recombine with remaining carriers of opposite sign in the material. This separate injection feature opens a fantastic way for us to probe the EL emission pathway and the carrier dynamic down to each injection cycle. By understanding this EL emission pathway and the carrier dynamic behavior, it provides us an insight into engineering and improving the performance of AC LED devices on the one hand. On the other hand, it also serves as a good opportunity to explore some special energy states such as different defect states, which are normally not dominated in photoluminescence (PL) measurement.

Currently, the strong EL emission from two-dimensional material based AC LED has been achieved.[7] However, the EL emission area is usually small and limited alone to the electrode contact in the undoped monolayer material. Time resolved EL measurement shows two similar and short EL decays appearing when AC voltage polarity changes. This drawback requires a very dense electrodes pattern when it is deployed to large scale applications. It becomes a bottleneck for future development in AC LED structure. To overcome this issue, a longer EL emission decay is required for increasing emission area. One possible solution could be increasing the doping level in the optical active material. In monolayer TMDs, the optical properties can be easily manipulated by tuning the initial carrier doping *via* many methods such as electrostatic doping and chemical doping.[8, 9] The strong PL is identified to exist in neutral TMDs monolayer samples. Several researches have claimed that with increasing initial doping in the monolayer, the PL emission could get weaker. [10, 11]

However, the effect of initial doping to electroluminescence emission in monolayer TMDs material has not been extensively studied. In this work, taken an advantage of the AC LED structure, we have demonstrated an ultra-long electroluminescence emission length in AC driving LED devices through an unsymmetrical pulsed carrier recombination mechanism. Contrary to the doping effect in PL emission, we will show that the initial doping in EL emission plays a positive role in increasing the emission area in AC LED devices. We present the emission area in our sample along one direction is measured as 3 times longer than the previous reported value.[7]

Solid-state defect engineering has been demonstrated to be an important technique to modulate the properties of semiconductors for various applications.[12, 13] Particularly, defect engineering in two-dimensional (2D) materials is critical and promising for the development of novel optoelectronic devices, such as defect LED[14] and single photon emitter.[15] Raman and PL spectroscopy are usually used to explore different types of defects. For TMDs, some new Raman peaks appear and their intensities are related to the density of defect, but the sensitivity is not very high.[16] At the same time, in low temperature PL measurement, defects related PL peaks could be observed due to the emission of excitons bound to the defect states, which could be used to monitor the number of defects in TMDs.[17, 18] However, those defect PL peaks are usually not dominated due to the optical pumping efficiency. Moreover, the PL spectroscopy is hard to give more detailed information on defect emission and defect carrier dynamic. Comparing to optical pumped PL spectroscopy, the AC driving EL emission spectroscopy is an excellent tool to study the defect carrier dynamics. Thanks to the feature of separate injection of electrons and holes, it provides a unique window for us to see and distinguish defect species, defect states evolution and ultra-high defect emission quantum efficiency. Here, we have demonstrated a novel way to probe the different defect states in monolayer WS_2 by using the AC driving WS_2 LED platform. In this AC driving LED, we have observed the wavelength tunable EL emission, which EL wavelength is switching from exciton and trion emission to defect emission. Moreover, we have resolved and visualized two different types of defects and the evolution of them in the WS_2 monolayer sample. The quantum efficiency of defect EL emission is 24.5 times larger than free exciton and trion EL emission. Our results provide crucial insights

into optimizing the performance of AC driving LED devices for future practical applications and open a new route to study the defect states and defect engineering for the tunable LED device.

6.2. Symmetrical and unsymmetrical pulsed carrier recombination mechanism

Figure 6.1 a shows an EL emission spectrum that is comparable with its PL spectrum. The LED device structure is schematically depicted in Fig. 1a inset. In device fabrication, a mechanically exfoliated monolayer WS_2 flake was dry transferred onto a SiO_2/Si substrate (275nm thermal oxide on n^+-doped silicon), in contact with a gold electrode that was peel-transferred onto monolayer sample.[19, 20] A part of the monolayer WS_2 was under the gold electrode and the other part on the SiO_2 substrate. The large area light emission can be observed from Figure 6.1 b, where an optical microscopy picture of the sample presented in the inset. Figure 6.1 c shows the emission profile along the solid white line in Figure 6.1 b. Here we define this lateral emission region length as the EL emission length. This EL emission length is the distance value of full width at half maximum of EL emission profile. In the previous report, the AC driving LED EL emission was only observed near the source contacts and the emission region laterally extended from the contact edge by around 3 μm.[7] In our recorded device, we have demonstrated an ultra-long EL emission length of 9.08 μm, which is 3 times larger than previously reported value as depicted in Figure 6.1 c. In order to understand this ultra-long EL emission, time resolved electroluminescence (TREL) measurements have been performed. At room temperature, the time resolved EL signals and their corresponding alternating driving voltage traces from the WS_2 LED device and the WSe_2 LED device are presented in Figure 6.1 d and Supplementary Figure. S5b, respectively. The driving voltages are $\pm$ 6.6 V for WS_2 LED and $\pm$ 10 V for WSe_2 LED. The driving frequencies are both 500 kHz. Firstly, two identical EL decay curves that are starting from both voltage rising and falling edges can be observed from both WS_2 and WSe_2 LED depicted in Figure 6.1 d and Figure S5b. These two decay components are exactly the EL origin of this type of AC driving LED device, which is consistent with the previous report.[7] In the monolayer WSe_2 LED device, two EL decay curves with the same decay shape emerge at both voltage rising and falling edges. The fast switching AC driving voltage causes WSe_2 band bending at the Schottky contact, leading to large transition

currents. New injected carriers (electron or hole) meet with the opposite type of carriers (hole or electron) that are accumulated in the previous cycle. Then those excess electrons and holes form excitons, therefore, result in pulsed light emission as presented in Figure S5c schematic plots. Owing to the similar shapes and the same origin in these two EL decay curves, this type of emission can be considered as a symmetrical carrier recombination. However, in Figure 6.1 d, these two EL decay curves from the WS_2 LED device have dramatically different shapes, indicating the different carrier recombination process, namely an unsymmetrical carrier recombination processes.

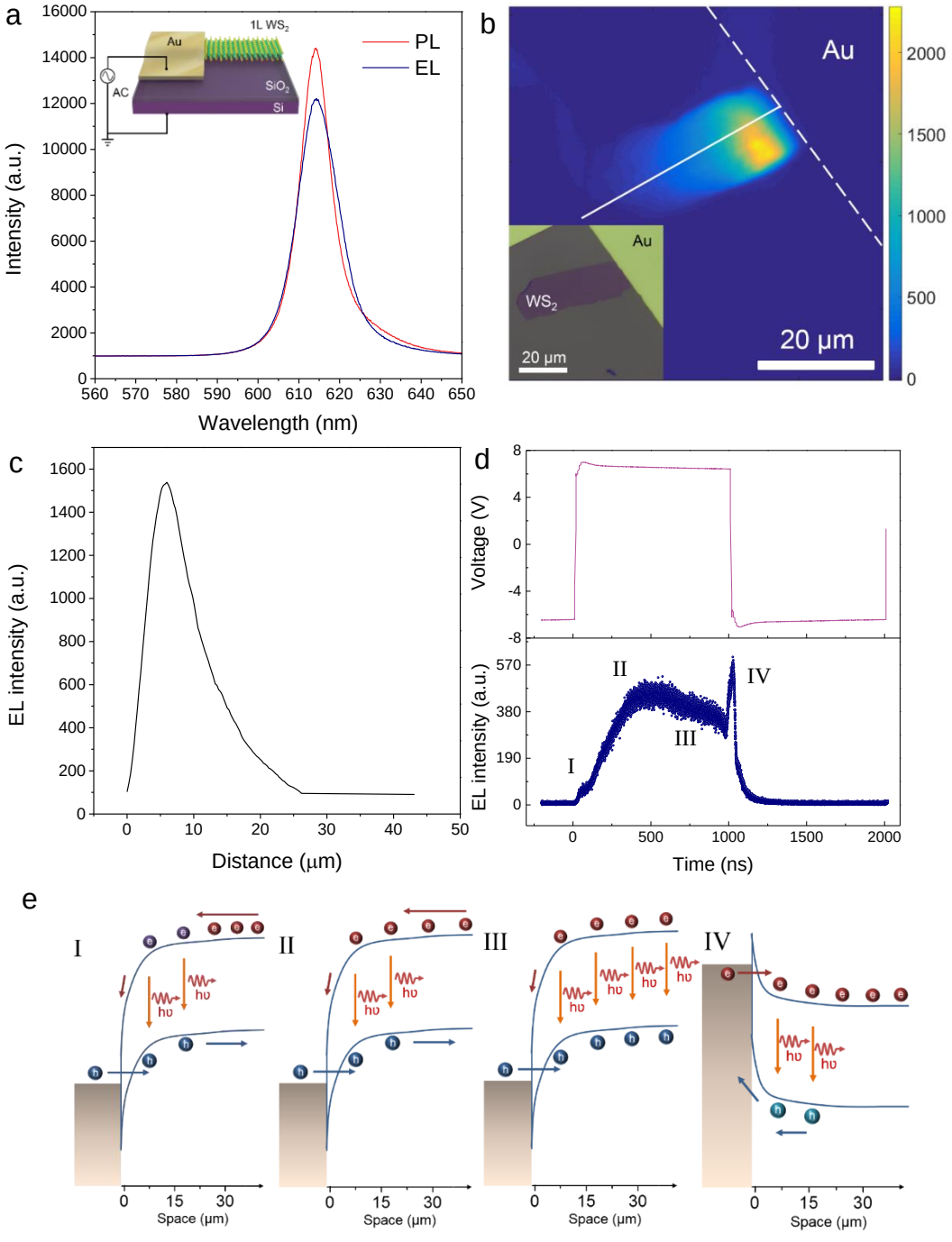

Figure 6. 1 Monolayer WS_2 LED devices with large area and ultra-long EL emission length at room temperature and the principle of the unsymmetrical pulsed carrier injection. a, EL and PL spectra measured for monolayer WS_2 devices (V_{ac} = 7.5 V at 500 kHz). Inset: the schematic of AC LED devices. b, EL mapping of the recoded WS_2 AC LED device with a large-area and the longest EL emission length (V_{ac} = 7.5 V at 500k Hz). The white dashed line indicates the contacted edge of the gold electrode. Inset: the optical image of this WS_2 device. c, EL emission profile along the solid white line shown in b. d, Time-resolved electroluminescence and the corresponding driving voltage trace for WS_2 AC LED device. Two different decay behaviours indicate the unsymmetrical carrier recombination process at two voltage transients. e, Schematic band diagrams corresponding to four emission stages labelled as I, II, III and IV in d.

To explain this unsymmetrical recombination process, the entire EL decay curve has been divided into four sections labeled as I, II, III and IV in Figure 6.1 d. The corresponding schematic band diagrams are illustrated in Figure 6.1 e. The reason for the unsymmetrical carrier recombination can be attributed to the initial doping of monolayer TMDs. Normally, the monolayer WSe_2 sample shows neutral initial doping which results in WSe_2 based field-effect transistors exhibiting ambipolar characteristics.[21, 22] The Fermi energy of WSe_2 is close to the mid gap due to large chalcogen vacancy formation energy. [23] The free electrons or holes are mainly forming by accumulating in the previous cycle. However, the monolayer WS_2 sample shows intrinsic n-type doping because of its natural Sulfur vacancy or halides substitutions during the growth process.[24] The doping level of monolayer WS_2 used in LED devices can be estimated to be $7.5 \times 10^{11}\ cm^{-2}$ by using gate dependent PL spectra. The estimated value matches very well with the crystal factory specifications. The detailed calculations are provided in the Supplementary Note 1. In our LED structure, the back gate is grounded. When the AC driving voltage is on the rising edge or positive values, the device is injected with holes (holes injection side). Oppositely, the device is injected with electrons if the voltage is on the falling edge or negative values (electrons injection side). In our WS_2 AC LED devices, the origin of section I and IV in the decay curve is similar with the decays in WSe_2 LED. In section I, the driving voltage is quickly switched from negative 6.6 V to positive 6.6

V. The energy band is bending upwards, leading a large number of holes injected into WS_2 samples. The new injected holes recombine with remaining electrons that are left by the previous cycle. Those electrons are different from electrons that comes from intrinsic initial doping as labeled with purple color in Figure 6.1 e panel I. Those remaining electrons quickly move to the electrode contact after the AC voltage is switched. Then they meet with fresh injected holes, resulting in fast and small EL emission at the beginning of the first decay. Now if the applied AC voltage suddenly change its polarity, then it will cause cut off the decay curve and emerges a second EL decay marked as IV. In Figure 6.1 e panel IV, the falling edge and negative voltage value quickly bend energy band downwards, causing electrons injection while holes exiting. Due to the nature of the initial n-type doping in the material, the free holes in the WS_2 monolayer are mainly left by the previous cycle labeled with cyan color. The large population of the injected electrons could rapidly capture and radiatively recombine with those free holes, rising a short and intensive emission pulse. After the depletion of free holes, no more light emits even if electrons keep injecting. In this case, the light emission area is very close to the Au contact edge again because electrons and holes will firstly meet in this area.

The section II and the section III belong to the main part of first decay, where the EL intensity is constantly increasing to the maximum followed by a long and slow decay. In the section II, the driving voltage is stabilized at 6.6 V, the holes are continuously injecting into the material. Due to the intrinsic n type doping nature, the injected holes could find excess electrons to form excitons and emitting light as illustrated in Figure 6.1 e panel II. Because of the n-type doped material, there are a lot of free electrons in the conduction band. The population of injected holes is far less than those initial free electrons. With more holes inject into the system, the EL emission is steadily increasing. The emission now is closed to the Au contact edge. In the section III, the injected holes will diffuse inward accompanying with radiative recombination until they reach their longest diffusion length. Therefore, the emission area is extending inward from Au contact edge to the far end, and finally it generates an ultra-long emission length as depicted in Figure 6.1 e panel III. Meantime, the EL intensity reaches its maximum and then slowly decays. During this process, the Au contact could continuously provide holes into the system to compensate holes

consumption. This causes an almost flat decay curve and an ultra-long decay lifetime. Here, the EL decay curve can also describe the EL emission time. Thus, this EL decay lifetime can be approximated to EL emission lifetime. Actually, this EL emission lifetime could be further longer if the AC frequency is decreased (Supplementary Figure S4). The longest EL emission lifetime in our WS_2 AC LED device is ~1980 ns when AC frequency is 200 kHz, indicating extremely high crystal quality and non-contamination device fabrication method (Supplementary Note 2). Now, if we define the section I and IV as a fast decay process while section II and III as a slow decay process, the relationship between fast decay and slow decay can be established as presented in Supplementary Figure S6. The integrated EL intensities from fast and slow decay components as a function of AC frequency have been extracted in Figure S6a. The total contribution of EL intensity from the fast decay component does not change when the frequency increased. However, the EL intensity from slow decay dramatically increases as frequency increased. It suggests that the slow decay component plays a significant role in the EL emissions in WS_2 AC LED devices. Now, by comparing TREL behaviors in monolayer WS_2 and monolayer WSe_2 sample, we can understand the origin of this symmetrical and unsymmetrical carrier recombination processes. It can be contributed from two facts: 1. new injected electrons (or holes) radiatively recombine with the remaining holes (or electrons) that are accumulated in the previous cycle; 2. new injected electrons (or holes) recombine with system initial free holes (or electrons). On the one hand, if the initial doping of the material is small, the population of system free carriers becomes small then the first fact dominates EL emission. The TREL decay behavior is symmetrical. On the other hand, if the initial doping of the material is large, the population of initial free carriers is large, leading the EL emission is dominated by the second fact. The TREL decays are unsymmetrical.

In order to justify this AC driving EL emission model, we performed two more TREL measurements in this WS_2 LED device to verify the influence of the material's doping effect. The measurement conditions for those two tests are kept the same. After the TREL measurement on the fresh exfoliated WS_2 LED device, then this LED device has been treated by the p-type chemical dopant. We used 7,7,8,8 – tetracyanoquinodimethane (TCNQ) as the p-type dopant to modulate initial doping

levels in the monolayer WS_2 sample as previously reported.[9] The TCNQ solution preparation and sequential doping method have been described in the Supplementary Note 3. Interestingly, the TREL decay curves can be significantly tuned as elucidated in Supplementary Figure S7. When the monolayer WS_2 sample has not been treated by TCNQ, the initial doping is n-type and the material has more electrons. In the holes injection side, a long and flat decay curve can be obtained. However, this long and flat decay curve from the holes injection side has been suppressed after the TCNQ treatment. With the treatment of p-type dopants, electrons in the monolayer WS_2 have been neutralized causing the decrease of initial doping level where free electrons in the system dramatically decrease, leading to a strong reduction of EL emission lifetime. This has confirmed that the material's initial doping is favor for unsymmetrical recombination processes in this AC driving LED structure. This provides us an opportunity to enhance the EL emission area and EL performance by tuning the material's doping level.

6.3. Temperature dependent EL emission length

Normally, the initial doping comes from thermal activated free carriers. They should be very sensitive to temperature. In order to further prove that the initial doping plays a crucial role in this unsymmetrical EL emission model, temperature dependent EL mappings and TREL measurements are performed. In Figure 2 a-d, we show the EL emission mapping of the monolayer WS_2 as a function of temperature. The driving voltage and frequency are kept the same at V_{ac} = 7.5 V and 500 kHz, respectively. A very clear trend of EL quenching and emission area shrinking toward the Au electrode can be observed when the temperature is decreasing. The cross-section profiles of EL emission along the solid white line under 290 K and 80 K have been extracted in Figure 6.2 e and f. The EL emission length is decreasing from 5.822 μm at room temperature to 0.016 μm at 80 K. The shrinking factor can be as high as 363.9 times in this scenario. The temperature dependent EL emission length can be extracted in Figure 6.2 g. The corresponding EL emission mapping images are presented in Supplementary Figure S8. The emission length is firstly saturated when the temperature is higher than 230 K. Those saturated emission lengths might result from the dimensional limitation of the sample size. When the temperature has further decreased below 230 K, the emission length is dramatically decreasing. The

measured data can be perfectly fitted by the traditional temperature dependent carrier mobility model indicated in Figure 6.2 g red curve. In this AC driving LED structure, the injected carriers firstly tunnel through the air barrier under the Au electrode into the monolayer WS_2 sample. Then those accumulated carriers laterally diffuse inward the monolayer WS_2. Therefore, the emission length is highly related to carrier diffusion ability as well as mobility. Considering the emission principle that has been discussed earlier, the hole diffusion length will be proportional to emission length. In 2D materials, the carrier mobility is attributed to two facts: impurity scattering and phonon scattering from the crystal lattice. In 1L WS_2, the carrier mobility can be separated into two regimes, which are insulating regime at low gate voltages and metallic regime at high voltages.[24] In the temperature dependent EL measurement, the driving voltage was fixed at 7.5 V, the LED system was under insulating regime. In this regime, the carrier mobility behavior follows the frameworks of thermally activated and variable range hopping models.[24] Therefore, the carrier mobility decreases as the temperature decreases, leading to a short carrier diffusion length and a short emission length.

The EL emission intensity from the same single point indicated in Figure 6.2 a as a function of temperature is presented in Figure 6.2 h. The intensity is constantly decreasing with temperature decreases. We attribute this to the reduction of initial free carriers which are thermally activated. In our monolayer WS_2 samples, the initial doping level is n-type. There are many thermal activated electrons in the system. For n-type semiconductors, the majority are electrons, and the minority are holes. Under disequilibrium, $\Delta p \gg p_0, \Delta p < n_0$, where Δp is the number of the injected holes, p_0 is the number of the initial holes, and n_0 is the number of the initial electrons. Considering the AC driving LED working principle, holes and electrons injection processes are continuous, which means that there will be endless holes injected into the material if it is in holes injection side as an example. Then the population of exciton will follow the equation: $N_{exciton} \propto B_r \cdot n_0$, where $N_{exciton}$ is the population of the formed exciton and B_r is the radiative recombination rate. The total exciton population is proportional to the initial free electrons. The population of initial free electrons follow the equation: $n_0 = (\frac{N_D N_C}{2})^{\frac{1}{2}} \cdot \exp\left(-\frac{\Delta E_D}{2k_0 T}\right) =$

$(\frac{N_D(2\pi m_* k_0 T)^{\frac{3}{2}}}{2h^3}) \cdot \exp\left(-\frac{\Delta E_D}{2k_0 T}\right)$. Here, N_D is the concentration of the donor, which is substitutional Br in the monolayer WS_2 sample. m_* is an effective electron mass, which is 0.46 m_e for monolayer WS_2.[25] k_0 and h is Boltzmann and Planck's constant, respectively. ΔE_D is impurity ionization energy. Therefore, the total EL intensity can be fitted by this equation: $N_{exciton} \propto B_r \cdot (\frac{N_D(2\pi m_* k_0 T)^{\frac{3}{2}}}{2h^3}) \cdot \exp\left(-\frac{\Delta E_D}{2k_0 T}\right)$. The measured temperature dependent EL intensity data can be excellently fitted by this model as showed in Figure 6.2 h red fitting line. From the fitting, the ionization energy can be extracted to be 140.4 meV, which matches very well with a theoretically calculated activation energy of 0.14eV for Br doped WS_2.[26] This temperature dependent EL intensity behavior further confirms that the sample initial doping plays an important role in this type of AC driving LED device. To understand the temperature dependent carrier injection dynamic in time aspect, temperature dependent TREL measurements are also performed and presented in Figure 6.2 i. At the 290 K, two decays can be observed. They are corresponding to holes injection side and electrons injection side, respectively. However, the EL decay in electrons injection side vanishes after temperature decreases to 200 K. This behavior is consistent with our previous thermal activated free carriers model. When the temperature decreases, the population of thermal activated electrons and holes are both reduced. In the electron injection side, the EL emission significantly quenched due to a lack of initial holes. Besides, the EL emission lifetime is also decreasing as temperature reduces from 290 K to 80 K. The TREL oscillation might come from the current oscillation from our instruments (Supplementary Figure S10 and Supplementary Note 4) From a lifetime point of view, it also proves that the drop of the EL emission intensity is highly related to initial doping of the two-dimensional monolayers. The above analysis further confirms that the initial doping dominates the EL emission behaviors especially the unsymmetrical recombination in this AC driving LED device.

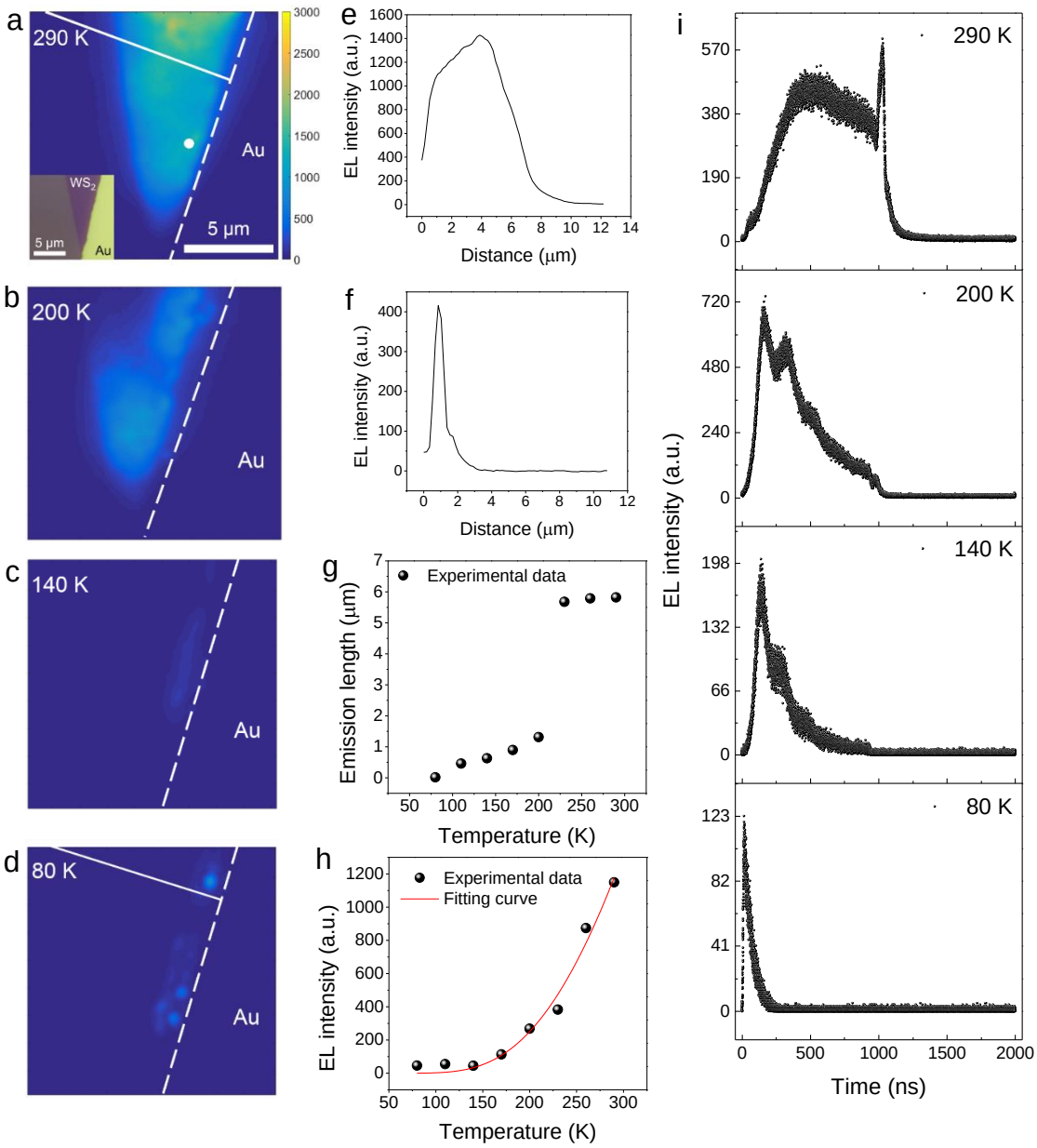

Figure 6. 2 Temperature dependent EL emission length. a-d, Temperature dependent EL emission mapping at 290 K, 200 K, 140 K and 80 K. Scale bar is 5 μm. Inset: the optical image of this WS_2 device. e, EL emission cross section profile alone the solid white line in a. f, EL emission cross section profile alone the solid white line in d. g, EL emission lengths as a function of the temperature. h, EL emission intensities from the same single spot indicated as a white dot in a versus the temperature. The red solid line is the fitting curve. i, Temperature dependent time resolved electroluminescence at 290 K, 200 K, 140 K and 80 K.

6.4. AC driving frequency induced wavelength tuneable EL emission

Interestingly, when we conducted low temperature EL mapping and TREL measurement, we found a novel EL emission behaviour, where the EL emission wavelength is AC driving frequency dependent. When the AC driving frequency is changing from 100 kHz to 1 MHz, the dominated EL emission wavelength can be switched from 599 nm/ 609.6nm (exciton/trion) to 628 nm (defect 1) and 638 nm (defect 2) as shown in Figure 6.3 a and Supplementary Figure S11. In Figure 6.3 b, the different emission species have been extracted. In the lower frequency regime, the exciton and trion emission dominates spectra. However, when the frequency goes up to 400 kHz, the defect species start to dominate, and it reaches the maximum when the frequency is at 900 kHz. This exciton and trion to defect transition can be explained as AC frequency induced static electrical doping effect. In the device structure, the Au metal is directly transferred on the top of the monolayer WS_2 sample. The contact between Au and the monolayer WS_2 is easier for electron transportation. The metal is pinning close to the conduction band of the monolayer WS_2 as shown in Supplementary Figure S12. When the AC voltage is applied to the device, the carrier injection is slightly unipolar. In each cycle, there will be more electrons injected into the system than holes. When the AC frequency is increased, this effect becomes more and more important. It is equivalent to dope the material into a more n-type regime. Initially, the defect level is closed to the valence band. The quasi-Fermi level of holes is below the defect level as shown in Figure 6.3 d. At this moment, the defect levels do not be exposed. Most of the holes are in the maximum of the valence band. Electrons and holes are forming excitons and trions. However, when the AC driving frequency increases, the quasi-Fermi level of hole moves upward, causing defect levels to be exposed. The injected holes can be quickly captured by those defect levels. Thus, the EL emission transit from exciton/trion to defect emission. The more interesting thing is when the AC driving frequency increases from 400 kHz to 1 MHz, the dominated defect peak is moving to a longer wavelength from 628 nm (D1) to 638 nm (D2), indicating it exists two different defect levels within band gap. The transition frequency is 800 kHz as shown in Supplementary Figure S11. This is the first time that we observed the defect evolution as a response to the increasing of driving frequency.

In Figure 6.3 b, the intensity ratio of those two defects to the exciton as a function of AC frequency has been extracted. The maximum ratio can be 24.5. This defect to the exciton ratio provides us with rich information regarding to the internal quantum efficiencies of the electrically pumped exciton and the defect in the monolayer WS_2. The internal quantum efficiency can be defined as: $\eta = \frac{photons/cycle}{(n_0+p_0)\times area}$, where n_0 and p_0 are the steady-state electron and hole concentrations corresponding to a positive and negative bias.[7] Here, we modified this equation for the monolayer WS_2 under initial n-type doped. The equation can be written as: $\eta = \frac{photons/cycle}{(n_0+\Delta p)\times area}$. n_0 is the initial doping concentration of the monolayer WS_2. Δp is the population of injected holes. Then the ratio of defect intensity to exciton intensity represents the internal quantum efficiency of those two species: $\frac{\eta_{defect}}{\eta_{exciton}} = \frac{Photons_{defect}}{Photons_{exciton}}$.[27] In Figure 6.3 b, the defect to exciton ratio for D2 is larger than D1, which suggests that the quantum efficiency of D2 defect is much larger than D1 due to the lower energy level of D2. It indicates that the injected free holes are much easier captured by lower energy level defects. In addition to it, the maximum quantum yield of a defect localized exciton is around 24.5 times larger than that from a free exciton in the WS_2 monolayer, which is hardly seen in optical pumped WS_2 monolayer samples.[28] For the optical pumped process, the photo excited electron and hole quickly relax into conduction band minima and valence band maxima, forming an exciton due to optical selection rule. Then the exciton has a probability to be captured by the defect level.[28] Some excitons have already radiatively recombined before they are captured by the defect. Unlike the optical pumping process, the electrical pumping is injecting carrier directly into the material's conduction or valence band. Those injected electrons or holes will firstly occupy a lower energy level filling the defect level. Then they form exciton and radiatively recombination, leading to higher defect quantum yield than optically pumped method. To understand the origin of the large quantum yield enhancement of the defect emission, we used TREL to characterize the time resolved emission behaviours of the defects, exciton and trion species as depicted in Figure 6.3 c. Compared with the TREL curve of exciton and trion, the two defects curve shows a fast process before it reaches the maximum. The injected holes can be captured by the defect levels that are closed to the electrodes. However, for exciton and trion, the injected holes will diffuse inward the monolayer WS_2 accompany with

forming excitons. The time between the start of injection and the EL reaching its maximum can be defined as the hole diffusion lifetime. This diffusion lifetime can also map to the real emission space. The longer diffusion lifetime is, the more ability for holes travels far inside the material which means more emission area of the device. Therefore, exciton and trion can still form a little bit far away from electrodes. However, the defect can and only can form inside the defect levels where are right close to electrodes as shown in Figure 6.4 a-c. In the defect level, the injected holes can be quickly captured and radiative recombination. After it emits light via radiative recombination, the defect level becomes empty again so that it could capture new holes inside. While the free holes and electrons will wander in the material until their momentum match to form exciton or trion. This process takes time comparing to defect level assist exciton formation. Thus, the total population of excitons formed in defect levels is much larger than those free excitons and trions resulting in enhanced quantum yield. The radiative emission lifetime for D1 and D2 are 46.6 ns and 43.3 ns, respectively. However, exciton and trion have longer emission lifetimes of 181.2 ns and 192.4 ns. This double confirms that carriers quickly recombine within defect states, leading to stronger defects emission.

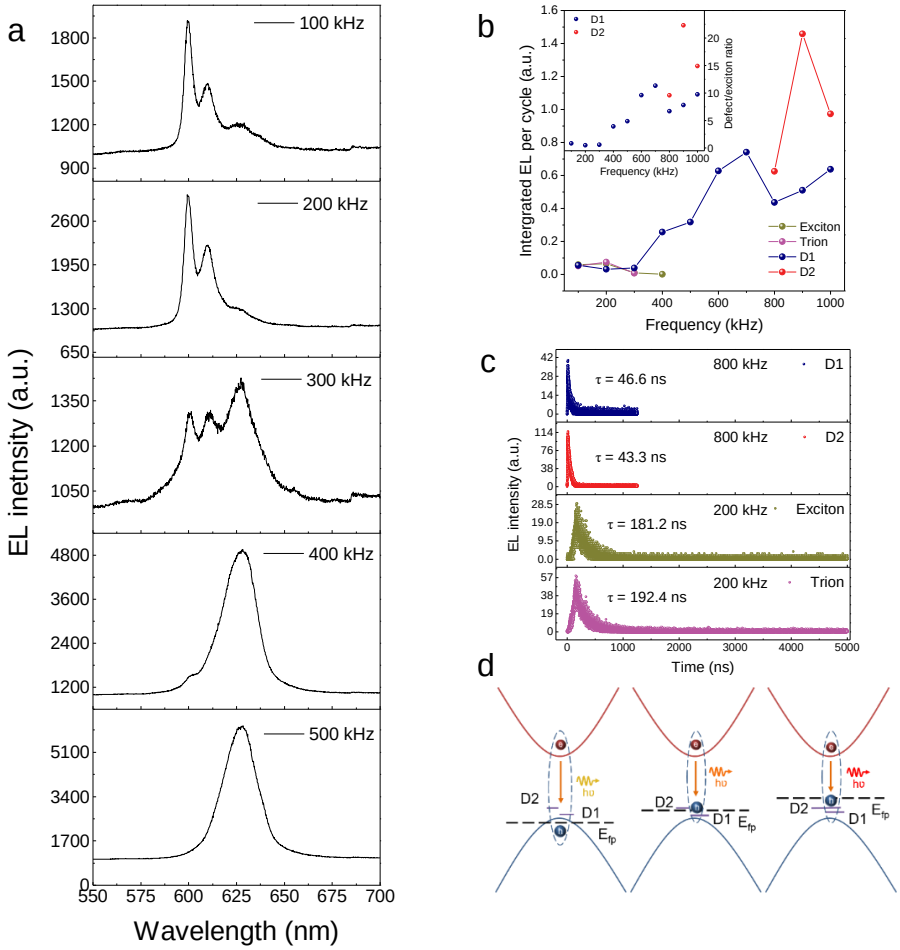

Figure 6. 3 AC driving frequency induced wavelength tuneable EL emission. a, Frequency dependent EL spectra from the monolayer WS_2 AC LED at 80k (V_{ac} = 7.5 V). b, Frequency normalized integrated intensities of four emission species versus AC driving frequency. Inset: defects and exciton emission ratio as a function of AC driving frequency. c, Time resolved electroluminescence of exciton, trion and defect 1 and defect 2 species under driving frequency at 500 kHz. d, Schematic band explanation of frequency induced exciton/trion to defect 1 and defect 2 transitions.

6.5. Visualization of exciton/trion to defect emission transition and defect levels evolution

After observing the wavelength tuneable EL emission in spectra, we are very keen to see the spatial distribution of the emission pattern. The low temperature EL mapping measurements are conducted, we surprisingly found that we can directly visualize the transition of exciton/trion to defect and different defect levels emission. Figure 6.4 a-

c show the EL emission images in real space from the AC driving WS_2 LED device with different driving frequency. Three emission spots are observed at a frequency of 200 kHz labelled as S1, S2 and S3. When the driving frequency is increasing, the middle spot S2 is emerging. By switching the horizontal axis to the wavelength dimension, the spectra of each spot under different frequencies can be extracted as shown in Fig. 6.4 d-f. The extraction method is provided in the Supplementary Figure S13. Under 200 kHz, spot 1 has already exhibited exciton, trion and defect emission behavior. Spot 2 has some defect components but the exciton and trion emissions are still dominated. Spot 3 emission is mainly contributed from exciton and trion. With the increase of frequency, all three spots show defect emission domination. However, the central defect emission wavelength is at 628 nm for spot 1 and 638 nm for spot 2 and spot 3. Here, we have successfully distinguished different defect types and see different defects evolution in real space by using this AC driving EL emission mapping. The origin of those two defect emissions can be attributed to the localization of excitons in sulfur vacancies, which has been observed by scanning tunneling microscopy (STM).[29, 30] On the basis of that STM luminescence,[30] the defect EL emission can be only observed when STM tip injects holes. In our experiment, the beauty of our AC injection is that it can separately inject holes or electrons. In this way, it provides a better chance for us to monitor the injection dynamic. The EL defect emission in our sample only appears in the hole injection section as shown in Figure 6.3 c TREL measurement, which is consistent with STM luminescence results. This suggests that the two defect states in our experiment are negatively charged. They prefer trap holes rather than electrons. On the basis of the STM luminescence peak energy,[30] we attribute the emission peaks of 628 nm and 638 nm to the negatively charged sulfur vacancies with different energy depth. Those sulfur vacancies can be triggered by increasing AC driving frequency as shown in Figure 6.4 g.

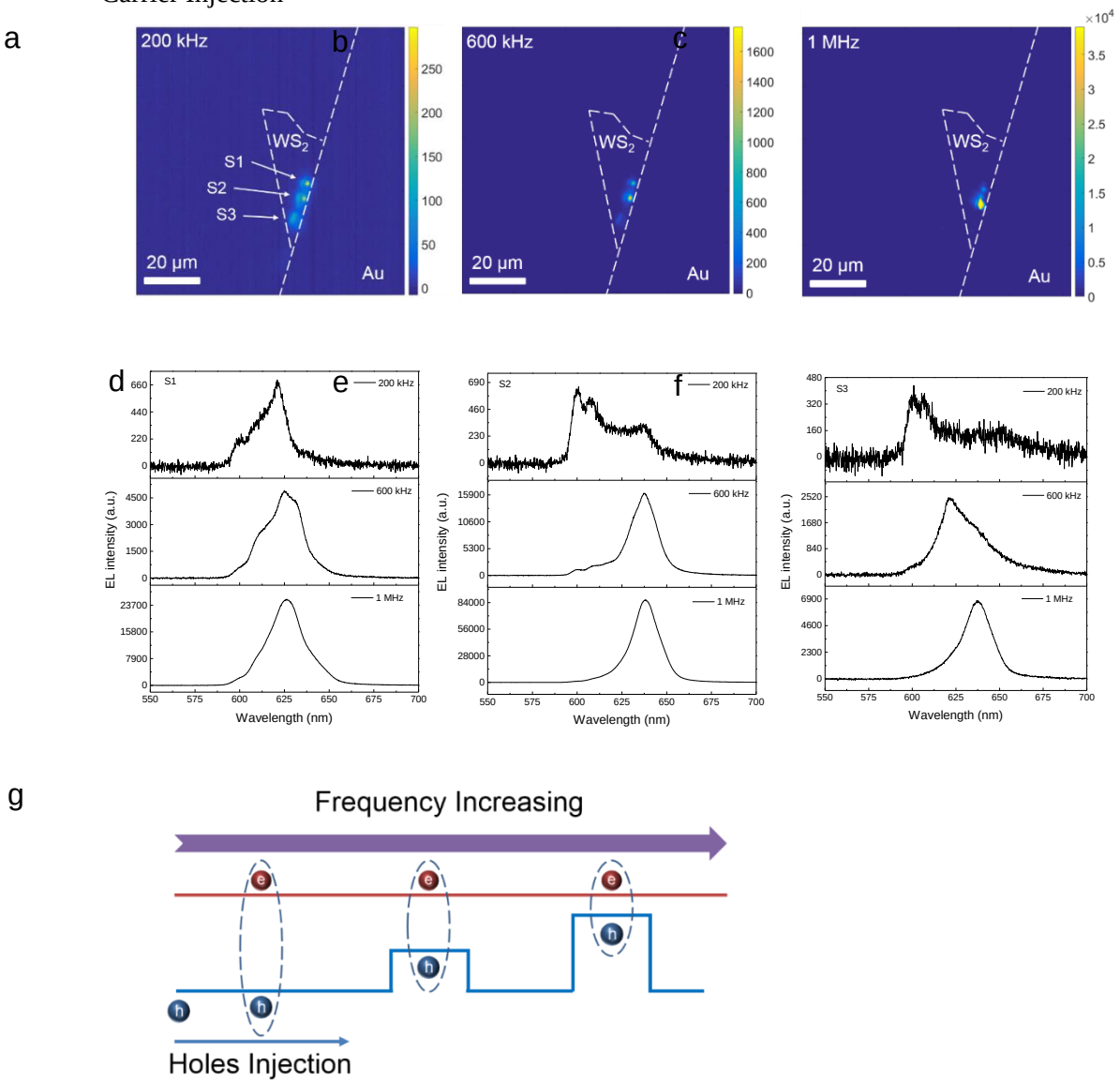

Figure 6. 4 Visualization of exciton/trion to defect emission transition and defect levels evolution. a-c, EL emission mapping of the same sample under the driving frequency of 200 kHz, 600 kHz and 1 MHz, respectively. (V_{ac} = 7.5V at 80K) d-f, EL spectra of three different emission spots labelled as S1, S2 and S3 in a. For each panel, the driving frequencies from top to bottom are 200 kHz, 600 kHz and 1 MHz, respectively. g, Schematic of wavelength tuneable EL emission with increasing AC frequency, where red and blue lines represent the conduction band and valence band.

6.6. Summary

In summary, we have demonstrated a monolayer WS_2 based AC driving LED device with an ultra-long electroluminescence emission length. The origin of the long EL

emission length is an unsymmetrical pulsed carrier recombination process due to the nature of the initial doping in monolayer WS_2. Temperature dependent TREL and room temperature TREL measurements with different 2D materials and different initial doping levels confirm that the initial doping level plays an important role in carrier injection dynamic and therefore realizing long EL emission length. The unsymmetrical recombination concept demonstrated in this work can be extended to other 2D materials under this AC driving LED structure for achieving a larger emission area and reducing fabrication cost. Besides, the wavelength tunable EL emission has been demonstrated under low temperatures. The quantum efficiency of defect EL emission is 24.5 times larger than free exciton and trion EL emission. The ability to realize high intensity defect emission opens rich potential opportunities in the field of defect engineering and defect based single photon emission. In addition to it, we have also successfully distinguished the different defect levels and their evolution in real space by using the sperate injection feature of the AC driving method. Those defect levels can be assigned to negatively charged sulfur vacancies. Our results not only illustrate important insights for further understanding the AC LED working principle and providing a general guideline for rationally designing high performance AC driving LEDs, but it also opens a new route to study the defect states and defect engineering for the tunable LED device.

6.7. Methods section

Device fabrication. The monolayer WS_2 and WSe_2 samples were mechanically exfoliated onto the SiO_2/Si substrate where had been already patterned 100 nm thickness gold electrodes by conventional photolithography. Another 100 nm thickness gold electrode was peeled off from the SiO_2/Si substrate through a homemade micromanipulator and then drop it between samples and electrodes to bridge them together. The WS_2 crystal used in this work is purchased from HQ graphene with the CVT growth method contains Br element. The WSe_2 crystal is purchased from 2D semiconductor with a flux zone growth method contains no halide elements.

Optical characterization. PL and EL measurements were conducted using a homemade photoluminescence setup equipped with an Andors iDu416 charge-coupled detector and a Kymera 328i spectrometer. A 532 nm diode-pumped solid state (DPSS) laser was used as the excitation source. The EL signal is generated by applying an amplified square wave generated from the function generator. All EL related measurements were conducted with a microscope-compatible chamber (Linkam Chamber) with electrical feedthrough. For temperature dependent measurement, a low-temperature controller would be linked to the chamber and use liquid nitrogen as the coolant. Time-resolved PL and EL (TRPL and TREL) measurements were conducted in a setup that incorporates an avalanche photodetector and a time-correlated single-photon counting (TCSPC). For TREL measurement, the reference signal from the function generator is synchronized to TCSPC as a start time tagger signal. Histogram measurement is performed by TCSPC, where the resolution of TCSPC could go down to 8 ps. It is noted that all the EL spectra, TREL and EL mapping spectra were generated with 0.7V to 1V peak-to-peak voltage with no offset and different frequency from 100 kHz to 1.5 MHz. All the spectra were corrected with the instrument response.

References

1. H. R. Gutiérrez *et al.*, Extraordinary room-temperature photoluminescence in triangular WS2 monolayers. *Nano letters* **13**, 3447-3454 (2012).
2. K. F. Mak, C. Lee, J. Hone, J. Shan, T. F. Heinz, Atomically thin MoS 2: a new direct-gap semiconductor. *Physical review letters* **105**, 136805 (2010).
3. Q. H. Wang, K. Kalantar-Zadeh, A. Kis, J. N. Coleman, M. S. Strano, Electronics and optoelectronics of two-dimensional transition metal dichalcogenides. *Nature nanotechnology* **7**, 699 (2012).
4. F. Withers *et al.*, Light-emitting diodes by band-structure engineering in van der Waals heterostructures. *Nature materials* **14**, 301 (2015).
5. J. S. Ross *et al.*, Electrically tunable excitonic light-emitting diodes based on monolayer WSe 2 p–n junctions. *Nature nanotechnology* **9**, 268 (2014).
6. F. Withers *et al.*, WSe2 light-emitting tunneling transistors with enhanced brightness at room temperature. *Nano letters* **15**, 8223-8228 (2015).
7. D.-H. Lien *et al.*, Large-area and bright pulsed electroluminescence in monolayer semiconductors. *Nature communications* **9**, 1229 (2018).
8. K. F. Mak *et al.*, Tightly bound trions in monolayer MoS 2. *Nature materials* **12**, 207 (2013).
9. S. Mouri, Y. Miyauchi, K. Matsuda, Tunable photoluminescence of monolayer MoS2 via chemical doping. *Nano letters* **13**, 5944-5948 (2013).
10. J. Yang *et al.*, Optical tuning of exciton and trion emissions in monolayer phosphorene. *Light: Science & Applications* **4**, e312 (2015).
11. B. Wen *et al.*, Ferroelectric Driven Exciton and Trion Modulation in Monolayer Molybdenum and Tungsten Diselenides. *ACS nano*, (2019).
12. H. Nan *et al.*, Strong photoluminescence enhancement of MoS2 through defect engineering and oxygen bonding. *ACS nano* **8**, 5738-5745 (2014).
13. Z. Lin *et al.*, Defect engineering of two-dimensional transition metal dichalcogenides. *2D Materials* **3**, 022002 (2016).
14. G. Clark *et al.*, Single defect light-emitting diode in a van der Waals heterostructure. *Nano letters* **16**, 3944-3948 (2016).
15. Y.-M. He *et al.*, Single quantum emitters in monolayer semiconductors. *Nature nanotechnology* **10**, 497 (2015).
16. S. Mignuzzi *et al.*, Effect of disorder on Raman scattering of single-layer Mo S 2. *Physical Review B* **91**, 195411 (2015).
17. Z. Wu *et al.*, Defects as a factor limiting carrier mobility in WSe 2: A spectroscopic investigation. *Nano Research* **9**, 3622-3631 (2016).
18. A. Sharma *et al.*, Defect Engineering in Few‐Layer Phosphorene. *Small* **14**, 1704556 (2018).
19. Y. Zhang *et al.*, Probing carrier transport and structure-property relationship of highly ordered organic semiconductors at the two-dimensional limit. *Physical review letters* **116**, 016602 (2016).
20. Y. Zhu *et al.*, High-Efficiency Monolayer Molybdenum Ditelluride Light-Emitting Diode and Photodetector. *ACS applied materials & interfaces* **10**, 43291-43298 (2018).
21. A. Allain, A. Kis, Electron and hole mobilities in single-layer WSe2. *ACS nano* **8**, 7180-7185 (2014).
22. V. Podzorov, M. Gershenson, C. Kloc, R. Zeis, E. Bucher, High-mobility field-effect transistors based on transition metal dichalcogenides. *Applied Physics Letters* **84**, 3301-3303 (2004).
23. Y. Guo, D. Liu, J. Robertson, Chalcogen vacancies in monolayer transition metal dichalcogenides and Fermi level pinning at contacts. *Applied Physics Letters* **106**, 173106 (2015).

24. D. Ovchinnikov, A. Allain, Y.-S. Huang, D. Dumcenco, A. Kis, Electrical transport properties of single-layer WS2. *ACS nano* **8**, 8174-8181 (2014).
25. F. A. Rasmussen, K. S. Thygesen, Computational 2D materials database: electronic structure of transition-metal dichalcogenides and oxides. *The Journal of Physical Chemistry C* **119**, 13169-13183 (2015).
26. A. Carvalho, A. C. Neto, Donor and acceptor levels in semiconducting transition-metal dichalcogenides. *Physical Review B* **89**, 081406 (2014).
27. R. Xu *et al.*, Exciton brightening in monolayer phosphorene via dimensionality modification. *Advanced Materials* **28**, 3493-3498 (2016).
28. P. K. Chow *et al.*, Defect-induced photoluminescence in monolayer semiconducting transition metal dichalcogenides. *ACS nano* **9**, 1520-1527 (2015).
29. B. Schuler *et al.*, Large spin-orbit splitting of deep in-gap defect states of engineered sulfur vacancies in monolayer WS 2. *Physical review letters* **123**, 076801 (2019).
30. B. Schuler *et al.*, Electrically driven photon emission from individual atomic defects in monolayer WS2. *arXiv preprint arXiv:1910.04612*, (2019).

Appendix:

Supplementary Information for Chapter 6

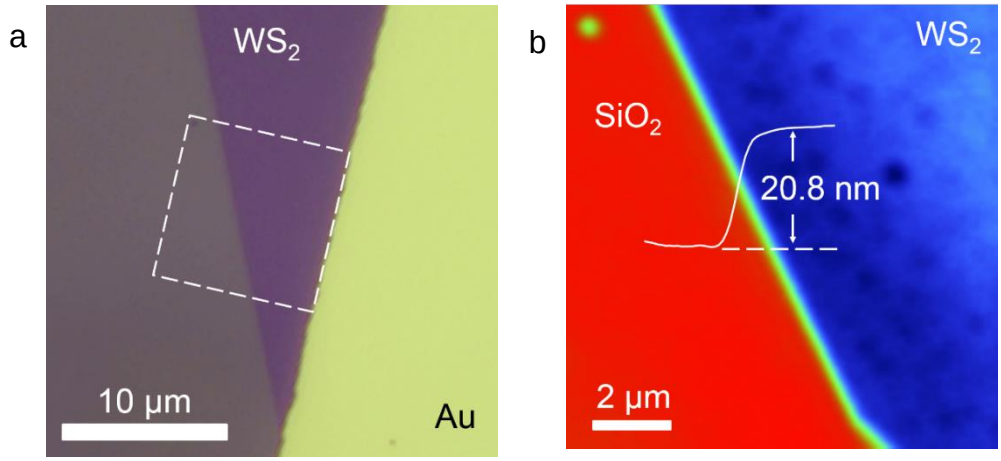

Figure S1 Sample characterization of monolayer WS_2 LED. a Optical microscope image of mechanically exfoliated WS_2 sample on SiO_2/Si substrate (275 nm thermal SiO_2) with the gold electrode on the WS_2. b Phase shifting interferometry (PSI) image of the region inside the box indicated by the dashed line shown in Fig.S1 a. The measured height difference from WS_2 to a substrate is 20.8 nm, which represents as a monolayer.[1]

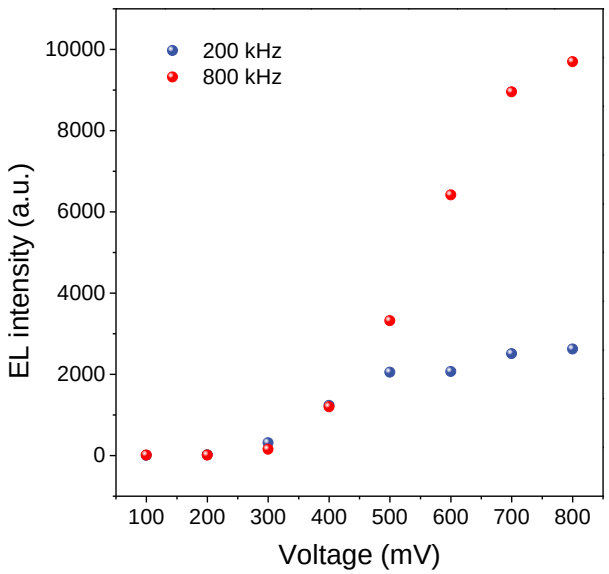

Figure S2 Room temperature driving voltage dependent EL emission. Red dots and blue dots represent WS_2 AC LED exciton EL intensity at 800 kHz and 200 kHz

respectively. Both frequencies excitation, the EL intensity would increase with the increase of driving voltage.

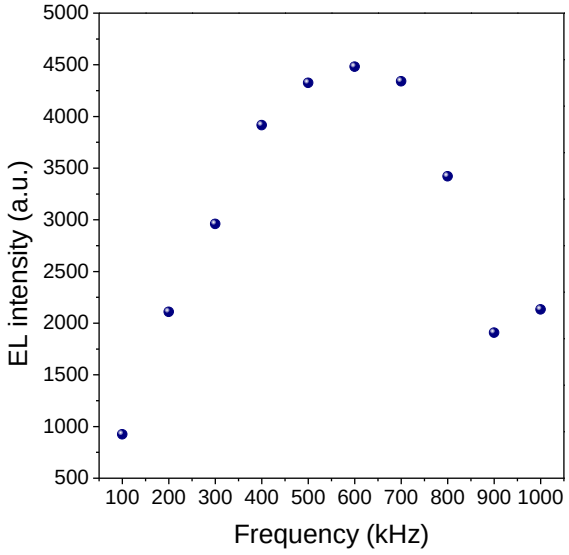

Figure S3 Room temperature driving frequency dependent EL emission at 500 mV. The WS_2 AC LED exciton EL emission intensity would be tuned with the frequency change. It would reach the maximum intensity when the frequency is 600 kHz.

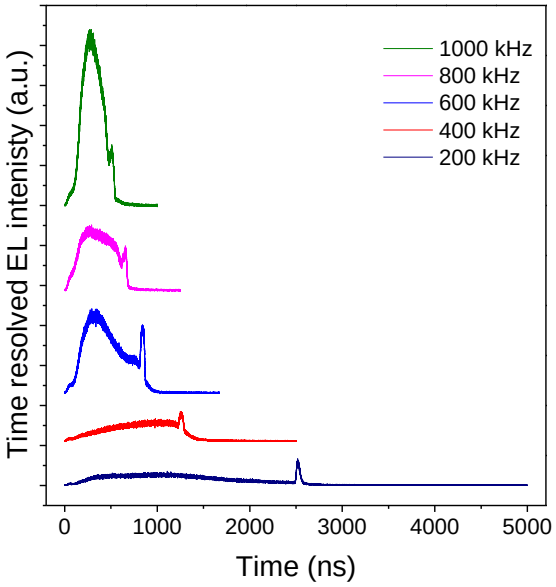

Figure S4 Room temperature frequency dependent TREL measurement. 290K Time-resolved electroluminescence (TREL) for WS2 sample excited by the same square wave of 800 mV. The green, pink, blue, red and purple lines represent the TREL

measurements under 1000 kHz, 800 kHz, 600 kHz, 400 kHz and 200 kHz respectively. With AC frequency decrease, the TREL decay could be tuned and decay could be longer.

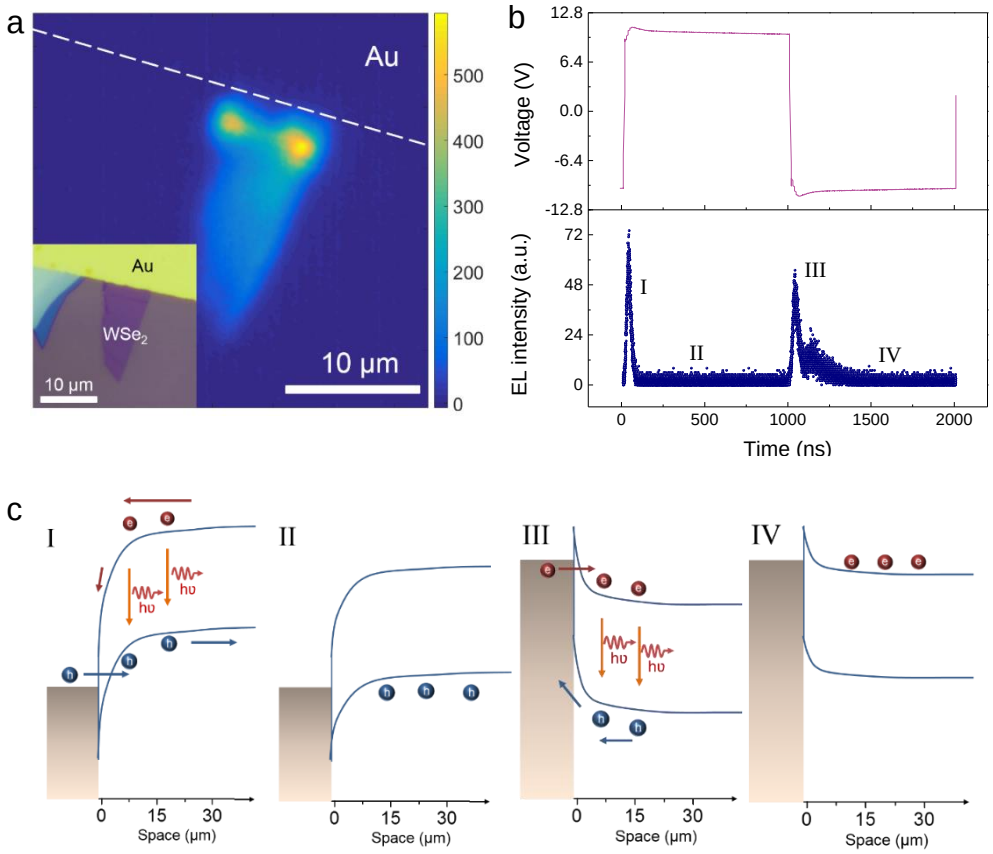

Figure S5 Room temperature TREL measurement of WSe_2 LED and symmetrical pulsed carrier injection. a, EL mapping of the WSe_2 AC LED device. (V_{ac} = 10 V at 500k Hz). The white dashed line indicates the contacted edge of the gold electrode. Inset: the optical image of this WSe_2 device. b, Time-resolved electroluminescence and the corresponding driving voltage trace for WSe_2 AC LED device. Two similar decay behaviours indicate the symmetrical carrier recombination process at two voltage transients. c, Schematic band diagrams corresponding to four emission stages labelled as I, II, III and IV in b.

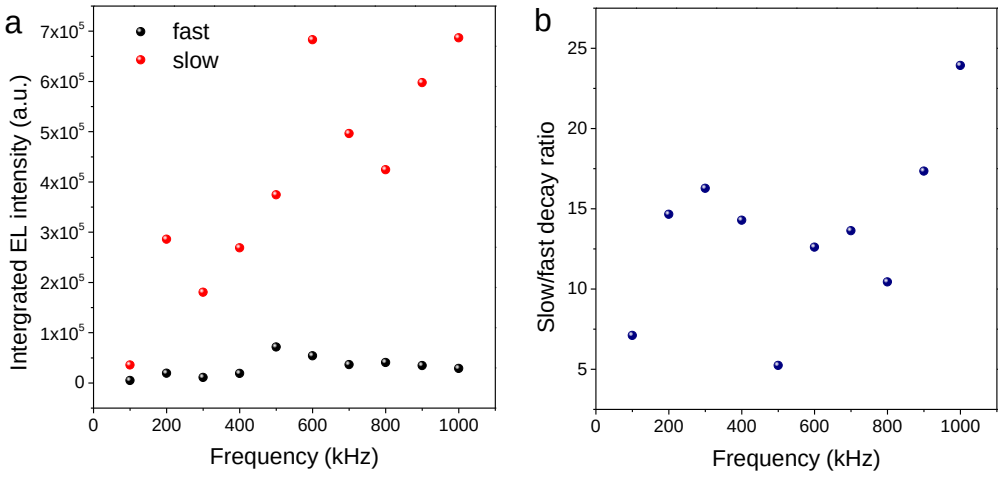

Figure S6 Fast and slow decay components in WS_2 AC LED devices at room temperature. a, Integrated EL intensities from fast and slow decay components as function of AC frequency. b, The ratio of integrated EL intensity from slow decay to fast decay versus AC driving frequency.

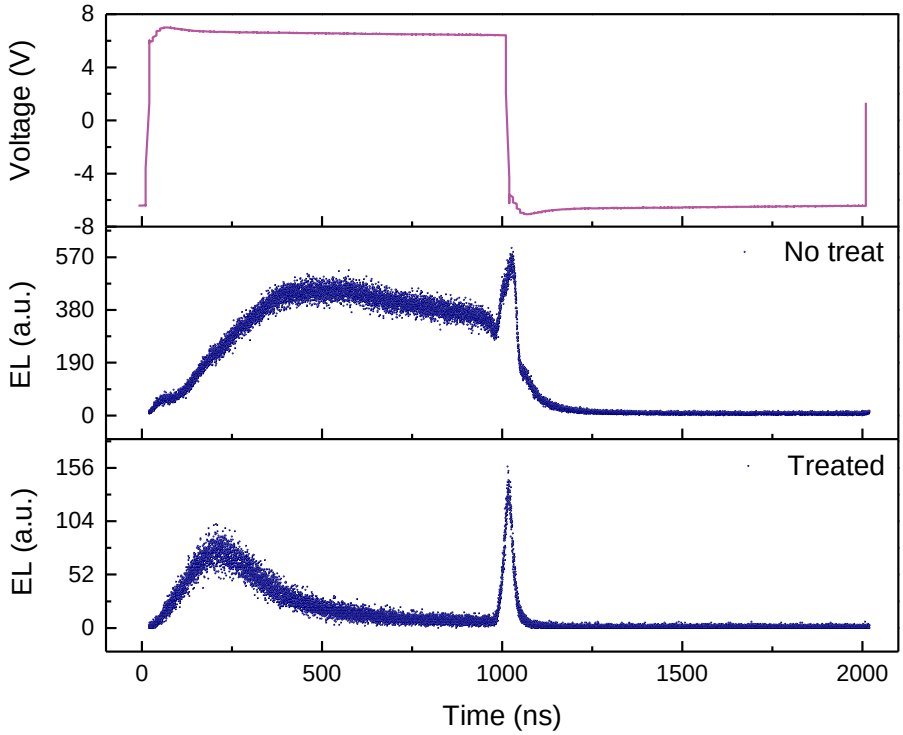

Figure S7 Room temperature TREL measurement with chemical doped WS_2 AC LED device. a WS_2 AC LED excitation square wave generated by a function generator and amplified by an amplifier with frequency of 500 kHz. b and c

Corresponding TREL for WS_2 AC LED with excitation square wave shown in Fig. S3 a, with and without treatment of n-type dopant TCNQ.

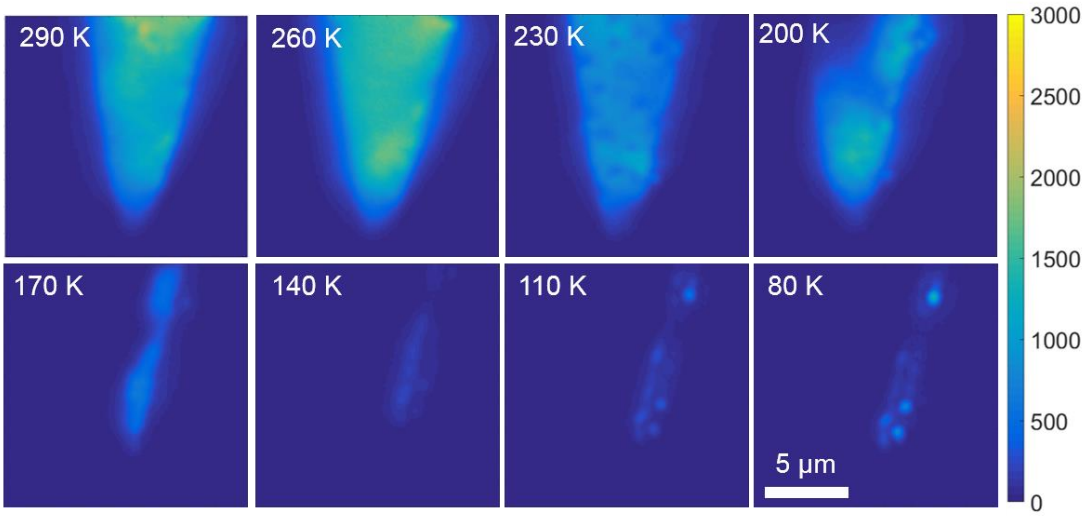

Figure S8 WS_2 AC LED temperature dependent EL emission mapping. 290 K, 260 K, 230 K, 200 K, 170 K, 140 K, 110 K and 80 K respectively. From 290 K to 230 K, the emission length is saturated but with emission intensity from high to low, the saturated emission length may be limited by sample size. With temperature continue decreasing, the emission length decreases significantly.

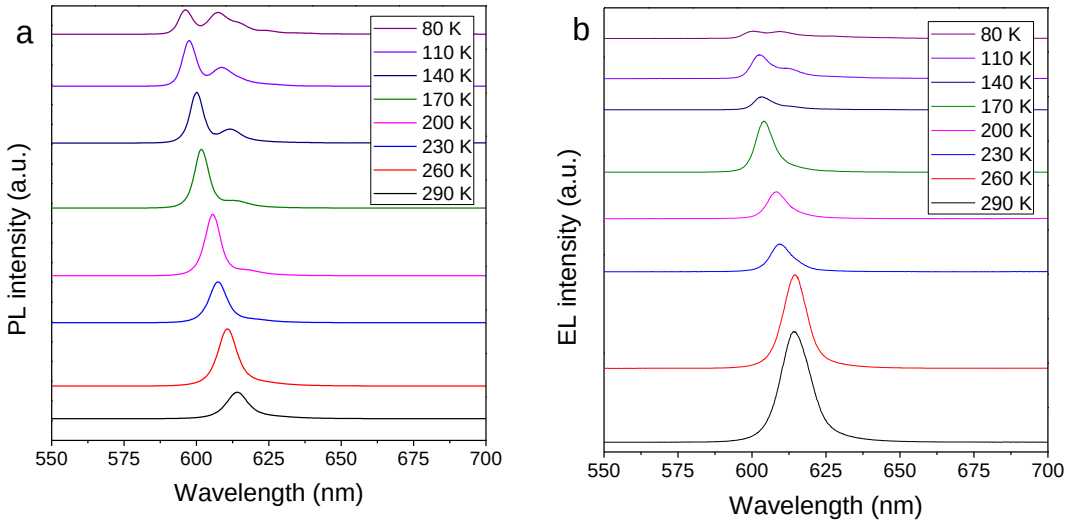

Figure S9 Temperature dependent WS_2 AC LED PL and EL spectra. a WS_2 AC LED PL emission spectra excited by 0.9 uW 532 nm laser at different temperatures. b WS_2 AC LED EL emission spectra excited by 500 kHz 700 mV square wave at different temperatures.

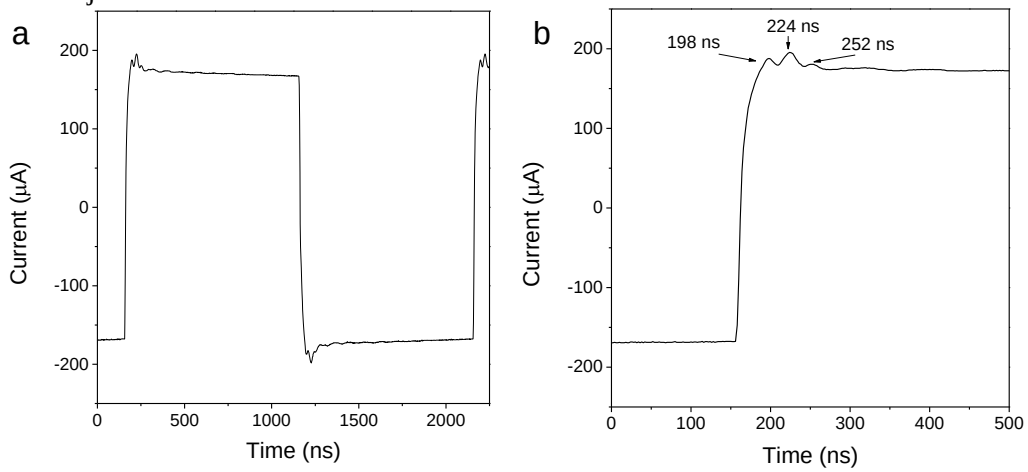

Figure S10 AC driving current trace showing current oscillation. a. AC driving current trace. b. Zoomed in image of current oscillation.

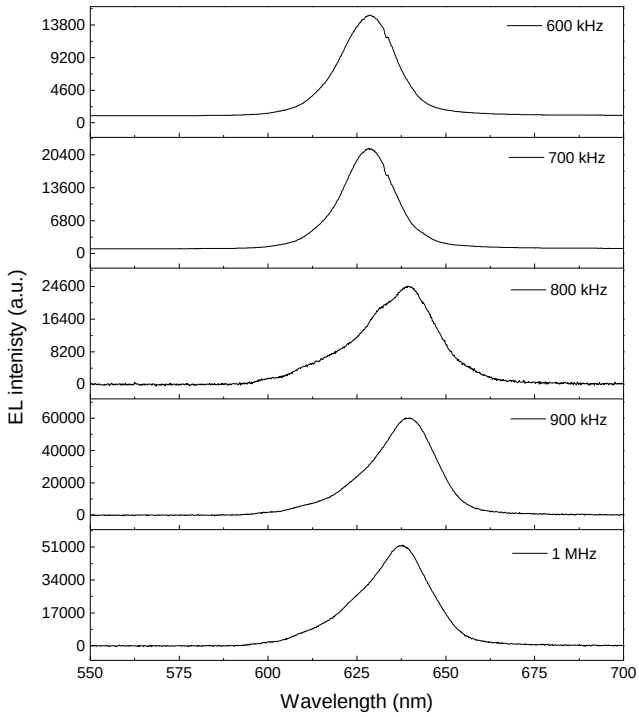

Figure S11 Frequency dependent defect emission switching from monolayer WS_2 AC LED at 80 K. EL spectra from 600 kHz to 1 MHz with 100 kHz step rates at 80K. From 800 kHz to 1 MHz, the dominated EL emission start sifting from the shallow defect (D1 at 629 nm) peak to deep defect (D2 638.5 nm) peak.

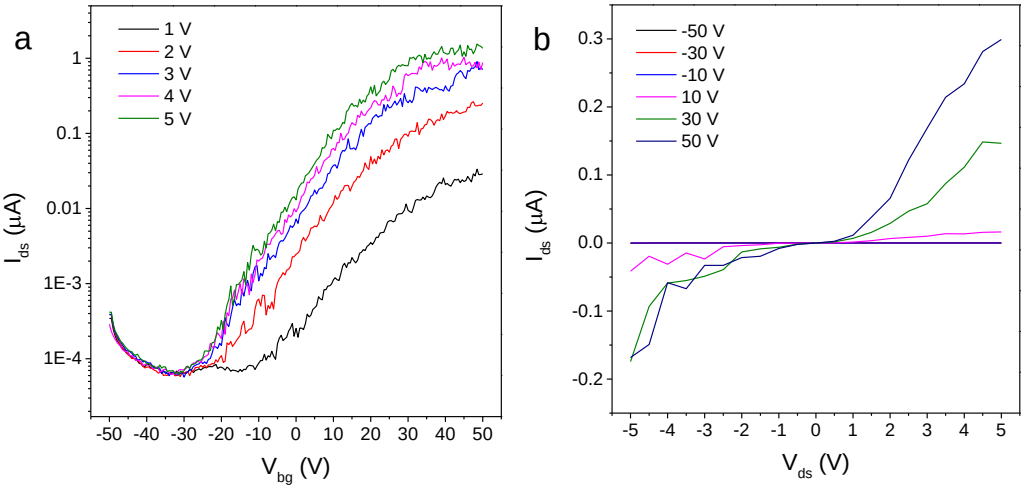

Figure S12 Room temperature monolayer WS_2 FET measurement. a Source-drain current I_{ds} VS. back-gate voltage V_{bg} measured for the 290 K WS2 FET at a source-drain bias voltage of 1 V to 5 V with 1 V step rate. Black, red, blue, purple and green represent bias as 1 V, 2 V, 3 V, 4 V and 5 V respectively. All curves are the plot for Ids in linear scale, the channel is of n-type. b I_{ds} VS. V_{ds} for V_{bg} sweep from -50 V to 50V with 20V step rates.

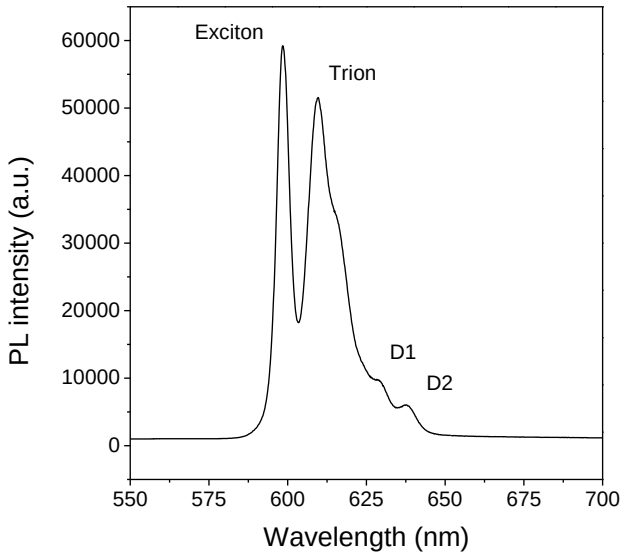

Figure S13 WS_2 AC LED PL spectrum at 80K. WS_2 AC LED PL spectrum shows 5 peaks at 80 K, which are exciton, trion, biexciton and two defects respectively.

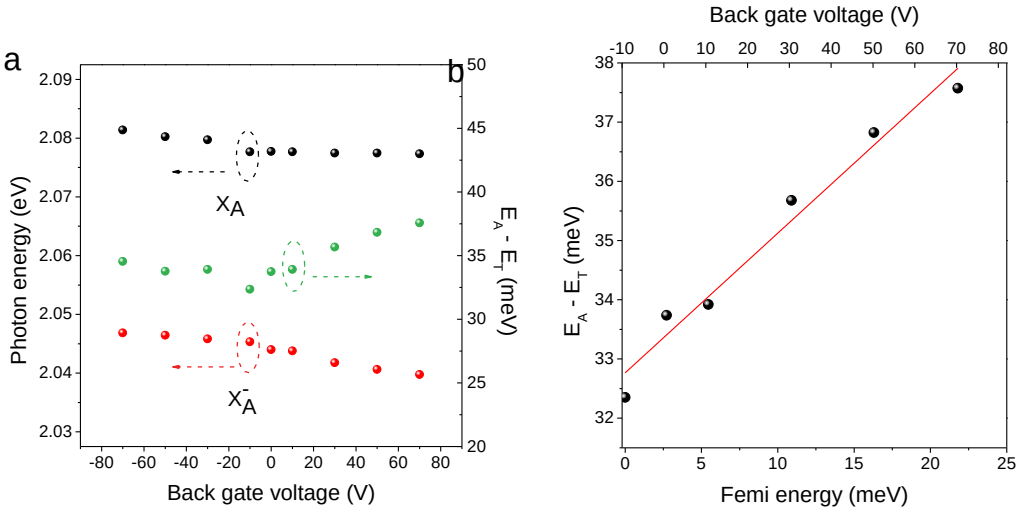

Figure. S14 | Electrical doping effect on excitonic emission in 1L WS_2 at 80 K. a. Photon energies of A exciton (X_A) and trion (X_A^-) (left vertical axis) versus gate voltage; dissociation energy of trion (X_A^-) (right vertical axis) versus gate voltage. b, dissociation energy of trion versus femi energy under different back gate voltage.

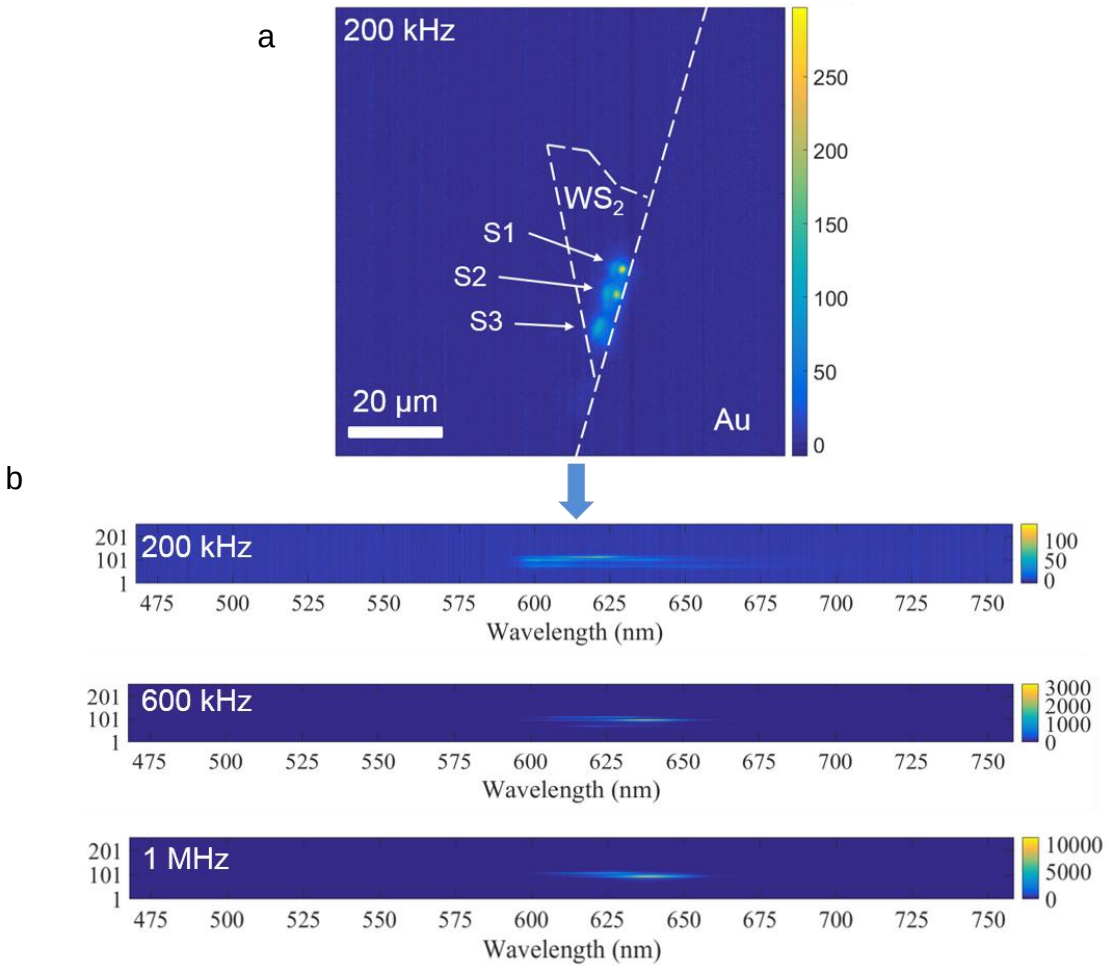

Figure. S15 CCD spatial image convert to wavelength spectra. a. CCD spatial image when spectrometer grating is set to be zero. b. EL spectra contain both spatial and wavelength information when convert x axis pixel to wavelength by rotating spectrometer grating to sample wavelength.

Supplementary Note 1

Estimation of initial doping level of monolayer WS_2 sample

In order to investigate initial doping that originates from material intrinsic defects, monolayer WS_2 metallic oxide semiconductor field effect transistor (MOS) devices were fabricated to obtain the electrically gated PL spectrum. Monolayer $MoSe_2$ and WSe_2 were exfoliated onto SiO_2/Si substrates from the same matrix crystal to keep the same of the initial doping level. The initial doping level in monolayer TMDs can be extracted by comparing the gate-dependent PL spectra from the MOS devices. Here, monolayer WS_2 was used to quantitively study charge transfer mechanisms. By fitting all of the PL spectra under different gate voltages, the exciton and trion peak energies can be extracted (Figure S11). Then the Fermi level can be calculated by a function

$$E_a - E_T = E_F + E_{binding} \qquad (1)$$

where E_a is the exciton peak energy, E_T is the trion peak energy, E_F is the Fermi energy level and $E_{binding}$ is the binding energy of trion.

Equation (1) was used to extract the Fermi level of monolayer WS_2. By plotting the difference of exciton and trion peak energy as a function of gate voltage, a clear linear trend between energy difference and Femi level was observed. For monolayer TMDs, the density of state in the conduction band and valence band is linearly distributed along the energy level[2]. The extracted binding energy of the monolayer WS_2 was 32.76 meV and this is consistent with previously reported experimental results[3, 4]. To extract the initial doping level of the monolayer WS_2, the following two equations have been used

$$E_F = \frac{\hbar\pi n}{2m_h e^2} \qquad (2)$$

$$ne = CV_g \qquad (3)$$

where h is Planck's constant, π is the pi constant, n is the electron density, e is the fundamental unit of charge, m_h is the effective mass of a hole, C is the back-gate capacitance and V_g is the gate voltage.

Equation (2) was used to extract the doping level n of the monolayer TMDs from the Fermi level. Equation (3) was used to convert the gate voltage into the induced hole doping level, where C is the back-gate capacitance $C = 1.2 \times 10^{-8}\ Fcm^{-2}$. As shown in Fig. S12, monolayer WS_2 will approach a zero Fermi level when a -10V back gate voltage is applied. This means monolayer WS_2 is slightly n-type doped with an initial doping level of $7.5 \times 10^{11}\ cm^{-2}$ (when no gate voltage is applied).

Supplementary Note 2

Device fabrication process

The device fabrication includes dry transfer and dry electrode transfer process. Mechanical exfoliation has been employed to prepare a clean sample on SiO_2/Si. Then the lithography free dry electrode transfer process is used to make electrode contacts. The details of this method are described here. The 100 nm thickness Au bar shape patterns are deposited onto a bare SiO_2/Si substrate by traditional photolithography following lift-off process. The 1 micro tip diameter tungsten probe is attached to the homemade micromanipulator. The bar shape gold pattern can be scratch into a designed length and then be peeled off from the original SiO_2/Si. This small section of gold metal is hanging in front of the tungsten probe tip wait for drop down to target monolayer samples. Because of electrical static force, when the peeled gold metal moves closely to target substrates, it can be automatically attracted and attached upon target samples. By using this method, the clean interface of monolayer 2D materials can be achieved.

Supplementary Note 3

TCNQ chemical doping process

The TCNQ chemical doping process includes solution preparation and drop casting solution to sample. The 7,7,8,8-tetracyanoquinodimethane (TCNQ) powder is

dissolved in DI Water, with a concentration of 0.02 μmol/mL, which corresponds to a dopant density on the monolayer of approximately 1/nm^2 after one doping step. The solution was performed using a drop-cast method following by drying up on 60 degrees hotplate. An approximately 10 μL droplet of the dopant solution was pipetted onto the SiO_2/Si substrate area of 1 cm^2 where the AC LED devices were prepared. The sequential doping by repeating this procedure was performed.

Supplementary Note 4

Low temperature TREL decay curve oscillation.

The TREL decay curve oscillation has been observed when temperature reduced to 200 K as shown in Fig. 3i. This decay curve oscillation could be attribute to injection current oscillation generated from the function generator. In the TREL curve, there are three dominated oscillation peaks in the first decay section. The corresponding times for those three peaks are 162 ns, 326 ns, and 503 ns, respectively. Coincidentally, there are also three oscillation peaks appearing in the measured the current trace as shown in Fig. S8. The times for three peaks are 198 ns, 224 ns, and 252 ns, respectively. The time differences among oscillation peaks in current trace are 26 ns for first and second peaks, 28 ns for second and third peaks. While, those time differences are 164 ns and 177 ns in TREL decay curves. Although, those time difference values are not exactly equal due to system caused delay, the time difference ratios are identically same for the current trace of 28/26 = 1.0769 and for TREL decay curve of 177/164 = 1.0792. This confirms that the oscillation observed in TREL decay curve results from the oscillation from the injected current.

References

1. J. Yang *et al.*, Atomically thin optical lenses and gratings. *Light: Science & Applications* **5**, e16046 (2016).
2. K. F. Mak *et al.*, Tightly bound trions in monolayer MoS 2. *Nature materials* **12**, 207 (2013).
3. D. W. Kidd, D. K. Zhang, K. Varga, Binding energies and structures of two-dimensional excitonic complexes in transition metal dichalcogenides. *Physical Review B* **93**, 125423 (2016).
4. W. Zhou *et al.*, Intrinsic structural defects in monolayer molybdenum disulfide. *Nano letters* **13**, 2615-2622 (2013).

7. Conclusions and Future work

7.1. Conclusions

In this dissertation, we have systematically investigated the optical and electronic properties of 2D materials and explored their optoelectronics applications. By using micro Raman and PL spectroscopy, the exciton behaviours in 2D materials have been studied and the different exciton dynamics have shown significantly effect on optoelectronics device performances.

Firstly, the fast and non-invasive method to identification layer numbers of 2D materials by PSI is presented in chapter 3. The 2D material dependent PSI measurement shows the high sensitivity and resolution in determining the thickness of 2D material. The quantized PSI values directly reflect the layer numbers in layered materials. Combining with AFM calibration, it has the capability of identifying any unknown and new 2D layered materials. The high sensitivity also provides the ability to resolve the fine structure on the surface of 2D materials such as quantum dots. Interestingly, the monolayer MoS_2 could give high PSI value, which is equivalent to giant OPL. It suggests that MoS_2 shows a great potential for micro-lens applications.[1] The substrate dependent PSI measurement suggests that the PSI value and OPL can be modulated by substrate. The material dependent PSI measurement shows that the high PSI value and OPL can be obtained while the large mismatching of refractive index between materials and substrates are existed. This finding opens the opportunity of tuning phase shift of ultrathin material by selecting the proper substrate with correct refractive index, which is a key step towards the 2D materials-based super lens.

In Chapter 4, we have shown that monolayer transition metal dichalcogenides (TMDs) $MoSe_2$ and WSe_2 can be interfaced onto the surface of ferroelectric lithium niobate (LN) and that the domain orientation of the LN has a strong effect on the TMD optoelectronic properties. Domain engineering of the LN substrate results in an in-plane heterostructure within the TMD which has been demonstrated by our measured spatial PL mapping. Due to the underlying domain engineered ferroelectric, PL emissions are modulated approximately 9 times by different surface doping

between the P^- and P^+ domains. Monolayer WSe_2 on LN also shows enhanced PL emission at the junction between domains with the increasing laser power, this is due to the cancelling of the micro internal electric field between the P^- and P^+ domains, which stops dissociation of excitons. With decreasing temperature, the PL emission from monolayer $MoSe_2$ was quickly quenched in the P^- domain in stark contrast to the behavior observed on non-ferroelectric substrates. This performance is the result of the fast increase of positive charge in the P^- domain due to the pyroelectric effect and the restructuring of the surface doping between $MoSe_2$ and the LN substrate. Overall, our research shows that monolayer TMD sheets can be engineered to create a p-n homojunction by engineering the underlying ferroelectric domains with sensitive response to laser power and ambient temperature. This approach has laid the foundation for creating active electrically driven and controlled optoelectronic components on LN integrated photonic platforms with the ultimate goal of electrically driven optical sources within LN photonic chips.

After introducing the interesting optical and electronic properties of monolayer TMDs, we have turned our focus to optoelectronic devices applications. In Chapter 5, the monolayer $MoTe_2$ based LED and photodetector have been demonstrated. The simplified Gr/hBN/$MoTe_2$ structure has been employed to realize high efficiency performance. When operate as an LED, the device shows extremely high performance with an EQE of ~9.5% at 83 K. By modulating the Femi level in few layer graphene, electrons can be injected efficiently into the monolayer $MoTe_2$. The hBN layer serves as a tunnelling barrier to reduce the current leakage by confine electrons within $MoTe_2$. It is expected that the device efficiencies can be further improved by creating multiple QWs and delicate tuning of the hBN barrier thickness.[2] When the device operated as a photodetector, large photoresponsivity and fast response time have been achieved. Owing to the hBN barrier layer, the dark current has been significantly suppressed, leading to high responsivity for this vertical stacking structure.

In Chapter 6, an AC driven monolayer WS_2 LED has been demonstrated. Double pulsed light emission pattern has been extracted. However, those double pulsed light

emissions exhibit an unsymmetrical decay behaviour with one ultralong decay and one short fast decay. We attribute this difference to the nature of the initial doping in monolayer WS_2. The long decay process corresponds to the hole injection cycle, while the fast decay process relates to the electron injection cycle. Temperature dependent TREL and room temperature TREL measurements with different 2D materials and different initial doping levels confirm that the initial doping level plays an important role in carrier injection dynamics, leading to long emission decay. The light emission efficiency can be enhanced compared with previous reported double fast decay AC LEDs.[3] The unsymmetrical recombination concept demonstrated in this work can be extended to other 2D materials under the AC driving LED structure to achieve a larger emission area and reduced fabrication cost. Besides, the wavelength tunable EL emission has been demonstrated under low temperature. The quantum efficiency of defect EL emission is 24.5 times larger than free exciton and trion EL emission. The ability to realize high intensity defect emission opens immense opportunities in the field of defect engineering and defect based single photon emission. In addition, we have also successfully distinguished the different defect levels and their evolution in real space by using the separate injection feature of AC driving method. Those defect levels can be assigned to negatively charged sulfur vacancies. Our results not only reveal important insights into the AC LED working principle and thus provide a general guideline for rationally designing high performance AC driving LED, but also lead to a new route to study the defect states and defect engineering for the tunable LED devices.

7.2. Perspectives for future work

Based on the results and knowledge achieved through this dissertation, we have identified the challenges and potential research opportunities in the field.

7.2.1. Optoelectronic applications based on surface ferroelectric modulation

In Chapter 4, we have introduced the ferroelectric modulation in 2D materials. The domain inverted lithium niobate causes changes in the TMDs due to electrostatic doping resulting from the remnant polarization from the substrate. The excitons dissociate rapidly at the interface between the P^+ and P^- domains due to the built-in

electric field. Therefore, the domain engineering of the lithium niobate substrate could spatially dope the 2D materials on its surface, achieving the spatially p-n junction in the materials. This substrate modulated heterostructures could potentially use for photodetectors or even electrically driven on-chip light source. However, the challenge here is to tune ferroelectric effect of lithium niobate substrate so that could modify the doping level of above 2D materials to achieve the adjustable p-n junction. Although, temperature could be one possible way through pyroelectric effect, the modulation range is limited. Therefore, how to modulate ferroelectric for lithium niobate would be a worthy point towards ferroelectric switching future optoelectronics applications.

7.2.2. Infrared light emitting devices based on black phosphorene

Infrared light spectral range is the vital part of wavelength band for optical communication and thermal imaging. It has been immensely used for civilian and military applications. Black phosphorus (BP) emerges as an another powerful 2D materials with the bandgap ranging from ~0.3 eV to ~1.8 eV.[4, 5] The tuneable bandgap with different thicknesses covers the visible to mid-infrared spectral range, bridging the gap between graphene and TMDs. For example, five layers of BP gives optical emission at 1550 nm, which is located in optical communication window. However, its stability issue greatly limits its optoelectronic application in terms of device fabrications. Although BP has been intensively studied since 2014, the demonstrated applications are mainly focused on its photodetection properties. The less than five layered BP based LEDs have not been barely reported, largely due to difficulties in fabrication process especially for mono layer BP devices. With the technological development in BP stabilization and large area material growth, more efforts may be devoted to BP based device applications.

7.2.3. High efficiency AC driven perovskite light emitting diodes and lasers

Perovskite have currently attracted widespread interest from both academic community and industries as a promising candidate for the next generation optoelectronic devices. The perovskite-based light emitting diodes has been reported with external quantum efficiency exceeding 20 percent.[6] Compared to the bulk

perovskite, two-dimensional perovskite films have gained further attention because of their unique structural characteristics and quantum confinement effect. Combined with appropriate optical cavity design as well as the AC driven method, there may be great opportunity to demonstrate high efficiency two-dimensional perovskite-based light emitting diodes and lasers.

References

1. J. Yang *et al.*, Atomically thin optical lenses and gratings. *Light: Science & Applications* **5**, e16046-e16046 (2016).
2. F. Withers *et al.*, Light-emitting diodes by band-structure engineering in van der Waals heterostructures. *Nature materials* **14**, 301-306 (2015).
3. D.-H. Lien *et al.*, Large-area and bright pulsed electroluminescence in monolayer semiconductors. *Nature communications* **9**, 1-7 (2018).
4. J. Lu *et al.*, Light–matter interactions in phosphorene. *Accounts of chemical research* **49**, 1806-1815 (2016).
5. J. Yang *et al.*, Optical tuning of exciton and trion emissions in monolayer phosphorene. *Light: Science & Applications* **4**, e312-e312 (2015).
6. K. Lin *et al.*, Perovskite light-emitting diodes with external quantum efficiency exceeding 20 per cent. *Nature* **562**, 245-248 (2018).